The role of soluble growth factors and inhibitors in the vascularisation of lymphoid organs

Roger Leigh

PhD

University of York

Biology

September 2011

Abstract

Lymph nodes contain complex vascular networks composed of lymphatic and blood vessels. The blood vasculature contains specialised high endothelial venules functioning to permit the efficient entry of blood-borne lymphocytes into the node, while the lymphatics contain antigen-presenting cells draining from tissues. In contrast to the well understood cellular interactions and signalling mechanisms driving development of the stromal networks upon which immune cell interactions occur, the processes by which the complex vascular networks develop are poorly characterised. This study aimed to determine the mechanisms by which vascularisation of lymph node anlagen occurs during development.

The structure of developing lymph nodes was studied using confocal microscopy to observe the organisation of basement membranes and the different cell types involved in the process. Expression of angiogenesis-related genes was studied using quantitative real-time PCR and microarrays. No evidence for vascularisation of the anlagen was found, though the markers used may not have stained nascent vessels. The lymph sac surrounding the anlagen was shown to exist as a two-layered structure composed of anastomosing blood and lymphatic endothelium.

In vitro models of vasculogenesis and angiogenesis were developed utilising human umbilical vein endothelial cells in three dimensional collagen gels, with and without smooth muscle coverage. A spheroid-based model of angiogenesis was used to study the net angiogenic environment in developing E14.5–E17.5 anlagen, which determined that a net anti-angiogenic environment existed at all timepoints in the lymph nodes and thymus, but not skin. Additionally, tensional forces were observed to affect angiogenic sprouting in addition to soluble growth factors.

As a consequence of the double-layered lymph sac observed *in vitro*, and the influence of anti-angiogenic factors and tensional forces observed *ex vivo*, a model of lymph node development involving anlagen patterning and vascularisation as a result of condensation-induced tensional forces was proposed, complementary to soluble growth factor-driven angiogenesis.

Contents

List of Figures

List of Tables

Acknowledgements

I would like to thank the BBSRC and AstraZeneca for funding this work; Dr Beverley Isherwood at AstraZeneca for help with HUVEC cell culture and high-throughput imaging of collagen gels; Fiona Frame for kind donation of fluorescent protein plasmids with mammalian selection; Dr Bridget Glaysher for collaboration on *in vitro*FRC differentiation; Matt Lakins for assistance with making and imaging collagen gels, and plasmid midipreps; Meg Stark for technical assistance with TEM sample preparation and imaging; Dr Abraham Stroock and his laboratory at Cornell University, Ithaca, NY, USA for sharing their micromoulding and microfluidic techniques; Dr Tom Cupedo and his laboratory at Erasmus University Medical Center, Rotterdam, Netherlands for the sharing of their human lymph node microarray data; Dr Jane Dalton and Dr Lynette Beattie for their helpful comments on draft copies of this thesis, and special thanks to Dr Mark Coles and Dr Peter O'Toole for supervising this work over the last four years.

Declaration

This thesis has not previously been accepted in substance for any degree and is not being concurrently submitted in candidature for any degree other than Doctor of Philosophy of the University of York. This thesis is the result of my own investigations, except where otherwise stated. Other sources are acknowledged by explicit references. I hereby give consent for my thesis, if accepted, to be made available for photocopying and for inter-library loan, and for the title and summary to be made available to outside organisations.

Signed ..... (candidate)

Date .....

Chapter 1

Introduction

1.1 Background to project

During embryonic development, the embryo undergoes many changes as it grows, from the general patterning of body axes to the differentiation of cells into the specialised types which will fulfil a unique role in the different organs of the developed adult. In addition to tissues and organs located at specific sites in the body, the nervous and vascular systems initially develop in a limited number of locations, but then proceed to migrate and ramify thoughout the body to give rise to the fully-developed nervous, blood and lymphatic vascular systems found in the adult (Adams and Alitalo, 2007). The process of vascular development has been studied in great detail, and today many of the key signalling molecules, receptors and cell types involved are well known. However, the majority of this work has used model systems such as the murine eye, chick chorioallantoic membrane, and zebrafish, as well as various simple *in vitro* models (Bishop, Bell *et al.*, 1999; Eichmann, Yuan *et al.*, 2005b; Gerhardt, Golding *et al.*, 2003; Vailhé, Vittet *et al.*, 2001). While these systems have been useful in the dissection of the signalling pathways, and the identification of the various molecules involved, the processes and mechanisms by which organs of the mammalian body become vascularised during development have been subjected to comparatively little investigation.

Lymph nodes (LNs) are secondary lymphoid organs, whose purpose is understood to be the enabling of efficient interaction between cells of the immune system, including antigen presenting cells (APCs) such as dendritic cells and macrophages (MØs), and T and B lymphocytes, in order to effectively initiate an immune response (Creusot, Mitchison *et al.*, 2002). Without the existence of such organs, the chance of an encounter of a T cell with an APC or B cell bearing an antigen specific for its T cell receptor is relatively small. The structure and organisation of a lymph node is related to its highly specialised function (Willard-Mack, 2006), and the cellular interactions and molecular mechanisms governing the development of secondary lymphoid organs are now well established (van de Pavert and Mebius, 2010). How-

ever, two major gaps remain. Firstly, the events which establish the specific sites of development are yet to be determined, though the subsequent steps involving development of the stroma and recruitment are well understood. The second gap is in our understanding of how the resulting structure is vascularised. The developed node is highly vascularised, containing an elaborate network of specialised *high endothelial venules* critical for its function, yet how this vascular network is established is not clear. Likewise, the node is also connected to afferent and efferent vessels of the lymphatic system, and while the node develops in the context of a lymph sac, how this is connected to the lymphatic system is also poorly understood.

LN development *in vivo* provides much information regarding changes in cellular organisation and structure over time (Mebius, 2003; van de Pavert and Mebius, 2010). However, dissecting the specific cellular interactions and signalling pathways involved is rather difficult, if not intractable, due to difficulties in manipulating a very complex system. While much work identifying the molecular players involved in vascular development has used animal models and selective knockout of genes to elucidate their function, in many cases the signalling pathways and mechanisms involved are not tractable *in vivo*, the principal problem being that a nonfunctional vascular system is simply incompatible with life past a certain developmental point, and hence many knockouts are embryonic lethal, resulting for example in œdema and hæmorrhage (Aszódi, Legate *et al.*, 2006). Of the genes discussed in the context of angiogenesis and LN development, only the Vegfa and Dll4 genes are heterozygous lethal, in the case of Vegfa due to haploinsufficiency, and in the case of Dll4 with incomplete penetrance, having complete lethality only on an inbred background(Carmeliet, Ferreira *et al.*, 1996; Ferrara, Carver-Moore *et al.*, 1996; Gale, Dominguez *et al.*, 2004). Nevertheless, *in vivo* models have been essential for the identication of the key components of signalling pathways affecting angiogenesis and LN development, and will continue to play an important role, particularly with the generation of mice with mutated or knocked-out genes as new genes are identified which may affect these processes. While useful, no *in vitro* model can replace *in vivo* models for the study of the functional role of particular genes and proteins in the context of a complete, living organism. However, an *in vitro* model of angiogenesis would allow the dissection of specific signalling pathways with an absent or reduced requirement for a functional vascular system, and hence permit the identification and study of mechanisms which are not feasible using *in vivo* models. In order to understand the developmental processes which drive the vascularisation of LNs, *in vitro* modelling may provide new insights into the mechanisms involved, due to such systems being readily amenable to manipulation, and additionally allowing single aspects to be studied in relative isolation.

In order for the process of LN vascularisation to be understood in context, the structure and organisation of the vascular system will be discussed in brief, followed

by the processes of vasculogenesis and angiogenesis which underlie its development and maintenance. The structure and function of the lymph node and our current understanding of the mechanisms underlying its development will then be covered. The genes and proteins relating to vascular and lymphoid development and function referred to in this and later chapters are summarised in Table 1.1.

1.2 The vascular system

The primary purpose of the vascular system is to deliver oxygen and nutrients to tissues, without which a tissue could be no larger than approximately $1\,\mu m^3$ due to oxygen diffusion being a limiting factor, resulting in hypoxia and necrosis in the centre of larger tissues (Chan and Giaccia, 2007). Inter-tissue signals are additionally communicated via the vascular system, through the delivery of endocrine signals such as hormones and growth factors, and the delivery of cells from one tissue to another.

1.2.1 Organisation, structure and function

The mammalian vascular system is responsible for the transport of fluid in the body, and is divided into two major compartments, the blood and lymphatic vasculature. The blood vascular system circulates blood, which actively pumped by the heart muscle, while the lymphatic vascular system passively drains lymph from tissues, ultimately returning the drained fluid to the blood circulation as the lymphatics empty into the subclavian vein (Lewis, 1905; Oliver, 2004).

The blood transports water, ions, oxygen, metabolites and cells to almost every part of the body, and removes the waste products of metabolism, carbon dioxide and cells. The blood vasculature is intimately associated with the basic functioning of every tissue, and is hence highly specialised for the tissue-specific functionality required of it, be it for example transport of absorbed nutrients (small intestine), storage and mobilisation of lipid deposits (adipose tissue), satisfying glucose and oxygen demand (brain), filtration and processing of waste products (kidney and liver), delivery of lymphocytes (thymus, lymph nodes and spleen), or delivery of immature macrophages and dendritic cells (all tissues). The lymphatic vasculature is responsible for return of interstitial fluid to general circulation and transport of dendritic cells and macrophages from tissues, particularly following their activation after immunological insult, which results in their leaving the tissue and entering the lymph in order to be transported to draining lymph nodes in order to engage in the initiation of an immune response with lymphocytes, which enter the node from the blood (Willard-Mack, 2006). The lymphatics are also required for the return of lymphocytes

Table 1.1: Genes relating to vascular function and remodelling.

Category	*Gene*	*Name*
Lymph node development and maintenance	Ccl19	Chemokine (C-C motif) ligand 19
	Ccl21	Chemokine (C-C motif) ligand 21
	Cxcl13	Chemokine (C-X-C motif) ligand 13
	Il7	Interleukin 7
	Lta	Lymphotoxin α
	Ltb	Lymphotoxin β
	Ltbr	Lymphotoxin β receptor
	Tnfrsf11a	Tumour necrosis factor receptor superfamily, member 11a; TRANCER; RANK
	Tnfrsf11b	Tumour necrosis factor receptor superfamily, member 11b (osteoprotegerin)
	Tnfsf11	Tumour necrosis factor (ligand) superfamily, member 11; TRANCE; RANKL
	Icam1	Intercellular adhesion molecule 1
	Madcam1	Mucosal vascular addressin cell adhesion molecule 1
	Vcam1	Vascular cell adhesion molecule 1
Angiogenesis related	Angpt1	Angiopoietin 1
	Angpt2	Angiopoietin 2
	Flt1	FMS-like tyrosine kinase 1; VEGFR1
	Kdr	Kinase insert domain protein receptor; VEGFR2; FLK1
	Pdgfa	Platelet derived growth factor, A polypeptide
	Pdgfb	Platelet derived growth factor, B polypeptide
	Pdgfc	Platelet-derived growth factor, C polypeptide
	Pgf	Placental growth factor
	Vegfa	Vascular endothelial growth factor A
	Vegfb	Vascular endothelial growth factor B
	Vegfc	Vascular endothelial growth factor C
Angiogenesis inhibitors	Serpinf1	Serine (or cysteine) peptidase inhibitor, clade F, member 1; pigment epithelium derived factor (PEDF)
	Thbs1	Thrombospondin 1

Table 1.1: Genes relating to vascular function and remodelling *(continued)*.

Category	*Gene*	*Name*
Proteases	Mmp*n*	Matrix metallopeptidase *n*
	Adam*n*	A disintegrin and metallopeptidase domain *n*
	Adamts*n*	ADAM metallopeptidase with thrombospondin type 1 motif *n*
	Cts*a*	Cathepsin *a*
MMP inhibitors	Timp2	Tissue inhibitor of metalloproteinase 2
	Timp3	Tissue inhibitor of metalloproteinase 3
Hypoxia related	Hif1a	Hypoxia inducible factor 1, α subunit
	Arnt	Aryl hydrocarbon receptor nuclear translocator; HIF-1β
	Ccl2	Chemokine (C-C motif) ligand 2; monocyte chemoattractant protein 1 (MCP-1)
	Csf1	Colony stimulating factor 1 (macrophage)
	Cxcl12	Chemokine (C-X-C motif) ligand 12
	Epas1	Endothelial PAS domain protein 1
	Ldha	Lactate dehydrogenase A
	Ldhb	Lactate dehydrogenase B
	Slc2a1	Solute carrier family 2 (facilitated glucose transporter), member 1; GLUT-1
	Angpt1	Angiopoietin 1
	Angpt2	Angiopoietin 2
	Flt1	FMS-like tyrosine kinase 1; VEGFR1
Endogenous controls	B2m	β-2 microglobulin
	Gapdh	Glyceraldehyde-3-phosphate dehydrogenase
	Hprt1	Hypoxanthine guanine phosphoribosyl transferase
	Leng8	Leukocyte receptor cluster (LRC) member 8

to the blood after exiting a lymph node. This process is further elaborated in Section 1.3.

The blood circulation is effectively a *closed loop*. Blood pumped by the heart muscle flows through a branching network of arteries. Upon entering a tissue or organ, an artery branches into smaller arterioles which then repeatedly branch into a capillary bed of very small vessels (Eichmann *et al.*, 2005b). The vessels of the capillary bed subsequently merge to form larger venules which again merge together to form even larger veins. Blood is returned to the heart via the venous circulation to complete the loop.

The capillary bed is the primary site for exchange of gases, nutrients and metabolites, as well as cells. The arterial vessels are subject to a high pressure, pulsatile fluid flow as a consequence of the pumping action of the heart, while veins experience a smooth low pressure flow (Eichmann *et al.*, 2005b; Jones, le Noble *et al.*, 2006). The capillary bed separates these two systems, and is responsible for smoothing the pulsatile flow, and having a pressure differential imposed upon it. Restricted flow in the capillaries, due to the limited capillary diameter, and the fact that the capillaries are somewhat leaky, causes fluid entering the capillary bed to be forced both through the capillaries and out into the surrounding tissue. The negative pressure at the venous side consequently causes some interstitial fluid to re-enter the capillaries and flow into the veins, but not all. The remaining interstitial fluid in the tissue, if not removed, would result in *œdema* (swelling due to fluid accumulation), reviewed by Alitalo, Tammela *et al.* (2005). The lymphatic system is responsible for the draining of this excess interstitial fluid and its return to the main circulation. While the lymphatic system is also closed, it is not a loop but a branched network of blind-ending tubules. Fluid and cells may enter the blind endpoints of the network from within a tissue, and travel along it as the tubules merge to form increasingly larger vessels (Alitalo *et al.*, 2005). Fluid flow in lymphatic vessels, and to an extent in veins, is passive and hence both of these vessels contain valves which prevent the fluid from flowing backwards. Flow is assisted where the vessels pass through skeletal muscle, whose contraction squeezes the vessel, forcing the fluid to flow in a forward direction, reverse flow being prevented by the valves.

Arteries, veins, capillaries and lymph vessels have common features in their structure and cellular organisation, as well as differences owing to the requirements of their differing function. All of the vessels contain an inner lining with endothelial cells (ECs), flattened cells which make contact with the fluid the vessel carries on their apical (lumenal) side, and the underlying extracellular basement membrane on their basal side. Adherens junctions contact adjacent neighbouring cells on all sides, providing a mostly watertight barrier to prevent unwanted egress of the vessel contents. These cell–cell contacts are reduced in the capillary bed, where the vessels become leakier (Dejana, Valiron *et al.*, 1997).

Vascular smooth muscle

Vascular smooth muscle cells (VSMCs, also known as mural cells) surround the blood endothelial cells (BECs) to provide structural integrity, as well as to regulate vessel diameter (vasodilation and constriction) and permeability (Bergers and Song, 2005). Smooth muscle is also responsible, along with ECs, for the secretion and maintenance of the vascular basement membrane separating them, and also critical in maintaining the stability of the vessel. Vascular smooth muscle may be identified by expression of a number of markers, including desmin, α-smooth muscle actin (α-SMA), neuron-glial 2 (NG2) and platelet-derived growth factor receptor β (PDGFRβ) (Bergers and Song, 2005; Ozerdem, Grako *et al.*, 2001). Pericytes are also believed to play a role in sprouting angiogenesis, where they may guide the tip of the endothelial sprout (Bergers and Song, 2005). While platelet-derived growth factor (PDGF) is believed to be the main molecular regulator of VSMCs, being attracted to PDGF-secreting ECs, vascular endothelial growth factor (VEGF) has been found to play the role of a negative regulator in PDGF-mediated angiogenesis involving vascular endothelial growth factor receptor positive ($VEGFR^+$) VSMCs (Greenberg, Shields *et al.*, 2008). Pericyte abnormalities can result in poor coverage of vessels, leading to loss of vessel integrity and fluid leakage. This is one reason for the tortuous and leaky vasculature observed in some tumours (Morikawa, Baluk *et al.*, 2002).

In arteries and veins, smooth muscle and elastic fibres surround the vessel, providing mechanical support to prevent the vessel from rupturing under the high pressure pulsatile flow in arteries, or collapsing under negative pressure in veins. The smooth muscle may additionally constrict to regulate blood pressure and flow. Capillaries have a much sparser distribution of smooth muscle cells, with coverage being limited to around one smooth muscle cell to ten endothelial cells. In capillaries, these cells are referred to as *pericytes*, and are also involved in maintaining vascular integrity and regulating flow by constricting and opening the vessels they surround as they contract and relax (Bergers and Song, 2005).

Extracellular matrix

The basement membrane separating the inner endothelial and outer smooth muscle layers is composed of several proteins, the primary components being collagen IV, the proteoglycan perlecan, laminin, fibronectin and additional linker proteins such as the non-collagenous glycoprotein nidogen, other components including collagen I and the proteoglycan decorin (Davis and Senger, 2005). Elastins are also found, but are found primarily in larger vessels. The basement membrane is secreted by both ECs and VSMCs and exists as a sheet sandwiched between the two cell layers, providing a strong surface for the basal surface of the endothelial layer to adhere. The smooth muscle layer is also able to adhere to the basement, and in capillaries the two cell types are additionally also able to make direct contacts with one another

through holes in the membrane (Armulik, Genové *et al.*, 2011). Integrin $\alpha_2\beta_1$ is expressed by both ECs and VSMCs, enabling both of the cellular components of blood vessels to interact with collagen I, IV and laminin (Languino, Gehlsen *et al.*, 1989). ECs also express $\alpha_5\beta_1$, which binds fibronectin. Integrin signalling is required for establishment of EC polarity (Languino *et al.*, 1989).

Laminin, collagen and fibronectin are all capable of polymerising to form independent networks, which may be in close proximity and yet not physically interconnected. A variety of adapter and linker proteins exist to bridge the different networks, including perlecan (connecting collagen IV and laminin), nidogen (also known as entactin; it binds collagen IV, laminin, fibronectin, and more), and fibronectin can bind collagen IV directly (Aszódi *et al.*, 2006; Davis and Senger, 2005). The result is a complex arrangement of different matrix molecules capable of participating in many different interactions. An overview of how collagen I polymerisation proceeds to form increasingly larger, higher-order structures is shown in Figure 1.1(A). The composition and structure of some of the most common basement membrane components are shown in Figure 1.1(B), and their properties are discussed in more detail, below. Collagen, laminin and fibronectin all promote EC survival, growth, migration and tube formation (Kim, Bakre *et al.*, 2002).

Collagen IV

Collagen IV is a major component of the basement membrane, existing as a heterotrimer composed of a combination of six different α chains. The process of matrix formation has been reviewed by Hudson, Tryggvason *et al.* (2003); the non-collagenous C-terminal domains of three α chains associate to form a trimer, the collagenous domains zipping up to form a triple helix. The non-collagenous domains of two trimers can dimerise to form a hexamer, and the N terminal end of the triple helix can associate with three other ends to form a tetramer. Additionally, the triple helix is capable of supercoiling, winding tightly around other triple helices. Through these three mechanisms of self-association, assembly of large networks is possible, the structure of which may be altered by the use of different α chains.

While not strictly required for basement membrane assembly, collagen IV has been found to be required for maintenance of vascular integrity under conditions such as mechanical stress and fluid pressure. Vessels in heterozygotes are weaker, leading to hæmorrhage and death by E11.5 (Aszódi *et al.*, 2006).

Fibronectin

Fibronectin plays an important role in matrix turnover, as well as in regulating EC behaviour as discussed above. Its multiple effects include influencing the cell cycle (Sechler and Schwarzbauer, 1998) and modulating the activity of sequestered growth factors, *e.g.* VEGF complexed with fibronectin has greater activity than unbound

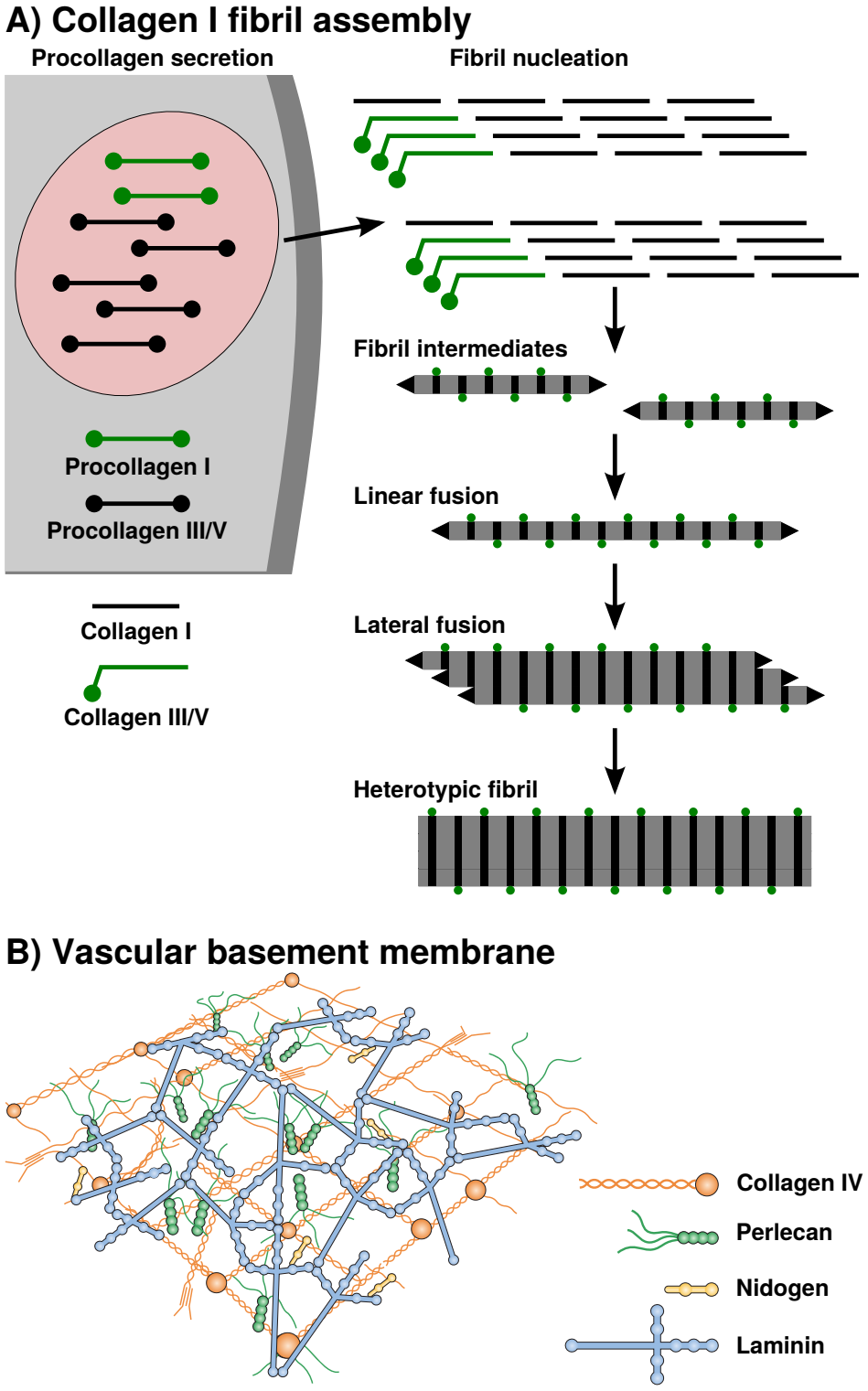

Figure 1.1: Matrix polymerisation and organisation. The formation of complete collagen type I fibrils is shown in (A). Secreted in precursor form, the enzymatic cleavage of the C- and N-terminal ends of both procollagen I and procollagen III or V produce tropocollagens capable of fibrillogenesis. Collagen III or V trimers are required to organise collagen I fibrils correctly during nucleation. Following the formation of fibril intermediates, linear and lateral fusions increase the length and width of fibrils to produce a complete heterotypic fibril. The structural organisation of the vascular basement membrane is shown in (B). Collagen IV and laminin are shown to assemble into separate networks, linked together through both nidogen and perlecan. A is after Aszódi *et al.* (2006); B is from Sorokin (2010).

VEGF (Wijelath, 2002), enhancing EC migration. Inhibition of fibronectin deposition or disruption of the matrix inhibits EC growth. Additionally, fibronectin polymerisation also regulates matrix turnover and retention of other components such as thrombospondin. Inhibition results in loss of thrombospondin and inhibition of collagen I and III deposition, which also causes loss of existing collagen I fibrils, thus regulating extracellular matrix (ECM) turnover and stability (Sottile and Hocking, 2002). As for collagen IV, fibronectin knockout is embryonic lethal as a result of vascular defects (Aszódi *et al.*, 2006)..

Fibronectin also has the interesting property of being sensitive to stress forces within the ECM, having cryptic integrin binding sites which are exposed upon mechanical deformation (*i.e.* extension), a mechanotransduction mechanism to transduce ECM stress into altered integrin binding, and consequent cellular response (Jean, Gravelle *et al.*, 2011).

Laminin

Like collagen IV, laminin is one of the principal components of the basement membrane. Laminin exists in the basement membrane as a heterotrimer, having a cross shape, and composed of α, β and γ chains, multiple types of each chain giving rise to 15 different isoforms, reviewed by Hallmann, Horn *et al.* (2005). The α subunit isoforms are expressed in both developmentally- and tissue-specific patterns, with the regulation of isoform expression believed to confer tissue-specific functionality to the matrix. Basement membrane expresses laminin 8 ($\alpha4\beta1\gamma1$) and laminin 10 ($\alpha5\beta1\gamma1$) (Hallmann *et al.*, 2005). Laminin 8 is expressed in all basement membranes, while laminin 10 is expressed during development and under inflammatory conditions. Laminins self-associate to form supra-molecular assemblies, as a result of dimerisation or trimerisation between the C- and N- termini of its component α, β and γ chains. Laminin in the vascular basement membrane is secreted by ECs, and potentially also by pericytes and VSMCs (Hallmann *et al.*, 2005). Knockout of $\alpha4$ results in defects in basement membrane, including in the deposition of other membrane components (Thyboll, Kortesmaa *et al.*, 2002).

Laminin contains sites which are known to interact with a variety of other ECM molecules, including perlecan and nidogen to cross link the collagen IV and laminin networks (Aszódi *et al.*, 2006). It also allows cell–matrix interactions via cell surface molecules, including integrins and α-dystroglycan. Integrins and α-dystroglycan both connect intracellularly to the actin cytoskeleton, and binding of laminin results in the activation of multiple signalling pathways (Aszódi *et al.*, 2006; Sorokin, 2010). In consequence, laminin binding can result in changes to cellular behaviour and function.

Proteoglycans

Proteoglycans consist of a core protein with glycosaminoglycan side chains, which regulate the hydration and osmotic properties of ECM (Rozario and DeSimone, 2010). They additionally interact with matrix components, growth factors and cell surface receptors.

Perlecan The most abundant heparan sulphate proteoglycan, cross-linking the matrix through binding of multiple components, including laminin, collagen IV, entactin/nidogen, fibulin, collagen XVIII/endostatin (Aszódi *et al.*, 2006). It additionally binds integrins, alpha-dystroglycan and growth factors which include fibroblast growth factors (FGFs), VEGFs, and PDGF. While not required for development, it is required to preserve the integrity of the basement membrane under mechanical stress (as for collagen IV) (Aszódi *et al.*, 2006). It acts to stabilise mural cells by sequestering basic fibroblast growth factor (bFGF), promoting proliferation and angiogenesis, while also inhibiting proliferation via the tumour suppressor PTEN (Aszódi *et al.*, 2006; Garl, Wenzlau *et al.*, 2004).

Nidogen Expressed by the mesenchyme and ECs in all embryonic basement membranes, having multiple binding partners including collagen IV, laminin, fibronectin, elastin (larger arteries) and perlecan (Aszódi *et al.*, 2006). Its most significant role is probably the cross-linking and stabilisation of laminin and collagen IV networks, which is stabilised by the formation of covalent bonds by transglutaminase 2 (Ho, Böse *et al.*, 2008). Additionally, it contains an RGD motif for integrin engagement.

1.2.2 Vascular development

The early stages of vascular development have been studied extensively, with the stages having been reviewed by Eichmann *et al.* (2005b) and Adams and Alitalo (2007), and illustrated in Figure 1.2. The vascular system arises as the result of the differentiation of hæmangioblasts from the mesoderm, multipotent progenitors of both hæmatopoietic and angioblast lineages, which subsequently aggregate and differentiate to form *blood islands*, small pockets of hæmatopoietic cells lined with endothelium. Fusion of the blood islands leads to the formation of the *primary capillary plexus*, an interconnected endothelial network (vasculogenesis). Subsequent elaboration and remodelling of this network (angiogenesis) results in the formation of a hierarchical network. The major vessels consist of the dorsal aorta and cardinal veins, which are largely assembled from angioblasts (Adams and Alitalo, 2007). The complete blood vascular system is subsequently formed as a result of further outgrowth from this initial network.

The cardinal veins are of particular importance due to being the origin of the cells forming the jugular lymph sacs, which is the origin of the interconnected (but

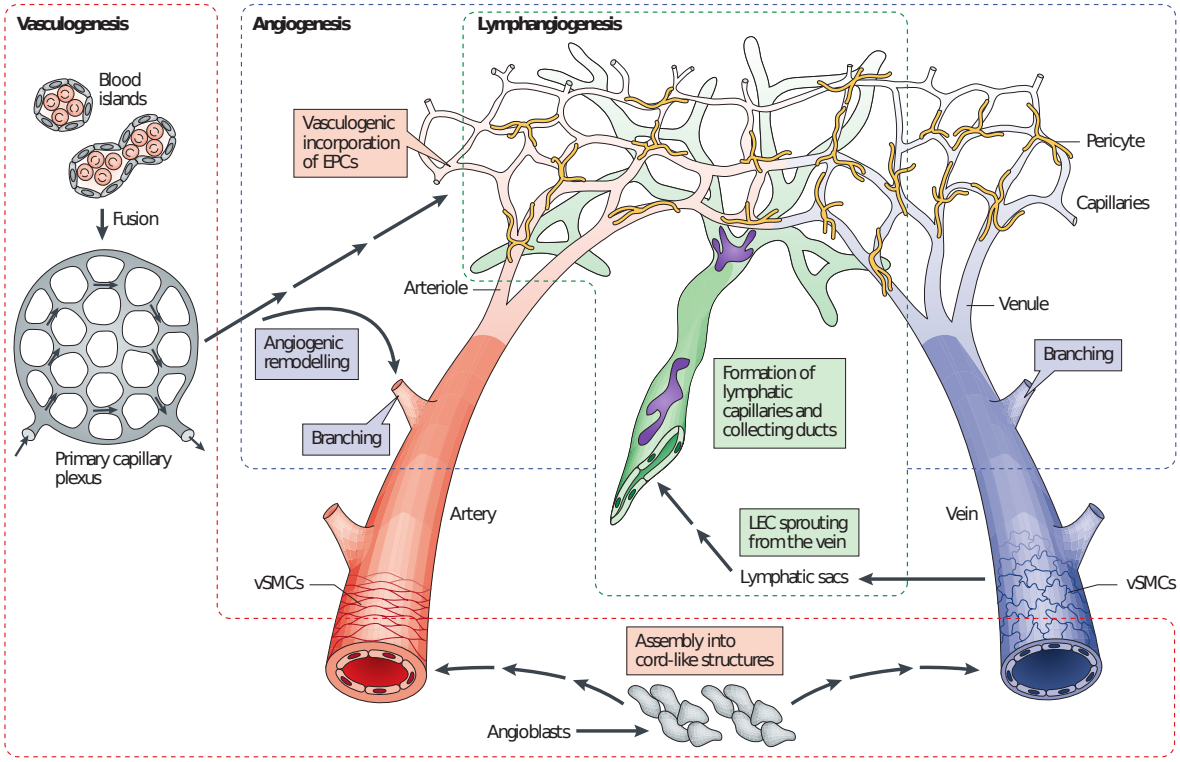

Figure 1.2: Vascular development. Blood islands formed from the mesenchyme fuse to give rise to the primary capillary plexus. Angiogenic remodelling of the plexus results in the formation of the hierarchical vasculature, containing arteries, veins, arterioles, venules and capillary beds. Larger arteries and veins are assembled directly from angioblasts rather than through remodelling. Arteries and veins gain coverage from smooth muscle layers, while capillaries recruit pericytes to stabilise the networks. Later, the lymphatic system of blind-ended collecting ducts and capillaries develops alongside the vascular system, but does not have smooth muscle coverage. From Adams and Alitalo (2007).

separate) lymphatic system, and also a site for subsequent lymph node development (Sabin, 1913; Srinivasan, Dillard *et al.*, 2007), discussed in more detail in Section 1.3.

1.2.3 Vasculogenesis

Vasculogenesis, the *de novo* formation of a capillary plexus from angioblasts, occurs in the developing embryo. Subsequently angiogenesis, branching and outgrowth of the existing network, is responsible for the extension and modification of this network. Both processes have been reviewed previously (Bohnsack and Hirschi, 2004; Davis, Bayless *et al.*, 2002; Eichmann *et al.*, 2005b). Capillaries are formed as endothelial cells (ECs) elongate and join end-to-end. The formation of open lumens occurs inside ECs, which endocytose their own plasma membrane and construct an intracellular vacuole through vesicle fusion to create a tube running through the interior of the cell (Davis and Camarillo, 1996; Kamei, Saunders *et al.*, 2006). Patterning of blood vessels involve many of the same signalling and positive and negative guidance cues used for patterning neurons, such as netrins and semaphorins (Adams and Alitalo, 2007; Freitas, Larrivée *et al.*, 2008; Suchting, Freitas *et al.*, 2007), leading to the general hypothesis that the nervous and vascular systems are developmentally related, and that their gross structure may be defined using the same signals.

Over the last two decades, many of the extracellular signalling molecules, transmembrane receptors, and components of the intracellular signalling pathways controlling EC proliferation, migration, differentiation, and survival have been elucidated, though our understanding is still incomplete. Reviews by George Davis outline the mechanisms governing endothelial cell lumen formation and tube assembly, from integrin–matrix interactions to activation of Rho GTPases, Cdc42 and Rac1 (Davis, Koh *et al.*, 2007; Davis and Senger, 2005). The process is additionally dependent upon VEGFR2 and VEGF signalling (Shalaby, Rossant *et al.*, 1995).

Subsequently, pericytes are recruited to the nascent vascular network via PDGF signalling, and the association of ECs and pericytes results in the production and deposition of basement membrane proteins, as well as upregulation of integrins, resulting in stabilisation of the network (Stratman, Malotte *et al.*, 2009a; Stratman, Schwindt *et al.*, 2010). Later, arterial and venous differentiation occurs, and this was previously shown to be a result of blood flow (le Noble, Moyon *et al.*, 2004), however later work has shown that it is also a result of Notch and Eph/Ephrin signalling, the principal effect of which is to downregulate the expression of VEGFR2 in order to limit cellular responsiveness to VEGF (Gridley, 2007; Harrington, Sainson *et al.*, 2008; Siekmann, Covassin *et al.*, 2008).

1.2.4 Angiogenesis

Angiogenesis is the outgrowth of an established vascular network, typically by the sprouting of new outgrowths. However, other forms of angiogenesis also occur, including intussception, the splitting of a vessel by insertion of tissue pillars (Adams and Alitalo, 2007), and more recently a third form, "looping angiogenesis", was described, acting through the generation of tensional forces in granulation tissue (Kilarski, Samolov *et al.*, 2009).

Pro-angiogenic factors

Basic fibroblast growth factor (bFGF) and vascular endothelial growth factor (VEGF) are the two main inducers of EC proliferation and differentiation (Bohnsack and Hirschi, 2004; Eichmann *et al.*, 2005b). Both VEGF and bFGF act synergistically to stimulate angiogenesis, affecting EC migration along growth factor gradients, proliferation and survival. bFGF also induces EC expression of VEGF. VEGF is required for tube formation (Seghezzi, Patel *et al.*, 1998), existing in several variants (VEGF-A–D and placental growth factor (PlGF), as well as splice variants), which bind to the VEGF receptors, VEGFR1 (FLT1), VEGFR2 (KDR or FLK1) and VEGFR3 (FLT-4) as well as neuropilins 1 and 2 (Dormer and Beck, 2005; Neufeld, Cohen *et al.*, 1999). VEGF-A has six splice variants in the mouse, of which five have been observed *in vivo*, and several of which are, along with bFGF, heparin binding and hence may be sequestered by the ECM with differing matrix affinities and biological activities, and released by matrix proteolysis (Lohela, Bry *et al.*, 2009; Park, Keller *et al.*, 1993). The VEGF-A splice variants and their properties are listed in Table 1.2. The relationship between the different ligands and receptors is complex, due to the differing affinities of the receptors for their ligands, as well as their differing intracellular tyrosine kinase activities. VEGFR1 has a higher affinity for VEGF-B, while VEGFR2 has a higher affinity for VEGF-A (Fischer, Mazzone *et al.*, 2008). VEGF-A plays an important role in the differentiation and chemotaxis of ECs through VEGFR2, though its activity may be modulated by upregulated expression of VEGFR1, which has a weaker tyrosine kinase activity (Adams and Alitalo, 2007; Huang, Andersson *et al.*, 2001; Waltenberger, Claesson-Welsh *et al.*, 1994), and it may also signal via FGF pathways (Jonca, Ortéga *et al.*, 1997). VEGF-A expression is regulated by hypoxia through hypoxia inducible factor-1α (HIF-1α), which binds hypoxic response elements (HREs) in its promoter (Ho and Kuo, 2007). Intracellular signalling from VEGFR1 is believed to be mediated by nitric oxide (NO), which drives reorganisation and negatively regulates signalling from VEGFR2, which acts via a traditional MAP kinase kinase (MEK)/mitogen-activated protein kinase (MAPK) pathway, driving proliferation (Bussolati, Dunk *et al.*, 2001). VEGF is also sequestered by the ECM, and is released upon matrix degradation by matrix metallopeptidases (MMPs) (Ahn and Brown, 2008), and hence angiogenesis may be triggered due to changes in the ex-

tracellular matrix, for example upon injury, during an inflammatory response, and by tumour secretion of MMPs (Sorokin, 2010; Stetler-Stevenson, 2008).

The platelet-derived lipid sphingosine-1-phosphate (S1P) is also known to have a pro-angiogenic and pro-migratory role, as well as playing a role in adherens junction formation, acting via extracellular-regulated kinases (ERKs), MAPK and the G_i protein-coupled receptors Edg-1 and Edg-3 (Bayless, 2003; Lee, Thangada *et al.*, 1999a; Lee, Lee *et al.*, 1999b; Wang, van Brocklyn *et al.*, 1999), and is inducible by the agonist FTY720 via S1P receptors (Butler, Lana *et al.*, 2004).

CD31, also known as platelet/endothelial cell adhesion molecule 1 (PECAM-1), is expressed on ECs and platelets, and has been implicated in both angiogenesis and EC migration (though evidence is conflicting), as well as cell survival (Bird, Taylor *et al.*, 1999; Cao, O'Brien *et al.*, 2002). CD31, in cooperation with CD144, also known as vascular endothelial cadherin (VE-cadherin), is associated with endothelial cell–cell adherens junctions. These play a role in junction formation, rearrangement, and permeability, for example in response to bFGF, as well as contact-inhibition of cell growth, signalling via intracellular pathways through binding partners such as β-catenin (Bazzoni and Dejana, 2004; Halama, Èger *et al.*, 2001; Yang, Graham *et al.*, 1999). Blockade of CD31 and CD144 with monoclonal antibodies demonstrated that both molecules play a critical role in formation of a vascular tube, including formation and fusing of intracellular vacuoles to create the vessel lumen (Yang *et al.*, 1999). ECs can also form tight junctions, important in the regulation of vascular permeability (Bazzoni and Dejana, 2004).

ECs are classified according to their role, being termed *phalanx*, *tip* or *stalk* cells depending upon whether they are quiescent (normal stationary state), invasive and migratory (leading) or migratory (following), respectively (Augustin, Koh *et al.*, 2009; Gerhardt *et al.*, 2003). During angiogenesis, the basement membrane must be degraded in order to allow ECs to exit the vessel. New basement membrane, consisting primarily of collagen IV and laminin, is laid down as new vessels form (Sephel, Kennedy *et al.*, 1996). Control of which cells become tip and stalk cells is controlled by Notch, Delta and Jagged signalling, causing tip cells secreting delta-like 4 (Dll4) to inhibit surrounding stalk and phalanx cells also becoming tip cells (Suchting *et al.*, 2007). Jagged signalling results in an opposing pro-angiogenic effect, antagonising Dll4–Notch signalling (Benedito, Roca *et al.*, 2009). As a result of these opposing signals, branching and sprouting in response to pro-angiogenic stimuli are tightly controlled.

Tumour vascularisation is driven by VEGF secretion from tumour cells as well as infiltrating macrophages and fibroblasts (Ho and Kuo, 2007), and this may also play a role in organ vascularisation during development. VEGF signalling has been a widely studied as a potential target for pro- and anti-angiogenic cancer therapeutics, with inhibitors being developed targeting both extracellular receptor domains and

Table 1.2: VEGF-A isoforms. This table shows the association between splice variant number and name of all known and predicted VEGF-A splice variants, based upon their human counterparts and multiple alignment of the splice variants (Krüssel *et al.*, 2001; Robinson and Stringer, 2001).

Isoform	*Length (aa)*	*Name*
1	392	$VEGF_{188}{}^{a,c,d,e}$
2	368	$VEGF_{164}{}^{a,c,e,f,g}$
3	324	$VEGF_{120}{}^{a,c,e,f}$
4	137	$VEGF_{115}{}^{b,c,e}$
5	113	$VEGF_{102}{}^{b,e}$
6	69	None[b]

[a] Secreted
[b] Predicted only
[c] Binds heparin
[d] Cell membrane-bound due to strong heparin binding affinity
[e] Binds VEGFR1
[f] Binds VEGFR2
[g] Binds neuropilins

the intracellular tyrosine kinase domain (Bozec, Gros *et al.*, 2008; Lacal, Morea *et al.*, 2008). To date, several potent endogenous inhibitors have been found, discussed in detail below, and reviewed several times (Cao, 2001; Folkman, 2004; Nyberg, Xie *et al.*, 2005; Zhang and Ma, 2007).

PEDF

One such example of an endogenous inhibitor is pigment epithelium-derived factor (PEDF), a secreted protein which has been found to strongly suppress angiogenesis through direct signalling upon contact with ECs, originally identified by Dawson (1999) as an inhibitor in the eye secreted by retinal cells, later reviewed by Bouck (2002); Ek, Dass *et al.* (2006). Intriguingly, PEDF was originally identified as a neurotrophic factor, again highlighting the similarities between neural and endothelial signalling and regulation (Becerra, 1997). The putative receptor for PEDF is a transmembrane receptor having intracellular phospholipase A(2) activity (Subramanian, Notario *et al.*, 2010). This matches previous work describing PEDF acting via cytosolic phospholipase A(2), triggering apoptosis by sequential activation of proliferator-activated receptor γ (PPAR-γ), MAPK and p53 (Ho, Chen *et al.*, 2009). Like VEGF, PEDF associates with collagen ECM via heparin binding (Sekiya, Okano-Kosugi *et al.*, 2011). Recently, PEDF has also been shown to also play a protective role in blocking tumour metastasis (Ladhani, Sánchez-Martinez *et al.*, 2011).

Thrombospondin

Thrombospondin is the major component of platelet alpha granules, released on platelet activation during blood clotting, but also secreted by many cell types, including ECs, VSMCs and fibroblasts (Jaffe, Ruggiero *et al.*, 1983; Mosher, Doyle *et al.*, 1982; Raugi, Mumby *et al.*, 1982) and incorporated into the surrounding extracellular matrix. It has been implicated in several diseases, reviewed in Esemuede, Lee *et al.* (2004), giving some insight into its normal function.

Thrombospondin localises to the ECM both *in vivo* and *in vitro*, associating via collagen IV binding, but plays a regulatory, rather than structural, role and is termed a *matricellular* protein (Aszódi *et al.*, 2006). It also associates with fibronectin, fibrinogen and heparin sulphate proteoglycans. It is a multifunctional protein, having several different domains dedicated to different roles. It is responsible, for the binding and activation of latent TGF-β, but is also capable of binding other growth factors containing heparin-binding domains, cytokines and proteases (Armstrong and Bornstein, 2003; Aszódi *et al.*, 2006). It is also capable of binding to cells via transmembrane receptors, since it possesses the integrin-binding RGD peptide sequence also found in collagens (Armstrong and Bornstein, 2003). Such integrin interactions can influence cell behaviour and migration. Thrombospondin expression is highest

during embryogenesis, then declines postnatally (Morwood and Nicholson, 2006; Sun, Hopkins *et al.*, 2009).

Both variants of thrombospondin (Thbs1 and Thbs2) are potent inhibitors of angiogenesis (Good, Polverini *et al.*, 1990), thought to act via endocytosis mediated via the low density lipoprotein receptor-related protein (Godyna, Liau *et al.*, 1995). Knockout models exhibit increased neovascularisation, with deficiency leading to an increased vascular density in several tissues and increased incidence of tumours (Aszódi *et al.*, 2006), indicating that thrombospondin plays a role in the regulation of angiogenesis. Additionally, Thbs1 or Thbs2 knockouts show impaired wound healing responses (Esemuede *et al.*, 2004); normally thrombospondin is present at wound sites as a result of release from platelet alpha granules, and impaired healing due to loss of thrombospondin may be due to changes in the neovascularisation or fibroblast infiltration of granulation tissue, or due to loss of growth factor sequestration which results in impaired signalling and/or reduced inmigration of cells, for example ECs in response to damping of pro-angiogenic signals, or fibroblasts and VSMCs in response to reduction of latent TGF-β activation (Esemuede *et al.*, 2004).

Thrombospondin has been shown to inhibit metastatic tumour growth (Volpert, Lawler *et al.*, 1998), and additionally thrombospondin expression levels in platelets are also related to the pro-angiogenic environment created by tumours, illustrated by Zaslavsky, Baek *et al.* (2010), who demonstrated that levels rise in the presence of a tumour, and fall upon tumour resection. This again demonstrates the anti-angiogenic role of thrombospondin, but also shows that its anti-angiogenic effects are, in the case of platelet-derived thrombospondin, both systemic in nature and responsive to the systemic "angiogenic environment" of the entire organism, playing an important role in the suppression of unwanted angiogenesis. In contrast, thrombospondins secreted directly in the basement membrane may have their actions and effects much more spatially restricted.

The anti-angiogenic activity of thrombospondin is due to several factors. Firstly, Thbs1 reduces MMP-9 activity by suppressing the conversion of pro-MMP-9 to MMP-9 by MMP-3, while Thbs2 suppresses MMP-2 (Aszódi *et al.*, 2006), hence reducing degradation of the basement membrane and thereby invasive angiogenesis. Thrombospondin can also exert its anti-angiogenic effects directly, with blocking antibodies shown to increase EC cord formation *in vitro* by Iruela-Arispe, Bornstein *et al.* (1991). While this paper does not demonstrate the mode of action, the implication is that it was by direct contact, though the possibility exists that the antibodies may have blocked something else other than integrin binding. However, the observation was made that thrombospondin expression and secretion was related to cell shape, which may mean that phalanx cells, which are by their nature the most sessile and stable, may secrete more and promote their ongoing stabilisation, while tip and stalk cells do not. Thrombospondin can also inhibit bFGF-stimulated angiogenesis (Tolsma,

Volpert *et al.*, 1993). However, later work by Jiménez, Volpert *et al.* (2000) demonstrated that thrombospondin is also capable of inducing apoptosis in ECs; given the ubiquitous nature of thrombospondin and its production and secretion by ECs, this would lead to the hypothesis that if thrombospondin is capable of inducing EC apoptosis, it must be counterbalanced by opposing pro-survival signals which would normally prevent this course of action. It is most likely that this direct action is due to VEGF signalling inhibition via protein kinase B (PKB)/Akt, resulting in decreased survival (Sun *et al.*, 2009).

Collagen and fibrin

Other factors are also known to induce EC proliferation, growth and tube formation, including basement membrane components such as collagen (Madri and Williams, 1983), and wound-triggered clotting products such as fibrin (Olander, Bremer *et al.*, 1985), which may play a critical role in wound repair by driving revascularisation of damaged tissue and repair of damaged vessels.

Matrikines

"Matrikine subdomains" are domains in ECM proteins which can signal through cell surface receptors and regulate biological functions. Matrikines may act directly (natural matrikines) or may require exposure of via conformational change or proteolysis (cryptic matrikines). Arresten, canstatin and tumstatin are derived from proteolysis of collagen IV non-collagenous domains, and endostatin from collagen XVIII (Kamphaus, Colorado *et al.*, 2000; Petitclerc, Boutaud *et al.*, 2000). These are all potent angiogenesis inhibitors *in vivo* and *in vitro*. These factors are released from collagen by the action of MMPs which degrade basement membrane, MMP9$^{-/-}$ mice having reduced levels (Aszódi *et al.*, 2006). Fragments of Thbs1, fibronectin, perlecan (endorepellin) and fibrinogen additionally inhibit EC functions needed for angiogenesis or inhibit angiogenesis (Mongiat, Sweeney *et al.*, 2003).

However, there is also evidence that pro-angiogenic matrikines also exist, such as collagen IV sites exposed by MMP activity in the retina (Hangai, Kitaya *et al.*, 2002).

Soluble VEGFR1

The VEGF receptor VEGFR1 also exists in a secreted, soluble form, sVEGFR1 (Chappell, Taylor *et al.*, 2009; Kappas, Zeng *et al.*, 2008). Being catalytically inactive due to the lack of an intracellular tyrosine kinase domain, sVEGFR1 serves to sequester free VEGF and thus modulates pro-angiogenic signalling.

Apoptosis

EC are susceptible to apoptosis under certain circumstances, which may play an essential role in the natural balance of pro- and anti-angiogenic factors which influence the expansion or regression of the vascular network. Serum albumin is known to inhibit EC apoptosis and promote adherence to the basement membrane (Zoellner, Höfler *et al.*, 1996), and conversely serum starvation has long been known to result in EC apoptosis, and as such may play a role in the "pruning" of the vasculature when blood flow is restricted, which may result in decrease in exposure to albumin, promoting apoptosis (Zoellner *et al.*, 1996). Additionally, ECs are also susceptible to apoptosis on loss of adhesion with the basement membrane, and this is not rescued by the presence of serum (Zoellner *et al.*, 1996). The consequences of ECs detaching and entering the circulation to survive and lodge elsewhere are potentially rather serious (*e.g.* blockage of microvessels, and even stroke), so it is logical that detachment is a fatal condition for an EC.

Angiostatin is a degradation product of plasmin or its precursor, plasminogen (O' Reilly, Holmgren *et al.*, 1994), having anti-angiogenic properties. Upon internalisation, it promotes mitochondrial apoptosis and also upregulates Thbs1 (Lee, Muschal *et al.*, 2009b).

1.2.5 Basement membrane degradation

Degradation of the basement membrane by proteolysis can be both pro- and anti-angiogenic, depending upon the context. Activation of MMPs 1 and 9 results in endothelial tube regression (Davis, Pintar Allen *et al.*, 2000b; Saunders, Bayless *et al.*, 2005), and addition of exogenous RGD peptide can result in disruption of sprouts and apoptosis (Korff and Augustin, 1999), presumably a result of loss of matrix attachment via integrins. However, some proteolysis is required for tube outgrowth and lumen formation, such as MT1-MMP which degrades collagens I and III (Roy, Zhang *et al.*, 2006; Sacharidou, Koh *et al.*, 2010; Stratman, Saunders *et al.*, 2009b). As discussed above, proteolysis can also expose cryptic binding sites, and release matrix-bound factors such as VEGF, bFGF and matrix fragments such as arresten, endostatin and angiostatin which may result in a variety of pro- and angiogenic effects (Mundel and Kalluri, 2007; Roy *et al.*, 2006). Degradation additionally reduces the density of the ECM, potentially allowing EC migration through the basement membrane.

The major proteases influencing angiogenesis have been previously reviewed by Roy *et al.* (2006). The MMP, a disintegrin and metallopeptidase domain (ADAM) and a disintegrin and metallopeptidase domain with thrombospondin motifs (ADAMTS) families can collectively degrade all matrix components. MMPs and ADAMTS are soluble, secreted enzymes while the related membrane-type matrix metallopepti-

dases (MT-MMPs) and ADAMs are membrane-bound, acting upon their immediate environment. Some have additional activities, such as direct sequestration of VEGF by ADAMTS1 (Luque, Carpizo *et al.*, 2003) in addition to its generation of anti-angiogenic Thbs1 and Thbs2 (Lee, Sato *et al.*, 2006b). Of relevance to basement membrane remodelling are MMPs 1 and 8 which degrade collagens I and III, and MMPs 2, 3, 9 and 10 which degrade collagen IV (Roy *et al.*, 2006), though all have affinities for multiple substrates. The substrates of the ADAM and ADAMTS families are less well characterised, ADAMs 10, 12 and 15 cleaving collagen IV and ADAMTS 2, 3 and 14 cleaving procollagen I (*i.e.* are involved in collagen fibrillogenesis), and ADAMTS 4, 5 and 9 cleave chondroitin sulphate proteoglycans such as versican, which are also found in the basement membrane (Roy *et al.*, 2006).

1.2.6 Summary

The process of the development of the mammalian vasculature is well understood, with many of the signalling processes involved having been identified using *in vivo* knockout models and several different *in vitro* systems. The main feature of vasculogenesis and angiogenesis is the requirement for the growth factor VEGF, whose effects are modulated via the different isoforms of VEGF, including different genes and splice variants, and their differing affinities for the several VEGFRs, which have different tyrosine kinase activities, resulting in the differential activation of intracellular signalling pathways. The activity of VEGF is also modified by inhibitors, including sequestration by sVEGFR1 and ADAMTS1, and additionally by direct inhibition by factors such as PEDF and thrombospondin. After establishment of the blood vasculature, many of the same molecules are involved in continual maintenance and repair of the vasculature. However, *organ vascularisation* is relatively poorly studied. Every organ is vascularised, and contains vasculature specialised for its specific function. While the structure and function of these specialised vascular systems have been widely studied in the context of the developed, functional tissues, the literature contains very little information regarding the mechanisms and processes of *initial* organ vascularisation.

1.3 Secondary lymphoid organs

This section discusses the development, structure and function of peripheral lymph nodes, which are intimately associated with the blood and lymphatic vascular systems. However, our current understanding of the role of of the vasculature in LN development is poor, and in common with other organs the mechanisms driving vascularisation are poorly understood.

The lymphatic system consists of blind ending vessels which drain *lymph*, the fluid arising in the interstitial spaces in the tissues of the body, ultimately returning the lymph to the main blood circulation via the thoracic duct. Lymph nodes (LNs) are found at the major points of convergence of lymphatic vessels, the human body containing around 450 individual lymph nodes, whilst the mouse contains 22 (Willard-Mack, 2006).

1.3.1 Origin of the lymphatic system

The origins of the lymphatic system and lymph nodes have been a question studied by researchers for several hundred years. Many of the prevailing hypotheses at the time were disproved by Sabin and her peers, covered in detail in her book (Sabin, 1913) and in Sabin (1916). Sabin carefully mapped the structure of the lymphatic vasculature using the technique of ink injection and light microscopy of cleared tissues, and by studying embryos throughout their development was able to determine how the lymphatic system developed, but lacking the availability of modern molecular biology was unable to examine the mechanisms involved. Sabin concluded from her observations that the lymphatics originated from lymph sacs, most importantly the jugular lymph sac, that lymph sacs were derived from veins at junctions, and that lymph sacs were the site of lymph node development (Sabin, 1909). It is only in recent years that these observations have been confirmed definitively using mouse mutants, demonstrating that all lymphatic endothelium is derived from venous origin (Srinivasan *et al.*, 2007). More recently, it has been shown that the lymph sacs are not strictly required to initiate LN formation, though the process is less efficient (Vondenhoff, van de Pavert *et al.*, 2009b).

The steps involved in the formation of the lymphatic vasculature have been previously been reviewed by Oliver (2004). Some of the molecular regulators of lymphatic endothelial cell (LEC) specification are known, such as the activation of the transcription factor Prox1, whose expression is induced by the co-expression of both the venous transcription factor COUP-TFII and the Sox18 transcription factor to result in lymphatic differentiation (François, Caprini *et al.*, 2008; Lee, Kang *et al.*, 2009a; Srinivasan, Geng *et al.*, 2010; Wigle and Oliver, 1999). Prox1 expression is preceded by expression of the lymphatic marker LYVE-1. However, LYVE-1 is a marker of lymphatic competence only. LECs also express VEGFR3 and fibroblast growth factor receptor (FGFR)-3 (Shin, Min *et al.*, 2006), resulting in sensitivity to VEGF-C and FGFs which is not shared with BECs. VEGF-C is capable of activating BECs via VEGFR2, but only following proteolytic processing (Joukov, Sorsa *et al.*, 1997), again resulting in different effects upon LECs and BECs.

Given the fact that lymph sacs are always located at branchpoints in veins, it is possible that this is a result of *physical forces* acting at the confluence, for example a pressure differential and/or shear stress. On a two dimensional surface, increased

shear stress reduced EC migration (Hsu, Thakar *et al.*, 2005), but the effects of defined physical forces on cells *within* a vessel remain to be investigated. However, what is known is that the putative signal results in vascular endothelium biased towards a lymphatic lineage being induced to migrate out from the vessel wall into the tissue as a series of vessels which anastomose to form the *lymph sac*, the site of the origin of the lymphatic system and also of a site of lymph node development (Sabin, 1909). This process will be discussed in more detail, below.

1.3.2 Lymph node structure and function

The major purpose of the lymph node is to act as a focal point for the immune system's surveillance of the body, where an adaptive immune response may be triggered in response to foreign antigen. The activation of a T cell on encounter with an APC presenting its cognate antigen is a very low probability event, and it appears that the structure of the LN increases the probability of such an encounter in order to efficiently initiate an immune response (Bajénoff, Egen *et al.*, 2006).

An overview of the various aspects of the structure, cellular composition, compartmentalisation and vascularisation of an idealised lymph node is illustrated in Figure 1.3 and reviewed by Blum and Pabst (2006); Willard-Mack (2006). The external surface of the lymph node is bounded by a tough capsule composed primarily of connective tissue containing type I collagen, providing structural support to the organ. Larger lymph nodes, as illustrated, are divided into several lobules separated by trabeculæ, extensions of the capsule which extend radially toward the centre of the node. In the mouse, lymph nodes are typically smaller and are composed of a single lobule with no subdividing trabeculæ. The number of lobes is likely to be a function of the size of the organism, given that there will be a larger number of draining lymphatic vessels at points of confluence. Each lobule is segmented into three major compartments. Moving from the cortex in to the hilum, these are the cortex, mainly composed of B cell follicles, the paracortex (or deep cortex) composed mainly of T cells, with a lesser frequency of B cells and interdigiating dendritic cells (IDCs), and the medulla, containing B cells and plasma cells, as their major components. The most distinctive division is the segregation of the lobule parenchyma into distinct B cell areas (follicles) surrounded by the T cell area.

Draining lymph containing interstitial fluid, cells, soluble antigen and inflammatory chemokines *etc.* enters the lymph node via the afferent lymphatics. Upon entering the cortical (subcapsular or marginal) sinus, the lymph may either drain around the lobule via the intermediate (trabecular) sinus, and then the medullary sinus, to exit in the draining lymph node at the hilum, or it may enter the lobule via the leaky subcapsular sinus floor or the conduit system (Roozendaal, Mempel *et al.*, 2009; Sixt, Kanazawa *et al.*, 2005). Macrophages and dendritic cells (DCs) in the lymph may enter the lobule through the subcapsular sinus floor and/or the other lymphatic si-

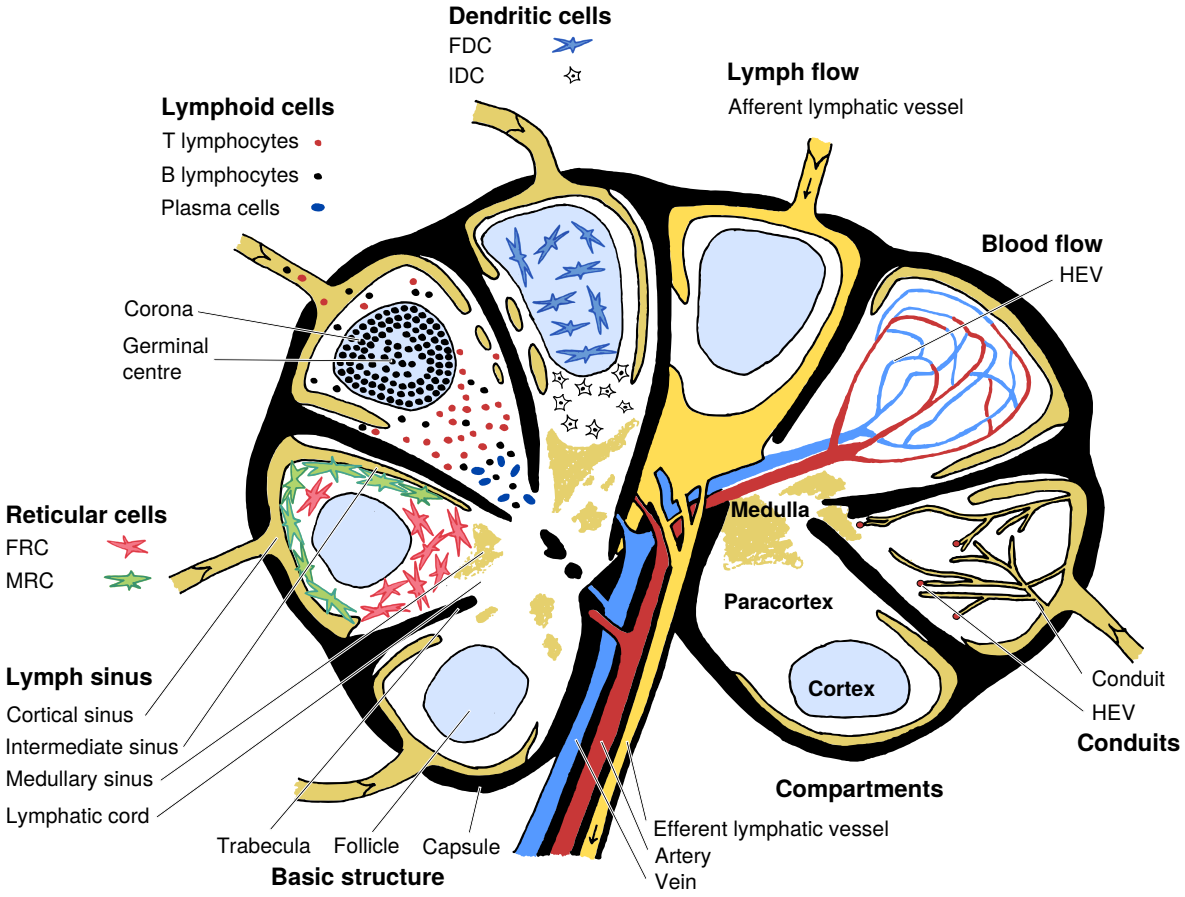

Figure 1.3: Structure and composition of the lymph node. The basic organisational unit of the lymph node is the lobule, bounded by trabeculæ, which are continuous with the surrounding capsule. Each lobe may be separated into cortical, paracortical and medullary regions, which possess different cellular composition and organisation. The cortex primarily contains follicles comprised of B cells, supported by an FDC stromal network. The paracortex is primarily comprised of T cells, supported by an FDC stromal network. B cells (including plasma cells) and T cells exit the node via the medulla and draining efferent lymphatic vessel. B and T cells enter the node from the blood via the HEVs to enter the cortex and paracortex, while IDCs enter via the afferent lymphatics. Soluble antigen and cytokines in the afferent lymph may enter the node via the conduit system, which terminates at HEVs. The lymph entering via the cortical (subcapsular) sinus drains through intermediate (trabecular and paracortical) and medullary sinuses to form the efferent lymph. After Blum and Pabst (2006).

nuses passing through the cortex and paracortex (Randolph, 2001). T and B cells do not typically enter the node via this route, and will instead flow around the lobule to enter the efferent lymphatic vessel without interaction with other cells in the node. The main route of entry for these cells is from the blood, extravasating via high endothelial venules (HEVs) to enter predominantly the paracortex, and also the cortex (Willard-Mack, 2006).

Lymphocytes ultimately exit the node via via the paracortical and medullary sinuses, entering the lymph draining into the medulla, and flowing out of the node via its afferent lymphatic vessel. The process of crossing the lymphatic endothelium to enter the sinus is a S1P-dependent process (Matloubian, Lo *et al.*, 2004); S1P is found at a relatively high concentration in the blood and lymph, but at low concentration inside the lymphoid tissue, and is produced in the LN by the lymphatic endothelium lining the sinus signals via the $S1P_1$ receptor found on lymphocytes. Blocking this signal results in retention of lymphocytes within the node (Pham, Baluk *et al.*, 2010).

The relationship between fluid flow and cellular migration in the rat lymph node has been shown using confocal and scanning electron microscopy (SEM) by Ohtani and Ohtani (2008), clearly showing entry of cells in the subcapsular sinus, exit of lymphocytes in the paracortical sinus, and the structure of the medullary cords (containing HEVs) and medullary sinus. Ohtani also shows the structure of the reticular networks in the cortex and paracortex, their loose association with packed lymphocytes, and intriguingly, continuity between the conduits and reticular networks of the cortex with pillars spanning the roof and floor of the subcapsular sinus. These pillars may play a role in loading the conduit system with small molecular weight antigen and signalling molecules, as well as keeping the subcapsular sinus from blocking afferent lymph flow when the node expands in size. All sinuses, which are continuous with the afferent and efferent lymphatics, stain positively for LYVE-1, indicating that they are all lined with lymphatic endothelium (Ohtani and Ohtani, 2008).

The lymph node is composed of several different types of cell, which can be divided broadly into different categories (Link, Vogt *et al.*, 2007). Cells may be classed as hæmatopoietic or non-hæmatopoietic, based upon CD45 expression). The $CD45^+$ population includes T lymphocytes, B lymphocytes, IDCs and MØs, and hence may be further characterised using the lineage-specific markers for these cell types. The $CD45^-$ fraction may be subdivided based upon CD31 and glycoprotein 38; podoplanin (Gp38) expression. CD31 distinguishes between $CD31^+$ endothelial cells and $CD31^-$ stromal cells. The endothelial population may be divided into $CD31^+Gp38^-$ BECs and $CD31^+Gp38^+$ LECs. Stromal cells including fibroblastic reticular cells (FRCs) are $CD31^-Gp38^+$, while $CD31^-Gp38^-$ comprises multiple cell types, not all of which have been characterised.

The reticular networks in the cortex and paracortex are partitioned into two dis-

tinct areas: follicles containing predominantly B cells, with the surrounding area occupied mainly by T cells (Willard-Mack, 2006). Based upon the expression of different markers, the reticular cells may be classified as follicular dendritic cells (FDCs) (within B cell follicles) or FRCs. FRCs are identified using the fibroblast marker ERTR-7 or gp38 or vascular cell adhesion molecule (VCAM)-1, all absent from FDCs which may be identified by complement receptor 1 (CD35) expression (Katakai, Hara *et al.*, 2004; Ma, Jablonska *et al.*, 2007). The follicles are also marked by their lack of HEVs, and also contain less blood vessels than the surrounding FRC network. Recently, a third stromal subset, marginal reticular cells (MRCs) has been identified (Katakai, Suto *et al.*, 2008). Found immediately underneath the subcapsular sinus, these cells express intercellular adhesion molecule (ICAM), VCAM and mucosal addressin cellular adhesion molecule (MAdCAM) and share similarities with lymphoid tissue organisers (LTos) seen during LN development, discussed below.

A network of collagen I fibrils enclosed by FRCs forms the conduit system linking the subcapsular sinus and transporting low molecular weight antigen and soluble factors from the lymph to the HEVs. The conduits consist of a core of collagen fibres surrounded by a microfibrillar zone consisting of fibrillin and ERTR7. This is enclosed by a basement membrane consisting of perlecan, collagen IV, nidogen, laminin and fibronectin, which is ensheathed by (and presumably synthesised by) FRCs. The contents of the conduits are sampled by fibre-associated DCs (Sixt *et al.*, 2005). Recent evidence also indicates that conduits also exist to transport antigen to B cells in the follicles (Roozendaal *et al.*, 2009).

In summary, the developed lymph node is dependent upon an intricate association of blood and lymphatic vessels, required for it to perform its unique function of bringing together antigen presenting cells from peripheral tissues with T and B lymphocytes recruited from the blood. The different reticular networks within the node serve to support and segregate the lymphocytes, as well as providing a platform for their interaction with other cell types. The question arising from these observations is how these unique and intricate vascular structures develop, and how their formation is initiated. This is a process which begins, at least partially, with the formation of the LN stromal networks, discussed next.

1.3.3 Development of lymph nodes

Peripheral draining lymph nodes are generally formed by the same set of basic cellular interactions between lymphoid tissue inducer (LTi) and LTo cells. Our current understanding of the process has been reviewed by Blum and Pabst (2006); Nishikawa, Honda *et al.* (2003) and most recently by van de Pavert and Mebius (2010). An overview illustrating the process is shown in Figure 1.4. The first secondary LNs begin to form at day E12.5, when LTis are seen to begin to cluster at the sites of LN formation. Pre-LTi cells are derived from hæmatopoietic precusors, and are characterised

by their expression of CD45 and CD4 but are not from a T cell lineage (lacking CD3), nor are from a B cell lineage ($CD3^{-}CD4^{+}CD35^{-}$) (Mebius, Rennert *et al.*, 1997). They are additionally characterised by the expression of interleukin (IL)-7Rα, retinoic acid receptor-related orphan receptor-γt (RORγt), inhibitor of DNA binding 2 (ID2), TNF-related activation-induced cytokine (TRANCE) and TNF-related activation-induced cytokine receptor (TRANCER). (TRANCE was previously known as receptor activator of NF-κB ligand (RANKL) and TRANCER as RANK.) Human LTis express the equivalent human markers, but lack CD4 expression. LTi derive from $CD35^{+}cKit^{int}$-$IL7R\alpha^{+}CD3^{-}CD4^{-}$ precursors found in fœtal mouse liver (Coles, Kioussis *et al.*, 2010). The IL-7Rα-expressing precursors only differentiate into pre-LTi cells following expression of the protein ID2 which suppresses the transcription factor E2A. In the absence of ID2, the precursors differentiate down a B cell lineage, whereas in the presence of ID2 form pre-LTi cells; the pre-LTi cells are also characterised by their expression of RORγt (Coles *et al.*, 2010).

Circulating pre-LTi cells are recruited to the sites of LN development via the action of several chemokines secreted by the local stromal environment such as CXCL13 and CCL21. Pre-LTis possess the chemokine receptors CXC chemokine receptor (CXCR)5 and CC chemokine receptor (CCR)7 and can hence respond to the CXCL13 and CCL21 paracrine signals, respectively. This results in a local clustering of recruited LTi cells. The source of the CXCL13 signal is the local stroma, but the trigger for the induction of CXCL13 expression has not yet been firmly established. CXCL13 expression is induced by retinoic acid (RA)-driven expression driven via retinoic acid response elements (RAREs) in its promoter, which has been demonstrated using DR5/RARE reporter mice, which express luciferase where RA is expressed; these show that all $CXCL13^{+}$ cells express luciferase and hence have also expressed RA (van de Pavert, Olivier *et al.*, 2009). While the mechanism of RA paracrine signalling is not yet firmly established, CXCL13-expressing LTo cells were shown by van de Pavert *et al.* (2009) to exist adjacent to neurons expressing retinaldehyde dehydrogenase 2 (RALDH2), the major enzyme responsible for production of RA from retinal, and CXCL13 was shown to result in the ileum from stimulation of the vagal nerve.

LTis express both TRANCE and TRANCER, and in consequence signalling is induced via juxtacrine and paracrine signalling as the cells cluster and come into intimate contact with one another. The expression of LT is induced by signalling via TRANCER, leading to LT$\alpha\beta$ expression on mature LTis, which binds LTβR on LTos, activating them. The lymphokine cytokine LT, a member of the tumour necrosis factor (TNF) family formerly known as TNF-β, has been shown to be required for LN development. LT-$\alpha^{-/-}$ knockout mice have no draining LNs, but the lymphatic vessels are present, demonstrating that LT is critically required in order to drive formation of LNs, but is not important in the development of lymph vessels (Nishi-

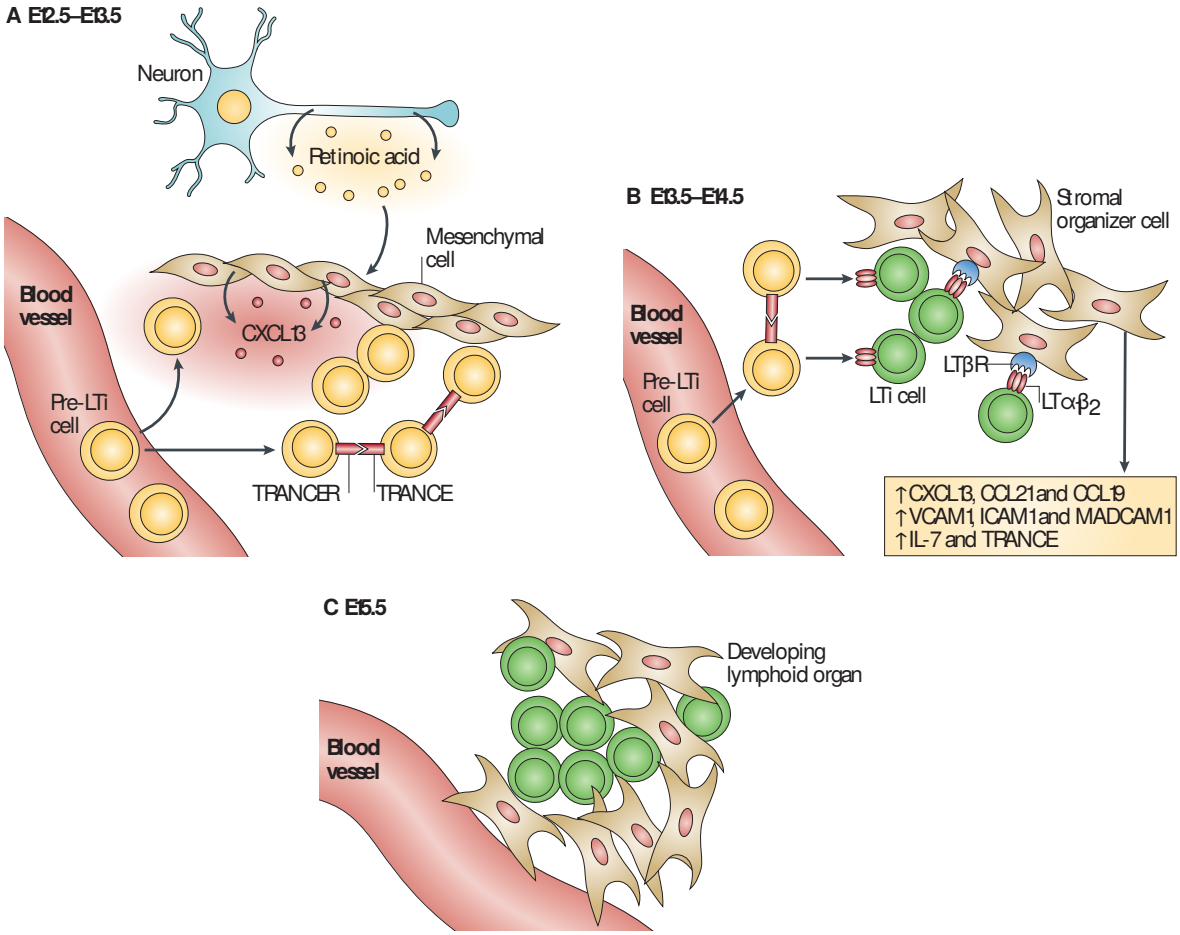

Figure 1.4: LN development from lymphoid tissue inducers and stromal organisers. CXCL13 arising from the mesenchyme results in the recruitment of pre-LTi cells from the circulation. CXCL13 production may be initiated through retinoic acid production from neurons, but this is not yet confirmed. Clustering LTis are mutually activated by TRANCE–TRANCER signalling, becoming mature LTis expressing LT. LT signalling through LTβR present on mesenchymal cells activates them to become stromal organisers, resulting in increased production of chemokines (CXCL13, CCL19 and CCL21), adhesion molecules (ICAM, VCAM and MAdCAM), IL-7 and TRANCE, leading to further LTi recruitment, clustering and activation. From van de Pavert and Mebius (2010).

kawa *et al.*, 2003; White, Carragher *et al.*, 2007).

LTo cells are derived from the local mesenchyme at the site of LN development, and are characterised by the expression of MAdCAM, ICAM and VCAM and a lack of CD45 expression. Activation of the stroma by LT signalling leads to upregulation of MAdCAM, ICAM and VCAM, and the chemokines CCL19, CCL21, CXCL13 and TRANCE, leading to further LTi recruitment and hence more LTo activation, *i.e.* a cycle of positive feedback resulting in increased LTi clustering and LTo activation (van de Pavert and Mebius, 2010). VEGF-C expression by LTos is also upregulated, which may a role in the establishment of lymphatic structures. Upregulation of IL-7 by the stroma may further stimulate the LTis, as well as serving to support the homeostasis of T lymphocytes, which are required to maintain the node after initial development (Coles, Veiga-Fernandes *et al.*, 2006; Vivien, Benoist *et al.*, 2001).

Following these steps, it is currently accepted that the microvasculature differentiates into a functional HEV network to allow recruitment and ingress of T and B cells, attracted to the node by HEV expression of CCL21 which can recruit DCs expressing CCR7; DCs in turn express CCL18, 19 and 21 which can recruit T cells expressing CCR7, and B cells are recruited by CXCL13 (Blum and Pabst, 2006). Segregation of the stroma into T and B zones follows, CXCR5-expressing B cells being attracted by FDC secretion of CXCL13, while T cells are attracted to the CCL19 and 21-expressing FRCs.

While these steps are of critical importance in the establishment of the lymph node, and the concepts of LTi and LTo interaction are now well understood, there is a large gap in our understanding. These processes describe in detail how the formation of LN stroma is induced, but they do not relate these changes to the concomitant changes in the vasculature. These cellular interactions and signalling processes take place in close proximity to the lymph sac, and additionally the blood vasculature from which the sac originates, but the process by which the lymphatics and blood vessels within the node form the complex interrelated networks found within the developed, functional node is unclear.

If the process of CXCL13 production is initiated by RA production by neurons, this leads to the question of whether the budding of the lymph sac is driven by the same process, or if both events are a result of an earlier, as yet unidentified signal. Given the close spatio-temporal association of lymph sac formation and stromal specification, it is unlikely that these events are not closely coordinated. Angiogenesis and neural development both involve the migration of adventitious cells, and endothelial and neural cell types have been observed to make use of the same guidance molecules to direct their movement (Eichmann, Makinen *et al.*, 2005a), and evidence exists that neural cells can use an existing vascular network for guidance during migration (Nagy, Mwizerwa *et al.*, 2009). It is therefore possible that the patterning of both networks results in the formation of lymph nodes at discrete points where cer-

tain conditions are met. Particular interactions between the endothelium and mesenchyme may also play a role.

Due to the small size of early LN anlagen, and difficulty in identifying and obtaining them, it would be desirable to be able to model the specific cellular interactions and signalling processes using an *in vitro* model to study factors which may control angiogenesis, and hence vascular development, in the developing LN anlagen.

1.4 Overall Aims

This PhD research project aims to investigate the processes involved in lymphoid tissue organogenesis required to form a functional LN. The effects of vascularisation upon cell and matrix organisation, and the mechanisms driving vascularisation will be determined, using both *in vivo* and *in vitro* models. Thus the aims of the PhD are:

1. Analysis of vascularisation of lymph node anlagen *in vivo*.
2. Development of an *in vitro* model of angiogenesis.
3. Modelling the role of vascularisation in lymph node development.

1.4.1 Aim 1: Analysis of vascularisation of lymph node anlagen *in vivo*

During the process of organogenesis, hypoxia is thought to induce the vascularisation of organs. The process of vascularisation may be important not only to meet the metabolic oxygen and nutrient demands of the tissue, but may also drive the structural organisation of organs through both deposition and organisation of the extracellular matrix. The pattern and kinetics of the formation and development of vascular networks in LNs is currently unknown, thus confocal microscopy will be used to determine and quantify the formation of vascular networks in LN anlagen, and use microarrays and quantitative real-time reverse transcriptase PCR (RTPCR) to determine if hypoxia plays a role in this process, and also examine the role of pro- and anti-angiogenic genes to determine if a switch in their balance occurs during development.

1.4.2 Aim 2: Development of *in vitro* model of angiogenesis

In order to study the role and mechanism of angiogenesis during lymphoid tissue development, an *in vitro* model will be required which phenotypically resembles *in vivo* angiogenesis, and which is both reproducible and quantifiable. Three-dimensional (3-D) models of both vasculogenesis and angiogenesis will be established and tested. It would be desirable to have a model which closely resembled the vasculature *in*

vivo, thus a microfluidic network will be integrated within the 3-D model to simulate a perfused capillary network, modelling the physical forces and bulk flow of tissue perfusion, in addition to incorporating vascular endothelial and smooth muscle cells into the vascular model. Imaging changes in the model in real-time using multiphoton (MP) imaging to visualise changes in the organisation of cells and the extracellular matrix would also be desirable. Changes in the model must be quantifiable by image analysis, and the model must be responsive to pro- and anti-angiogenic factors to allow it to be used to answer important biological questions.

1.4.3 Aim 3: Modelling the role of vascularisation in lymph node development

Using the developed *in vitro* model of angiogenesis, the process of LN vascularisation will be studied using LN explants from timepoints throughout LN development. The model will be used to study the effects of the explants upon angiogenesis in detail, and dissect the signalling pathways involved in the process of tissue vascularisation.

Chapter 2

Materials and Methods

2.1 Cell culture

2.1.1 Culture conditions

Human Umbilical Vein Endothelial Cells Primary human umbilical vein endothelial cells (HUVECs; HUVEC-c, PromoCell, Heidelberg, Germany) were grown from passages 1–7 in endothelial cell growth medium (ECGM, PromoCell), supplemented with 10% fœtal bovine serum (FBS), at 37 °C with 5% CO_2. Note that the addition of 10% FBS is atypical and may have undesirable effects, so is not recommended without good reason. HUVECs were seeded at a density of 5–10 $\times$ 10^3 cells/cm^2.

Human Dermal Lymphatic Endothelial Cells Primary human dermal lymphatic endothelial cells (HDLECs; HDLEC-c, PromoCell) were grown from passages 1–7 in endothelial cell growth medium (microvascular) 2 (ECGM MV2, PromoCell), supplemented with 10% FBS, at 37 °C with 5% CO_2. Note that the addition of 10% FBS is atypical and may have undesirable effects, so is not recommended without good reason. HDLECs were seeded at a density of 10–20 $\times$ 10^3 cells/cm^2.

Vascular Smooth Muscle Cells Vascular smooth muscle cells (VSMCs) isolated from the aorta of the Immorto mouse (Foo, Turner *et al.*, 2006; Jat, Noble *et al.*, 1991), a gift from Prof. Ralf Adams, Max Planck Institute for Molecular Biomedicine, Münster, Germany, were cultured from passages 1–12 in Dulbecco's modified Eagle's medium (DMEM, Sigma-Aldrich, Gillingham, UK), supplemented with 10% FBS, 2 mM L-glutamine (Invitrogen, Paisley, UK), and 5 ng/mL interferon γ (IFN-γ, Peprotech, Rocky Hill, NJ, USA), at 33 °C with 5% CO_2. This cell line expresses the simian virus 40 (SV40) large tumour antigen (TAg) under the control of an IFN-γ-inducible promoter (Jat and Sharp, 1989), used to induce proliferation. The TAg is temperature sensitive, only allowing proliferation at the permissive temperature (33 °C). Upon removal of IFN-γ from the medium and raising of the temperature to 37 °C, the cells

growth arrest in stages G_1 or G_2 of the cell cycle (Jat *et al.*, 1991). VSMCs required seeding at high density and were split 1:3.

C3H/10T½, clone 8 cells obtained from the American Type Culture Collection (ATCC) were cultured from passages 9–20 in DMEM, supplemented with 10% FBS, and 2 mM L-glutamine at 37 °C with 5% CO_2. C3H/10T½ were seeded at a density of 3×10^3 cells/cm^2.

2.1.2 Recovery and subculture of cell lines

Subconfluent cells were subcultured by aspiration of the culture medium followed by two washes in Ca^{2+} and Mg^{2+} free Dulbecco's phosphate buffered saline (DPBS, PAA) and addition of Trypsin-ethylenediaminetetraacetic acid (EDTA) (6 µL/cm^2, 0.05 % trypsin, 0.2 g/L EDTA.4Na, Invitrogen). Primary cells requiring more delicate handling, such as HUVECs and HDLECs, were incubated in Trypsin-EDTA at room temperature (RT), while established lines such as C3H/10T½ were incubated at 37 °C, until over half the cells were rounded, then cells were detached with gentle tapping. An alternative form of trypsin was used for HDLECs (DetachKit, PromoCell), using 4-(2-hydroxyethyl)-1-piperazineethanesulfonic acid buffered saline solution (HEPES-BSS) in place of DPBS, and trypsin neutralising solution in place of FBS-containing media to inhibit trypsin activity).

Cells were split in order to seed at the appropriate seeding density; HUVECs and HDLEC were a counted in order to seed at the recommended densities, while split factors were used for other cells. Depending upon the required number of cells for experiments or maintenance of stocks, T25, T75 or T175 flasks were used (Corning, Corning, NY, USA).

When specific numbers of cells were required for experiments, HUVECs and HDLECs were spun down at 220 *g* and all other cell types at 300 *g* prior to resuspension in growth medium, freezing medium or collagen using the appropriate quantity of cells.

2.1.3 Cryopreservation

Cells were frozen in a 1:1 mixture of their specific medium and freezing medium (20 % dimethyl sulphoxide (DMSO) (Sigma) and 80 % FBS) to give a final concentration of 10 % DMSO and at least 40 % FBS. A defined number of cells were spun down prior to resuspension in growth medium, then an equal amount of freezing medium was added dropwise. The cell suspension was then aliquoted into cryovials (Corning and Nunc) and transferred to a -80 °C freezer to freeze in a "Mr Frosty" 1 °C/min freezing container (Nalgene, Fisher Scientific, Loughbrough, UK), or a polystyrene tube tray wrapped in foil, prior to long-term storage in liquid and vapour phase nitrogen (-196 °C and -190– -135 °C, respectively).

Cells were recovered from cryopreservation by rapid thawing in a 37 °C water bath until a small amount of frozen material remained. The cryovial was washed with copious 70 % ethanol and allowed to dry prior to aspiration of the contents along with 1 mL normal culture medium and transferred to a 15 mL centrifuge tube containing 4 mL culture medium and spun down. The supernatant was aspirated and the cell pellet resuspended in 5 mL pre-warmed culture medium, then transferred to an appropriate number of culture flasks also containing pre-warmed medium. The flasks were checked under a phase contrast microscope to ensure the presence of cells at the appropriate density and transferred to an incubator at the appropriate temperature to allow cells to attach.

2.1.4 Growth factors and media supplements

A summary of the growth factors used is shown in Table 2.1. In order to induce vasculogenesis and capillary outgrowth in 3-D, a cocktail of growth factors was used. Tube forming medium, derived from Yang *et al.* (1999) and Davis, Black *et al.* (2000a), contained 40 ng/mL human VEGF ($hVEGF_{165}$, Peprotech, Rocky Hill, NJ, USA), 40 ng/mL basic fibroblast growth factor (bFGF, Peprotech), 50 ng/mL phorbol 12-myristate 13-acetate (PMA, Sigma) and 50 µg/ml L-ascorbic acid 2-phosphate sesquimagnesium salt hydrate (ascorbate, Sigma) in ECGM. VEGF and bFGF were reconstituted in phosphate buffered saline (PBS) with 0.1 % bovine serum albumin (BSA) carrier, PMA in ethanol and ascorbate in PBS.

Lyophilised human transforming growth factor β_1 (TGF-β_1, Peprotech) was reconstituted in 10 mM citrate buffer, pH 3 with 0.2 % BSA carrier at a concentration of 4.5 µg/mL. TGF-β_1 was used to differentiate C3H/10T½ toward a smooth muscle lineage.

2.1.5 Labelling cells

CFSE and CMTMR Cells were labelled by resuspending in 1 mL labelling buffer, and mixing with 1 mL labelling buffer containing 5 µM carboxyfluorescein succinimidyl ester (CFSE) or chloromethyl tetramethylrhodamine (CMTMR) (Invitrogen), and incubated at room temperature for 8 min. Excess probe was removed by the addition of 1 mL FBS, followed by three washes in labelling buffer containing 20 % FBS. Labelling buffers used included serum-free medium (DMEM, RPMI, M199) and PBS.

Transfection HUVECs and VSMCs were transfected using Amaxa nucleofection (Lonza, Cologne, Germany) with the appropriate cell-specific solution. 5×10^5 cells were resuspended in 100 µL nucleofection solution, and 1–2 µg plasmid DNA was added. Following transfer to an Amaxa cuvette, the cells were transfected using the

Table 2.1: Growth factors used for inducing vasculogenesis, capillary outgrowth and smooth muscle differentiation.

Name	*Targets*	*Supplier*
PMA	PKC	Sigma
bFGF	FGFR	Peprotech
$hVEGF_{165}$	VEGFR1, VEGFR2	Peprotech
TGF-β_1	TGF-βR	Peprotech

appropriate programme, then transferred into plates or flasks to allow recovery for 24 hours prior to further use.

The newer Neon system (Invitrogen) as also used for transfection. Cells were resuspended in the provided transfection buffer, plus the plasmid being transfected, and then drawn into the pipette tip cuvette with integrated electrode used by the system. The appropriate settings (voltage, pulse width and pulse count) were set for the cell type being transfected. Transfected cells were then transferred into plates prior to use.

2.2 Mice

C57BL/6 human-CD2-GFP (hCD2-GFP) transgenic mice (de Boer, Williams *et al.*, 2003) express green fluorescent protein (GFP) in LTi cells, as well as other cell lines deriving from the same lineage (thymocytes, T cells and natural killer (NK) cells). In the developing embryo, GFP-expressing LTi cells present in LN anlagen primordia and thymi allowed visualisation of the developing organs using a stereo fluorescence microscope (Zeiss). During development, mature T cells are yet to complete their development and exit the thymus, so clusters of GFP^+ cells in the periphery can be assumed to be LTi cells. LN anlagen, thymi, fœtal liver and skin samples were finely dissected with Dumont № 5 forceps (Fine Science Tools, Heidelberg, Germany), using GFP expression to identify the developing axillary, brachial, cervical and inguinal nodes below the skin, and the thymus in the thoracic cavity, and placed on ice in Iscove's modified Dulbecco's medium (IMDM) prior to use in experiments, or fixed with 4 % paraformaldehyde (PFA, Sigma) for immunohistochemical staining. All mice were bred at the the National Institute for Medical Research under Home Office licence and guidance.

2.3 Glass and metal surface preparation

2.3.1 Cleaning

A saturated solution of KOH in isopropanol was used to clean glass slides and stainless steel metalwork prior to use, removing all traces of grease and dirt. Glass was further cleaned in 0.1 M HCl overnight. Both glass and metal were rinsed with water before oven drying, or autoclaving for use in cell culture.

2.3.2 Non-stick non-wetting coating

To render glass surfaces non-stick and non-wettable, glass slides were washed with chloroform, 5 % (v/v) dimethyldichlorosilane (DMDCS, Sigma) in chloroform, and

again with chloroform (10 min for each wash), before baking at 65 °C for 3 hours.

2.3.3 Collagen binding coating

Glass slides and metal collagen supports may be coated with poly(ethylenimine) (PEI, Sigma) and functionalised with glutaraldehyde in order that they react and covalently bond with a collagen extracellular matrix, stabilising and supporting the matrix along all contacting surfaces.

Under sterile conditions, glass or metal supports were cleaned with ethanol and air dried prior to coating with PEI 1 % (v/v) in H_2O for 30 min. Excess unbound PEI was washed away using 95 % (v/v) ethanol and the support air dried. The support was then functionalised with glutaraldehyde 1 % (v/v) for 30 min and the glutaraldehyde removed by at least six washes with H_2O, then air dried prior to use.

2.4 Collagen matrix

2.4.1 Preparation of collagen type I from rat tail

All solutions were 0.02 µm filter sterilised and kept on ice. All equipment was autoclaved or sterilised with ethanol prior to use, and all steps were performed under sterile conditions since collagen cannot be sterilised after preparation.

Tendon isolation Frozen tails collected from adolescent rats were thawed, then rinsed in 95 % ethanol. Using a scalpel, the distal end of the tail was removed, and the epidermis removed by cutting down the length of the tail and separating with hæmostats. This exposed the tail tendons, seen running in four bundles down the length of the tail. The proximal end of the tail was clamped with a hæmostat and the collagen bundles severed immediately distal to it. The tendons were removed by clamping the tail at the proximal end using a second hæmostat, then fracturing this end by bending and gentle pulling until the tail tendons slid out along the entire length. The exposed tendons were cut off into sterile water and the process repeated for each joint, working towards the proximal end. The tendons were washed in sterile water three times and teased apart with forceps to form a fine mesh, then quickly washed in 95 % ethanol and air dried before weighing.

Monomeric collagen extraction The tendons were dissolved in 50 mL 0.5 M acetic acid per 1 g of tendon at 4 °C in a 200 mL flask, stirring as slowly as possible for 26–36 hours, 30 hours being optimal, then spun down at 20000 *g*, 4 °C for 60 min to pellet the remainder, using 250 mL polypropylene centrifuge tubes (Nalgene). The supernatant was retained and stored at 4 °C. The acidity was subsequently reduced by either dialysis or by lyophilisation and reconstitution.

Dialysis Dialysis was performed to remove excess acid while retaining a low pH (collagen gels under alkaline conditions). Monomeric collagen in 0.5 M acetic acid was dialysed against 2 L of 0.1× DMEM in 0.02 M acetic acid using high retention seamless cellulose tubing (Sigma), replacing the dialysis buffer twice over three days. Dialysed aliquots were stored at 4 °C. Following dialysis, the concentration of the collagen solutions was determined using Coomassie Plus staining (BioRad, Hemel Hempstead, UK), comparing with a standard curve determined using a type I rat tail collagen standard (Becton Dickinson, Oxford, UK). This step was unnecessary for redissolved lyophilised collagen whose concentration was already known.

Lyophilisation Lyophilisation was used as an alternative to dialysis in order to more accurately determine the collagen concentration. Monomeric collagen in 0.5 M acetic acid was lyophilised for at least three days using a Lyotrap lyophiliser (LTE, Oldham, UK), giving a dry white solid, stored at room temperature. Collagen stock solutions were prepared by dissolving specific mass fractions of collagen solid in 0.02 M or 0.04 M acetic acid for further dilution.

Support An artificial collagen gel does not possess great mechanical strength, being easy to compress and stretch, and so can not hold its shape without external support. In order to create collagen gels of defined size and shape, several support structures were designed and fabricated for this purpose. Figure 2.1 shows the designs for several different supports for use in different situations. Plates with holes of defined diameter and height were used to create larger gels, including wells to contain media for live imaging of cell-seeded gels, while rings were used to allow the culture of cells-seeded gels of defined size in multi-well plates. 24 well glass-bottomed imaging plates were used for imaging collagen gels in metal rings (PAA and Iwaki, Tokyo, Japan), and also glass-bottomed dishes with a 14 mm window (Iwaki). Supports in 2.1(A) and (B) were machined from aluminium sheet and steel washers, respectively, by the Biology department workshop, while (C) and (D) were machined from stainless steel by computer aided design / computer aided manufacturing (CAD/CAM) , contracted to Aztech Precision Engineering, Riccall, York, UK using CAD drawings drafted by myself.

Gelation Existing collagen stock was diluted as required with 0.02 M acetic acid, then further diluted with 1 part 10× DMEM containing phenol red to 9 parts collagen to create a working solution (containing 1× DMEM for buffering). For all the experiments shown in this thesis, all working solutions contained collagen at a concentration of 3 mg/mL. An appropriate amount of the working solution was then neutralised with 0.8 M $NaHCO_3$ or 1 M NaOH on ice to pH 7.5, using the phenol red indicator colour change to monitor neutralisation, and pH indicator strips (Neutralit pH test strips pH 4.5-10.0, VWR, Batavia, IL, USA) to check the resulting pH.

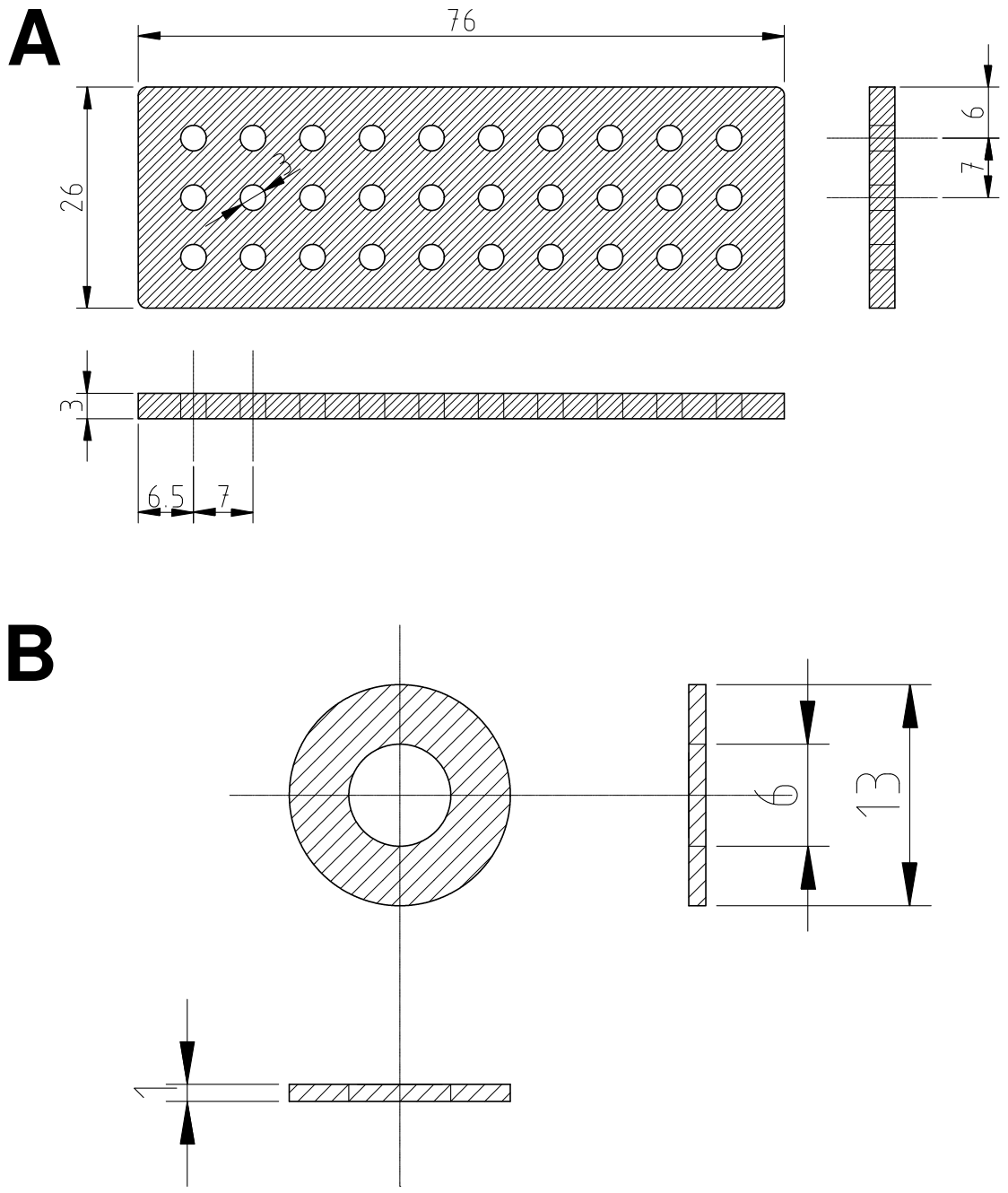

Figure 2.1: Collagen matrix supports. (A) Support slide for 30× 3 mm diameter, 3 mm thick collagen gels. (B) Support ring for 6 mm diameter, 1 mm thick collagen gels.

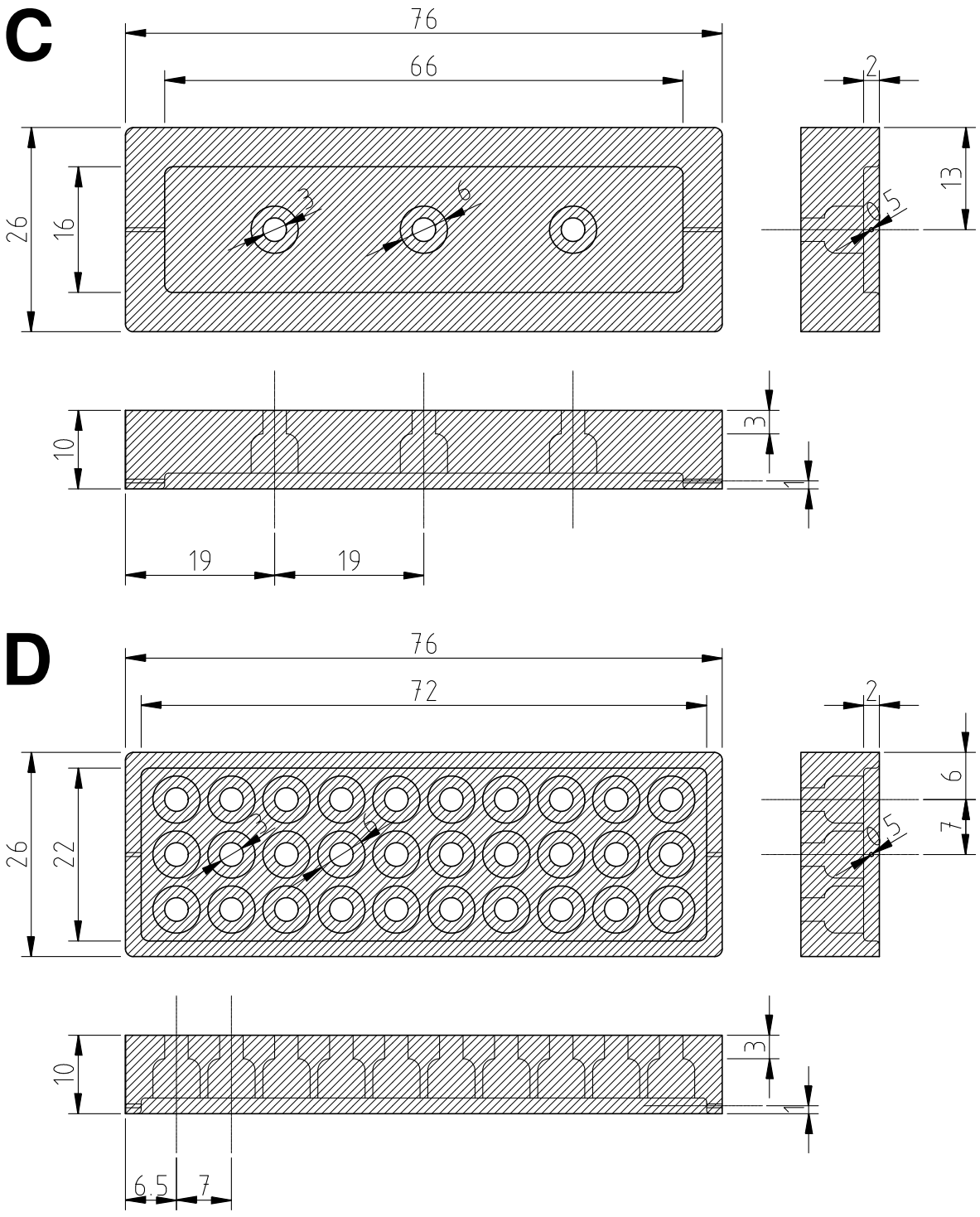

Figure 2.1: Collagen matrix supports (continued). (C) Support with 3 wells and (D) support with 30 wells for 3 mm diameter, 3 mm thick collagen gels. The flat base allows coverslip attachment to permit imaging. Side ports permit gas entry and exit for live imaging, with a recess to allow attachment of top slide to maintain sterility.

The required number of cells or spheroids were spun down, and seeded in the collagen gel by resuspending in a suitable volume of neutralised collagen. The seeded collagen solution was then transferred into a suitable container for gelling (see Figure 2.1). The solution was gelled for 2 hours at 15 °C before covering with the appropriate medium and culturing at 37 °C with 5% CO_2. Faster gelation times were used for spheroid cultures, gelling at 37 °C for 10 min. Gelation may be performed at any temperature from 15 °C to 37 °C. Gelling was faster at higher temperatures, but the gel would contain a large number of very short fibres. Gelling would take longer (1–2 hours) at lower temperatures, but the gel would contain a smaller number of long fibres. Cell viability during the gelling period was also taken into consideration.

Culture medium was added on top of the gel following gelation, taking care to pre-wet the gel surface to prevent surface tension from disrupting the gel. In order to minimise risk of infection when using dishes containing metal plates, penicillin/streptomycin (Invitrogen) or gentamycin (Sigma) was added to a final concentration of 100 U penicillin, 100 µg/mL streptomycin (1 % (v/v)) or 50 µg/mL, respectively, to the medium.

2.5 Formation of methylcellulose spheroids

This protocol is derived from previously published work (Korff and Augustin, 1998; Laib, Bartol *et al.*, 2009), which describe the production of HUVEC spheroids using a methylcellulose hanging drop culture method.

2.4 % (w/v) methylcellulose stock was made using 6 g methylcellulose (Sigma M-0512, 4000 centipoises), autoclaved in a 500mL Schott bottle containing a magnetic stirrer, and dissolved in 150mL unsupplemented basal growth medium prewarmed to 60 °C, stirring at RT for 20 min. A further 100 mL unsupplemented basal medium was added (RT) to make a final volume of 250 mL, and the solution mixed for 2–3 hours at 4 °C to give a clear, viscous solution. The solution was cleared by centrifugation at 3600 *g* for 2 hours at RT, retaining the clear viscous supernatant.

2.4 % (w/v) methylcellulose stock in unsupplemented basal growth medium was diluted to a working concentration of 0.3 % (w/v) in supplemented growth medium. HUVECs were, for example, resuspended at a concentration of 0.3×10^6 cells/mL and 25 µL drops of the cell suspension were hung from the lids of 10×10 cm^2 Petri dishes (Sterilin, Caerphilly, UK) and cultured for 24 hours. Each spheroid contained 750 cells.

Spheroids were recovered by gentle washing in 10 % (v/v) FBS in PBS, the FBS being used to reduce adherence of spheroids to the plastic. The spheroid suspension was spun down at 100 *g* with no brake prior to aspiration of the supernatant and resuspension of the spheroid pellet in neutralised collagen.

2.6 Imaging

2.6.1 Immunohistochemistry using frozen sections

Fixation Samples were prepared by fixation in 4 % PFA for 20 mins, and washed twice in PBS prior to putting through a sucrose gradient: 15 % sucrose for at least 4 hours followed by 30 % sucrose overnight. A sucrose gradient was required to preserve GFP fluorescence and permit staining with anti-GFP antibodies. The samples were then embedded in Tissue-Tek optimal cutting temperature embedding medium (OCT, Baxter Diagnostics, McGaw Park, IL, USA). The OCT was set on dry ice mixed with isopropanol, or snap frozen in liquid nitrogen, and then transferred to a -80 °C freezer prior to sectioning.

Sectioning 6–10 µm sections were cut from samples embedded in OCT using a cryostat (Leica Microsystems, Wetzlar, Germany) and placed on poly-L-lysine- or SuperFrost-coated glass slides (VWR). Sections were air dried at RT for at least one hour and stored at -80 °C in slide boxes containing silica gel beads (Sigma) to absorb moisture.

Staining A complete list of all primary and secondary antibodies used is shown in Tables 2.2 and 2.3. Additional non-antibody stains are also shown in Table 2.2.

Slides were defrosted at RT in covered boxes and fixed in ice cold acetone (-20 °C) or 4 % PFA for 5 min. A wax circle was drawn around each section using a hydrophobic pen (PAP pen, Fisher Scientific, Loughbrough, UK) and allowed to dry. Sections were then rehydrated using washing buffer (PBS containing 0.05 % (w/v) BSA) for 10–15 min in a slide bath, and then blocked using blocking buffer (PBS containing 5 % (v/v) serum from the same species as the secondary was raised in) for 30 min at RT, then washed again for 5 min in washing buffer. The primary antibody cocktail was made up in blocking buffer and one drop added to each section, then incubated at RT for 45 min. The slides were covered with a lid to prevent dehydration, and foil to prevent photobleaching of any fluorochromes. The slides were then washed quickly with wash buffer, and then again three times, incubating for 10 mins each time. The secondary antibody cocktail was made up in blocking buffer and added as for the primary antibody, incubating for 30 mins at RT, then washed again as for after the primary antibody. A final wash was performed using PBS only, then mounted using ProLong Gold antifade reagent (Invitrogen), covering with № 1½ coverslip glass (Agar Scientific, Stansted, UK) and stored overnight at 4 °C before sealing with nail varnish. Sealed slides were stored at 4 °C in aluminium foil prior to imaging.

Table 2.2: Primary antibodies and other reagents.

Specificity	*Species*	*Clone*	*Supplier*	*Fluor*
Mouse CD31	Rat IgG2a,κ	390	eBioscience 14-0311-85	None
Mouse CD31	Rat IgG2a,κ	390	eBioscience E93-0311-41	EF 605
Human CD31	Mouse IgG1	10G9	Santa Cruz sc-13537	None
Human CD31	Mouse IgG2a,κ	M89D3	BD Pharmingen 558068	AF488
Mouse CD54	Rat IgG2b,κ	YN1/1.7.4	BioLegend 116113	AF647
Mouse CD54	Rat IgG2b,κ	YN1/1.7.4	eBioscience 12-0541-82	PE
Human CD54	Mouse IgG1,κ	HA58	eBioscience 12-0549-71	PE
Mouse CD106	Rat IgG2a,κ	429	eBioscience 51-1061-80	AF647
Mouse CD144	Rat IgG1	BV13	eBioscience 51-1441-80	AF647
Mouse CD144	Rat IgG2a,κ	11D4.1	BD Pharmingen 555289	None
Endomucin	Rat IgG2a	V.7 C7	eBioscience 51-5851-82	AF647
Pan-endothelial	Rat IgG2a,κ	MECA-32	BioLegend 120504	None
LYVE1	Rabbit	poly	Millipore 07-538	None
Human LYVE-1	Rabbit IgG	poly	AngioBio 11-032	None
Mouse LYVE-1	Rabbit IgG	poly	AngioBio 11-034	None
NG2	Rabbit	poly	Chemicon ab5320	None
α-SMA	Mouse IgG2a	1A4	Sigma C6198	Cy3
Collagen I	Rabbit	poly	Abcam ab34710	None
Collagen IV	Rabbit	poly	Abcam ab6586	None
Desmin	Rabbit	poly	Abcam ab8592	None
Fibronectin	Rabbit	poly	Abcam ab23750	None
Laminin	Rabbit	poly	Sigma L9393	None
Perlecan	Rat IgG2a	A7L6	Millipore MAB1948	None
GFP	Rabbit IgG	poly	Invitrogen A21311	AF488
GFP	Rabbit IgG	poly	Invitrogen A21312	AF594
GFP	Rabbit IgG	poly	Invitrogen A31852	AF647
Pimonidazole	Rabbit	poly	Hypoxyprobe 2627	None
Phalloidin	N/A	N/A	Sigma 65906	Atto647
Genomic DNA	N/A	N/A	Invitrogen D1306	DAPI

Table 2.3: Secondary antibodies.

Specificity	*Species*	*Supplier*	*Conjugation*
Mouse IgG H+L	Goat polyclonal	Invitrogen A11001	AF488
Mouse IgG H+L	Goat polyclonal	Invitrogen A11005	AF594
Mouse IgG H+L	Goat polyclonal	Invitrogen A21235	AF647
Rabbit IgG H+L	Goat polyclonal	Invitrogen A11008	AF488
Rabbit IgG H+L	Goat polyclonal	Invitrogen A11037	AF594
Rabbit IgG H+L	Goat polyclonal	Invitrogen A21245	AF647
Rat IgG H+L	Goat polyclonal	Invitrogen A11006	AF488
Rat IgG H+L	Goat polyclonal	Invitrogen A11081	AF561
Rat IgG H+L	Goat polyclonal	Invitrogen A11007	AF594
Rat IgG H+L	Goat polyclonal	Invitrogen A21247	AF647

2.6.2 3-D immunohistochemistry using wholemount specimens

Dissected tissue samples were fixed in 4 % PFA for 1 hour, and whole embryos fixed overnight at 4 °C, then washed three times in PBS and stored at 4 °C prior to staining. Embroyos from timepoints E15.5 and later were slit longitudinally along the abdominal cavity and thorax to permit more efficient fixation of internal visceral and thoracic tissues and organs. Embryos and organs were embedded in 8 % low melting point agarose (Invitrogen) and sectioned on a vibratome (Leica) to a thickness of 250–300 µm. To stain, fixed sections and smaller unsectioned fixed pieces were washed three times in PBS containing 0.15 % (v/v) Triton X-100 (Sigma) (PBS-Triton) over 30 mins. The samples were then blocked in PBS-Triton containing 3 % (v/v) serum from the same species as the secondary antibody was raised in) for 30 min at RT (blocking solution). A primary antibody cocktail was prepared in blocking solution, and each sample incubated in the cocktail overnight at 4 °C on a rocker. The samples were then washed at least three times over the day with PBS-Triton. A secondary antibody cocktail was prepared in blocking solution as for the primary antibody and again incubated overnight in the dark. If necessary, further blocking, staining and washing steps were performed for additional antibodies, then the samples were fixed for 15 mins with 4 % PFA and washed three times in PBS-Triton over 30 mins. Note that the staining times are minimum times, and were routinely extended up to several days in order to improve the staining of thick sections.

The samples were dehydrated in a methanol series (25 %, 50 %, and 75 % (v/v) methanol in PBS-Triton for 15 mins, then 100 % for 5 mins and again for 1 hour, and then cleared using benzyl alcohol benzyl benzoate (BABB). BABB is a 1:2 mixture of benzyl alcohol:benzyl benzoate (Sigma). Samples were transferred to a glass container of BABB:MeOH for 15 mins, then to BABB for 15 mins. Cleared samples were mounted in BABB using metal slides with holes for samples as shown in Figure 2.2(A). № 1½ coverslip glass was sealed to one side of the slide using nail varnish, then the wells were filled with BABB and the samples placed in the wells, then a second coverslip was sealed to the upper side and the slides stored at 4 °C in the dark. The parts shown in Figure 2.2 were machined from aluminium sheet by the Biology department workshop using CAD drawings drafted by myself.

2.6.3 3-D immunohistochemistry using collagen gels

Collagen gels were fixed 4 % PFA for 1 hour, then stained using the wholemount staining protocol in Section 2.6.2. Note that due to the less dense nature of collagen gels in comparison to tissue, the minimum staining times could be reduced to hours rather than days. Less dense samples such as collagen gels were not dehydrated or cleared and were imaged in slides such as shown in Figure 2.2(B).

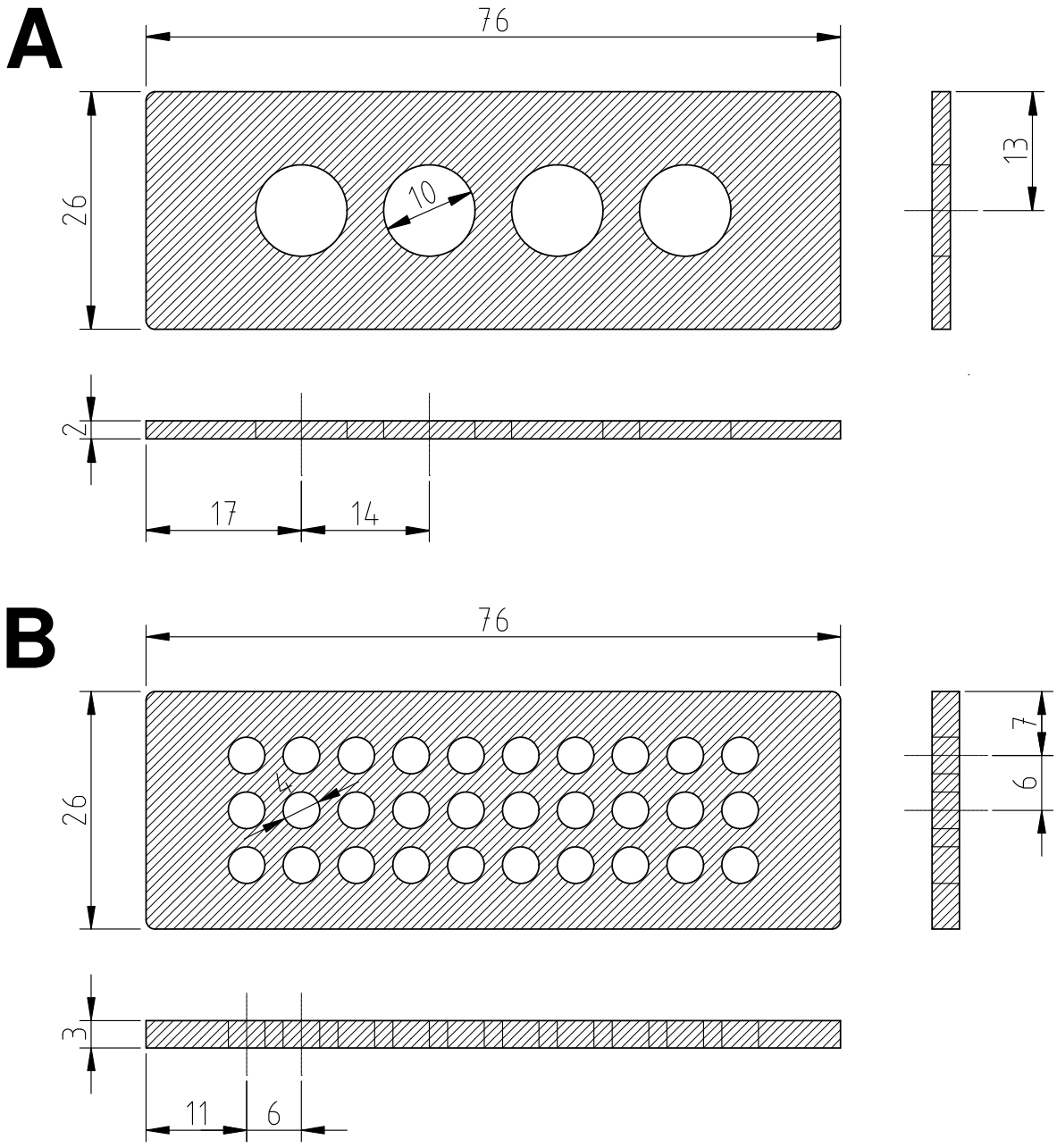

Figure 2.2: Imaging slides, fabricated from aluminium sheet. (A) Wholemount imaging slide with 10 mm diameter, 2 mm thick holes to accommodate vibratome-sectioned, BABB-cleared samples in BABB. (B) Gel imaging slide with 4 mm diameter, 3 mm thick holes to accommodate 3 mm diameter, 3 mm thick collagen gels after fixation and clearing.

2.6.4 Confocal and multiphoton imaging

Fixed, stained samples were imaged using single photon confocal microscopy using LSM 510 META and LSM 510 META NLO systems on Axiovert 200M inverted bases, and an LSM 710 system on an Observer.Z1 inverted base (all Zeiss) using 0.3, 0.5 and 1.4 numerical aperture (NA) 10×, 20× and 40× objectives, respectively. The laser power (where applicable) and photomultiplier gain voltage and offset were set to use the full 8- or 12-bit sampling range with a minimum of under- and over-saturation. When imaging different treatments and controls, the laser and photomultiplier settings were kept constant to permit direct comparisons between samples. Multi-track imaging ensured that bleedthrough was minimised through the excitation of only one fluorochrome at once by only exciting with one laser line in each pass. Additionally, when imaging z-stacks, depth correction was employed to ramp the laser power and/or gain in order to attain consistent signal at all z depths. Line averaging was used to improve the signal:noise ratio.

Live samples, including collagen gels, were imaged using the the LSM 510 META NLO with non-descanned detectors (NDDs) and a Chameleon Ti:Sapphire femtosecond pulsed, tunable laser (Coherent, Santa Clara, CA) for MP imaging, later replaced with an LSM 780 system with GaAsP and binary GaAsP (BiG) NDDs and the same MP laser. The same considerations as for single photon confocal imaging applied for multiphoton imaging, with the addition of controlling for photobleaching, phototoxicity and ablation of cells by the MP laser. This required reducing the laser power and increasing the NDD photomultiplier gain at the expense of noise. Additionally, line averaging was replaced with with frame averaging and the number of averaging passes were reduced in order to decrease the energy being put into the sample by avoiding rapid, repeated excitation of the same volume. Collagen was imaged label-free using second harmonic generation (SHG). Due to the constraints of the available filters and the tunable range of the MP laser, SHG was visualised between 415–435 nm as a result of excitation at $\sim$ 840 nm, or 435-485 nm from 870-890 nm excitation.

2.6.5 Stereo imaging

A SteReo Lumar stereo fluorescence microscope (Zeiss) with HBO100 mercury lamp and EBQ100 isolated power supply were used to dissect hCD2-GFP embryos and to image microfluidic network parts (see below) using both transmitted and reflected white light and darkfield illumination, and fluorescent excitation with an AxioCam digital CCD camera (Zeiss). Microfluidic network parts were also separated and cleaned up using an MZ8 stereo microscope (Leica) with both transmitted and reflected white light, using Dumont № 5 forceps and 0.10 and 0.15 mm insect pins (Austerlitz, Interfocus, Cambridge, UK) for delicate manipulation.

2.6.6 Whole gel imaging

Large (6 mm diameter) gels were imaged by hand using an Axiovert 40 CFL inverted epifluorescence microscope (Carl Zeiss) with a Lumen 200 metal arc lamp (Prior Scientific Inc., Rockland, MA, USA) a 5× objective and exiBlue CCD camera (QImaging, Surrey, BC, Canada). Due to the large scale of the gels, gels was imaged as a set of 1/3 overlapping tiles which were stitched together using ImageJ and a globally optimal stitching algorithm to automatically align and blend all tiles to form a single image (Preibisch, Saalfeld *et al.*, 2009). Due to the use of a monochrome camera, the process was repeated for each colour required. Single images of gels without tiling were also taken using a DM IRB inverted epifluorescence microscope (Leica) with a DC500 colour CCD camera (Leica).

6 mm diameter gels were also imaged using a high-throughput ImageXpress epifluorescence system (Molecular Devices). Gels were imaged as a series of 3×3 tiles using a 4x objective at a resolution of 2.48 µm/pixel. In addition to tiling, the gels were imaged in multiple (15–40) z planes as a z-stack, and in multiple colours. ImageJ macros were used to assemble a composite stack from the separate images. Images were first combined into 3×3 tiles; no specialised alignment and blending was possible due to there being no overlap between tiles. The colour channels were then merged to give a single image per plane, and then each plane was combined to produce a final colour z-stack.

2.6.7 Cell imaging

Adherent cells on glass or plastic were imaged using the Axiovert 40 CFL and DM IRB inverted epifluorescence microscopes described above.

2.6.8 Transmission electron microscopy

Whole collagen gels and tissue samples were prepared for transmission electron microscopy (TEM) by fixation in TEM fixative, composed of 5 mM 200 mM phosphate buffer, pH 7.2, 2.5 mL 16 % PFA (Sigma), 1 mL 25 % glutaraldehyde (Sigma) and 1.5 mL distilled water to give a final concentration of 4 % PFA and 2.5 % glutaraldehyde in 100mM phosphate buffer. Phosphate buffer, pH 7.2, was made from 77 mL 200 mM Na_2HPO_4 and 23 mL NaH_2PO_4 adjusted to pH 7.2 using a pH probe and dropwise addition of the needed buffer component.

Samples were fixed in TEM fixative overnight at 4 °C, then washed three times in phosphate buffer and stored at 4 °C in phosphate buffer. Fixed samples were stained with 1 % (w/v) osmium tetroxide followed by dehydration using an acetone series and embedding in Spurr's resin. Thick sections were stained with toluidine blue and used to identify features of interest prior to making ultrathin sections (approximately

80 nm). Ultrathin sections transferred to grids were stained with uranyl acetate and Reynold's lead citrate prior to imaging.

Samples were imaged using an TECNAI G2 TEM (FEI, Hillsboro, Oregon, USA) with a MegaView III CCD (Olympus Soft Imaging Solutions, Münster, Germany).

2.7 Image analysis

2.7.1 Manual analysis

Example spheroid measurements using ImageJ are shown in Figure 2.3. For each image to be analysed, every spheroid was assigned a unique identifier to allow the generated numerical data to be uniquely associated with each spheroid. Spheroids which were either out of focus or inseparable from neighbouring spheroids were excluded. For each spheroid:

- The total number of sprouts tips (endpoints) were counted, classified as protrusions outside the inner cell mass circumference, plus any further branching (*i.e.* total number of endpoints from initial protrusions).
- Circles were drawn around the inner mass (initial size) and the entire spheroid (to the extent of the largest outgrowth) centred on the inner mass, using the previously drawn border as a guide. The minimum width of the inner mass was used in the case that it was not perfectly spherical. From this, the ratio of the outer:inner radius was calculated, which gave an approximation of the change in size from the initial radius.
- A border was drawn around the spheroid and any outgrowing tubes, allowing measurement of the surface area and perimeter length. Tubes touching from neighbouring spheroids were split equidistantly between the two. From this, a perimeter:surface area ratio was calculated (akin to surface area:volume ratio, but in 2D). This additionally allowed the calculation of Feret's diameter (or maximum caliper), the longest distance between any two points.
- The total outgrowth length was calculated, defined as the summed outgrowth length of all sprouts, including all branches.
- The straight-line distance between the circumferences of the inner cell mass of the spheroid and its nearest neighbour, and between the circumference of the inner cell mass and the edge of tissue explant (if present) were measured.

2.7.2 Automated analysis

Example spheroid measurements performed using ImageJ for whole-well tiled images from the ImageXpress imaging platform are shown in Figure 2.4.

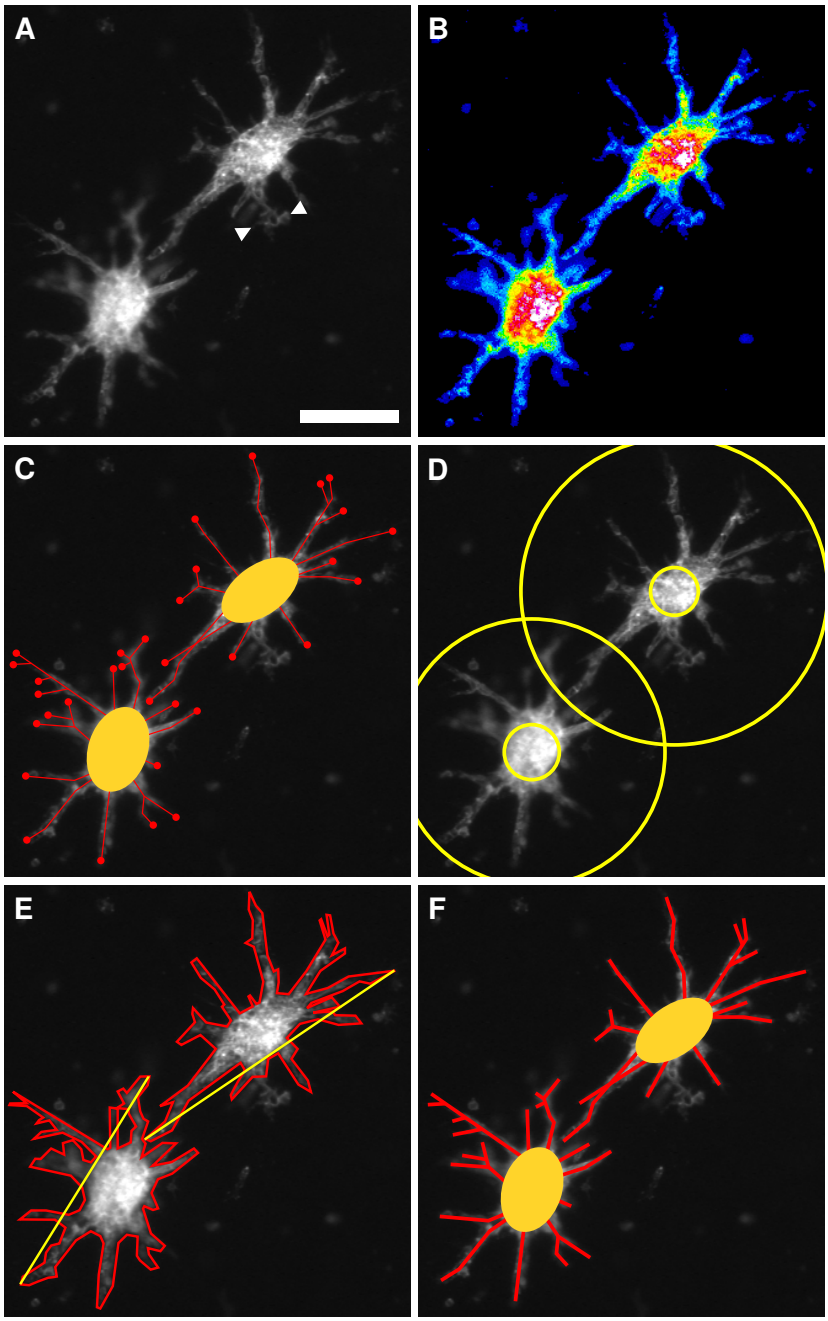

Figure 2.3: Image analysis strategies. An example of the outgrowth of two HUVEC spheroids labelled with anti-CD31 (white) following 24 hours of culture in a collagen gel is illustrated in (A). Angiogenic outgrowth via sprouting into the gel is clearly visible; arrows indicate additional 2D outgrowth where a sprout has made contact with the gel surface, which will not be included in the analysis. The angiogenic outgrowth may be quantified by (B) computing the total integrated density by summing the pixel values of all pixels in the image, the pixel intensities are shown here as a colour ramp from black to red, (C) counting the total number of sprout tips or endpoints, (D) measurement of the initial minimum spheroid diameter and maximum outgrowth length as a radius from the centre of the spheroid, (E) computing the perimeter length, surface area (red outline) and Feret's diameter (yellow line), and (F) measurement of the total amount of outgrowth by summing the outgrowth length of each sprout from the spheroid edge. Scale bar is 200 µm.

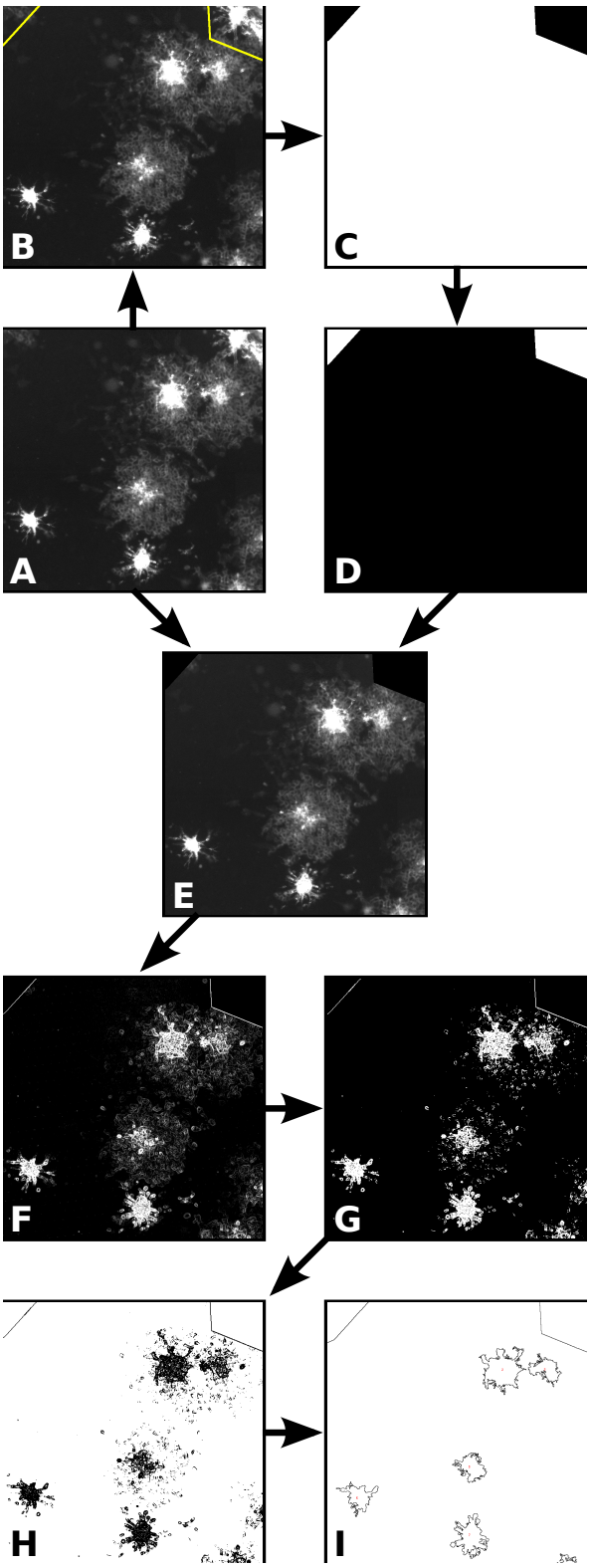

Figure 2.4: Analysis of images with ImageJ. A single field of view for a larger well is illustrated here to allow individual spheroids to be seen. The original image (A) is has the region of interested selected by hand with a polyline (B), shown as a yellow line which is then converted to a bitmask (C) which is subsequently inverted (D). The bitmask was subtracted from the original image to form a new image containing only the region of interest (E). This image may then be processed to detect edges (F) and then thresholded to select the edges (G) and inverted (H). All objects larger than a specified minimum size may then be quantified (I).

- Using the original image (A), a region was drawn around the features of interest using a polyline, excluding the well edge and any spheroids touching the edge (B) From this region, a mask was created (C) and then inverted (D). The inverted mask was then subtracted from the original image to give an image containing only the features of interest (E).

- The edges of the spheroids were found using an edge-detection algorithm (F). A threshold was then set to select pixels less than or equal to the threshold intensity (G). The image was then inverted and converted to a binary image (H).

- To quantify the spheroids, the "analyse particles" algorithm was used to determine the surface area and perimeter length of each object, as well as the x and y coordinates of the centres, used for measuring the distance to the tissue explants. The Feret diameter may also be calculated at this point.

- The same process was used for both the CD31 (HUVEC) and GFP (LN anlagen) channels. The distances between spheroids and explants may then be computed based upon their object centres or nearest points using simple trigonometry.

2.8 Quantitative Real-Time Reverse Transcriptase PCR

2.8.1 Tissue isolation

Lymph node anlagen from hCD2-GFP embryos were finely dissected and kept on ice in IMDM prior to transfer to RNAlater (Ambion) and stored at 4 °C and -80 °C for short- and long- term storage, respectively.

2.8.2 RNA extraction

The tissue was macerated on ice and RNA isolated using a Nucleospin RNA II kit (Macherey-Nagel). Briefly, 350 µL of extraction buffer was added to the homogenised sample, and the sample vortexed vigorously. The lysate was further homogenised and cleared by repeated passage through a 23 gauge needle followed by passage through a NucleoSpin column (all columns were centrifuged at 11000 g). 350 µL ethanol was mixed with the homogenised lysate and the entire mixture, including precipitate, passed through a NucleoSpin RNA II column (RNA binding). The spin column membrane was washed with 350 µL membrane desalting buffer, then incubated at RT for 10 min with 95 µL DNase reaction mixture. The DNase was inactivated by passage of 200 µL buffer RA2, followed by two washes with buffer RA3. Finally, pure RNA was eluted using 60 µL RNase-free H_2O.

The RNA concentration and quality were determined using a NanoDrop spectrophotometer (ThermoFisher). RNA was stored at -20 °C.

2.8.3 cDNA synthesis

Previously extracted total RNA was used for first strand cDNA synthesis using an EZ-first strand cDNA synthesis kit (Biological Industries, Geneflow, Fradley, UK) using the provided protocol. Briefly, 1 µg total RNA was mixed with 1µL 40 µM oligo(dT) primer and made up to a total volume of 10 µL with DEPC-treated water, then incubated for 10 min at 70 °C in a thin-walled PCR tube. Following rapid cooling on ice, 2 µL dithiothreitol (DTT) and 8 µL 2.5× RT reaction mix were added to give a final volume of 20 µL. The tube contents were mixed by gentle pipetting, and then the following incubation was performed using a thermal cycler (Labcycler, SensoQuest, Göttingen, Germany): 42 °C for 60 min, then held at 4 °C. Finally, 80 µL DEPC-treated water was added to give a final volume of 100 µL, and the synthesised cDNA was stored at -20 °C.

2.8.4 Primer design

Primers were designed using Primer-BLAST (NCBI, 2009) to both span an exon-exon boundary and create a product ideally between 90–200 base pairs in length, shown in Table 2.4. Primers were additionally checked against the mouse *genome+transcript*, *refseq_rna* and *nr* databases (*Mus musculus* only, where the mouse *genome+transcript* database lacked more recent entries) to ensure their specificity. Primer efficiencies were determined using serial dilution of cDNA from E14.5 whole embryo lysate, shown in Figure 2.5.

2.8.5 Polymerase chain reaction

The annealing temperatures of the primers were tested using gradient polymerase chain reaction (PCR) using each of the primers at a concentration of 10 μM and 5 ng template per reaction with SYBR green (Applied Biosystems, Carlsbad, CA, USA). The PCR protocol used a 5 minute 95 °C initialisation followed by a 40× cycle of denaturation at 57 °C (15 s), annealing at the specified temperature (30 s) and extension at 72 °C (30 s). A final elongation was performed at 72 °C (7 min) and then held at 4 °C (∞).

Conventional PCR to test primers and perform non-real-time analysis utilised GoTaq polymerase and GoTaq Green master mix containing loading dye (Promega, Madison, WI, USA), performed using a LabCycler thermal cycler (SensoQuest). PCR products were run out on a 1 % (w/v) agarose gel in TAE buffer (UltraPure, Invitrogen) using an iMyRun gel electrophoresis system (Cosmo Bio, Carlsbad, CA, USA)

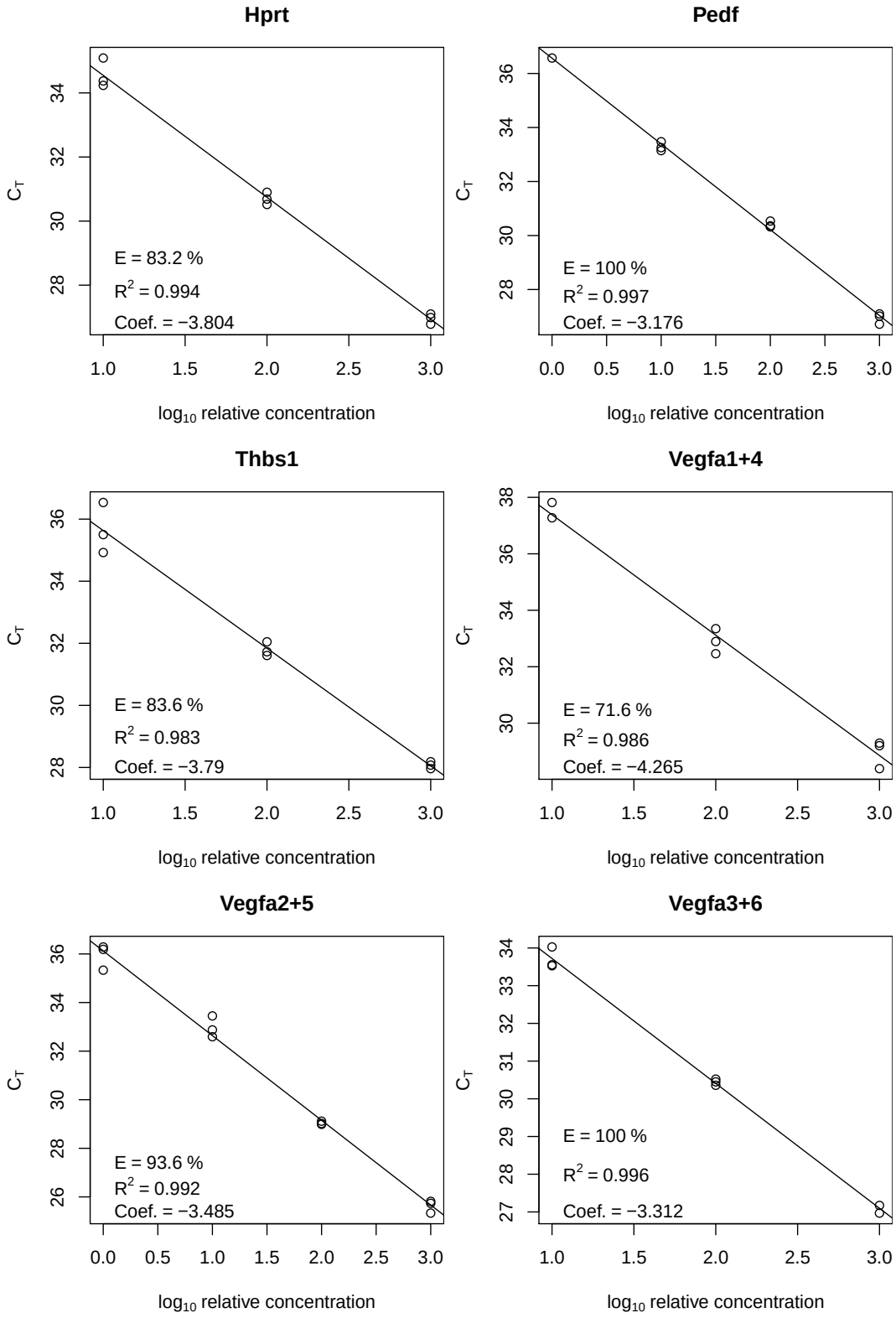

Figure 2.5: Primer efficiencies. For each primer pair being tested, control cDNA (E14.5 whole embryo lysate) was diluted 1:10 three times to give four dilutions, and tested in triplicate for each dilution. Some genes were not present in great abundance, and so did not cross the threshold for the greatest dilution and hence have been excluded. Reactions which failed have also been excluded. The efficiency was calculated using least squares linear regression using the formula $E = (10^{(-\frac{1}{\text{coef}})} - 1)$, where coef is the slope of the fitted line, and then converted to a percentage.

Table 2.4: Primers for RTPCR. Underlined pairs of bases indicate the position of exon–exon boundaries crossed by one of the primer pairs.

Gene	*Refseq*	*Direction*	*Sequence*
Hprt	NM_021704.3	Forward	CCTCACTGCTTTCCGGAGCGG
		Reverse	TCGCTAATCACGACGCTGGGACT
B2m	NM_009735.3	Forward	GGCCTGTATGCTATCCAGAAAACCCCT
		Reverse	TTGGATTTCAATGTGAGGCGGGTGG
Eef2	NM_021704.3	Forward	TCCCTTGTGTGCAAGGCTGGC
		Reverse	GTAGAAGAGGGAGATGGCGGTGGATT
Leng8	NM_021704.3	Forward	CGGGAGCGAGCGGTCCTAAC
		Reverse	TGTACTGAGAAGACCAGTCTGCAGCA
Hif1a	NM_010431.2	Forward	TGCTTACACACAGAAATGGCCCAGTG
		Reverse	TCGTCCTCCCCCGGCTTGTT
Arnt[a]	NM_009709.4	Forward	CGCTGGGTCCCACCATTGCTT
		Reverse	AAAATCCAGCCCTGACCGTCGC
Vegfa 1,4[b]	NM_001110268.1	Forward	GCACAGCAGATGTGAATGCAGACCA
		Reverse	ACCGGGATTTCTTGCGCTTTCGT
Vegfa 2,5[b]	NM_001110268.1	Forward	AGCCAGAAAATCACTGTGAGCCTTGTT
		Reverse	TCAAGCTGCCTCGCCTTGCAA
Vegfa 3,6[b]	NM_001110268.1	Forward	TGCGGATCAAACCTCACCAAAGCC
		Reverse	CACCGCCTTGGCTTGTCACATTTTTC
Vegfa[c]	NM_001110268.1	Forward	GCACAGCAGATGTGAATGCAGACCA
		Reverse	TCCCGAAACCCTGAGGGAGGC
Flt1	NM_010228.3	Forward	GTTGAAAGAGGGGGCCACAGCC
		Reverse	CCTTGCTTCGTGCAGGCTCCC
sFlt1	NM_021704.3	Forward	CCTATGCGTGCAGAGCCAGGAAC
		Reverse	TTGCCGCAGTGCTCACCTCTAAC

[a] Amplifies all splice variants as products of same length
[b] Amplifies two splice variants as numbered as products of same length
[c] Multiple products of different length
[d] No product

Table 2.4: Primers for RTPCR *(continued)*. Underlined pairs of bases indicate the position of exon–exon boundaries crossed by one of the primer pairs.

Gene	*Refseq*	*Direction*	*Sequence*
Epo[d]	NM_007942.2	Forward	GATGGGGGTGCCCGAACGTC
		Reverse	GTCGCAGATGAGGCGTGGGG
Epo (2)[d]	NM_007942.2	Forward	CGGGTACTGGGAGCTCAGAAGGAAT
		Reverse	CCCCGGAGGAAGTTGGCGTAGA
Nos2	NM_010927.3	Forward	TGGAGGCCTTGTGTCAGCCCT
		Reverse	GACAGCAGGAAGGCAGCGGG
Nos3	NM_008713.4	Forward	CCCTTGCTCCAGCCCCGGTA
		Reverse	AGAGGGCCCAGCCCATCCTG
Slc2a1	NM_011400.3	Forward	CGAGCTGTTCAGCCAGGGGC
		Reverse	GGCCGCACAGTTGCTCCACA
Ldha	NM_001136069.2	Forward	GTGCTGCTCTGCGTGCTGGA
		Reverse	GCAAGCTCATCCGCCAAGTCCTTC
Ccl2	NM_011333.3	Forward	GCCAGCTCTCTCTTCCTCCACCA
		Reverse	GGGCGTTAACTGCATCTGGCTGA
Csf1[a]	NM_001113529.1	Forward	AGCAGGTGGTGGACAGTGCCT
		Reverse	CCCCAGAGGGTGTCTGCGCT
Cxcl12[a]	NM_021704.3	Forward	GCCCCTGCCGGTTCTTCGAG
		Reverse	AGCCGTGCAACAATCTGAAGGGC
Pedf1	NM_021704.3	Forward	CTGAAGCCTGCTGGACGCTGG
		Reverse	TGCATCCCGGAACTGTGGTTGC
Pedf1 (2)	NM_021704.3	Forward	TCTCTGCCCTTTCTCTGGGAGCTG
		Reverse	GTGCTGTGGATGTCAGGGTTGGT
Pedf1 (3)	NM_021704.3	Forward	CCTCTCTGCCCTTTCTCTGGGAGC
		Reverse	AGGGGCAGTAACAGAGGCAAGGA
Thbs1	NM_021704.3	Forward	CACACAGGCTCCGTGTTGGGC
		Reverse	CTCTGGAATGCGGTTGCTTCCACA
Timp3	NM_021704.3	Forward	CAGTAAGATGCCCCACGTGCAGT
		Reverse	CCTTCATACACGCGCCCTGTCA

and imaged using an InGenius gel documentation system (Syngene, Cambridge, UK).

Analysis using RTPCR was performed with SYBR green PCR master mix (Applied Biosystems), and the appropriate primers and template using ABI PRISM 7000 and 7300 sequence detection systems (Applied Biosystems) on 96 well optical reaction plates (Applied Biosystems). The protocol used an initialisation at 50 °C (2 min) and then 95 °C (10 min). This was followed by a 40× cycle of extension and denaturation at of 95 °C (15 s) and annealing at 60 °C (60 s), *i.e.* extension occurs in the denaturation step temperature ramp. 2 ng cDNA was used per reaction in a total reaction volume of 25 µL containing 400 nM of both forward and reverse primers. Following data acquisition, the C_T values were exported for analysis from the acquisition software, following the setting of a suitable threshold value for all samples.

2.8.6 Data analysis

Computation of C_T values:

S Sample.

C Calibrator.

NRQ_{samp} Normalised relative quantity for a comparison between sample and calibrator sample.

NRQ_{gene} Normalised relative quantity for a comparison between gene and calibrator gene.

ΔNRQ_{samp} Error in NRQ_{samp}.

ΔNRQ_{gene} Error in NRQ_{gene}.

$C_{T,T}$ Cycle threshold for target gene.

$C_{T,R}$ Cycle threshold for reference gene.

E_T Efficiency of primer for target gene.

$E_{T,C}$ Efficiency of primer for target calibrator gene.

$E_{T,S}$ Efficiency of primer for target sample gene.

E_R Efficiency of primer for reference gene.

ΔC_T Normalised cycle threshold for target gene, relative to reference gene.

$\Delta C_{T,T}$ Change in $C_{T,T}$ between Normalised cycle threshold for target gene, relative to target calibrator gene.

$\Delta C_{T,R}$ Change in $C_{T,T}$ between Normalised cycle threshold for reference gene, relative to reference calibrator gene.

Relative quantification of real-time RTPCR data is commonly analysed using the $2^{-\Delta\Delta C_T}$ method (Livak and Schmittgen, 2001), shown in Equation 2.1. The expression of a target gene, relative to a reference gene, is compared with a target calibrator gene, again relative to the same reference gene. This allows comparison of the expression of the target gene between different tissues, relative to a calibrator tissue, or between different timepoint, relative to a calibrator timepoint, for example.

$$NRQ_{\text{samp}} = 2^{-\Delta\Delta C_T} = 2^{-[\Delta C_T(S) - \Delta C_T(C)]} = \frac{2^{\Delta C_T(S)}}{2^{\Delta C_T(C)}} = \frac{2^{C_{T,T}(C)}/2^{C_{T,T}(S)}}{2^{C_{T,R}(C)}/2^{C_{T,R}(S)}} \tag{2.1}$$

where

$$\Delta C_T(X) = C_{T,T}(X) - C_{T,R}(X) \tag{2.2}$$

However, this method makes the assumption that all primers amplify their targets with 100% efficiency ($E = 1$; $1 + E = 2$). This is not the case for all the primers used in this work, and so a modified version derived by Pfaffl was used which takes primer efficiency into account (Pfaffl, 2001), shown in Equation 2.3.

$$NRQ_{\text{samp}} = \frac{(1+E_T)^{C_{T,T}(C)}/(1+E_T)^{C_{T,T}(S)}}{(1+E_R)^{C_{T,R}(C)}/(1+E_R)^{C_{T,R}(S)}} = \frac{(1+E_T)^{\Delta C_{T,T}(C-S)}}{(1+E_R)^{\Delta C_{T,R}(C-S)}} \tag{2.3}$$

Standard error propagation methods were used to calculate the total error in the above calculation, shown in Equation 2.4, derived from (Muller, Janovjak *et al.*, 2002).

$$\Delta NRQ_{\text{samp}}(x_i \ldots x_n) = \sqrt{\sum_{i=1}^{n} (\ln(E_{x_i} \cdot C_T(x_i))^2)} \tag{2.4}$$

$$\Delta NRQ_{\text{samp}} = \sqrt{(\ln(E_T) \cdot C_{T,T}(S))^2 + (\ln(E_T) \cdot C_{T,T}(C))^2 + (\ln(E_R) \cdot C_{T,R}(S))^2 + (\ln(E_R) \cdot C_{T,R}(C))^2} \tag{2.5}$$

It is also possible to study the expression of a target gene, relative to a reference gene, within the same sample. Again, both are normalised relative to a reference gene. This allows comparison of the changes in expression of the target gene between different tissues and/or timepoints, but normalised to the expression of a particular

calibrator gene in each sample. This is accomplished by a simple modification of Equation 2.3 to give Equation 2.6.

$$NRQ_{\text{gene}} = \frac{(1+E_{\text{T,C}})^{C_{\text{T,T}}(\text{C})}/(1+E_{\text{T,S}})^{C_{\text{T,T}}(\text{S})}}{(1+E_{\text{R}})^{C_{\text{T,R}}(\text{C})}/(1+E_{\text{R}})^{C_{\text{T,R}}(\text{S})}} = \frac{(1+E_{\text{T,C}})^{C_{\text{T,T}}(\text{C})}/(1+E_{\text{T,S}})^{C_{\text{T,T}}(\text{S})}}{(1+E_{\text{R}})^{C_{\text{T,R}}(\text{C}-\text{S})}} \tag{2.6}$$

Error propagation is identical to Equation 2.3, using Equation 2.4.

2.9 Microfluidic networks

An overview of the key steps in patterning a collagen gel with a microfluidic network are shown in Figure 2.6.

2.9.1 PEN slide preparation

Poly(ethylene 2,6-napthalate) (PEN) was used in the form of 12, 25 and 50µm thick biaxially oriented sheets (Goodfellow, Cambridge, UK).

PEN coated slides were produced as follows. Glass slides were cleaned as described in Section 2.3.1. The slides were then rendered non-wettable by treating with DMDCS for 10 min, as described in Section 2.3.2. PEN film cut to the appropriate size were affixed to the slides by floating on the meniscus of water and drawing onto the slide. The PEN was secured to the slide at two opposing edges using nail varnish, and then dried at 40 °C overnight. The remaining two edges were subsequently secured with nail varnish.

2.9.2 UV laser cutting of PEN sheets

All UV laser cutting utilised a PALM Microbeam system with Zeiss Axiovert 200 base (Carl Zeiss) containing a pulsed nitrogen UV laser. The controllable parameters of the system are UV laser energy, UV laser focus offset (relative to the camera focus) and stage movement speed. All three parameters require careful adjustment in order to optimally cut PEN film.

The manufacturer recommends the use of a 40× objective for the cutting of the standard 1.5 µm thick PEN film. However, this is unsuited to cutting thick materials, requiring a 5× objective for cutting 25 and 50 µm thick film. 1.5 µm thick PEN film used slides with the PEN film oriented on top of the slide, with the microscope objective located underneath; this is the configuration used for laser-capture microdissection. Thicker film (12, 25 and 50 µm) required the film to be oriented underneath the slide, in order to prevent the high laser power and dwell time from burning

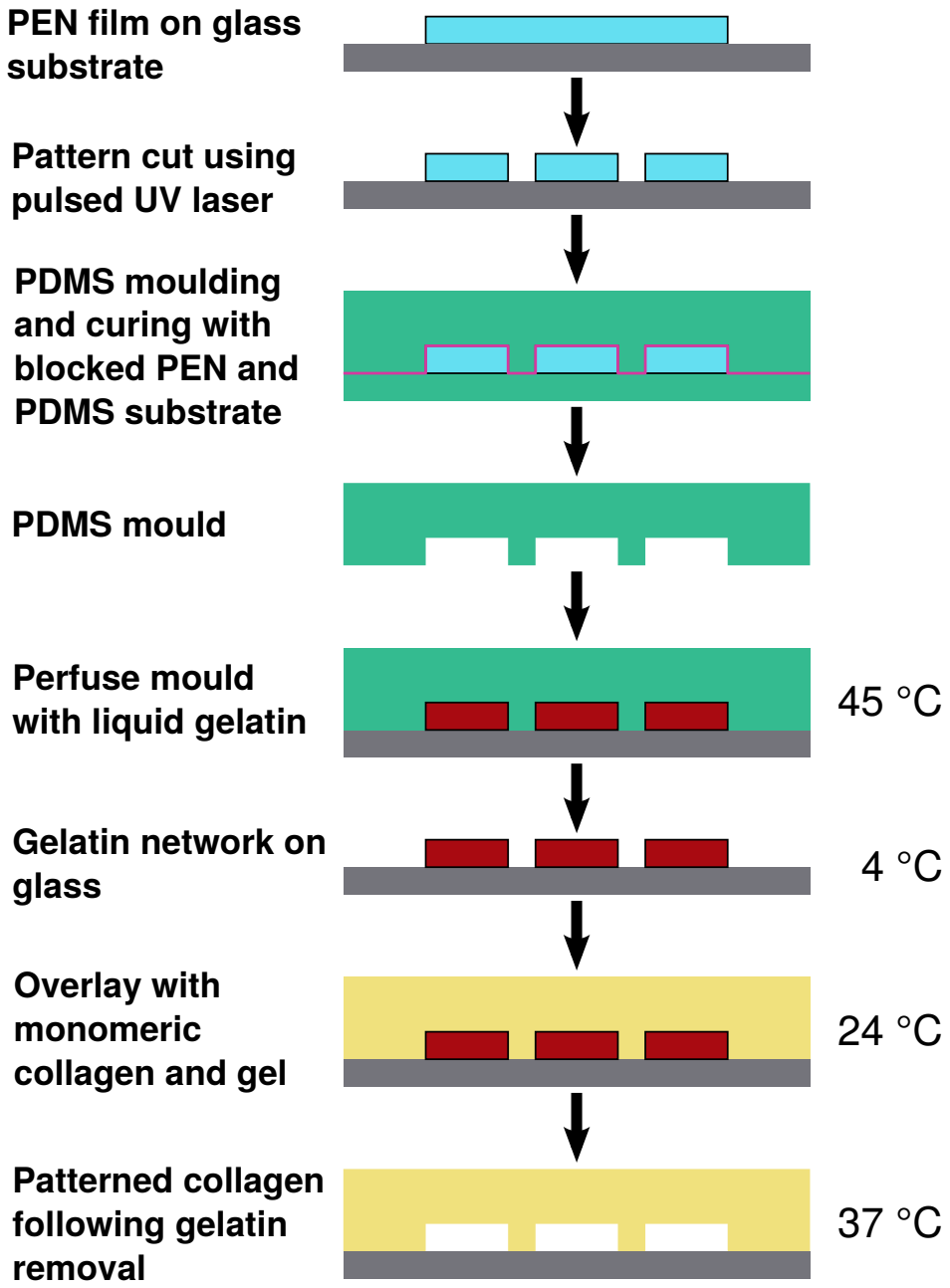

Figure 2.6: Method for making microfluidic collagen gels. PEN film attached to a glass slide is cut to form a positive relief representation of the microfluidic network using a pulsed UV laser. After attachment to pre-cured PDMS substrate and blocking with Pluronic F-127 to prevent adhesion, uncured PDMS poured on top and set forms a negative relief representation of the network. When placed upon a glass substrate and blocked with Pluronic F-127 to permit wetting of the channels, liquid gelatin may be perfused through the network at high temperature and gelled at low temperature. Following removal of the mould, the gelatin network, which has the same physical shape as the original PEN network, may be overlaid with monomeric collagen. After gelation of the collagen matrix the temperature may be raised, and the liquified gelatin perfused from the matrix to leave a collagen matrix with open microchannels.

the PEN film and ejecting glass chips from the slide surface. This orientation also permitted more precise cutting and lower laser power to be used than in the upward orientation. Due to the PEN film being oriented underneath the glass slide, any part of the PEN film which was cut around entirely had the potential to fall down onto the objective, it no longer being attached to the slide or any other part of the film. This did have the potential to cause problems with the beam focus, it being directly in the light path. This problem was mitigated by placing a 120 mm fan attached to a 12 V power supply to pass a stream of air under the stage to direct any falling debris away from the objective.

The UV laser focus was adjustable separately from the primary focus, permitting independent adjustment of the camera focus and the relative offset for PEN cutting. This permitted simultaneous adjustment of both the sample focus and the laser focus, a requirement for accurately observing and controlling cutting. Additionally, the laser power was also adjustable as a percentage of its total (fixed) power output, via a neutral density filter with a circular gradient rotated by a stepper motor, permitting fine control of the cutting in addition to the stage speed. Due to localised melting and cooling as the material passes through the laser beam, this must be set sufficiently wide for a gap to be retained due to flow as the material cools. If set up correctly, the result is a narrow, deep cut.

While the provided PALM Robo software allowed one to manually draw lines, circles and polygons for calibrating the cutting parameters and performing microdissection, this was insufficiently precise and too labour intensive for creating microfluidic networks. The microfluidic network designs were drawn at a 1:1 scale using the Inkscape vector graphics editor (Inkscape Project, 2011). The PALM system is only capable of drawing straight lines, and so curves represented as Bézier curves in the drawing were interpolated to series of straight lines with µm resolution. The drawing was then exported as PostScript (Adobe Systems Incorporated, 1999), a format which consists of drawing commands which are amenable to conversion into the import/export format used by the PALM Robo software (Carl Zeiss MicroImaging GmbH, 2007). Conversion was performed using the GNU R statistical package (R Development Core Team, 2006) following a simple search and replace to transform the PostScript into a valid R program which would output the the pattern in the PALM Robo import/export format. This conversion required a series of matrix transforms to translate and transform the physical coordinates used in the drawing to the origin, scale and orientation used by the stepper motors of the PALM Microbeam stage, which had a scale of 12.8 steps/µm and an inverted y axis. The separate transforms can be logically represented as a single affine matrix transform, which performs translation, scaling and rotation in a single step. The conversion process only required performing once for each unique pattern. Once completed, the conversion to the PALM Robo format permitted the patterns to be loaded into the

PALM Robo software and aligned on the PEN film using the CCD camera for guidance, and reused multiple times to create several copies of a pattern. Once correctly configured, the system could run unattended for several hours.

2.9.3 Perfusion and imaging jig

Technical drawings for the creation of metalwork for perfused 3-D cultures and imaging are shown in Figure 2.7. Parts A–C and E–F were machined from aluminium, and part D from perspex. Part H was cut from acetate sheet (standard overhead projector sheet of 100 µm thickness) with the design laser printed onto it. CAD/CAM for parts A–F was contracted to Aztech Precision Engineering, using CAD drawings drafted by myself. $90 \times 40 \times 3.5$ mm glass plates were made from flat, toughened window glass, obtained from a local glazing supplier.

2.9.4 Silicone elastomer moulding

Room temperature vulcanising silicone elastomer (RTV) was used in compositions of different shore hardness, including RTV3040A (base) and RTV3040B (curing agent), and RTV3436 (base) and RTV3428B or 3436Bred (curing agents), all supplied by Bentley Chemicals Ltd., Kidderminster, UK. Base and curing agent were mixed in a 10:1 ratio. Due to the high viscosity, bubbles introduced during mixing were not removable under vacuum, and were removed by spinning at 1400 g for 5 min.

The silicone elastomer PDMS, also known as Sylgard 184, was obtained from Dow Corning, Midland, MI, USA. It is also composed of a base and curing agent, used in a 10:1 ratio. The two components were mixed in a dish using a plastic spatula and degassed in a 50 mL plastic centrifuge tube (Corning) with a female Luer-Lok fitting bonded to the screw cap to permit secure connection to a vacuum line. Compared with RTV elastomer, the low viscosity of PDMS permitted handling and moulding without the introduction of bubbles.

Non-patterned PDMS blocks were moulded using $90 \times 40 \times 3.5$ mm glass plates and thick shims as shown in Figure 2.7(E). The shim was placed on a glass plate and PDMS poured in , contained by the edges of the shim, and then sealed in by placing a second glass plate on top, using excess PDMS to avoid the introduction of bubbles into the sealed volume. This assembly was then held under compression between a threaded base plate, either Figure 2.7(A) or (B) and an unthreaded top plate (C), (E) or (F) using using machine screws. This both prevented leakage and ensured that the moulded PDMS would have precise dimensions, with exact and uniform thickness.

Patterned PDMS blocks were moulded by placing the PEN network on either a glass or non-patterned PDMS backing surface and then pouring PDMS over the top, contained again by a shim and second glass plate, which was then placed under compression as for non-patterned PDMS moulding. Precise network alignment was

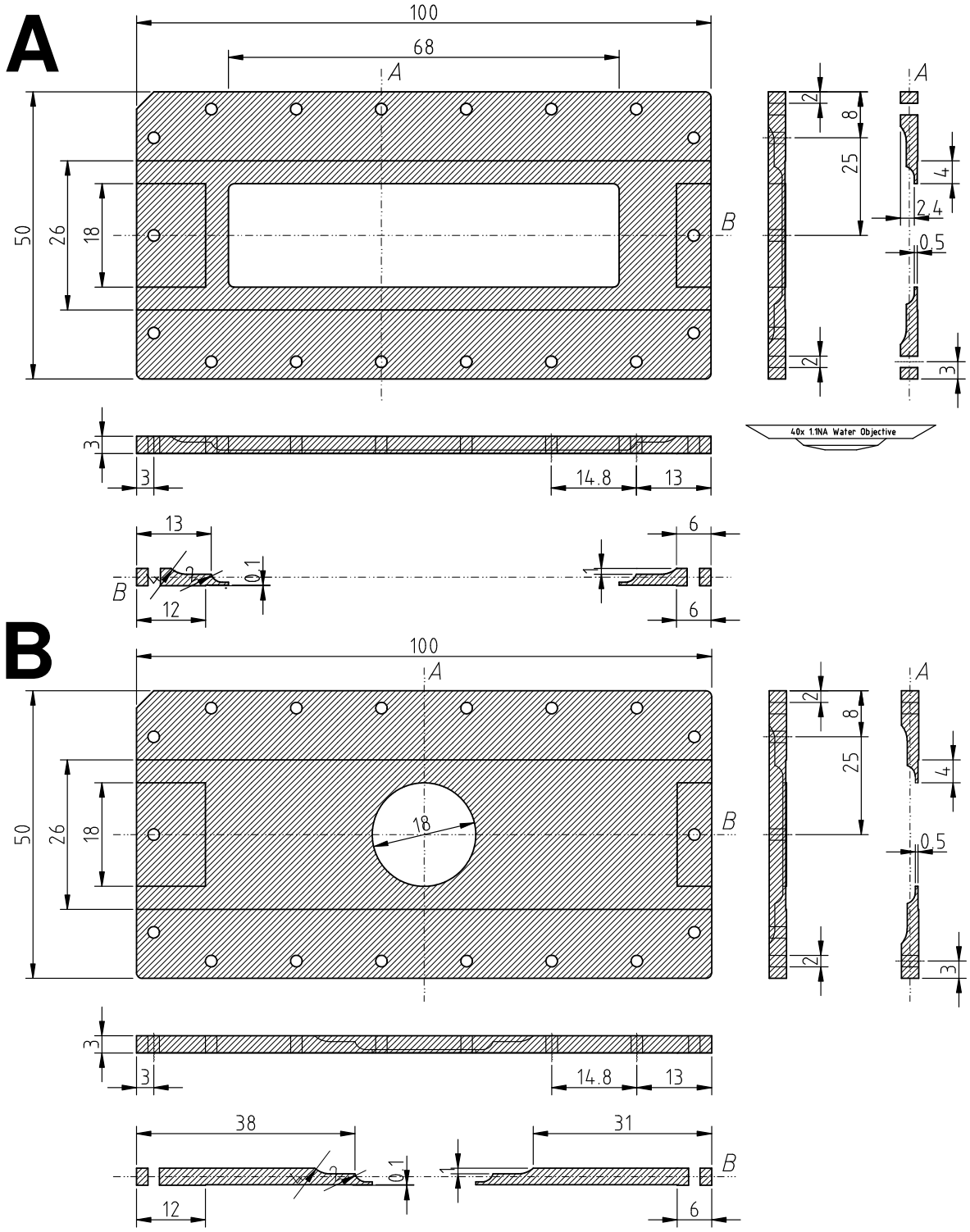

Figure 2.7: Microfluidics jig parts. (A) Multiple sample imaging frame. (B) Single sample imaging frame. Both these parts have a 0.1 mm rebate to accommodate a slide-sized glass coverslip on the top face, with the bottom face machined to permit the use of a Zeiss 40× water-dipping objective.

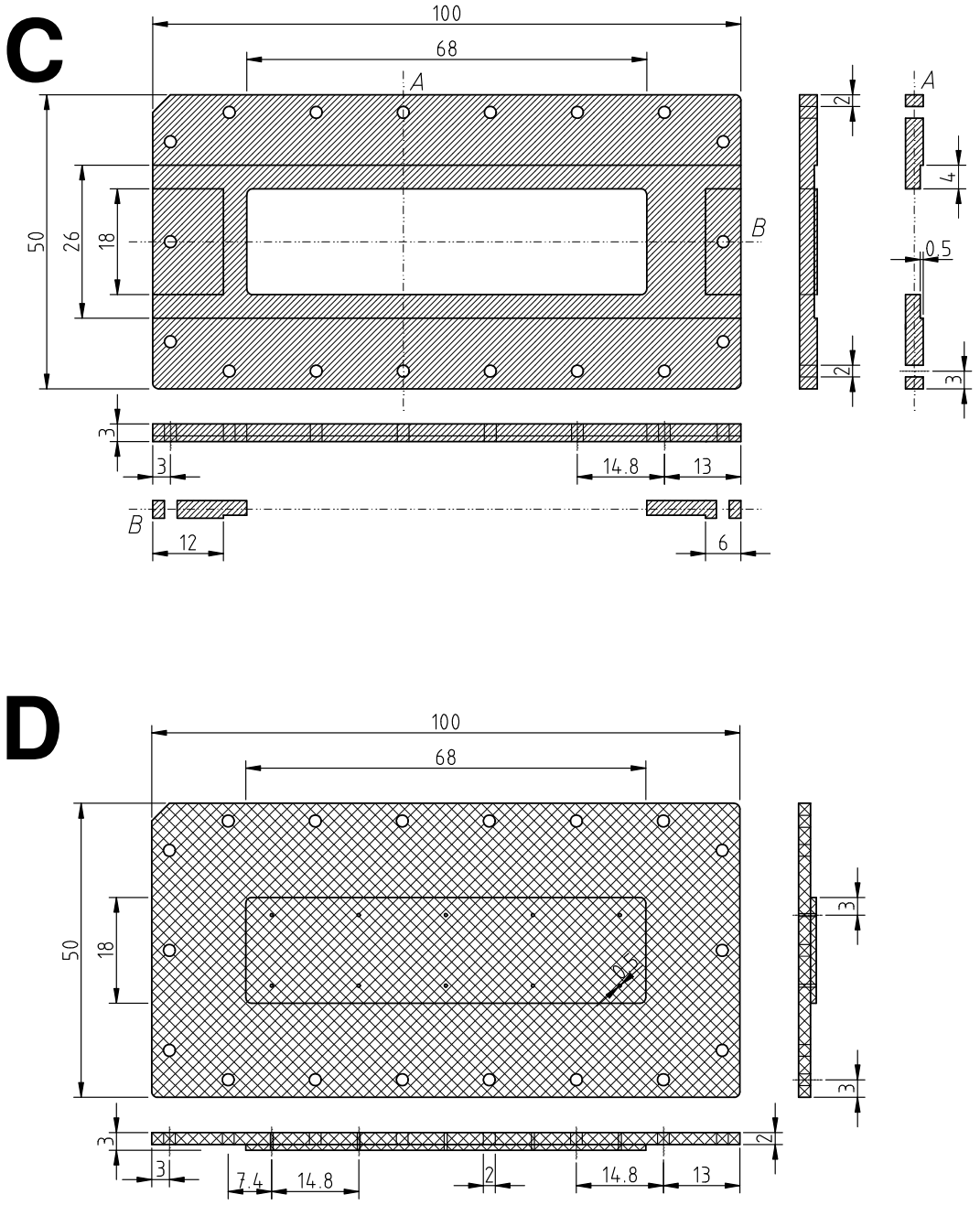

Figure 2.7: Microfluidics jig parts (continued). (C) Slide holding frame, with 1 mm rebate to accommodate a standard slide, used for aligning moulds and parts such as the perfusion manifold. (D) Perfusion manifold with five parallel sets of ports.

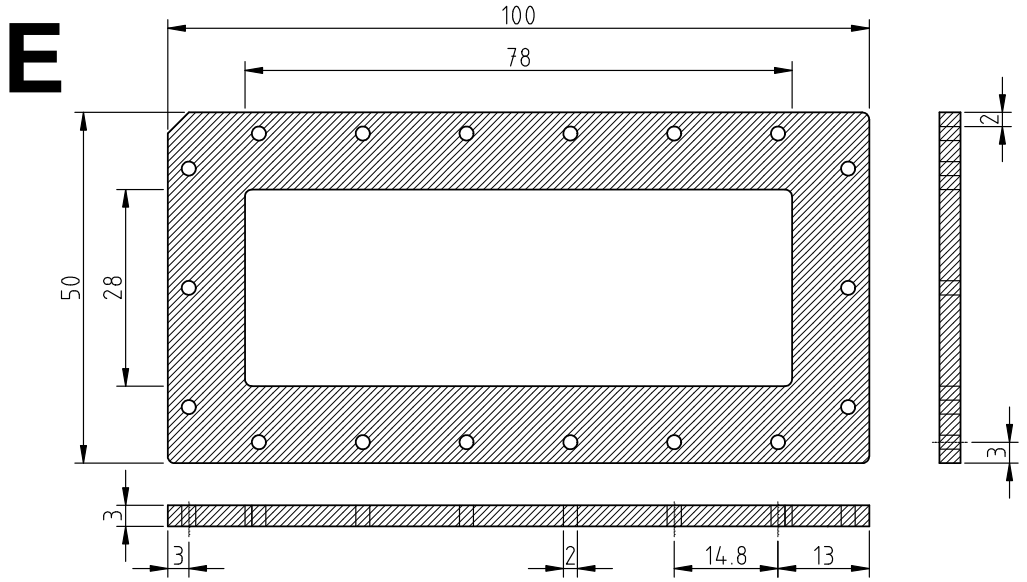

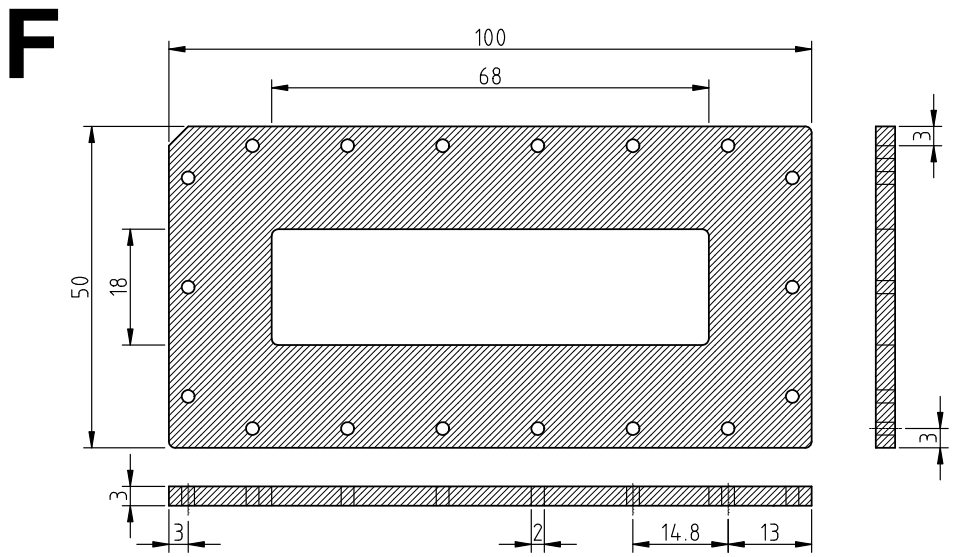

Figure 2.7: Microfluidics jig parts (continued). (E) Large and (F) small shims, used for retaining and holding PDMS during and after moulding.

G

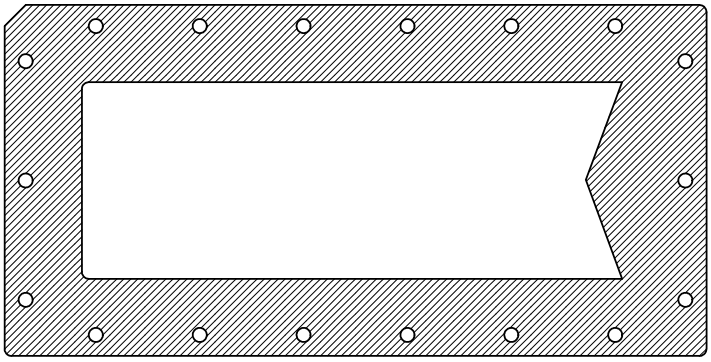

Figure 2.7: Microfluidics jig parts (continued). (G) Acetate shim with tab for PDMS–PDMS separation (100µm thickness).

achieved by aligning the slide using the slide guides shown in Figure 2.7(C) with the perfusion manifold (D) to ensure the manifold would align with the microchannel endpoints when assembled for perfusion. In order to allow removal of the PEN from the moulded PDMS after curing, the PEN and glass or PDMS backing were blocked with Pluronic F-127 1 % (w/v) for 1 hour, followed by washing three times with distilled water and drying, which allowed easy separation of the PEN from the PDMS. When moulding PDMS on PDMS, an acetate shim with a tab (Figure 2.7(G)) was used to allow separation, as well as to provide an additional 100 µm PDMS depth for compressive sealing of the microchannels to glass substrate when under perfusion.

Chapter 3

Vascularisation of lymph node anlagen *in vivo*

3.1 Introduction

3.1.1 Timecourse of LN development

During the process of LN organogenesis, the developing organ acquires a functional vasculature. When development commences, as LTi and LTo cells accumulate at the site in response to chemoattractive cues, little or no blood vasculature is initially present, and there is little evidence of a requirement for blood vasculature to be present at the site in order for LN development to progress, vascularisation being thought to occur later on during development (Coles *et al.*, 2010). The fully developed LN contains an elaborate blood vascular network which is critical for its function . Without a vascular network, lymphocytes would not be able to enter the LN via the HEVs, and the metabolic demands of the LN could not be met by diffusion alone. At some point during LN development, a functional blood vasculature develops. The timecourse and nature of this process are not well characterised, and nor are the driving forces and mechanisms behind the process.

An overview of the timeline of development of the different LNs is detailed in Mebius (2003), showing that the cervical LN begins development at E11.5, the axillary and brachial after E12.5, and the inguinal after E15.5. In Section 1.3.3, the major steps undertaken during the development were described. The process is initiated at E11.5, when LTi cells first appear at sites of LN development and accumulate over subsequent days (Coles *et al.*, 2006). However, the development of the lymph sac is initiated somewhat earlier, as described in the review by Blum and Pabst (2006): lymphatic competence is first detected at E9.5 by the expression of LYVE1 on cells in the cardinal veins, leading to lymphatic bias on E10.5 seen by expression of the lymphatic marker and transcription factor Prox1. This is followed by migration away from the vein by E11.5 and assembly of the lymph sac by E12.5. In a recent review

(van de Pavert and Mebius, 2010), LN development is described starting at E12.5 with the initial influx of LTis in response to CXCL13, followed by their activation and maturation by E13.5, leading to stromal activation and LTo formation, but this does not consider the lymph sac. By E13.5, some structure is detectable, the inguinal LN being shown as a bud of cells (described as "endothelial") surrounded by mesenchyme, which subsequently reorganises as the outer layer invades the inner by E17.5 (Bénézech, White *et al.*, 2010). Some similarities are observed in the brachial node, such as being surrounded by LYVE1$^+$ cells, but the axillary and brachial anlagen are generally heterogeneous, even at E14.5, containing both LTis and LTos (Vondenhoff, Greuter *et al.*, 2009a), possibly due to the axillary, brachial and cervical nodes being in a more advanced stage of development compared to the inguinal node as a result of developing earlier. The E14.5 brachial node was shown by Vondenhoff *et al.* (2009a) to be extensively vascularised, showing MECA32$^+$ vessels in the centre of the anlagen, and LYVE1$^+$ vessels surrounding it, both expressing VEGFR2. This observation does not fit in with the existing concept of vascularisation occuring later during development. T cells are able to enter the lymph node from P2, when HEVs begin to express peripheral node addressin (PNAd) (Hoorweg and Cupedo, 2008), at which time the vasculature is unquestionably functional.

In the adult, the LN vasculature is believed to be regulated by the stroma, which Chyou, Ekland *et al.* (2008) demonstrated to produce VEGF in response to LT signalling via LTβR. However, this work did not distinguish between FRC, FDC and MRC stromal subsets, so it is not entirely clear which are responsible. MRCs in the adult are thought to be analogous to LTo in the embryo, due to expressing many of the same chemokines, receptors and adhesion molecules (Katakai *et al.*, 2008).

3.1.2 Models of LN vascularisation

An outstanding question is the nature of the relationship between lymph sac development and stromal activation. Mebius (2003) presented a model for LN development depicting the stroma developing adjacent to the lymph sac, subsequently flattening the sac into a double-layered subcapsular sinus which surrounds it, except for at one side, which would presumably become the hilus. In this scenario, the blood vasculature would be predicted to invade from this point, which is where it will enter and exit in the developed node, and then ramify throughout. If vessels already existed inside at this point, then they would require connection to the external vasculature, if this was not already the case. However, this model does not fit with the observations of Vondenhoff *et al.* (2009a), which shows an almost continuous layer of LYVE1$^+$ cells surrounding vessels and stromal cells inside the sac of the E14.5 brachial node. Interestingly, MECA32$^+$ cells are seen to exit the sac at its major discontinuity, which may be the site of the future hilus. If this is genuine, and not a sectioning artefact, this would imply that the anlagen is vascularised from the

start, but raises questions as to how this structure develops. It could be hypothesised that the lymphatic endothelium may migrate to surround a bud of mesenchyme, or that the mesenchyme may migrate into the sac, or even that the mesenchyme may condense adjacent to the sac, pulling the sac around it as a result of physical forces acting upon it. It is also important to note that this observation in the brachial node is entirely the opposite of that made in the inguinal node by Bénézech *et al.* (2010) which shows that the lymphatic endothelium to be a solid bud of cells, encircled by stroma.

3.1.3 Factors affecting angiogenesis

Several of the major factors influencing angiogenesis were discussed previously in Section 1.2.4. The currently accepted dogma is that angiogenesis arises as a result of the combined effect of pro- and anti-angiogenic factors, the balance of which affects whether a vascular tube will outgrow, regress or remain static (Davis *et al.*, 2002; Zhang and Ma, 2007). Obtaining a clearer picture of which pro- and anti-angiogenic factors are being produced in the LN anlage may provide some insight into the mechanisms driving angiogenesis in this specific context. Hypoxia plays a critical role in both vascular homeostasis, and vascular development during embryogenesis, and hence may also be a contributing factor (Adelman, Maltepe *et al.*, 1999; Iyer, Kotch *et al.*, 1998).

3.1.4 Hypoxia

Hypoxia is the reduction of oxygen tension within a tissue below that of normoxia, usually considered to be 2–9 % (v/v) (Simon and Keith, 2008) or 40–60 mm Hg (Kaluz, Kaluzová *et al.*, 2008). The transcription factor HIF-1α is constitutively transcribed and translated, but under normoxia is continually degraded in an oxygen-dependent manner (Kaluz *et al.*, 2008). Under hypoxia, HIF-1α is no longer degraded, permitting the formation of a HIF-1$\alpha_2$1β_1 complex which initiates the transcription of genes containing HREs (Kaluz *et al.*, 2008). Hypoxia-responsive genes have a wide range of effects, including changes to cellular metabolism, survival, increasing angiogenesis and recruiting macrophages (Fong, 2009; Fraisl, Mazzone *et al.*, 2009; Kaluz *et al.*, 2008; Murdoch, Muthana *et al.*, 2005; Shweiki, Neeman *et al.*, 1995). One of the principal angiogenic responses is the upregulation of VEGF (Shweiki *et al.*, 1995), but many other factors are also upregulated including VEGFRs, angiopoietins, erythropoietin, placental growth factor and insulin-like growth factors, and MMP9 (Fong, 2009). Chemoattractive and chemotactic factors are also induced which attract macrophages, including CCL2, M-CSF and CXCL12 (Murdoch *et al.*, 2005). Macrophages are themselves sensitive to hypoxia, resulting in their transcription of multiple hypoxia-responsive genes, including VEGF (Murdoch and Lewis, 2005). Hyp-

oxia can also increase collagen synthesis and additionally, lysyl hydroxylases responsible for hydroxylation and cross-linking of collagen are upregulated by hypoxia (Myllyharju and Schipani, 2010).

Hypoxia may play an important role in vascularisation during development, hypoxic responses driving VEGF production having been previously shown to be required for the proliferation and development of hæmatopoietic precursors (Adelman *et al.*, 1999). Embryos are hypoxic and require HIF-1α expression to develop beyond E11 (Adelman *et al.*, 1999; Iyer *et al.*, 1998), HIF-1α being involved in embryo patterning as a result of controlling the differentiation of condensing mesenchyme, at least in the case of chondrogenesis (Provot, Zinyk *et al.*, 2007) and bone formation (Dunwoodie, 2009). In these examples, condensing tissues became hypoxic and began to upregulate HIF-1α. Hypoxia may therefore also play an equivalent role in the case in the LN, which also develop by the condensation of mesenchymal progenitors.

Various approaches exist to measure hypoxia within tissues (Evans, Mattock *et al.*, 2011), though many are invasive. Reduced oxygen tension in tissue results in an altered redox environment, detectable non-invasively using pimonidazole hydrochloride (hypoxyprobe-1, Hypoxyprobe, Inc), a small 2-nitroimidazole compound which forms stable adducts in hypoxic cells and tissues (Raleigh, Calkins-Adams *et al.*, 1998; Varia, Calkins-Adams *et al.*, 1998). These adducts are detectable with a rabbit polyclonal antibody, hence allowing visualisation using standard immunohistochemical techniques. This may be a suitable method for determining if the developing LN anlagen are hypoxic both in absolute terms, and relative to their surroundings.

3.1.5 Aims

1. To determine the timescale and nature of lymphoid organ vascularisation during development through immunofluorescence imaging, in particular in its relation to the changing organisation the of LN stroma.

2. To determine how changes in the organisation of cellular and extracellular matrix components of the developing LN anlagen relate to the process of LN vascularisation and development.

3. To determine if localised hypoxia is related to lymphoid organ vascularisation in the developing embryo using the hypoxia sensing probe pimonidazole.

4. To determine the balance of major pro- and anti-angiogenic factors in the developing lymphoid organs throughout the timecourse of their development, and in the fully developed state in the adult, and to correlate their influences upon observed vascularisation during development.

5. To compare the expression of pro- and anti-angiogenic factors in the embryo with those in the adult, and to identify differences between the FRC and MRC stromal compartments which may play a role in LN patterning.

3.2 Results

3.2.1 Lymphoid organ visualisation using wholemount microscopy

In order to observe developing lymphoid organs in the three-dimensional context of the embryo as a whole, wholemount confocal microscopy was used to visualise development. Stage E15.5 of development was used as a starting point for testing the various antibodies to be used for immunohistochemical staining, which would then be extended to other timepoints during development. E15.5 hCD2-GFP embryos were fixed, vibratome sectioned and stained as described in Section 2.6.2, using the antibodies and reagents described in Tables 2.2 and 2.3. Samples were stained with GFP-Alexa Fluor (AF)594 or AF647 to show LTi cells (and additionally lymphocytes in the case of the thymus). Samples were additionally stained with α-SMA-Cy3, endomucin-AF647, or the basement membrane proteins collagen IV, laminin or fibronectin (all rabbit polyclonals) with goat anti-rabbit AF594 or AF647 secondary. In order to improve staining quality, staining and wash times were extended from overnight and several hours, respectively, to several days to ensure antibody penetration into, and removal from, thick sections. The results are shown in Figure 3.1. Panels (A) and (B) show GFP^+ cells, presumably LTis, in relation to vasculature. Note the diffuse nature of LTis—they not yet associated intimately. However, the high level of autofluorescence in the tissue resulted in a great deal of ambiguity when selecting genuine LTis, as illustrated by rotating the sample in (B), where it is difficult to differentiate between GFP^+ cells and autofluorescence, there being continuous variation in fluorescence intensity between cells which appear to be GFP^+ in (A) and the remainder of the cells within the field of view as shown in (B). Panels (L) and (M) illustrate the major differences between staining controls, which vary widely in autofluorescence depending upon their location within the embryo.

The remaining images are of the thymus, which was readily identifiable within the thoracic cavity without GFP staining. Despite this, the large concentration of lymphocytes within the organ did make identification possible by fluorescence, since the amount of fluorescence resulting was above the background autofluorescence. Panels (C–K) all illustrate vascular structures in the thymus. Endomucin staining clearly shows a complex vascular network throughout the entire organ, appearing to extend around the entire capsule, ramifying throughout the cortex in a series of loops and extending into the medulla where the structure appears to be more branched. There appears to be a partial disconnect between the vasculature of the cortex and

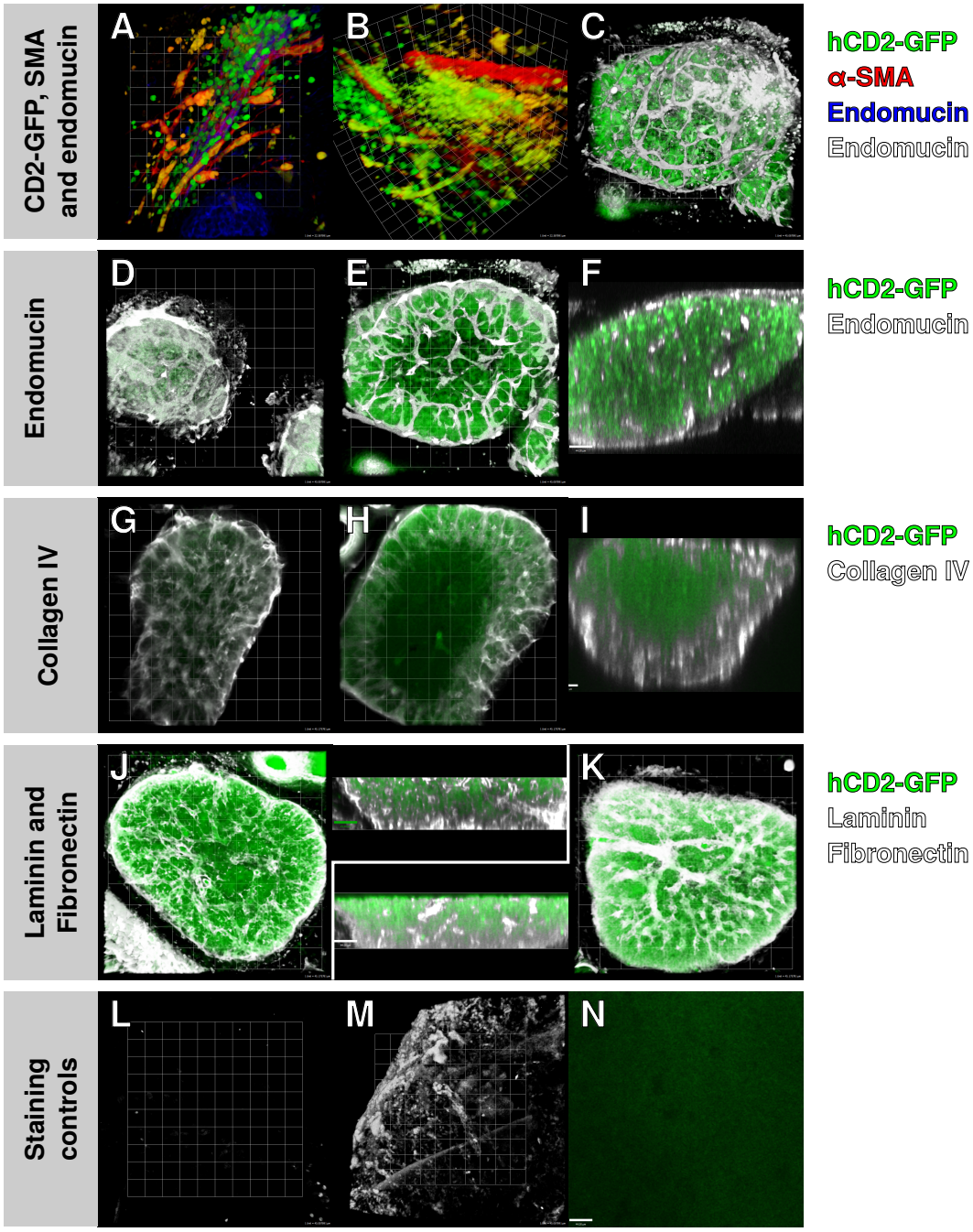

Figure 3.1: Wholemount microscopy of developing lymphoid organs. Vibratome-sectioned slices of E15.5 mouse embryos were stained for GFP (LTis in A and B, LTis and thymocytes in C–K), α-SMA, endomucin and several basement membrane proteins. (A) Putative LN anlagen, showing LTi in close proximity to α-SMA$^+$ vessels. However, the LTi staining is ambiguous when viewed from the side (B). Endomucin staining shows a complex vascular network in the thymus (C), and when viewed as a series of 30µm sections at the edge (D) and middle (E), shows vascularisation throughout, and an apparent difference between cortical and medullary regions. A representative *xz* section (F) also shows extensive vascularisation. Collagen IV at the edge (G) and middle (H) shows staining only in the cortex, the same being seen in *xz* (I). This is not, however, the case for laminin (J) and fibronectin (K), which show a staining pattern similar to endomucin, including in *xz* projection. The staining controls for A–F (L and M) show that staining is specific, but that autofluorescence varies greatly between tissues; (N) is the control for G–K. Scales are 22.5 µm (A, B), 45 µm (C, D, G, H, L, M and main view of J and K), 44 µm (F, N, and side view of J and L) and 38 µm (I).

medulla. Basement membrane staining highlights an interesting contrast between laminin and fibronectin and collagen IV. Laminin and fibronectin both show staining throughout the tissue as for endomucin, delineating structures with repeated hierarchical branching, particularly in the case of fibronectin. In contrast, collagen IV stains the capsule and extends into the cortex, but does not extend into the medulla, despite major vessels being visible due to autofluorescence.

A number of different directly-conjugated rat anti-mouse monoclonal antibodies against CD31 and CD144 were additionally used to label the vasculature, listed in Table 2.2. However, these all failed to demonstrate any specific staining (not shown).

3.2.2 Live imaging of lymphoid organs

In order to visualise the structure of the LN anlagen without the need for fixation and staining, anlagen (axillary, brachial, cervical and inguinal) and thymi were dissected from E15.5 hCD2-GFP embryos and embedded within a collagen I gel in a glass-bottomed dish, and were overlaid with IMDM. The gel was for support and to prevent movement of the tissues during imaging. Using MP microscopy, second harmonic generation was used to visualise the collagen I matrix around the anlagen, the anlagen itself being visualised using the GFP fluorescence of the LTi cells within as well as SHG highlighting collagen I structures around the anlagen (Figure 3.2).

Few LTis are visible in the axillary node, possibly a result of the main population not having been dissected or was not within the working distance of the objective. Intense collagen I SHG around the edge of this sample is most likely to be the edge of the skin taken along with the node, or alternatively the edge of the tissue has acted as seed points for the supporting matrix during gelation. In comparison, the brachial nodes contain densely-clustered LTis, in the case of panel (C), being surrounded by a band of collagen I which may indicate the boundary of the lymph sac. In the lower left of the anlage, the collagen is present in at least two parallel bands, which may delimit the forming subcapsular sinus and/or lymph sac. This extends to the upper left, which may be the site of an afferent lymphatic vessel entering the sac. It is notable that in all cases the LTis themselves are present in a void space apparently absent of collagen I SHG, whether or not they are bounded by a visible collagen I layer. In comparison, the thymus shows little supporting matrix inside the organ, which is densely populated with GFP^+ lymphocytes. However, a dense collagen I matrix is present around the organ, presumably being the capsule.

3.2.3 Lymphoid organ visualisation using frozen sections

While live imaging, unlike wholemount microscopy, readily permitted visualisation of the LTis within the anlagen, it did not permit simultaneous study of other features such as their relation to other cell types, the extracellular matrix (other than colla-

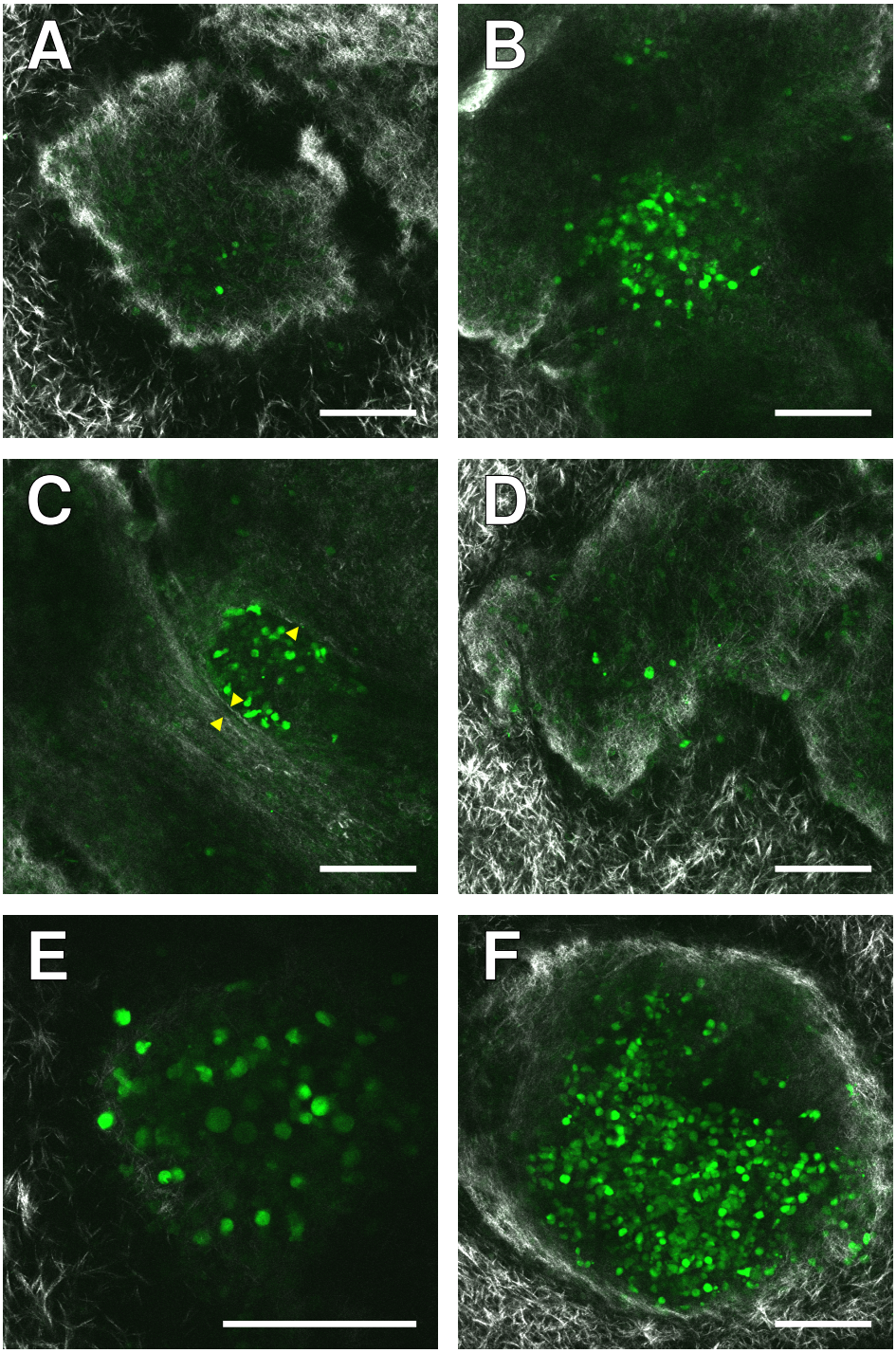

Figure 3.2: Live imaging of developing lymphoid organs. GFP-expressing LTi cells are shown in green, and collagen type I SHG in white. LN anlagen and thymi dissected from E15.5 embryos were embedded in a rail tail collagen support matrix and imaged using a Zeiss LSM 510 NLO MP microscope. The tissues imaged were (A) axillary, (B) brachial, (C) brachial LNs, showing collagen immediately around the LTis (yellow arrowheads), with the LTis in a less dense void space. The double arrowheads indicate parallel collagen bands which may be the subcapsular sinus, and which also extends away from the anlage. (D,E) Cervical **LNs!**s. (F) Thymus, showing dense collagen surround. The collagen support is visible as larger, brighter fibres surrounding the tissue, particularly noticeable in (A) and (D). Collagen fibres surrounding the edge of the dissected tissue are visible in (A,B,D), and may be the edge of the skin in the section. (C,E) have only weak collagen SHG in comparison. Scale bars are 100 µm.

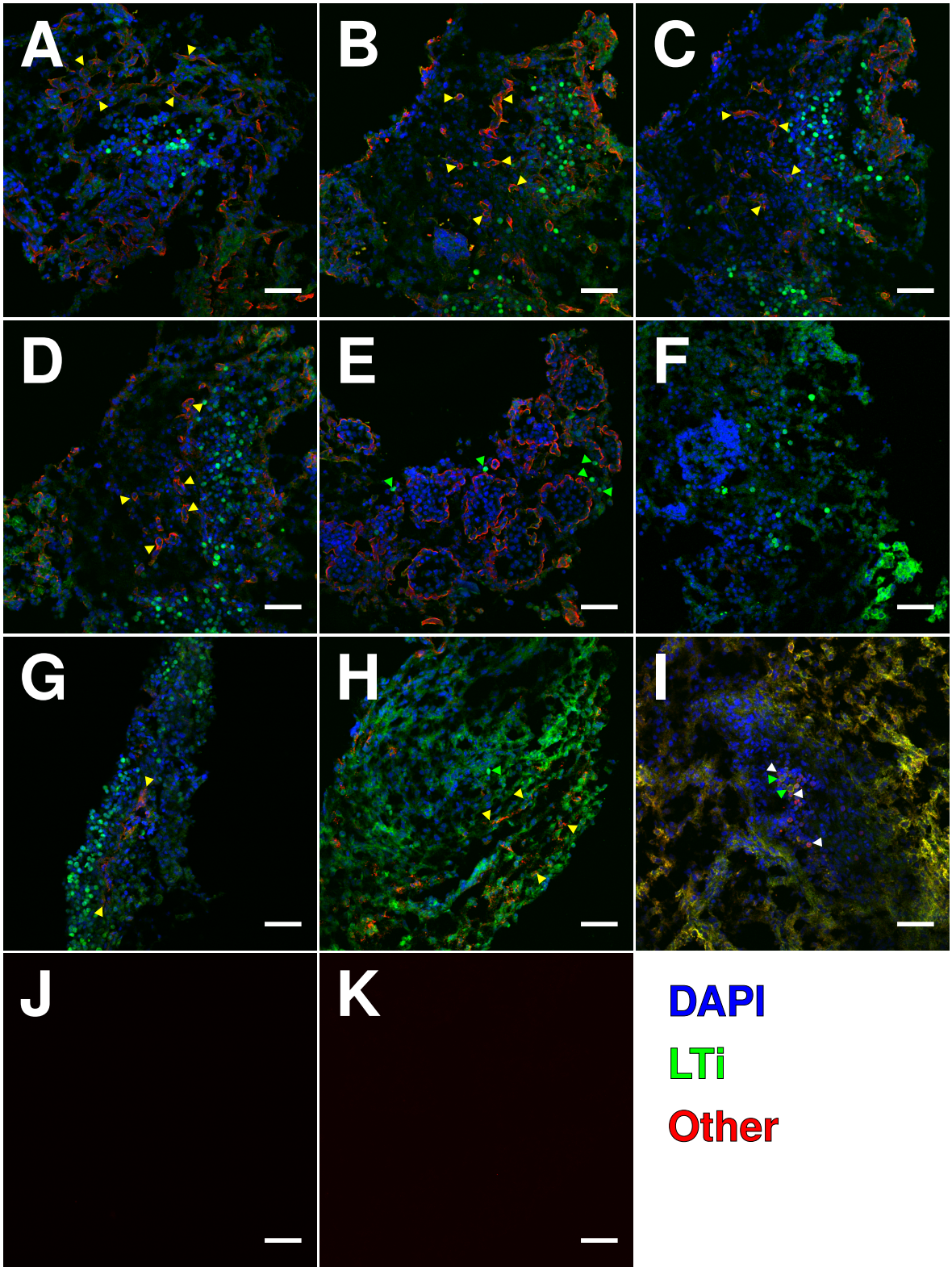

Figure 3.3: Frozen section imaging of developing lymphoid organs. All hCD2-GFP sections of LN anlagen are stained with DAPI (blue) and GFP (green). Stains in red are collagen IV (A–C), collagen I (D), laminin (E), endomucin (F), MECA-32 (G), LYVE-1 (H), VCAM (I). (J) and (K) are staining controls. Arrowheads indicate vascular structures (yellow), LTis (green) and LTos (white). Collagen IV and I show the presence of an anastomosing vascular bed surrounding the LTi-containing anlagen, existing as two interconnected layers (paired arrowheads). This structure is partially LYVE-1$^+$. VCAM-1 staining illustrates close association between a small cluster of GFP$^+$ LTis and VCAM$^+$ LTos. Endomucin did not show positive staining of vessels, while MECA-32 stained a vessel running along the edge of the anlagen. Scale bars are 50 µm.

gen I), and the general structure of the surrounding tissue. Frozen sections were therefore used as an alternative to wholemount.

As for live imaging, LN anlagen (axillary, brachial, cervical and inguinal) and thymi were dissected from E15.5 embryos. The dissected tissues were processed and cut into 7 µm thick sections as described in Section 2.6.1. All samples were stained using DAPI and anti-GFP to show all cell nuclei and LTis, respectively. Samples were then individually stained for extracellular matrix and basement membrane proteins (collagens I and IV, and laminin), vascular markers (endomucin, MECA-32, LYVE-1) and the LTo marker VCAM-1. Channel subtraction was used to correct for crosstalk between channels post acquisition. The results are shown in Figure 3.3. Note that, as for wholemount, CD31 and CD144 monoclonal antibodies were additionally used, but again failed to show any specific staining (not shown).

Collagen I and IV showed very similar staining patterns, staining a bright band surrounding the LTi cells, which is presumably the lymph sac. Interestingly, this appeared to surround the anlagen in two layers, which appeared to be interconnected by small vessels bridging the gap between the layers (seen in panels (B) and (C), which are serial sections of the same anlage. Collagen I was present in a single inner layer, with some evidence of an incomplete outer layer. LYVE-1 staining gave the impression of there being an incomplete LEC layer surrounding the developing node, but was less defined than the basement membrane staining which may imply that it is of mixed BEC/LEC composition. Sections stained for laminin unfortunately did not include any anlagen; the sample shown here is most likely to be a section between the anlagen and the skin surface. Migrating LTis are present in the spaces between dense cell clusters bordered with laminin, from which the LTis appear to be excluded. Neither endomucin nor MECA-32 stained any ECs within the anlagen, endomucin being restricted to two regions around the periphery, and MECA-32 staining a long vessel running alongside a streak of LTis, but no staining being apparent within the LTi cluster.

3.2.4 Hypoxia in developing LN anlagen by pimonidazole imaging

If the hypothesis that vascularisation of developing LN anlagen is a result of localised hypoxia is correct, the hypoxic environment should be detectable using pimonidazole. Pregnant female hCD2-GFP mice bearing embryos from E14.5–E17.5 were injected intraperitoneally with 200 μL 9 mg/mL pimonidazole hydrochloride in PBS or 200 μL vehicle (PBS only). The mice were killed after 120 mins and the embryos and adult liver and spleen taken for analysis. The embryos were sorted into GFP positive and negative groups and all embryos and tissues were fixed overnight in 4 % paraformaldehyde. Embryos and tissues were embedded in 4 % agarose and vibratome sectioned prior to wholemount staining with 1:25 2627 rabbit antisera (Hypoxyprobe, Inc) and 1:500 AF594 goat anti-rabbit secondary (Figure 3.4).

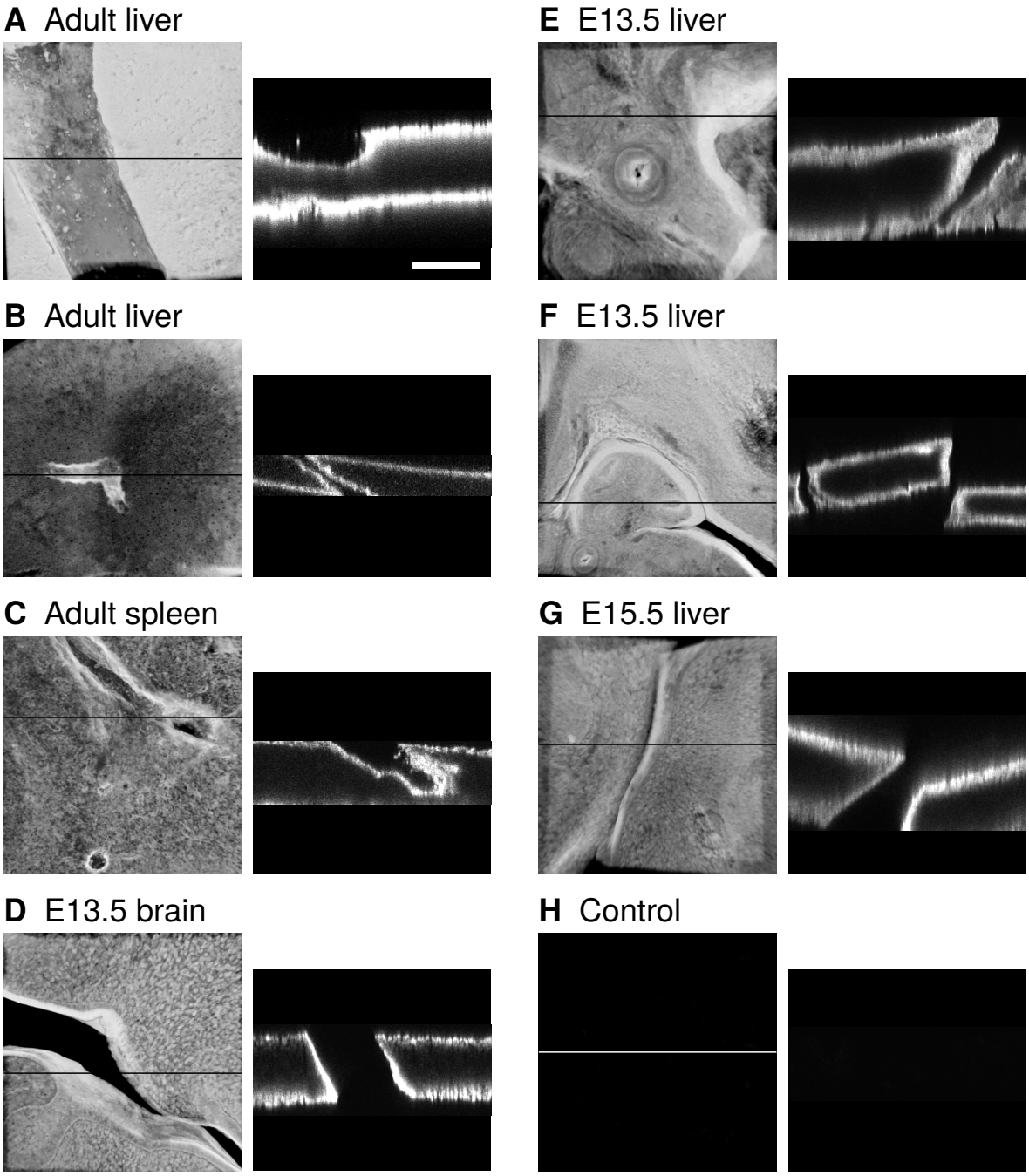

Figure 3.4: Detection of hypoxia with pimonidazole. Pregnant hCD2-GFP female mice were injected intraperitoneally with pimonidazole, and GFP positive embryos and adult liver and spleen were taken after 120 mins, then stained with 2627 rabbit antisera following PFA fixation and vibratome sectioning. For each sample, the 3-D rendering shown on the left contains a horizontal line indicating the position of the xz projection shown to the right. In all tissues and at all timepoints, staining was most intense at the sectioned surface of the tissue, and additionally at any other exposed surface such as vessel lumens and tissue boundaries (folds and edges). Secondary only controls showed no staining. Scale bar is 250 µm.

Localised hypoxia was not observed in any of the adult or embryo samples, the same staining pattern seen in all samples. All samples show intense staining along sectioned surfaces, with no staining in the sample interior. The exceptions to this are interior areas connected to the surface, such as resulting from tissue infolding, and where vessels running through the tissue reach the edge. The surface staining shown in Figure 3.4 was not due to the secondary antibody not being washed out, since the secondary-only control showed no staining, it appearing entirely black due to the intensity of the anti-pimonidazole staining being orders of magnitude more intense than intrinsic autofluorescence.

3.2.5 Gene expression in lymphoid organs by RTPCR

As an alternative to studying hypoxia using imaging of redox potentials, it should be possible to demonstrate hypoxia through the quantification of hypoxia-driven transcription products, *i.e.* through analysis of the expression of hypoxia-responsive genes. Genes were chosen whose expression is increased or decreased under hypoxia, having a direct functional activity such as enzymes, transporters, receptors and soluble factors rather than indirect effects, such as matrix components, Thbs1 being the exception. These included genes with specific effects upon metabolism and metabolite transport (Ldha and Slc2a1; Greijer, van der Groep *et al.* (2005); Iyer *et al.* (1998); Semenza, Jiang *et al.* (1996)), angiogenesis and erythropoiesis (Flt1, Kdr, Vegfa and Epo; Elvert, Kappel *et al.* (2003); Forsythe, Jiang *et al.* (1996); Gerber, Condorelli *et al.* (1997); Madan and Curtin (1993)), vascular function (eNos and iNos; Coulet, Nadaud *et al.* (2003); Palmer, Semenza *et al.* (1998)) and macrophage-specific chemotaxis and proliferation (Ccl2 and Cxcl12; (Bosco, Puppo *et al.*, 2004; Ceradini, Kulkarni *et al.*, 2004)). As positive controls the constitutively transcribed Hif1a and Arnt genes were used to demonstrate the presence of functional hypoxia response machinery in the tissues of interest in addition to Gapdh and Hprt as internal controls. Csf1 was additionally used as a pro-angiogenic hypoxia-independent marker with effects upon VEGF production in macrophages (Curry, Eubank *et al.*, 2008). Genes with anti-angiogenic effects (Thbs1, sFlt1, Pedf1 and Timp3; Dawson (1999); Good *et al.* (1990); Kappas *et al.* (2008); Saunders, Bohnsack *et al.* (2006)) were selected to allow comparison of the balance between pro- and anti-angiogenic mRNA levels.

Standard rules for real-time primer design were followed, as detailed in Section 2.8.4. In the case of genes with several splice variants, the primer was designed to amplify all variants. Total RNA from was obtained from an E14.5 hCD2-GFP whole embryo lysate in order to test the designed primers and determine their efficiency and specificity. The primers were tested using gradient PCR as described in Section 2.8.5. The results are shown in Figure 3.5. As a result of the initial test, the Epo, Vegfa and Pedf primers needed redesigning. Separate primer pairs were required to amplify the splice variants individually because the placement of the splice points in

the Vegfa transcripts precludes the use of a single primer pair for all splice variants, given the requirement for one of the real-time primers to cross an exon–exon boundary to prevent simultaneous amplification of genomic DNA, and length restrictions again due to the location of exon boundaries. The results for the modified primers are also shown in Figure 3.5.

Using cDNA derived from the thymus of hCD2-GFP at E17.5, as described in Sections 2.8.2 and 2.8.3, all primers (with the exception of Epo) were tested using conventional PCR as described in Section 2.8.5. The results are shown in Figure 3.6. While this is not quantitative, several observations may be made. Firstly, the pro-angiogenic growth factor VEGF-A is transcribed, and this includes a minimum of three of its splice variants, and potentially up to six given that the splice variants were detected in pairs. The VEGF receptors Kdr (VEGFR2) and Flt1 (VEGFR1) were additionally expressed. Interestingly, the soluble decoy receptor sFlt1 (sVEGFR1) was additionally present, as was the anti-angiogenic factor Pedf1 (PEDF). Molecules having a potential anti-angiogenic role, such as thrombospondin (Thbs1) and tissue inhibitor of metalloproteinase 3 (Timp3) were also present. GLUT1 (Slc2a1) and lactate dehydrogenase (Ldha) are involved with glucose transport and glycolytic metabolism, respectively, as well as being upregulated during hypoxia, and were both highly expressed. Ccl2, Csf1 and Cxcl12 are also upregulated during hypoxia and were seen to be expressed. However, Cxcl12 and Ccl2 are also found in normally functioning LN stroma, hence may not be truly be representative of hypoxia in the context of a lymphoid organ (Katakai *et al.*, 2004).

The above experiments demonstrated that the primers were specific, resulting in only a single product of a size suitable for quantitative real-time PCR. LN anlagen (axillary, brachial, cervical, inguinal), thymi, fœtal liver and skin from directly above the brachial node were dissected from embryos for all days from E14.5–E17.5. RNA was extracted as described in Section 2.8.2, and cDNA synthesised as described in 2.8.3. Due to the small size of the dissected anlagen, LN samples were pooled for each timepoint in order to provide a sufficient quantity cDNA for analysis. The small amount of material reduced the number of genes which could be studied, which were reduced to soluble pro-angiogenic factors (Vegfa splice variants), a soluble anti-angiogenic factor (Pedf1) and a matrix-bound anti-angiogenic factor (Thbs1) plus an endogenous control (Hprt).

The PCR reactions were run on ABI PRISM systems as described in Section 2.8.5, and analysis was performed as described in Section 2.8.6, using Hprt as the endogenous control and the E17.5 timepoint as the calibrator (Figure 3.7). The last developmental timepoint was used rather than the first due to E14.5 being a less reliable timepoint as a result of the diffuse nature of the anlagen causing extraneous material to be included at this timepoint. This analysis was entirely standard, computing NRQ_{samp} as described in Equation 2.3, but due to being normalised by timepoint,

only permits comparison of individual genes *between timepoints*. It does not, however, permit comparison *between genes* at a single timepoint. This is due to using *relative* rather than *absolute* quantification. However, this is possible with some caveats by rearranging Pfaffl's equation to compute NRQ_{gene} (Equation 2.6). Because this is comparing two unrelated genes without any knowledge of the absolute quantities, this means that the computed ratio is meaningless. However, the *change* in the ratio does have meaning, even if the absolute values are not known. The same dataset has therefore been normalised in this manner using an anti-angiogenic gene (PEDF) and a pro-angiogenic gene (VEGF splice variants 2+5), shown in Figure 3.8, to illustrate the changes in pro-angiogenic factors relative to an anti-angiogenic factor, and vice versa.

When describing the changes in expression for Figure 3.7, below, only changes greater than twofold were treated as significant. E16.5 had lower values for all genes in the LN, and higher values for the skin which will not be considered when describing general trends due to being inconsistent with the other timepoints. The LN samples show more variation than for other tissues, perhaps due to the presence of undefined amounts of extraneous material, as opposed to the liver and thymus which were discrete and self-contained tissues. The skin also contained some variation over time, possibly due to the use of a rotor-stator homogeniser rather than a pestle as for the other samples, due to the fibrous nature of the tissue, which may have resulted in inconsistent RNA extraction.

In the LN, PEDF expression remained constant during development, but dropped over tenfold in the adult. Thrombospondin, however declined throughout development but was over tenfold higher in the adult. All VEGF variants were similar from E14.5 to 17.5, with a possible drop in between. Vegfa1+4 was similar in the adult, while 2+5 is higher and 3+6 lower. In the thymus, PEDF declined during development, and was expressed at a similar level in the adult. Thrombospondin declined at a slower rate, but was expressed over tenfold higher in the adult. All VEGF variants show an uneven decline during development, with the same trends in the adult as observed for the LN. In the liver, PEDF expression increased approximately exponentially over time during development, and was higher still in the adult. Thrombospondin also increased linearly during development, but was dramatically lower in the adult. VEGF expression increased during development (E14.5 being an anomaly). However, in the adult Vefga1+4 was much higher, 2+5 similar and 3+6 much lower than their levels as E17.5. In the skin, PEDF expression declined during development, being expressed at an intermediate level in the adult. Thrombospondin was relatively steady, and if the large decline at E17.5 was real, was subsequently upregulated back to its initial level in the adult. VEGF variants followed the same inconsistent pattern, declining overall during development, with Vegfa1+4 and 2+5 being expressed at a higher level in the adult, and 3+6 at a lower level.

The Vegfa 1+4, 2+5 and 3+6 primers created products of 107, 121 and 124 base pairs, respectively. In very general terms, Figure 3.8 showed that Vegfa1+4 was expressed more than 2+5, which was expressed more than 3+6. That is, $VEGF_{188}$ > $VEGF_{164}$ > $VEGF_{120}$, assuming translation is equivalent to transcription and that the differences in product lengths do not significantly affect interpretation. In the LN thrombospondin, Vegfa1+4 and 2+5 increased in the adult relative to PEDF, while in relative terms Vegfa3+6 changed little. A similar pattern was seen in the thymus, though Vegfa1+4 changed little relative to PEDF. Thrombospondin changed little relative to PEDF in the liver during development, but dropped dramatically in the adult. Vegfa levels were relatively constant during development but dropped in the adult, presumably as a result of the increase in PEDF expression in the liver in the adult. In the skin, thrombospondin dropped relative to PEDF during development, but increased back to the level at E15.5 in the adult. Vegfa1+4 slowly rose during development and was higher in the adult relative to PEDF, but 2+5 and 3+6 dropped slightly during development, 2+5 being higher in the adult and 3+6 being lower.

When considering the changes relative to Vegfa2+5 instead (Figure 3.8), opposite trends are observed between pro- and anti-angiogenic factors when compared with normalisation using PEDF. However, this does highlight changes in the ratios of VEGF isoforms, relative to $VEGF_{164}$. Vegfa1+4 is always higher than 2+5, and 3+6 lower. In the adult Vegfa3+6 is generally much lower in the adult than at all developmental stages, it being generally unchanging relative to 2+5 during development.

3.2.6 Gene expression in the fœtal human lymph node

Microarray analysis of mouse LN anlagen was not possible due to their small size (insufficient material could be obtained). FRC and MRC stromal subsets were sorted from human fœtal lymph nodes, ages 16–24 weeks post-conception, of unknown sex. The stromal cells were characterised as $CD31^{-}CD45^{-}gp38^{+}$ and TRANCE was used to differentiate between $TRANCE^{-}$ FRCs and $TRANCE^{+}$ MRCs. While both express ICAM and VCAM, MRCs additionally express MAdCAM. Following sorting, RNA was extracted using an RNA-XS kit (Machery Nagel, Düren, Germany). RNA concentration and quality were determined using a Bioanalyzer (Agilent, Wokingham, UK). cDNA was synthesised from the RNA using reverse transcription with random hexamer primers, with equal amounts of RNA for each sample, using the Ovation Pico WTA system (Nugen, Bemmel, The Netherlands). For both samples, 5 ng cDNA was hybridised to Affymetrix GeneChip Human Genome U133 Plus 2.0 arrays (Affymetrix, High Wycombe, UK), and normalised using R Bioconductor/MAS. Note that this work was done by the Cupedo lab at Erasmus University, who performed all the above steps from cell sorting to the microarrays, and who kindly shared the resulting normalised Affymetrix data.

Expression values less than 35 were set to 0 (MRC) or 1 (FRC) to eliminate insig-

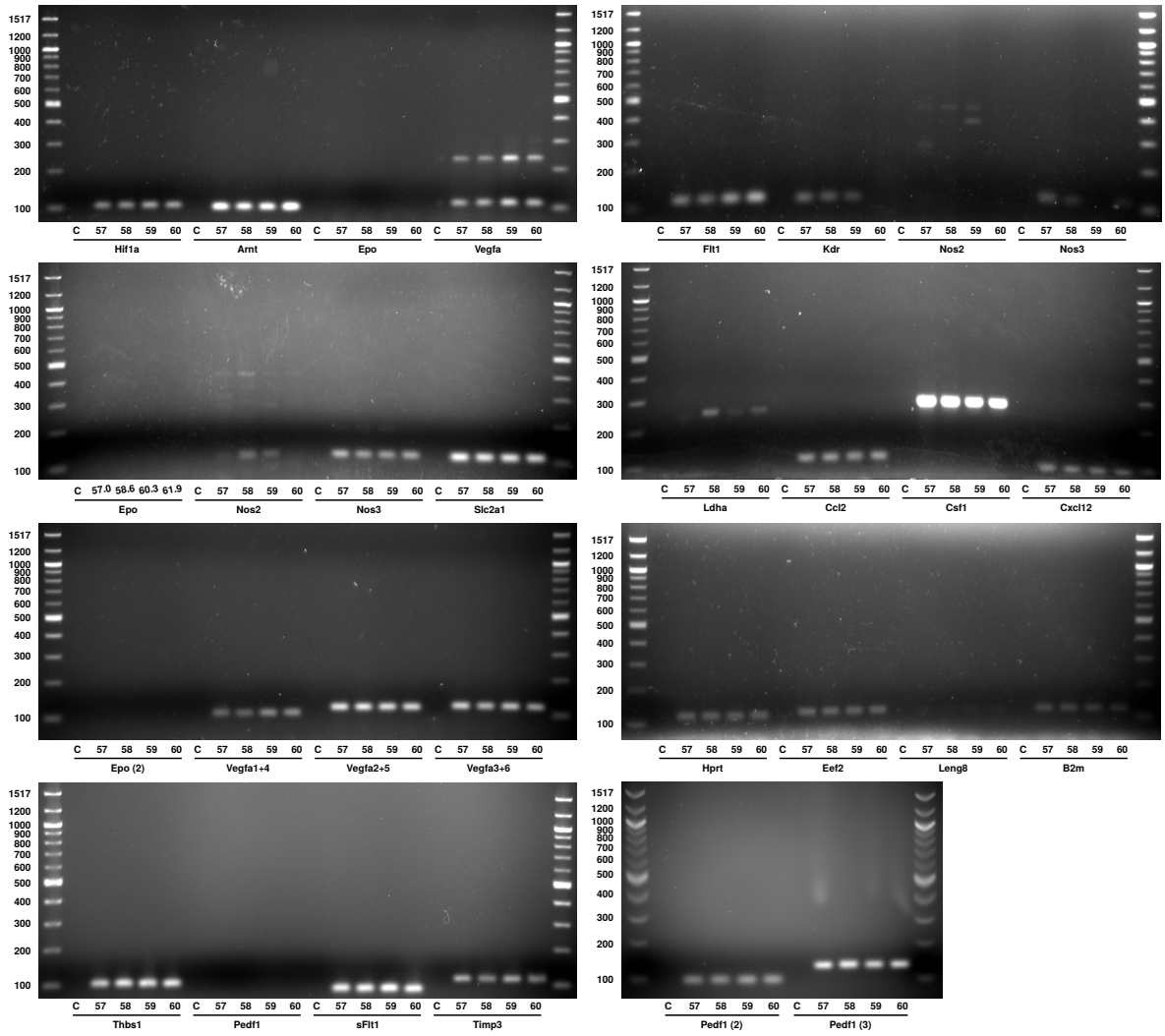

Figure 3.5: Gradient PCR testing of primers. All primers amplified a single product at all temperatures with the following exceptions: Epo and Pedf1 (no product at any temperature), Vegfa (two products), Nos2 (multiple products), Nos3 (varied with temperature, but worked during a subsequent test) and Ldha (no product at 57 °C). Epo and Pedf primers were subsequently redesigned, all of which worked except Epo. Vegfa primers were redesigned to amplify specific pairs of splice variants. The Leng8 product is present but only at very low quantity. *C* denotes a control without template cDNA annealed at 57.5 °C; numbers are annealing temperatures.

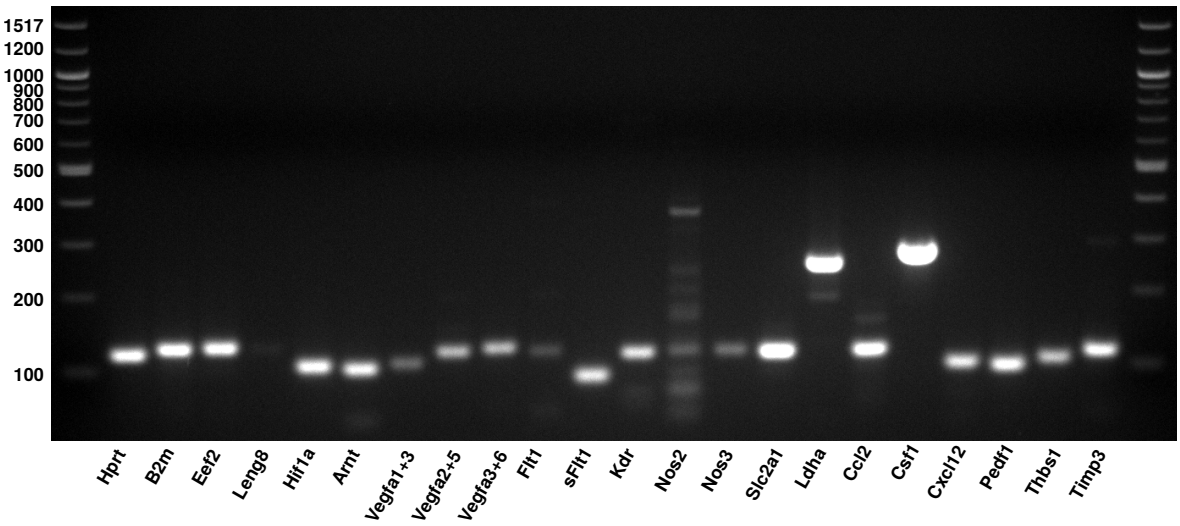

Figure 3.6: Gene expression in E17.5 thymus. With the exception of Nos2, which amplified multiple products, all genes were found to be expressed. These include genes for housekeeping (Hprt, B2m, Eef2, Leng8), hypoxia-driven transcription (Hif1a, Arnt), angiogenesis, including pro-angiogenic factors and receptors (Vegfa splice variants, Flt1, Kdr) and anti-angiogenic factors (sFlt1, Pedf1, Thbs1, Timp3), vascular function (Nos3) and hypoxia response (Slc2a1, Ldha, Ccl2, Csf1, Cxcl12).

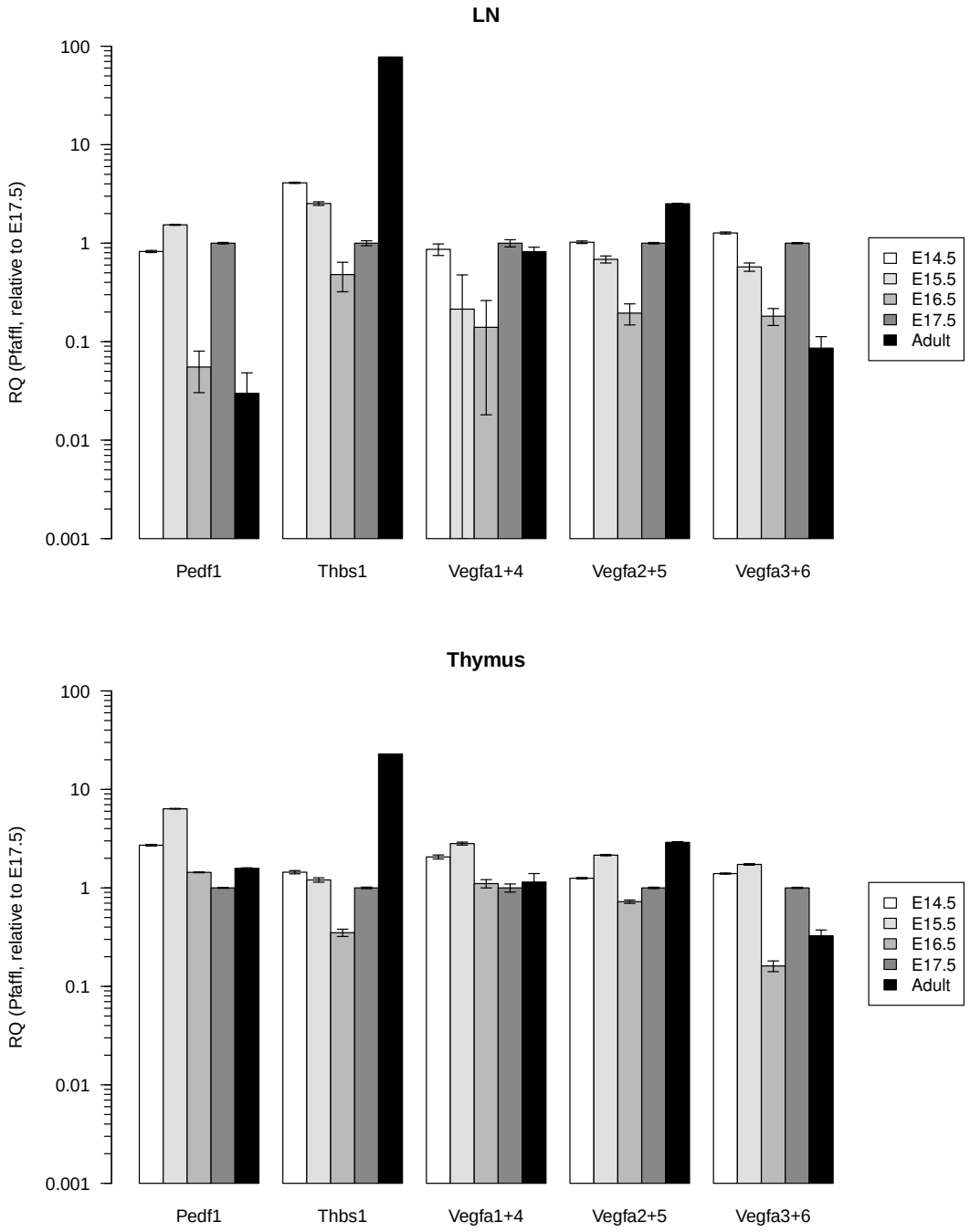

Figure 3.7: Gene expression between timepoints E14.5–E17.5 during development, and the adult. The mRNA levels of the transcripts of Vegfa (three sets of splice variants), Pedf1, Thbs1 and Hprt were analysed using cDNA from the LN (pooled), thymus (pooled), liver and skin at each timepoint. mRNA levels were normalised to the endogenous control Hprt, and E17.5 was used as the calibrator sample. Error bars are ± the standard error of the mean.

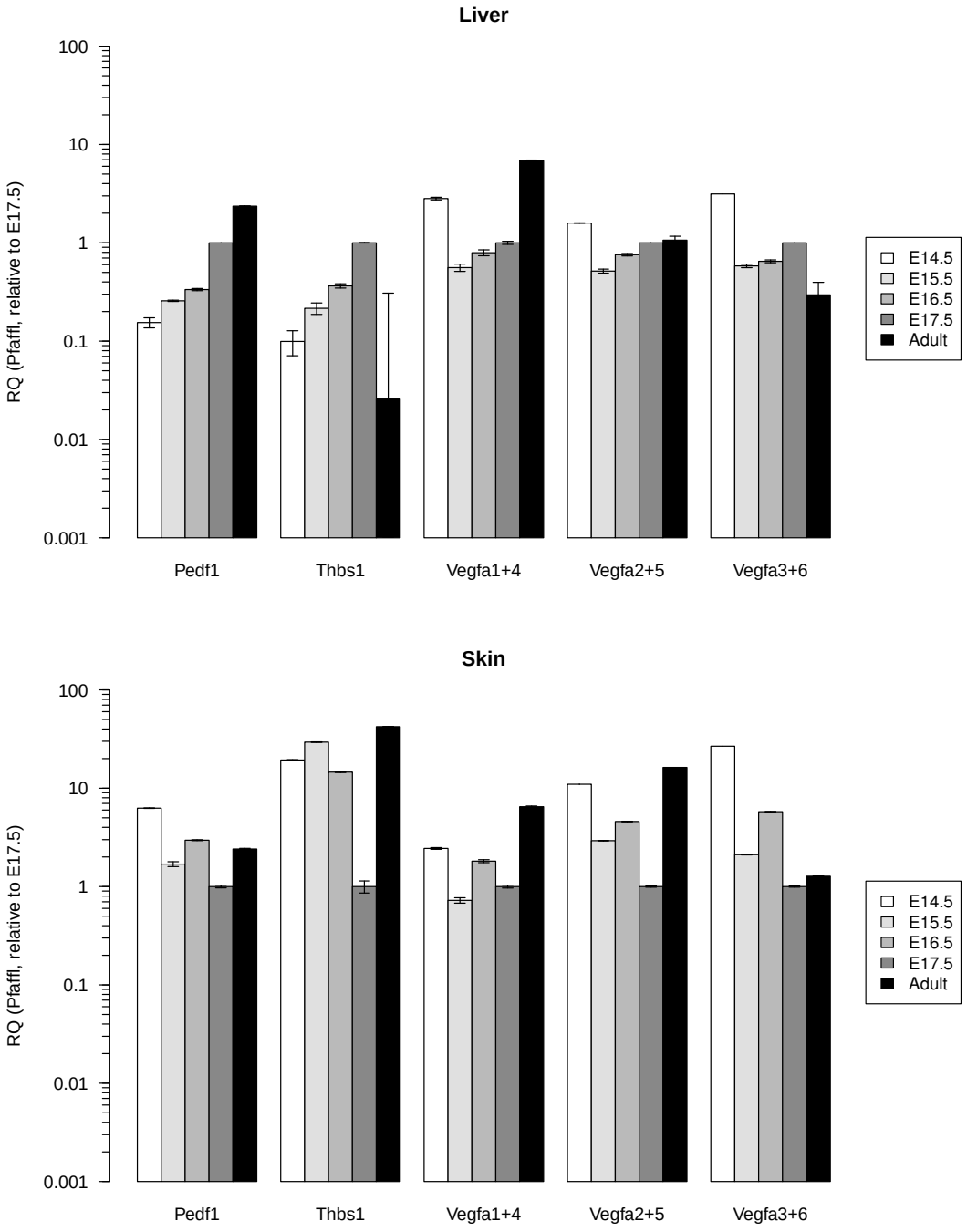

Figure 3.7: Gene expression between timepoints E14.5–E17.5 during development, and the adult (contd). The mRNA levels of the transcripts of Vegfa (three sets of splice variants), Pedf1, Thbs1 and Hprt were analysed using cDNA from the LN (pooled), thymus (pooled), liver and skin at each timepoint. mRNA levels were normalised to the endogenous control Hprt, and E17.5 was used as the calibrator sample. Error bars are ± the standard error of the mean.

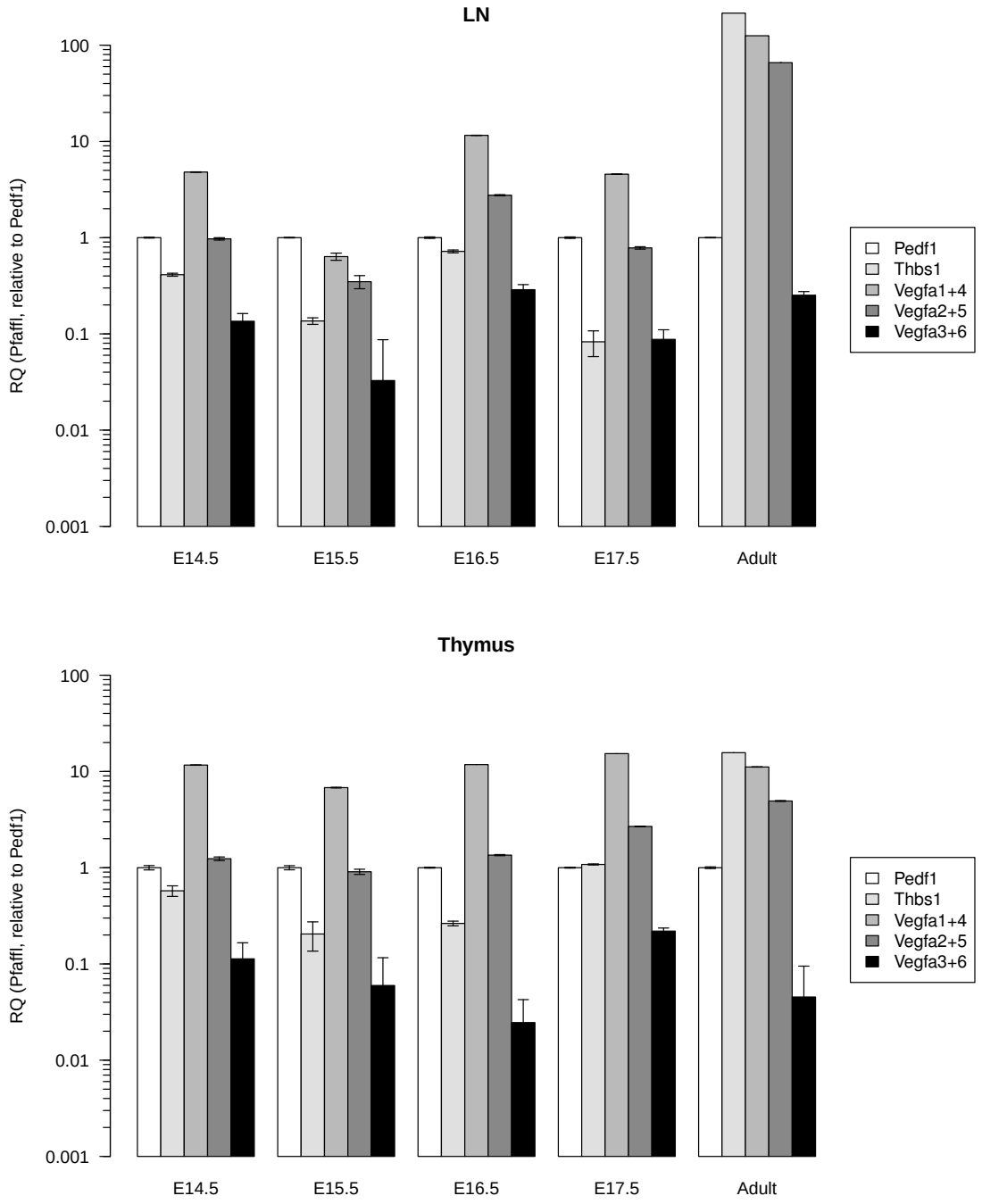

Figure 3.8: Gene expression between the genes Pedf1, Thbs1 and Vegfa splice variants during development. The mRNA levels of the transcripts of Vegfa (three sets of splice variants), Pedf1, Thbs1 and Hprt were analysed using cDNA from the LN (pooled), thymus (pooled), liver and skin at each timepoint. mRNA levels were normalised to the reference gene Hprt, and Pedf1 was used as the calibrator sample. Error bars are ± the standard error of the mean.

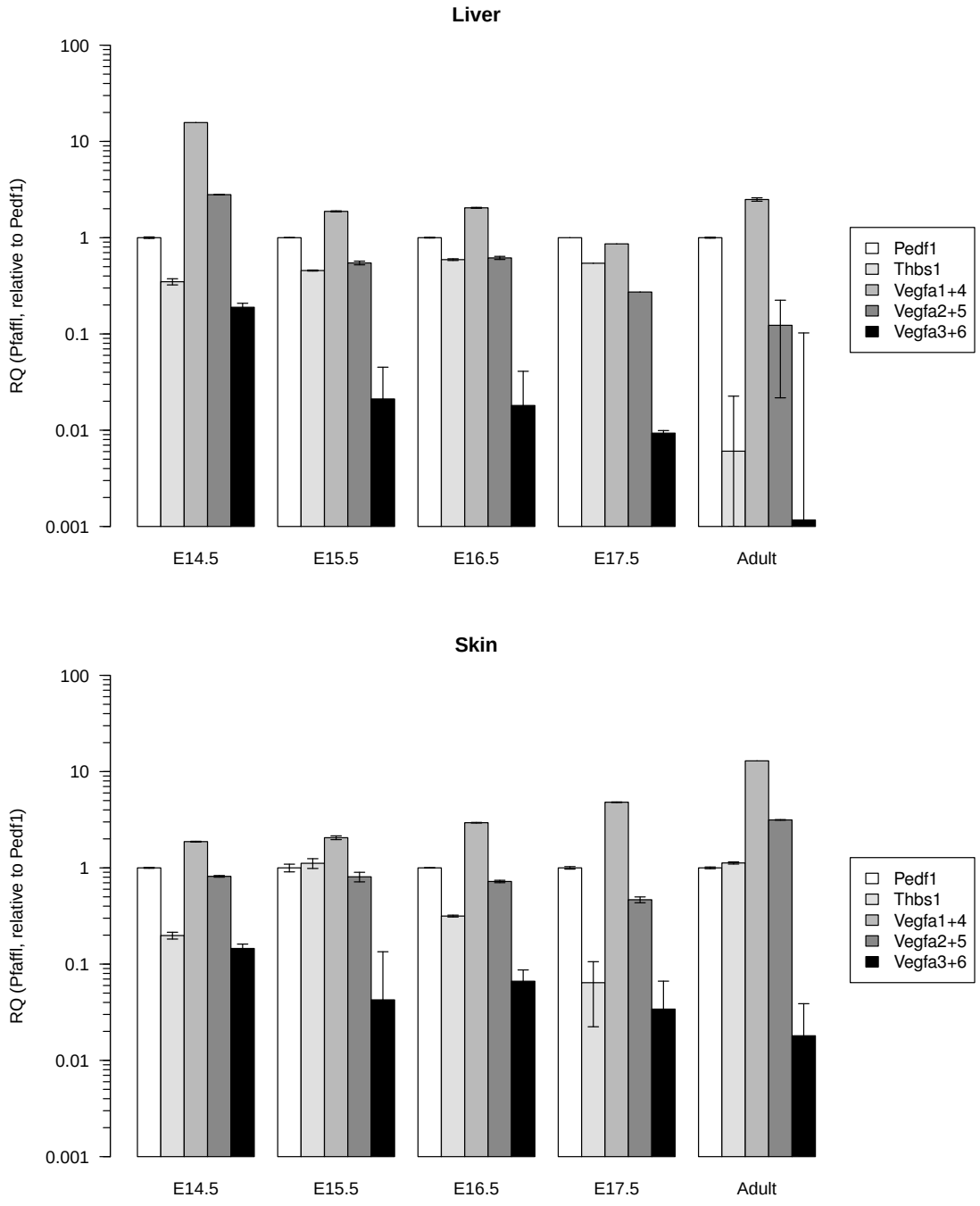

Figure 3.8: Gene expression between the genes Pedf1, Thbs1 and Vegfa splice variants during development (contd). The mRNA levels of the transcripts of Vegfa (three sets of splice variants), Pedf1, Thbs1 and Hprt were analysed using cDNA from the LN (pooled), thymus (pooled), liver and skin at each timepoint. mRNA levels were normalised to the reference gene Hprt, and Pedf1 was used as the calibrator sample. Error bars are ± the standard error of the mean.

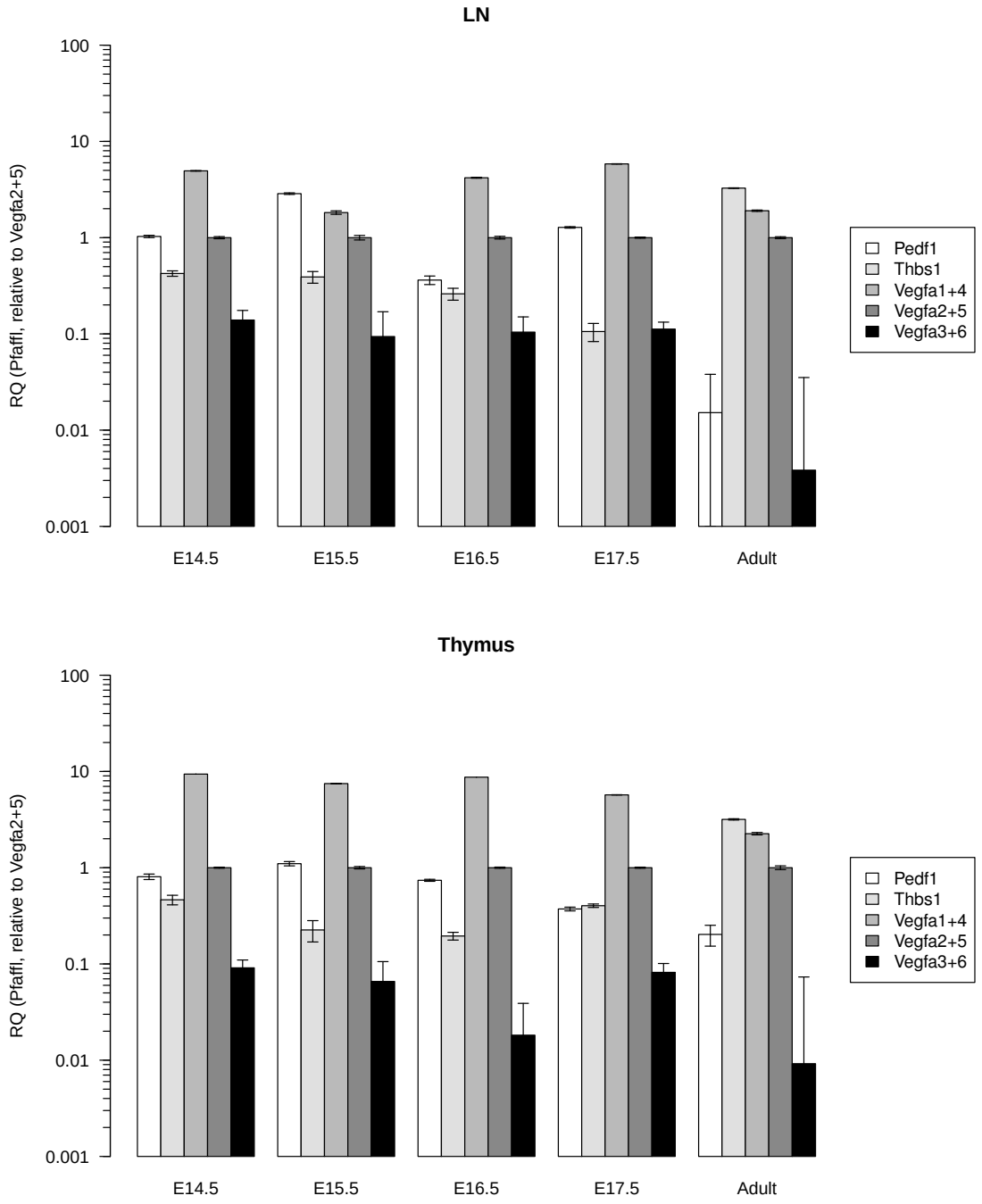

Figure 3.8: Gene expression between the genes Pedf1, Thbs1 and Vegfa splice variants during development (contd). The mRNA levels of the transcripts of Vegfa (three sets of splice variants), Pedf1, Thbs1 and Hprt were analysed using cDNA from the LN (pooled), thymus (pooled), liver and skin at each timepoint. mRNA levels were normalised to the reference gene Hprt, and Vegfa2+5 was used as the calibrator sample. Error bars are ± the standard error of the mean.

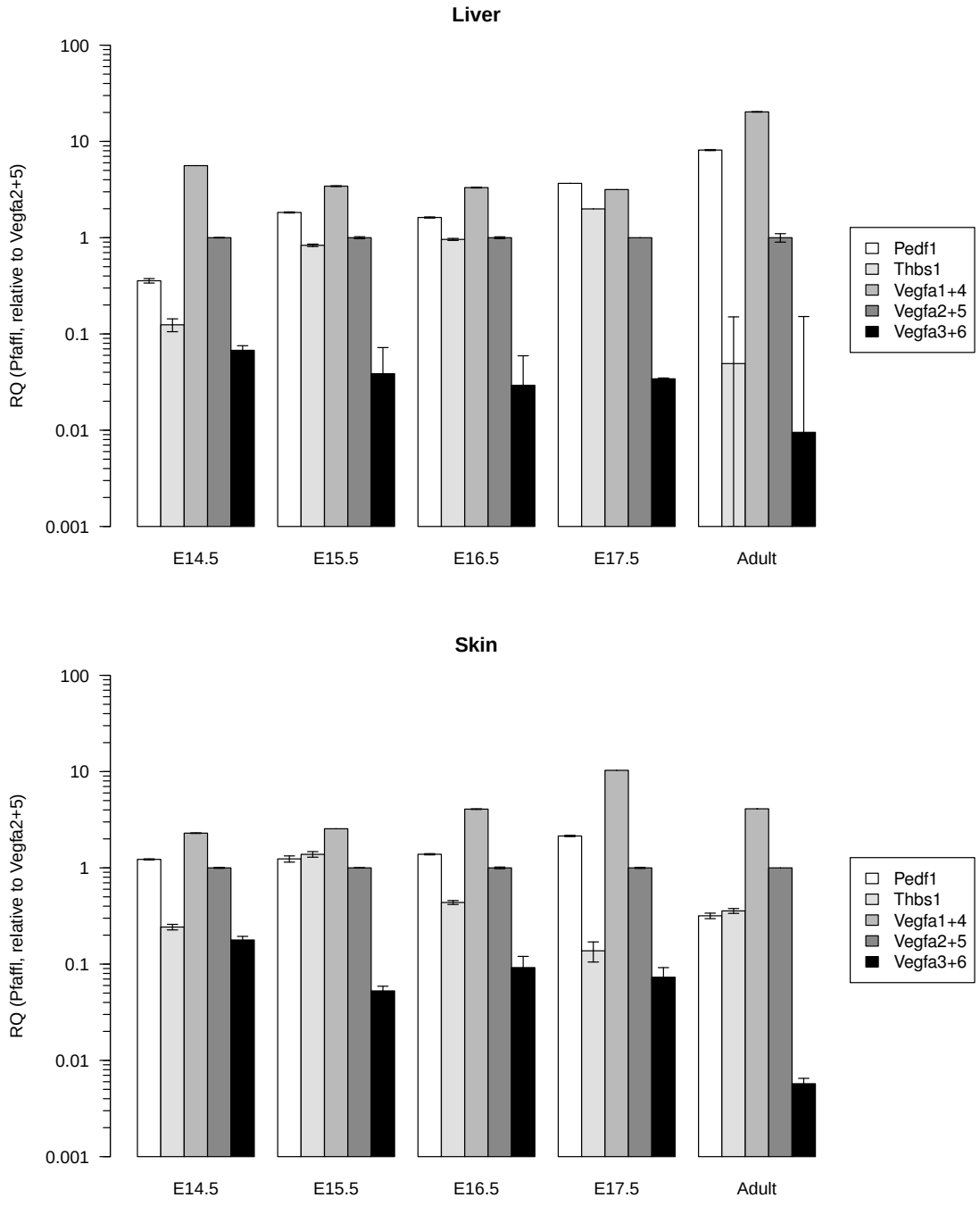

Figure 3.8: Gene expression between the genes Pedf1, Thbs1 and Vegfa splice variants during development (contd). The mRNA levels of the transcripts of Vegfa (three sets of splice variants), Pedf1, Thbs1 and Hprt were analysed using cDNA from the LN (pooled), thymus (pooled), liver and skin at each timepoint. mRNA levels were normalised to the reference gene Hprt, and Vegfa2+5 was used as the calibrator sample. Error bars are ± the standard error of the mean.

nificant probes and to avoid divide by zero errors when computing the MRC/FRC ratio. However, this does introduce some bias into the ratio when this only affects a single probe. The normalised data was analysed to look at the differences in absolute and relative terms between the two sets, and also to permit comparison with the RTPCR data from embryonic and adult mouse lymphoid anlagen and organs.

Genes were selected from the total probeset in three major categories: genes involved in hypoxia, LN development and angiogenesis. The hypoxia-related genes were identical to those selected in Section 3.2.5, with the addition of Angpt1 and 2, of which Angpt2 is hypoxia-inducible (Oh, Takagi *et al.*, 1999; Yamakawa, Liu *et al.*, 2003), Epas1, a HIF-like hypoxia-sensitive transcription factor found in ECs (Tian, McKnight *et al.*, 1997) and Ldhb, which unlike Lhda is not HIF-regulated (Kay, Zhu *et al.*, 2007). The LN development-related genes were chosen based upon those described as being key molecules upregulated during LN organogenesis as a consequence of LTi–LTo interactions in Section 1.3.3 and were reviewed by van de Pavert and Mebius (2010). The angiogenesis-related genes include those described in Section 1.2.4 plus Pdgfc (in lieu of a positive signal being observed for Pdgfb) and Timp3 (Gilbertson, Duff *et al.*, 2001; Saunders *et al.*, 2006; Wan, Chai *et al.*, 2011). Differences in absolute and relative expression levels for genes in each of these categories are shown in Figure 3.9. When describing the differences, below, only changes greater than twofold were considered to be significantly different, and for genes where one probe was significantly different from the other replicate probes, this probe was discounted. Note that some key genes are missing entirely; in most cases this was due to there being no probe on the microarray, or in some cases having no detectable level of expression for both MRCs and FRCs, *e.g.* Kdr. However, the probes present with detectable signal were sufficient to gain a general overview of possible active signalling pathways and cellular interactions within the LN.

Hypoxia-related genes Hypoxia inducible factor-1 α and β (Hif1a and Arnt) were both expressed at similar levels in MRCs and FRCs , but the level of expressed protein is not possible to determine based upon the mRNA level. The genes Ccl2, Csf1, Epas1, Flt1, Ldha and Ldhb were also expressed at similar levels in both samples. Angiopoietin 1 was around twice as high in FRCs, and angiopoietin 2 around ten times as high. Cxcl12 was around tenfold higher in MRCs. FRCs had about three times more expression of the glucose transporter GLUT1 (Slc2a1), but slightly lower levels of lactate dehydrogenase (Lhda and Ldhb).

LN development-related genes Both cell types expressed Ccl19, Ccl21, and Cxcl13 and TRANCE (Tnfsf11). However, all were upregulated in MRCs, particularly Cxcl13 and TRANCE. TRANCER (Tnfrsf11a) was present on the chip, but expression was not detected; its paralogue Tnfrsf11b is shown here, and was only seen in MRCs; this is thought to be a soluble decoy receptor. IL-7 and LTβR were only expressed by

MRCs, with LTβ being expressed by both, but upregulated in FRCs. The adhesion molecules ICAM and VCAM were expressed by both, but upregulated in MRCs, while MAdCAM was only expressed by MRCs.

Angiogenesis-related genes The genes VEGFR1, PDGF-C, placental growth factor (PlGF), thrombospondin, and VEGF-B were present in both MRCs and FRCs at similar levels. PEDF (Serpinf1), VEGF-A and VEGF-C were present in both, but were all upregulated in the MRCs, VEGF-C in particular. The absolute level of VEGF-A was much higher than VEGF-B or VEGF-C. Tissue inhibitor of metalloproteinases 3 (TIMP3) was expressed much more in FRCs than MRCs.

3.3 Discussion

3.3.1 Wholemount microscopy

Wholemount microscopy permitted detailed visualisation of the vascular networks within the developing thymus, both by the staining of the vascular endothelium with endomucin, and the basement membrane with collagen IV, laminin and fibronectin (Figure 3.1). This demonstrated that while staining and imaging of the LN anlagen did not yield usable results, this was not due to deficiencies in the wholemount staining protocol. In practice, it was not possible to identify LN anlagen in embryo sections stained using wholemount protocols, not because the GFP staining was deficient, but because the overnight PFA fixation resulted in such intense background autofluorescence that it was not possible to distinguish between GFP fluorescence and autofluorescence. The failure of all the CD31 and CD144 antibodies to stain any specific structures may have been a result of their inability to penetrate the vibratome-sectioned tissue, or perhaps a consequence of fixation and/or the epitopes being mainly restricted to cell–cell junctions (Halama *et al.*, 2001; Sandoval, Malik *et al.*, 2001) where the junctional complexes are inaccessible to the antibodies.

Foster, Sheridan *et al.* (2008) noted that endomucin only stained endothelial cells from E15.5 in the thymus as a result of endomucin only being expressed by mature endothelial cells. It is therefore possible that endomucin would not stain endothelium in the LN anlagen at E15.5, the LNs developing later than the thymus, and being less well formed at this stage, the thymus being partly developed at E13.5, at which point LN development has only just begun (van de Pavert and Mebius, 2010).

Changes were made to the wholemount protocol in order to improve staining, including extending the staining and wash steps from overnight to several days, but did not appear to result in more specific or brighter staining compared with the high autofluorescence.

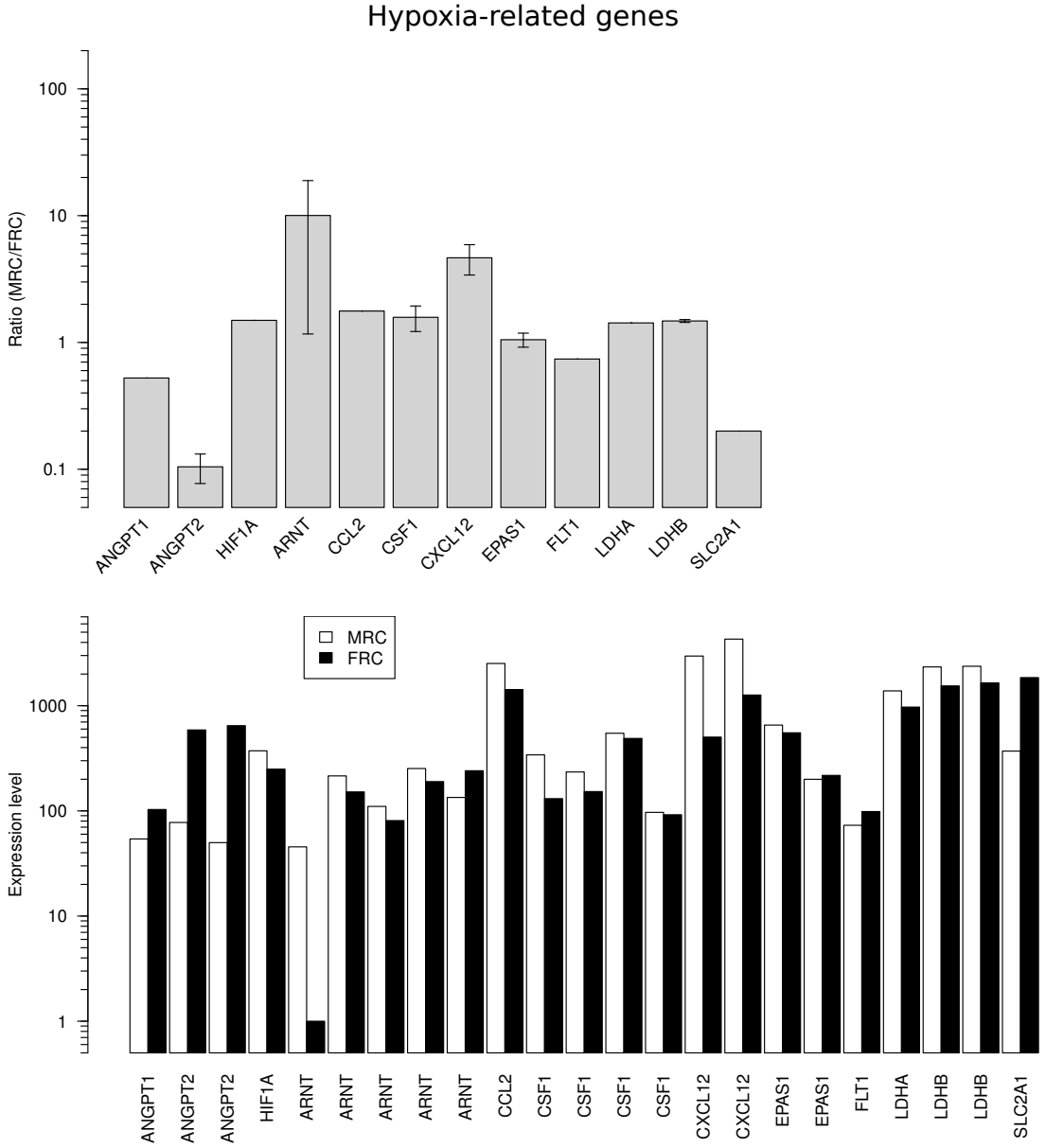

Figure 3.9: Microarray analysis of human LN mRNA levels. The FRC and MRC stromal subsets were sorted from human fœtal lymph nodes, ages 16–24 weeks post-conception, of unknown sex, and analysed using human Affymetrix gene chips. The ratio of the levels between the FRC and MRC subsets (top) was calculated from the mean of the levels for each probe on both chips (bottom). Error bars are ± the standard error of the mean, shown for genes where more than one probe is present on the array and where each probe had a signal above the threshold for one or both of the samples.

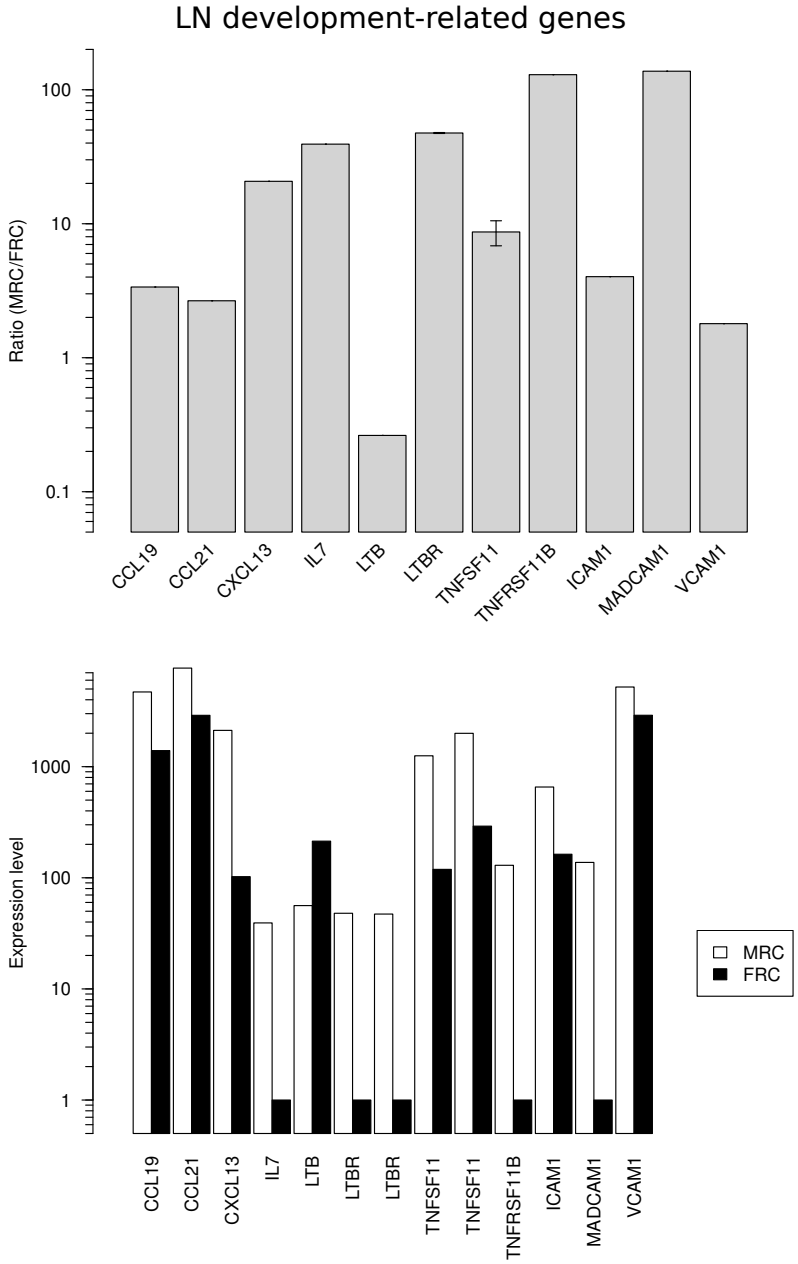

Figure 3.9: Microarray analysis of human LN mRNA levels (contd). The FRC and MRC stromal subsets were sorted from human fœtal lymph nodes, ages 16–24 weeks post-conception, of unknown sex, and analysed using human Affymetrix gene chips. The ratio of the levels between the FRC and MRC subsets (top) was calculated from the mean of the levels for each probe on both chips (bottom). Error bars are ± the standard error of the mean, shown for genes where more than one probe is present on the array and where each probe had a signal above the threshold for one or both of the samples.

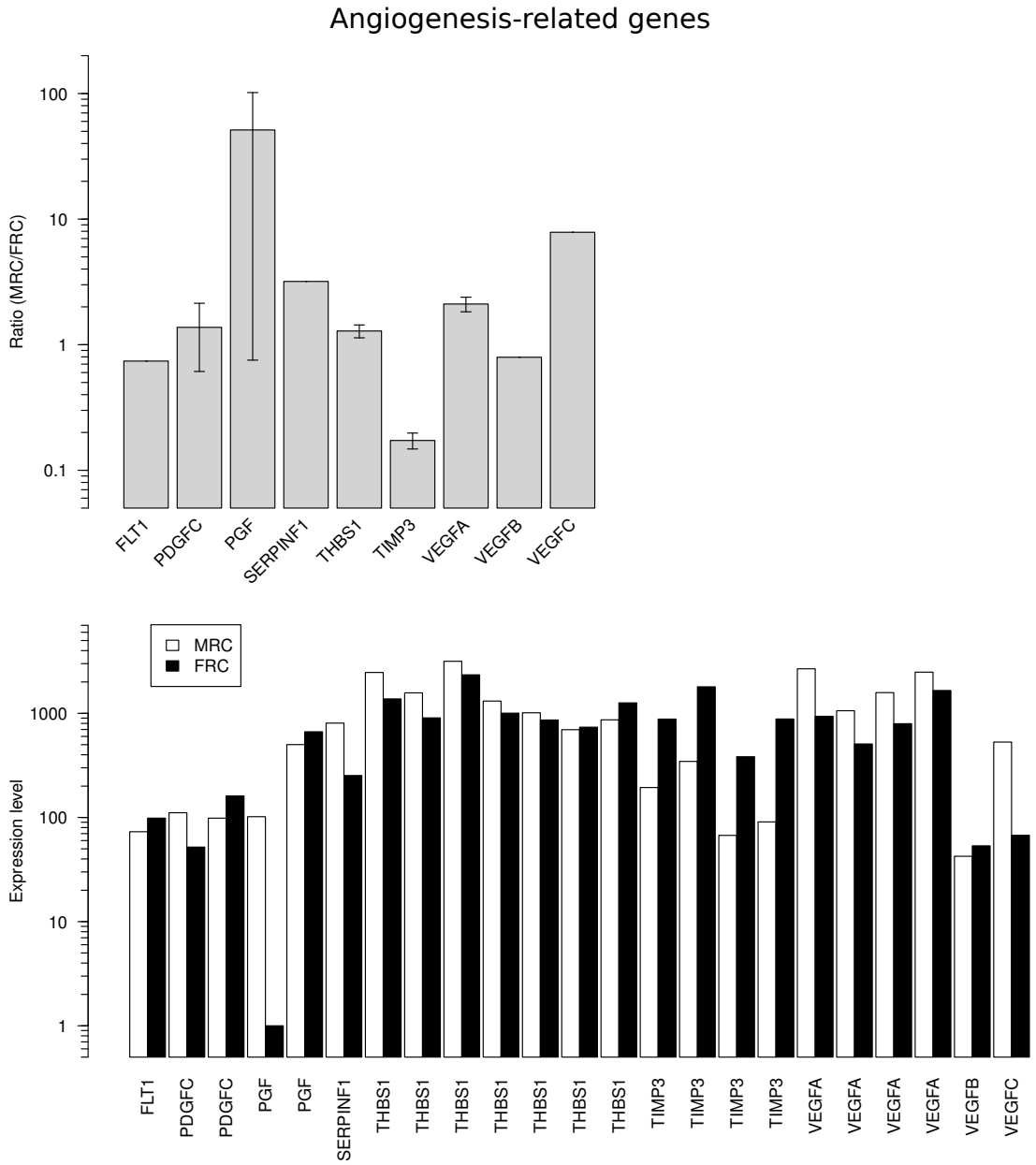

Figure 3.9: Microarray analysis of human LN mRNA levels (contd). The FRC and MRC stromal subsets were sorted from human fœtal lymph nodes, ages 16–24 weeks post-conception, of unknown sex, and analysed using human Affymetrix gene chips. The ratio of the levels between the FRC and MRC subsets (top) was calculated from the mean of the levels for each probe on both chips (bottom). Error bars are ± the standard error of the mean, shown for genes where more than one probe is present on the array and where each probe had a signal above the threshold for one or both of the samples.

In the E15.5 thymus, fibronectin was observed to be laid down throughout the whole vascular network, unlike collagen IV, which was restricted to the outer cortex. Laminin was also seen to have a similar distribution to fibronectin. This pattern may reflect two different processes occuring during vascularisation of the thymus. Firstly, basement membrane components are laid down in a specific order, starting with fibronectin, collagen I/III fibres requiring the pre-existence of a fibronectin matrix (Velling, Risteli *et al.*, 2002), which may also apply to collagen IV polymerisation. The process may also be recapitulated during wound repair and revascularisation, where fibronectin is laid down first as a component of the provisional matrix in granulation tissue, which is subsequently supplemented by collagen and laminin (Schultz and Wysocki, 2009). This process is also observed in the development of the vascular basement membrane (Sephel *et al.*, 1996). The second process is that of smooth muscle coverage as the vasculature matures and recruits VSMCs, which results in an increase in matrix biosynthesis (Stratman *et al.*, 2009a). In this paper, it was shown that several matrix components, including collagen IV and nidogen, were not produced unless ECs were cocultured with pericytes, while fibronectin, laminin and perlecan production was upregulated in the presence of pericytes. It was additionally demonstrated that collagen IV, unlike laminin, did not assemble into a network unless fibronectin was already present, as noted for collagen I, above. Together, these observations imply that the collagen IV staining observed in the thymus is a result of the ECs in the cortex having VSMC coverage, while the medullary ECs and inner cortical ECs do not, laying down fibronectin and laminin only, and from this it is logical to deduce that VSMCs migrate inward along the vascular network from the edge, assuming that they are not derived directly from the local mesenchyme.

While this process may be unique to the thymus, the process of vascularisation and ordered basement membrane production may be common to other organs, perhaps also including the lymph node. The thymus does contain a somewhat unique vasculature, capillaries being double-walled and having two basal laminæ (Kato, 1997), and may hence develop in a different manner to other systems. However, pericyte coverage is common to all capillaries, and as discussed in a recent pericyte review by Armulik *et al.* (2011), it is becoming clear that while pericytes do not have a common lineage, they originate from defined points such as the neural crest and mesothelium in the embryo and spread along the vasculature, hence it is probable that all of the pericytes within a single lymph node would all have a common origin, though the dynamics of migration and cell division during this process still require investigation.

Further work would be required to correlate collagen IV distribution with VSMC coverage, for example by additionally staining with a pericyte marker such as α-SMA, NG2, PDGFRβ or desmin (Armulik *et al.*, 2011).

3.3.2 Development of LNs

Due to the problems imaging LN anlagen in wholemount preparations, direct visualisation using SHG and immunohistochemistry were used as an alternative (Figures 3.2 and 3.3). It is unclear if ECs are present in the centre of the anlagen as a result of the endomucin staining showing no staining within the cluster of LTis (Mebius *et al.*, 1997); however, some endomucin staining was visible above and below the cluster, perhaps within a few ECs comprising the surrounding lymph sac. Rather than no ECs being present, this may be a lack of endomucin staining at this point in LN development (Foster *et al.*, 2008). MECA-32 staining did highlight a band of cells running alongside an LTi cluster (from the shape, this is likely to be a streak from the cervical node), but no staining was seen within the cluster. As observed in previous work, LTis and LTos were seen interacting at low frequency, LTos being identified by their VCAM expression and most being in direct contact with adjacent LTis, and as yet unactivated stroma being visible by DAPI staining (Vondenhoff *et al.*, 2009a).

The most interesting observations concern the placement of vascular basement membrane relative to the LTi clusters. While the anlagen in Figure 3.2 appear rather different, this may be an artefact of the limited optical sectioning possible due to the tissue thickness—features may depend on the location in the tissue, so different nodes may be more similar than apparent. Live SHG imaging showed tight clusters of LTis, in some cases bordered on three sides by a collagen I band, indicating that the LTis were clustering in a morphologically distinct "pocket", which was open at one end. This bears great similarity to the collagen I staining in Figure 3.3(D), which again showed a cluster of LTis surrounded by collagen I, which was open at one end. In both cases, a partial second layer of collagen I staining was observed. In the frozen section, LTis were also seen outside the pocket, towards the bottom of the figure. This might be an extension of the anlagen, which might not fit into the whole field of view, or it may indicate that the LTis were migrating into the pocket through this route. The LTis must arise from the circulation due to their hæmatopoietic origin (Mebius *et al.*, 1997), but whether they arise from the vessels surrounding the anlagen, or migrate after extravasation from distant major vessels is not known. Laminin staining of the skin, showing scattered LTis restricted in their movement by the basal lamina gives the impression of wandering cells; scattered LTis were also observed in or under the skin of hCD2-GFP embryos during dissection, implying that their distribution is not specifically restricted to the anlagen, but they are physically bounded by the basal lamina (Gao, DeRouen *et al.*, 2008).

Collagen IV staining correlated closely with the distribution of collagen I, implying that they demarcate the same structures. As for collagen I, LTi clusters are surrounded by a double layer of anastomosing vessels, the nature of which is clearly seen in serial sections showing vessels bridging the gap between the layers. Though a double-layered sac is predicted in the model described by Mebius (2003), in this

model this is a precursor to the subcapsular sinus, and does not contain any vessels spanning the gap. In contrast, in these images non-EC cells stained with DAPI are clearly seen filling the gap, though some empty spaces are present. In the data presented by Bénézech *et al.* (2010), a double layer of collagen I is seen in the E15.5 inguinal LN, but the inner mass is additionally heavily stained with collagen at both this timepoint and E17.5, whereas the inner LTi cluster is completely absent of collagen I staining in Figure 3.3, leading one to conclude that there is little similarity. Vondenhoff *et al.* (2009a) did not specifically examine basement membrane expression in the brachial node, but did stain with LYVE1 and VEGFR2 which should have stained the same cells; indeed, at E14.5 [Figure 1(F)] a three sided pocket of LECs is seen, and on the right-hand side a potential second cell layer is visible at the edge of the field of view, though this is less clear at E16.5.

Part of the discrepancy with the data of Bénézech *et al.* (2010) may lie in their use of Gp38 and CCL21 to identify lymphatic endothelium, neither of which are specific to LECs (Katakai *et al.*, 2004, 2008; Roozendaal and Mebius, 2011). However, the assumption that such cells are LECs may not be incorrect, especially given that they are PDGFRα^-.

While lymph sac structure appears to bear similarities with the work of Vondenhoff *et al.* (2009a), the data is different with respect to the vascularisation of the anlagen. In Figure 3.3(A–C), very little collagen IV is seen on cells within the anlagen, and certainly not in any pattern resembling a vessel as seen for the lymph sac, whereas Vondenhoff *et al.* (2009a) observed the presence of MECA32$^+$VEGFR2$^+$ and VEGFR2$^+$ vessels at E14.5, and additionally VEGFR1$^+$VEGFR2$^+$ vessels at E16.5. It is a possibility that the ECs express collagen I and IV after their initial migration (as discussed above and in Stratman *et al.* (2009a)), which would have resulted in only older, established vessels being stained.

The double-layered structure appears to be at least partially LYVE1$^+$, perhaps indicating that the lymph sac is not entirely committed to an LEC lineage at this point (Cupedo, Vondenhoff *et al.*, 2004). While being less clearly defined than collagen I and IV, it appears to be approximately similar, also having a partially double-layered structure. Structurally and functionally, it is unclear what the double-layered structure is, and what it will develop into from these images alone. There are two hypotheses worth considering. The first hypothesis is that due to the second layer being only a sparsely-distributed collection of cells, it may be a remnant of the cells migrating from the nearby vessel, the source of the cells comprising the lymph sac (Harvey and Oliver, 2004; Oliver, 2004). These might subsequently regress and disappear. The second hypothesis is that this double layer is a precursor to the subcapsular sinus. At least in the rat, the subcapsular sinus contains tissue pillars extending across the sinus, and appearing to have continuity with the cortical reticular network (Ohtani and Ohtani, 2008), which leads one to question how such a complex

structure might develop given that it would not be likely that cells could bridge the gap once lymphatic flow has commenced. It may be the case that the stromal cells interspersed amongst the anastomosing vessels will subsequently play a role in the formation of such structures. Like the inner and outer surfaces of the sinus, which are composed of lymphatic endothelium (Liersch and Detmar, 2007; Sixt *et al.*, 2005), the pillars themselves may be lined with an outer endothelial layer, perhaps with an inner VSMC or stromal layer continuous with the FRC network; the collagen IV-stained "bridge" structures between the two layers may be the forerunner of such structures, and may play both a structural role in keeping the sinus open, and potentially a functional role in the loading of the conduit system with low molecular weight soluble factors (Sixt *et al.*, 2005).

It has recently been shown that mice lacking lymphatics still have LNs (Vondenhoff *et al.*, 2009b). Conditional Prox1 mutant embryos defective in lymph sac formation were still shown to exhibit LTi clustering, but had impaired vascular development, in particular in the surrounding lymph sac and in the absence of major vessels inside (compared with Vondenhoff *et al.* (2009a)), with the loss of $Gp38^+$ and/or $VEGFR2^+$ vessels. This may imply that the vessels inside the sac originated from the sac, and that loss of Prox1 prevented sac formation and consequently their formation. However, their loss might also be a direct or indirect consequence of the altered phenotype.

3.3.3 Hypoxia

Pimonidazole imaging of hypoxia (Figure 3.4), if valid, showed that the embryos were so hypoxic that it appeared that the antibody used to stain bound probe appeared to be limiting. If the primary had not washed out properly, staining would also be seen in the interior. In consequence, the staining is likely entirely artefactual, due to unbound probe not being washed out, forming adducts prior to fixation, thereby showing all the tissues to be entirely hypoxic. Alternatively, the entire embryo may be hypoxic. In this situation, the antisera is likely to be limiting and will hence only penetrate a small distance into the tissue before it is almost all completely bound, which would result in the staining pattern observed, where staining is seen on all exposed external and internal surfaces including those exposed by sectioning, those of tissue boundaries, and vessels and ducts penetrating the tissue.

Specific staining of embryos has been achieved by others in the mouse (Lee, Jeong *et al.*, 2001) and also the quail (Nanka, Valásek *et al.*, 2006). The main experimental difference is that Lee *et al.* (2001) injected the probe intravenously rather than intraperitoneally; the same length of time was left between injection and collection of the embryos, which should be sufficient time for unbound probe to be excreted. The embryos were kept on ice for several hours during transport and while sorting the GFP^+ embryos, therefore it may be possible that an increase in hypoxia in the tissues

of the embryos during this period may have caused any unbound probe remaining to irreversibly bind. Given that pimonidazole has been shown to mark hypoxic areas specifically in both adult and embryonic tissues (Lee *et al.*, 2001; Raleigh *et al.*, 1998), it is likely that the staining observed here is a result of a technical deficiency in the experimental protocol.

3.3.4 Gene expression

While these data measure mRNA levels, this does not necessarily imply that these equate to functional effect, which would need to account for translation of protein product, sequestration, diffusion, lifetime, *etc.*

Changes in the balance of pro- and anti-angiogenic factors in the LN were inconsistent between timepoints, most likely due to undefined nature of the samples being pooled given that they contained surrounding mesenchyme in addition to the LTis, LTos and other cell types in the anlagen. Other tissues such as the liver, which were homogeneous in comparison, showed much more consistency over time.

Notable changes in the LN include a drop of over an order of magnitude in PEDF expression, which is coupled with a a reciprocal rise in thrombospondin expression. This may be related to differences in regulation during development and maintenance in the adult. PEDF, being a direct-acting inhibitor may be required in the embryo to act with immediate effect, whereas thrombospondin being a matrix component which must undergo proteolysis to exert its effects, and may hence act over longer timescales and play a role in the homeostasis of existing vessels. PEDF also acts upon new sprouts rather than older vessels, hence plays a role in the suppression of new sprouting angiogenesis (Ek *et al.*, 2006). A similar pattern is seen in all tissues for thrombospondin with the exception of the liver, and PEDF was only seen to rise appreciably in the liver. Thrombospondin expression was noted to decline in the adult by Morwood and Nicholson (2006); Sun *et al.* (2009), however for the tissues investigated, this only appeared to apply to the liver, where PEDF appears to continue to play an important role, unlike the other tissues. Unlike the LN, the skin is completely vascularised early in development, the lymphatics developing after the blood vasculature and being complete by E15.5 (Srinivasan *et al.*, 2007), and hence the changes may be reduced or effectively absent in consequence.

While an internal TaqMan probe would permit all splice variants to be quantified collectively, using a probe for a sequence common to all splice variants, here the relative levels of Vegfa splice variants were compared using SYBR green with three sets of primers to amplify three sets of two splice variants. In very general terms, Vegfa1+4 ($VEGF_{188}$) remains steady or increases in all cases, while 2+5 ($VEGF_{164}$) remains steady or increases and 3+6 ($VEGF_{120}$) decreases. Comparison relative to Pedf1 shows 1+4 to be produced at the highest level, followed by 2+5, with 3+6 being over two orders of magnitude less in the adult, the difference becoming greater

over time. This change may reflect the need for a smaller non-heparin binding isoform during vascularisation ($VEGF_{120}$), due to its lack of matrix interaction and its ability to diffuse further. During vascular maintenance in the adult, larger heparin-binding isoforms which act in a much more localised manner may be preferred, eg to promote the survival of existing vessels. The different isoforms have been shown to have differential effects upon EC proliferation and vessel branching (Park *et al.*, 1993; Ruhrberg, Gerhardt *et al.*, 2002), and in the case of bone growth plates, have been shown to have different spatio-temporal distributions, indicating that different isoforms play different roles during the process of development (Evans and Oberbauer, 2008). The VEGF-A isoforms also vary in their ability to bind the VEGFR co-receptors neuropilins 1 and 2, which are associated with BECs and LECs, respectively (Holmes and Zachary, 2005; Lohela *et al.*, 2009), thus changes in their composition may reflect changes in angiogenesis and lymphangiogenesis.

Figure 3.6 demonstrates non-quantitatively that pro- and anti-angiogenic factors are produced simultaneously, in this case in the thymus. However, this is the net expression within the tissue, and this (and all of the RTPCR data) do not localise expression, therefore it is not possible to determine whether pro- and anti-angiogenic factors are expressed evenly thoughout the tissue, or are localised to specific structures. This could be determined using immunohistochemistry (to localise the protein product), though growth factors may be present at too low a concentration to allow detection.

3.3.5 Differences between MRCs and FRCs

One approach to localise gene expression is to sort the LN into different subsets, which was done to separate MRCs and FRCs in the human, prior to analysis using a microarray. Note that the microarray data would require confirmation using RTPCR due to the reduced sensitivity of microarrays and the likelihood of bad probes which would result in false negatives. In consequence, only tentative conclusions may be drawn from these data. The small size of mouse LNs made cell sorting impractical, but would be a possibility if a sufficient quantity of material could be pooled.

The MRC and FRC stromal subsets may play rather different roles due to their spatial distribution within the LN. The MRCs are restricted to the subcapsular sinus, while the FRCs are present within the cortex and paracortex, in close association with the capillary and HEV networks running through. Using the microarray data presented in Figure 3.9, the signalling interactions which may occur between and within the layers are shown in Figure 3.10, and the relative levels of the genes involved are summarised in Table 3.1. In order to reduce the complexity, the pathways have been split into two separate diagrams.

While some changes in hypoxia-responsive genes such as GLUT1 were observed, no consistent pattern was seen, and hence it is not possible to conclude that one

subset is more hypoxic than the other.

Organisation and maintenance

The first pathway diagram in Figure 3.10 details the signalling molecules previously described as being involved in stromal induction in Section 1.3.3. MRCs retain many of the characteristics of LTos, while these are downregulated or absent in the FRCs. Of particular note is the absence of LTβR and IL-7 expression in the FRCs, and the upregulation of LT in the FRCs, which may imply that only the MRC layer is sensitive to LT. Both subsets were seen to produce LT however, with FRCs producing the most, perhaps suggesting that FRCs may maintain the peripheral MRCs through LT signalling, in addition to resident lymphocytes. FRCs were shown by Chyou *et al.* (2008) to be the main source of VEGF-A used to maintain the LN vasculature, and that this was a LT–LTβR-dependent process, but did not distinguish MRCs. LTβR signalling was also shown by (Katakai *et al.*, 2004) to be responsible for inducing formation of the FRC/conduit network, but LTβR was not specifically localised to the FRCs. LTβR distribution has been studied in lymphoid tissue including the thymus and spleen, but this study did not include LNs (Murphy, Walter *et al.*, 1998). White *et al.* (2007) showed that LTβR was mostly restricted to the $ICAM^{-}VCAM^{-}$ non-hæmatopoietic population, but did not distinguish between FRCs and MRCs. However, the lack of LTβR on FRCs may however be an artefact from the microarray, and would require confirmation using RTPCR.

The lack of IL-7 in the FRCs may imply that the MRCs are the sole source of IL-7 within the node (though as mentioned previously, the microarray data require RTPCR validation). IL-7 is required for T cell survival (Vivien *et al.*, 2001) and its levels are believed to be responsible for regulating the size of the peripheral T cell pool. Additionally, LTis in the embryo require IL-7 for survival, as do adult LTis, which are implicated in LN maintenance and reconstruction following damage (Hou, Mustafa *et al.*, 2010). An IL-7-ECFP reporter mouse was developed to study the cellular localisation of IL-7 production (Mazzucchelli, Warming *et al.*, 2009). However, while this demonstrated IL-7 expression in the thymus and spleen, the reporter failed to work in LNs. FRCs were shown by Link *et al.* (2007) to be a source of IL-7, CCL19 and CCL21, however this work did not distinguish between MRCs and FRCs, therefore it remains a possibility that IL-7 production is restricted to the MRC subset, and that the size of the T cell pool is proportional to the size of the MRC population.

Katakai *et al.* (2008) described the newly discovered MRC subset as "organiser-like", referring to their sharing of many markers with LTos and implying that MRCs were the adult equivalent. These findings are reflected in the microarray, MRCs expressing CXCL13, TRANCE, ICAM, VCAM and MAdCAM at higher levels than the FRCs. Katakai *et al.* (2008) also showed IL-7 to be produced upon stimulation with LT or anti-LTβR antibody; here it was observed that MRCs produced IL-7, but FRCs

Table 3.1: Genes involved in vascular maintenance and lymph node development. The level of mRNA shown for the MRC and FRC stromal subsets is based upon the levels shown in Figure 3.9, and indicates an approximate absent (blank), low (+), intermediate (++) or high (+++) level of abundance.

Category	*Gene*	*MRC*	*FRC*
	Vascular maintenance		
Promoter	PDGF C	++	++
	PlGF	++	++
	VEGF A	++	++
	VEGF B	+	+
	VEGF C	++	+
Inhibitor	PEDF	+++	++
	Thrombospondin 1	+++	+++
Stabiliser	Angiopoietin 1	+	++
	Angiopoietin 2	+	+++
	Lymph node development		
Signalling	CCL 19	+++	++
	CCL 21	+++	++
	CXCL 12	+++	++
	CXCL 13	+++	+
	TRANCE	+++	+
	LT	+	++
	LTβR	+	
	IL 7	+	
Adhesion	ICAM	+++	++
	VCAM	+++	+++
	MAdCAM	++	

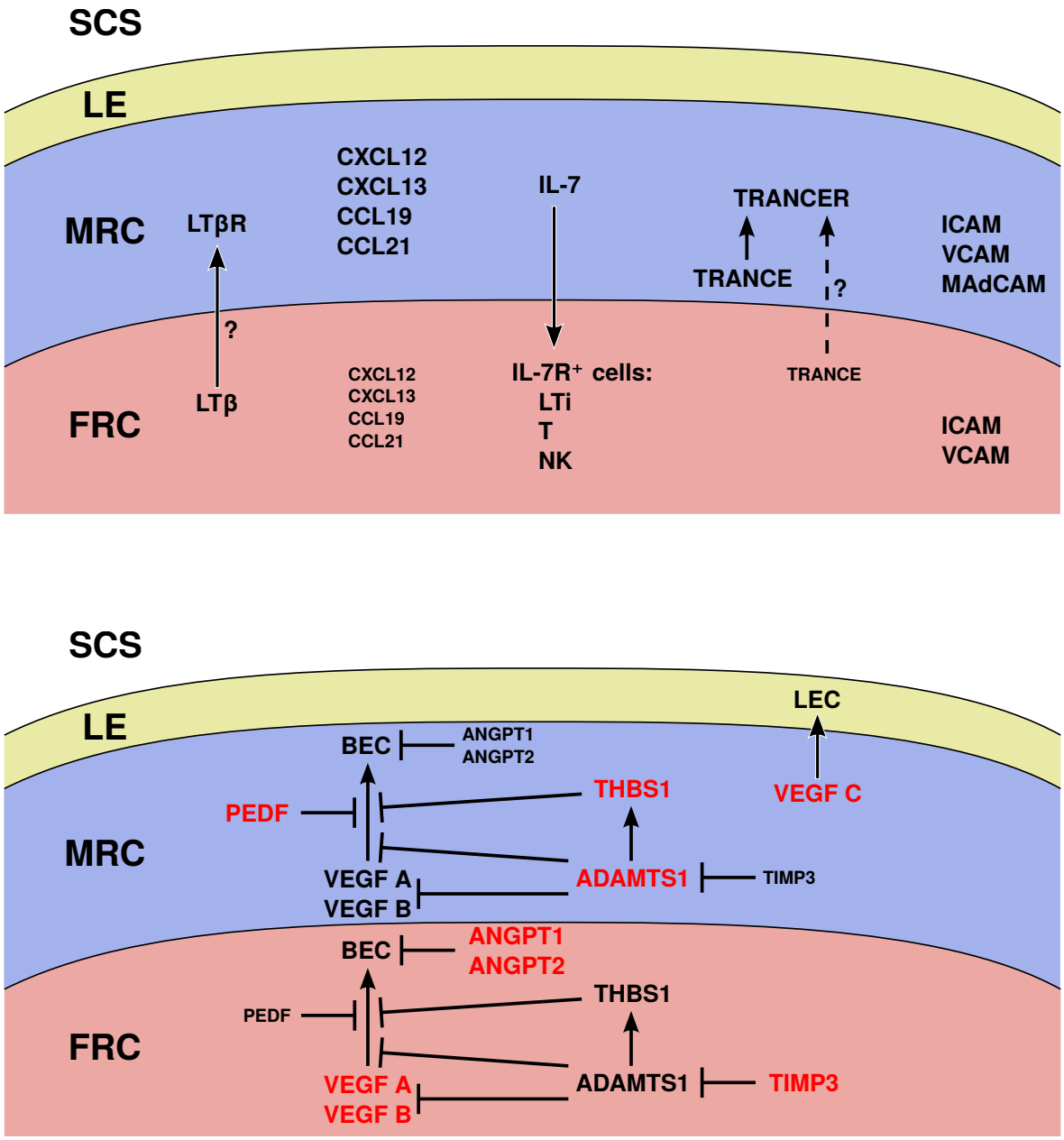

Figure 3.10: Models of LN organisation and angiogenesis. The spatial distribution of mRNA levels between the MRC layer and FRC zone is illustrated, with genes shown in a reduced size if they are less abundant in one compartment relative to another, and are highlighted in red if they are presumed to be active. Possible signalling interactions are indicated with arrows.

produced no IL-7 at all. Link *et al.* (2007) noted IL-7 production by FRCs, but being prior to the discovery of MRCs is likely to have included both subsets in their analysis. Given the requirement of both LTis and T cells for IL-7 to survive (Schmutz, Bosco *et al.*, 2009; Vivien *et al.*, 2001), it is possible that MRCs are the principal regulators of the pool size if it is the sole source of IL-7 in peripheral lymphoid organs. It is likely that IL-7, TRANCE and VEGF-C expression are a result of LT signalling (Vondenhoff *et al.*, 2009a).

Vascular homeostasis

The second pathway diagram in Figure 3.10 details potential interactions between pro- and anti-angiogenic factors in both MRC and FRC areas. The most obvious difference in the angiogenic environment between the two subsets is the upregulation of VEGF-C expression by MRCs. If validated by RTPCR, and given that MRCs underlie the LEC-lined subcapsular sinus, this may indicate that MRCs play a role in lymphangiogenesis and the maintenance of the lymphatic endothelium (Vondenhoff *et al.*, 2009a). VEGF-B, involved in vascular maintenance (Zhang, Tang *et al.*, 2009), is similar in both, while the upregulation of both PEDF and VEGF-A in the MRCs, again following RTPCR validation, may imply a need for suppression of neovessel growth underneath the subcapsular sinus, potentially to maintain separation between the sinus and blood vasculature. PEDF was recently shown to differentially regulate angiogenesis and lymphangiogenesis in the context of a prostate tumour model, where angiogenesis was suppressed, but lymphangiogenesis increased Halin, Rudolfsson *et al.* (2010); it is possible that in the LN, PEDF suppresses angiogenesis selectively, while promoting lymphangiogenesis and/or lymphatic maintenance with VEGF-C acting in a synergistic role. VEGF-A from inflamed tissues has been shown to induce angiogenesis in draining lymph nodes (Halin, Tobler *et al.*, 2007); it is therefore possible that some of the anti-angiogenic factors such as PEDF, TIMP3 and the angiopoietins exist to dampen responses to external factors.

The FRC zone has increased angiopoietin activity, which is normally associated with vascular stabilisation rather than angiogenesis. This raises questions regarding the nature of the association of the FRC network with the vasculature, and whether the FRCs are the origin of the pericytes covering and regulating the HEV network, or if they act in a pericyte-like manner in addition to the pericytes, being apparently continuous with them (Ma *et al.*, 2007).

Thbs1 was expressed at equal levels in both MRCs and FRCs. However, this accounts only for transcription, not translation or turnover. Turnover may affect sequestration of other components and matrix binding partners (Iruela-Arispe, 2008), hence the microarray data is not informative if the downstream effects are not observable as a change in gene expression.

While the exact effects upon the vasculature arising from the differences in gene

expression between the MRCs and FRCs are far from clear, there are differences between the two. Questions arising from these differences include determination of the roles the two subsets play in the normal functioning of the LN versus maintenance and repair following an inflammatory response.

3.4 Conclusions

Following observation LN anlagen using various different imaging strategies, the method of LN vascularisation is still unclear, with evidence in the literature appearing contradictory. Some evidence points to vascularisation at the earliest stages of development, while in other cases the anlagen appear avascular until much later. The developmental origin of the vessels is also unclear, the lymph sac and vessels in the mesenchyme both being possibilities.

The overall impression of the differences between FRCs and MRCs, based upon the microarray data is that MRCs are most likely to be involved in maintenance of the lymphatic endothelium of the subcapsular sinus, and upregulate a number of genes with anti-angiogenic potential, though some pro-angiogenic genes were also seen to be upregulated. FRCs also express genes promoting vascular stability, though given their differences it is clear that there are significant differences between the MRC and FRC compartments.

The RTPCR data highlighted changes in the balance of pro- and anti-angiogenic factors during development and in the adult. In order to determine how these factors affect endothelial cells in the vicinity of the anlagen, a functional *in vitro* angiogenesis assay was developed in the following chapter to allow the angiogenic environment of the anlagen to be measured, and to also allow dissection of the signalling pathways involved.

3.5 Future work

While hCD2-GFP embryos are sufficient for studying development once LTi infiltration commences, study of the earliest stages will still require identification of the site using some other means, perhaps using LYVE1-GFP or some other marker to identify the early establishment of the anlagen prior to LTi recruitment.

3.5.1 Wholemount imaging of LN anlagen

Given the problems identified with wholemount preparations, it is clear that the autofluorescence resulting from long fixation times must be reduced in order for immunohistochemical staining to achieve a signal greater than the background. The

obvious solution is to dissect the anlagen and fix the smaller pieces of tissue for a reduced amount of time prior to staining.

All of the recent papers investigating LN anlagen such as Vondenhoff *et al.* (2009a) and Bénézech *et al.* (2010) utilised frozen section staining. While this is a useful technique, important information about the true 3-D structure of the tissue is lost, resulting in ambiguity given that apparent features may simply be artefacts of the sectioning angle and/or slice used. Imaging the entire structure would eliminate such problems. For example, the complete structure of all collagen IV basement membranes could be visualised, together with all VEGFR1$^+$/VEGFR2$^+$/MECA32$^+$ cells to fully realise the spatial arrangement of ECs and basement membranes with respect to the lymph sac and LTis, and to also observe their orientation and placement relative to stromal induction.

Autofluorescence could additionally be eliminated or reduced with the use of spectral unmixing during imaging. Additionally, fluorophores in the far red could be used such as AF647, which would reduce the interference of autofluorescence given that autofluorescence declines with increased excitation wavelength.

3.5.2 Serial frozen sections

In addition to wholemount, it would also be useful to image the developing anlagen using serial frozen sections, which would allow for the use of antibodies which will not work with wholemount preparations, eg due to lack of penetration into thick sections or inaccessibility such as within junctional complexes, as well as techniques which will not work with wholemount such as the use of different antibodies of the same isotype labelled with fluorescent Fab fragments of different colour, such as Zenon kits (Invitrogen), again due to lack of penetration.

Using both wholemount and frozen sections, it should be possible to image the different LN anlagen throughout all timepoints during development to gain a detailed understanding of how the vascular network develops within and without the anlagen, and its origins within or external to the lymph sac and/or surrounding mesenchyme.

3.5.3 RTPCR to validate microarray

The microarray data highlighted some interesting and potentially significant differences between the MRC and FRC stromal subsets, most notably the differences in IL-7, LT and LTβR, TRANCE and TRANCER expression. These require validation with RTPCR in order to confirm that the observations are real.

Chapter 4

Development of a model system to study angiogenesis *in vitro*

4.1 Introduction

4.1.1 Models of angiogenesis and vasculogenesis

Angiogenesis is the result of changes in the gene expression, proliferation, migration and organisation of endothelial cells in response to various cues (Adams and Alitalo, 2007). Many different models have been established in order to study various aspects of this process. *In vivo* animal models include the chick chorioallantoic membrane (embryo yolk sac), which is both accessible and easy to visualise (le Noble *et al.*, 2004). Other models include implantation of *in vitro* constructs, *e.g.* subcutaneous implantation of ECs in collagen, fibronectin or Matrigel gels into mice (Auerbach, Lewis *et al.*, 2003; Koike, Fukumura *et al.*, 2004; Schechner, Nath *et al.*, 2000). *In vitro* models include basic tube formation on Matrigel, beads in fibrin gels to stimulate sprouting and anastomosis, and mouse aortic ring vessel outgrowth (Nakatsu, Sainson *et al.*, 2003). Other models include the vascularisation of embryoid bodies formed from embryonic stem cells (Vailhé *et al.*, 2001). Parameters measured in existing assays include disruption of the vascular basement membrane, EC migration, proliferation, and tube formation. However only tube formation (*i.e.* outgrowth and vessel assembly) is a direct measurement of angiogenesis (Auerbach *et al.*, 2003).

Human umbilical vein ECs (HUVECs) are the most commonly used primary EC line, though other lines are also used, for example bovine aortic endothelial cells (BAECs) (Korff and Augustin, 1999). Primary cells can only be passaged a limited number of times before growth is arrested, and while several attempts have been to derive immortalised cell lines, in most cases it is clear that these lines have altered gene expression which puts their physiological relevance in doubt (van Beijnum, van der Linden *et al.*, 2008; Rhim, Tsai *et al.*, 1998). HUVECs in culture have been found to exist in two main states, proliferative at low density and organised into tu-

bular structures at high densities (Maciag, Kadish *et al.*, 1982). Maciag *et al.* (1982) found that tube formation was driven by omission of proliferative factors from the culture medium (endothelial cell growth factor; bovine hypothalamus extract) and the fibronectin matrix. However, these *in vitro* observations may not truly reflect the *in vivo* behaviour, where proliferation is not the norm. *In vivo*, cells in an established network exist as *phalanx* cells, with sprouting angiogenesis occuring from this network as a result of the phalanx cells transforming into leading tip cells and following stalk cells (Augustin *et al.*, 2009). Growth factors such as VEGF and bFGF are responsible for the induction of angiogenesis (Pepper, Ferrara *et al.*, 1992), with factors such as angiopoietin being responsible for stabilising of an established network, and are also implicated in arterial–venous differentiation (Augustin *et al.*, 2009).

4.1.2 Requirements of an *in vitro* model

An *in vitro* model of angiogenesis should reflect the *in vivo* process to the maximum practicable extent, whilst allowing precise and accurate quantification and analysis of the process via extraction of meaningful features from the model, *e.g.* via microscopic imaging and analysis. A "complete" vascular model should include all of the major features of a vascular bed. The vascular bed is composed of an interconnected network of capillary vessels composed of vascular endothelial tubes, which are covered with a layer of pericytes (Bergers and Song, 2005). These two cell layers are separated by a basement membrane providing both structural stability and a barrier to endothelial cell migration (Armulik, Abramsson *et al.*, 2005; Sato and Rifkin, 1989). Vessels also experience fluid flow, perfused through the vascular network, providing hydrodynamic shear stress and pressure, which may also cause changes in endothelial behaviour (Jones *et al.*, 2006; Nguyen, Eichmann *et al.*, 2006; Price, Wong *et al.*, 2010). Vascular networks do not exist in isolation, being incorporated into a tissue throughout which they ramify and being specialised to satisfy the functional needs of that tissue, *e.g.* the blood-brain barrier (Bergers and Song, 2005) and HEVs in LNs (Willard-Mack, 2006). A vascular model should ideally contain both endothelial cells and pericytes, and must exist in the wider context of a specific tissue. The model will thus contain endothelial, pericyte and tissue-like components. The model must possess the potential for remodelling via sprouting and intussusceptive angiogenesis in response to cues from the local environment (*i.e.* in the tissue-like component and/or itself).

If a network is required from the start of an experiment, this would require *de novo* formation of a network, *i.e.* vasculogenesis to drive formation of a primary capillary plexus (Davis *et al.*, 2007). However, depending upon the process being studied, initial network formation may be foregone in favour of simpler methods, such as a starting point of a confluent monolayer or other forms of multicellular aggregate such as spheroids, or even a single cell suspension which will form a network, extend

tubes, or undergo some other *quantifiable change*. Examples include number of tip cells, sprout length, number of branchpoints, and area occupied by vessels (Wang, Nakayama *et al.*, 2010).

Given the important role of VSMCs and pericytes in stabilising, supporting and regulating the endothelial layer of vessels, having smooth muscle coverage would be an important component of a realistic vascular model. The behaviour of endothelial cells in the model, for example in response to exogenous or endogenous growth factors, may differ dramatically with the presence or absence of smooth muscle, and so may not accurately reflect *in vivo* behaviour in their absence. However, during development, sprouting vessels do not initially possess smooth muscle coverage, VSMCs being recruited and retained due to PDGF-B signalling from ECs, and so this may be an unnecessary complication depending upon the context (Hellström, Kalén *et al.*, 1999; Lindblom, Gerhardt *et al.*, 2003).

As discussed above, the *in vitro* model must include a component to model the tissue through which the capillary bed infiltrates. This may be adapted to model various different scenarios, for example inclusion of tissue-specific cell types, addition of medium- or matrix-borne growth factors, inhibitors or blocking antibodies, control of physical and chemical properties and/or combination of the vascular component with *ex vivo* tissue explants, tumours, spheroids, engineered tissue constructs or other implantable material.

Tissue-specific cell types may be used to model the specific features and behaviours of particular tissues, for example via the addition of stromal cells, solid or metastatic tumour cells, to study their influence upon vascular structure and function. Growth factors, inhibitors or blocking antibodies would allow the investigation of responses to specific factors in a tissue-free context, to remove the multiplicity of effects additional cell types would add, and to also permit the dissection of the signalling pathways involved. Controllable physical and chemical properties include mechanical stress and deformation, oxygen tension, pH, *etc.*, which vary between different tissues (Assoian and Klein, 2008; Nanka *et al.*, 2006). The use of *ex vivo* tissue explants would permit the effects of the tissue upon remodelling and outgrowth of the vascular component to be studied. Depending upon the processes one wishes to study *in vitro*, a simpler model may incorporate one or more of the above features.

Spheroid models have previously been used as a model for angiogenic outgrowth in collagen gels. Thomas Korff developed an *in vitro* model, using methylcellulose spheroids which could be embedded within a collagen gel and used to study the effects of soluble factors and forces (Korff and Augustin, 1998, 1999). A detailed protocol for producing spheroids in bulk was subsequently published (Laib *et al.*, 2009), and assay plates containing collagen gels seeded with HUVEC spheroids have recently become commercially available (3D-Angiogenesis Assay, PromoCell).

Fluid flow and the resulting pressure and shear stress are obviously integral fa-

cets of the normal functioning vascular system, and have been shown to have some influence upon certain aspects of the differentiation, organisation and morphology of endothelial cells in particular and vascular networks as a whole (Jones *et al.*, 2006; Nguyen *et al.*, 2006; Price *et al.*, 2010). The arterial side of the circulation is additionally subjected to high pressure pulsatile flow compared with the low pressure smoother flow experienced on the venous side and a pressure differential exists across the capillary beds connecting the two. Depending upon which parts of the vascular system one wishes to model, incorporating fluid flow, hydrodynamic pressure, pulsatile flow (and potentially even a low pressure fluid drain to mimic lymphatics) may be desirable. However, accurate modelling of fluid flow may not always be required. In development, until the major arterial and venous circuits complete, flow is absent, and consequently any pressure differential. Additionally, adventitious endothelial sprouts initially lack lumens or are blind-ended, so therefore lack flow entirely even after the initiation of circulation (Gerhardt *et al.*, 2003).

The purpose of the model is to observe and quantify changes in the vascular component in response to various treatments. Thus, it is paramount that it be possible to visualise the model, and extract from it parameters which accurately quantify certain aspects of the vascular component, thereby permitting meaningful comparisons to be made between treatments. In order to observe and record changes in the model, such as growth, regression and remodelling of the network, it should be possible to use microscopy to image, ideally in real time to allow the study of the kinetics and dynamic changes within a single sample, resulting in less variation and hence more statistically robust results, rather than comparing different samples at multiple timepoints. The ability to fluorescently label the cells used in the model would permit real time imaging, using epifluorescence, confocal and MP microscopy, as well as allowing easy separation from other cells using flow cytometry.

In this thesis, HUVECs have been chosen as a model endothelial cell. HUVECs are used in vascular modelling and angiogenesis research in a wide variety of models. While a variety of different endothelial cell types are available, HUVECs are widely used and can be cultured in large quantities (Bishop *et al.*, 1999; Korff and Augustin, 1998; Maciag, Hoover *et al.*, 1981; Nakatsu *et al.*, 2003). Utilising a commonly used cell type also permits comparisons to be drawn with the many published findings using the same cell type. Two smooth muscle cell lines were also used, the first being a primary culture of mouse aortic vascular smooth muscle and the second being the multipotent mouse mesenchymal line, C3H/10T½. The C3H/10T½ line (Reznikoff, Brankow *et al.*, 1973) is widely used as a model pericyte cell line; though they are not formally characterised as such, they can be differentiated into smooth muscle and are used in a wide variety of models. C3H/10T½ were shown to be of multipotent cells mesodermal origin, capable of differentiation into different mesenchymal lineages, including chondrocytes and smooth muscle (Pinney and Emer-

son, 1989). C3H/10T½ were additionally shown to be recruited to ECs via PDGF and TGF-β signalling, as well as by direct cell–cell contact, and differentiated into smooth muscle (Hirschi, Rohovsky *et al.*, 1998). A defining marker for pericytes (and other mural cells) during development is the NG2 proteoglycan (Ozerdem *et al.*, 2001), therefore any smooth muscle cell line used to model pericytes should be expected to express this unique differentiation marker. Note that NG2 is also found on neural cells, but is restricted to mural cells in the vasculature and is hence specific for pericytes and mural cells compared with other types of smooth muscle (*i.e.* is α-SMA$^+$NG2$^+$). The primary line was hypothesised to be a better choice, being derived directly from vascular smooth muscle.

4.1.3 Extracellular matrix

The extracellular matrix is composed of a number of proteins which link together to provide a "scaffold", to give a tissue mechanical support, and also play a role in defining its shape and structure. The ECM structure defines tissue boundaries, sequesters and present growth factors to cells, and allows cells to sense mechanical forces (Rozario and DeSimone, 2010). Within this loose meshwork, cells are able to firmly anchor themselves in position, or to exert directional force upon the fibrils of the network to allow locomotion and migration through the tissue (Friedl, Zänker *et al.*, 1998; Martins and Kolega, 2006). The cells, in turn, are also capable of sensing forces exerted upon the matrix such as tensile and compressive forces, and are hence capable of transducing signals at a distance from themselves, which serve to act as cues to influence their behaviour (Korff and Augustin, 1999). The matrix also permits free diffusion of small and large molecules through its pores, though the tortuous paths through the dense fibrillar network can impede the passage of molecules of increasing size, creating steeper concentration gradients than would exist in the absence of the matrix (Ramanujan, Pluen *et al.*, 2002). Additionally, many soluble factors contain matrix-binding domains which allow them to be sequestered directly by the matrix, allowing for the creation of very steep, localised concentration gradients, and also allows for controlled release into solution from the matrix under certain circumstances (Park *et al.*, 1993; Sottile, 2004). The extracellular matrix is a dynamic structure, being continually remodelled by cells synthesising and degrading the matrix surrounding them (Rozario and DeSimone, 2010).

In the context of the vasculature, there are two different types of ECM to consider. The first is the basement membrane, separating the endothelium from its surrounding smooth muscle or pericyte layer. Individual "phalanx" endothelial cells experience a polar environment, with their basal surface in intimate contact with the basement and apical surface exposed to the lumen (Davis and Senger, 2005). The basement not only provides a degree of structural stability, but also provides pro-survival signalling cues via integrin signalling and sequestration of growth factors

as discussed above. While phalanx cells are known to be a quiescent, non-migratory, cell type, the basement membrane plays a role in suppressing migration both by maintaining the differentiated state, and additionally by presenting a physical barrier to migration (Davis and Senger, 2005). Were the basement membrane to be physically disrupted or enzymatically degraded, loss of signalling from the matrix and removal of physical limitations upon migration may promote either cell death or permit switching to an invasive, migratory state which may result in migration into the surrounding tissue, *i.e.* angiogenesis.

The second type of ECM to consider is the composition of the matrix in the tissue being vascularised, *i.e.* outside the blood vessel. This may vary depending upon the tissue in question, but it may also serve to impede, or promote, angiogenesis depending upon whether a migratory endothelial cell can pass through it, and whether or not it contains pro- or anti-angiogenic factors.

The ECM may therefore be considered as a scaffold providing a physical framework to which cells may adhere, and within which they may migrate. Contact with the matrix provides a variety of signalling cues which may influence cellular function and behaviour, including effects upon cell cycle control, metabolic activity, motility and migration, and differentiation status. These effects may arise as a result of direct interaction between matrix components and cellular receptors, but may also be influenced by modulating factors such as the sequestration of growth factors, cytokines, chemokines, enzymes, and chemotactic factors which may enhance or attenuate other signalling pathways, or may have entirely orthogonal effects. The matrix alters the diffusion rates, lifetime and signalling effectiveness of soluble and sequestered factors. Sequestration in particular may enhance certain signal–receptor interactions by presenting growth factors conjugated to the matrix which can enhance signalling compared with the same factor in soluble form, and retard others for example by regulating their bioavailability (Wijelath, 2002).

Many different materials, of both biological and non-biological origin, have been used to create three-dimensional culture systems for both *in vitro* and *in vivo* use. When considering the most appropriate matrix to use for modelling, the primary concern is that it permits the biological process being studied to occur, and does not result in any adverse effects. Tissue engineering research has led to the creation of a wide variety of hydrogels for research and therapeutic purposes. These are typically polymers which are either polymerised with the cells in place, or seeded with cells following polymerisation. Example artificial matrices include cross-linked polyethylene glycol (PEG) and polylactic co-glycolic acid (PLGA) which have been shown to support vessel formation when seeded with ECs and implanted subcutaneously (Ford, Bertram *et al.*, 2006), and biodegradable polyurethane (Hofmann, Ritz *et al.*, 2008).

Many non-biological artificial matrices suffer from not permitting cell attach-

ment or remodelling due to lacking the appropriate peptide sequences. Artificial hydrogels not composed of peptides are often not intrinsically degradable by cells, given that MMPs can not cleave them, and they do not contain peptide motifs for cell attachment or degradation to permit remodelling. Consequently, many artificial matrices are functionalised using peptide sequences to allow cell attachment via integrin binding using the RGD peptide motif, and to permit matrix cleavage and remodelling with the addition of MMP-sensitive sequences to the hydrogel backbone (Seliktar, Zisch *et al.*, 2004). While such features may be added to allow an artificial polymer to mimic natural matrix, there are many other features of biological matrices which would still be absent, such as the ability to sequester growth factors. Additionally, the necessary covalent modifications to produce such specialised polymers require significant chemical engineering expertise.

Example biological matrices include collagen and Matrigel, both being capable of supporting tube formation . There is strong evidence that the matrix has profound effects upon EC phenotype, with cells grown on basement membrane collagens IV/V forming more tube-like structures than those grown on the interstitial collagens I/III, which tend to proliferate more and form a confluent monolayer (Madri and Williams, 1983).

Of the biological matrices suitable for studying angiogenesis, fibrin, collagen and Matrigel stand out as the most viable candidates, all having been used for many years and being capable of supporting tube formation (Montesano, Mouron *et al.*, 1985; Olander *et al.*, 1985). Matrigel would appear to be preferable, given that it contains mainly basement membrane proteins. However, differences do exist between collagen and Matrigel, indicating that different mechanisms may be involved in the formation of capillary- and lumen-like structures depending upon the matrix, with collagen being a more realistic model (Montañez, Casaroli-Marano *et al.*, 2002). This is most likely due to collagen I being a better model of the extracellular matrix within a tissue, which would not normally contain basement membrane proteins. Fibrin is normally associated with blood clotting and granulation tissue, *i.e.* wound repair, compared with collagen which is found in normal ECM (Schultz and Wysocki, 2009). Collagen would therefore appear to be a better model for developing and adult tissue than fibrin, and collagen has been used extensively in previous *in vitro* models of angiogenesis (Bayless and Davis, 2004; Korff and Augustin, 1998; Montesano *et al.*, 1985; Saunders *et al.*, 2005; Schultz and Wysocki, 2009; Stratman *et al.*, 2009b). In addition to accurately modelling biological processes, the matrix must also meet the physical requirements, *i.e.* modelling physical forces including compression, tension and hydrodynamic pressure, in addition to possessing sufficient physical robustness.

4.1.4 Microfluidics

In order to create an artificial perfused vascular system, it is necessary to create some form of tubular structure within the biological scaffold being used, which should be amenable to perfusion with liquid analogous to the perfusion of tissue microvasulature with blood. While a wide variety of techniques and processes have been used, the core concept is that of moulding or fashioning a vessel-like structure within the scaffold material. The process of forming microscale channels for fluid flow has spawned the relatively new field of *microfluidics* (Duffy, McDonald *et al.*, 1998; McDonald and Whitesides, 2002). While initially pioneered by chemical engineers using solid and semi-solid materials such as elastomers (Kim, Xia *et al.*, 1996, 1995), microfluidic networks are now created in cell-seeded biological scaffolds such as agarose, alginate and collagen, permitting the modelling of a variety of biological processes with precisely-controlled fluidic flow (Cabodi, Choi *et al.*, 2005; Golden and Tien, 2007; Ling, Rubin *et al.*, 2007). The available techniques may be separated into two main categories: those involving embedding and removal of a sacrificial element, leaving open channels behind in the scaffold, and direct moulding of the scaffold using a mould.

Pattern generation using photolithography

While many methods exist to create patterns for mould formation, photolithography is the most commonly-used technique, and may be used as a basis for both embedded sacrificial elements and direct moulding. George Whitesides' group in Cambridge, Massachusetts developed the technique of "soft" lithography used for micromoulding using conventional photolithographic techniques to create PDMS elastomer moulds (Kim *et al.*, 1995). The process is detailed below, and has been reviewed by McDonald, Duffy *et al.* (2000).

SU-8 is a negative i-line (365 nm) epoxy photoresist widely used in microfluidics because it may be used to create structures up to 2 mm in depth with a high aspect ratio, and for microfluidics up to 50 µm depth is common (Golden and Tien, 2007; Jackman, Duffy *et al.*, 1998). It is additionally both biocompatible and stable to attack by most solvents. When a silicon wafer spin-coated with SU-8 photoresist is exposed to 365 nm UV light, areas of the resist not covered by the photomask are cross-linked. The cross-linked areas remain solid and attached to the wafer when washed with solvent, whereas unexposed non-cross-linked areas are removed, exposing the bare wafer. The negative of the pattern on the photomask will be therefore be reproduced in the photoresist as a structure in relief (McDonald *et al.*, 2000).

"Soft" lithography is so named due to the use of PDMS to create a mould in inverse relief to the SU-8 "master". PDMS is one of a class of elastomers known as RTV elastomers, which consist of two parts, a base and catalyst (cross-linker). Both RTV components are liquids, typically mixed in a 10:1 ratio, which form an elastomeric

solid following curing. Cured PDMS is an optically clear and colourless solid, which makes it useful for use as a microfluidic material and for imaging (McDonald *et al.*, 2000). When moulded against pattered SU-8, PDMS is capable of reproducing features at the micron scale (Christensen, Chang-Yen *et al.*, 2005; Kurpinski, Chu *et al.*, 2006). Following curing, the PDMS may be peeled away from the master, which may be reused several times.

Following the creation of a PDMS mould, it may be used directly as a microfluidic device, given that it may be directly bonded to glass (Bhattacharya, Datta *et al.*, 2005; Cha, Kim *et al.*, 2006). Or it may in turn be used to pattern other materials, which will result in that material having the same features as those originally present on the SU-8 master (Xia, McClelland *et al.*, 1997). PDMS is relatively inert, chemically, and biocompatible, making it safe to use directly in model biological systems (Khetani and Bhatia, 2006).

Patterning with removable elements

Patterning with removable elements involves the creation of a gel containing elements which may be later removed. These may be simple linear arrangements, such as needles, wire or fibres which may be withdrawn from the gel following gelation. Examples include collagen gels created containing nylon fibres (Takei, Sakai *et al.*, 2006), or with a needle (Chrobak, Potter *et al.*, 2006), which may be removed to create a linear vessel lumen suitable for EC seeding and perfusion. However, more complex structures may be created, for example by twisting a wire or fibre to create nonlinear paths such as bends and loops (Takei, Sakai *et al.*, 2007). Branching and joining of paths may also be created using multiple fibres, for example as shown by Neumann, Nicholson *et al.* (2003), however it should be noted that this is creating multiple linear channels, rather than channels with branching. This paper is notable due to using the nylon fibres to create sleeves of VSMC suspended in media, rather than using a matrix directly (though it would be possible to subsequently embed within a matrix and flow in ECs to form a functional vessel).

Unfortunately, these strategies all create channels which are generally of a larger scale than may be achieved through SU-8 photolithography and PDMS moulding, and the networks are of limited size and complexity. A PDMS mould may be of arbitrary size, limited only by the size of the silicon wafer, and the channels may contain as many branchpoints as desired, as well as variations in channel width which are difficult, if not impossible, to achieve with removable elements with any degree of accuracy or reproducibility. However, such systems are useful, and simple variation in parameters such as channel width in one direction along a linear path are possible, enabling the study of the effects of physical factors such as variation in pressure and shear stress on EC in collagen gels (Price *et al.*, 2010).

Patterning with sacrificial elements

The use of PDMS to pattern sacrificial elements was pioneered by Joe Tien's group in Boston, Massachusetts (Nelson and Tien, 2006; Tang, Golden *et al.*, 2004) extending previous work using simple polymers by George Whitesides' group (Jeon, Choi *et al.*, 1999; Kim *et al.*, 1995). Microscale cavities may be created using patterned Matrigel surrounded by collagen, using dispase to digest the Matrigel leaving open cavities or channels (Tang *et al.*, 2004). Alternatively, the PDMS mould may be used to pattern a meshwork of gelatin, the gelatin being flowed through the PDMS in a liquid state. Once the gelatin has been set, it may subsequently be removed from the PDMS and then embedded within a collagen gel. Channels are created in the gel by by raising the temperature to liquefy the gelatin, which can then flow out of the gel to leave open channels in the gel interior. The process is outlined in the last five steps of Figure 2.7, based upon the work in Tang, Golden *et al.* (2003) and Golden and Tien (2007).

Non-linear vessels have also been created using sacrificial alginate fibres seeded with ECs placed inside collagen gels containing alginase (Takei *et al.*, 2007), but modelling larger scale vessels, rather than capillary networks or single-cell sprouting angiogenesis.

Patterning using direct moulding

Direct moulding is rather simpler than indirect methods using sacrificial elements; the gel to be patterned is simply poured onto the PDMS master and set into a solid which may then be subsequently removed and perfused. Examples include moulding and perfusion of agarose (Ling *et al.*, 2007), alginate (Cabodi *et al.*, 2005; Choi, Cabodi *et al.*, 2007) and collagen (Cross, Zheng *et al.*, 2010). However, the gel must be of sufficient strength to maintain its structure and integrity during handling while demoulding and subsequently perfusing.

4.1.5 Development of a microfluidic vascular model

Microfluidics have been used previously in various models and, as discussed in Section 4.1.4, vary from being crude and simple (but less technically demanding) to having micron-scale precision (but requiring a great deal of technical expertise and expensive photolithography equipment not usually found outside microelectronics fabrication). It would be greatly desirable to achieve the scale and precision of photolithography utilising equipment found in a biological research setting, given that access to photolithography equipment is difficult as well as prohibitively expensive. Being able to rapidly prototype different designs would also give flexibility which photolithography does not offer, and permit rapid, iterative prototyping and refinement of the model. This would require the creation of a template which could be

used as an analogue of the pattern etched into SU-8 photoresist to mould PDMS. Following the creation of a PDMS mould, subsequent experimental steps could utilise the same procedures used by existing work with PDMS microfluidics, as described above.

4.1.6 Aims

1. To develop a 3-D endothelial culture model capable of forming a vascular network, and which will remodel and/or outgrow under the appropriate angiogenic stimuli.

2. To incorporate microfluidic flow into the model to reproduce flow and shear forces experienced by ECs *in vivo*.

3. To incorporate VSMCs into the model as an EC-stabilising and -modulating perivascular component.

4. To derive GFP-expressing endothelial and VSMC cell lines to allow real-time imaging in 3-D.

5. To develop methods for accurate quantification of network remodelling and angiogenesis.

6. To demonstrate that the model is responsive to growth factors and that the responses may be accurately quantified.

4.2 Results

4.2.1 PDMS microfluidic networks

PEN template creation

PEN slides were prepared as described in Section 2.9.1, and cut as described in Section 2.9.2. Fine tuning of the stage movement speed, laser focus and laser power resulted in successful cutting of 25 and 50 µm thick PEN film. In practice, only a narrow range of laser power settings were suitable, with there being a hard lower cutoff below which no cutting will occur, and an upper limit above which the sample is damaged. Using all three adjustments, the system was set up to cut the finest line possible.

An example PEN network cut with the PALM system is shown in Figure 4.1(A–C), showing the process from the initial scale drawing, conversion to points, and finally the cut PEN template. The PALM Robo software showing the PEN surface during cutting is shown in (D). Note the current cutting point indicated by the red triangle.

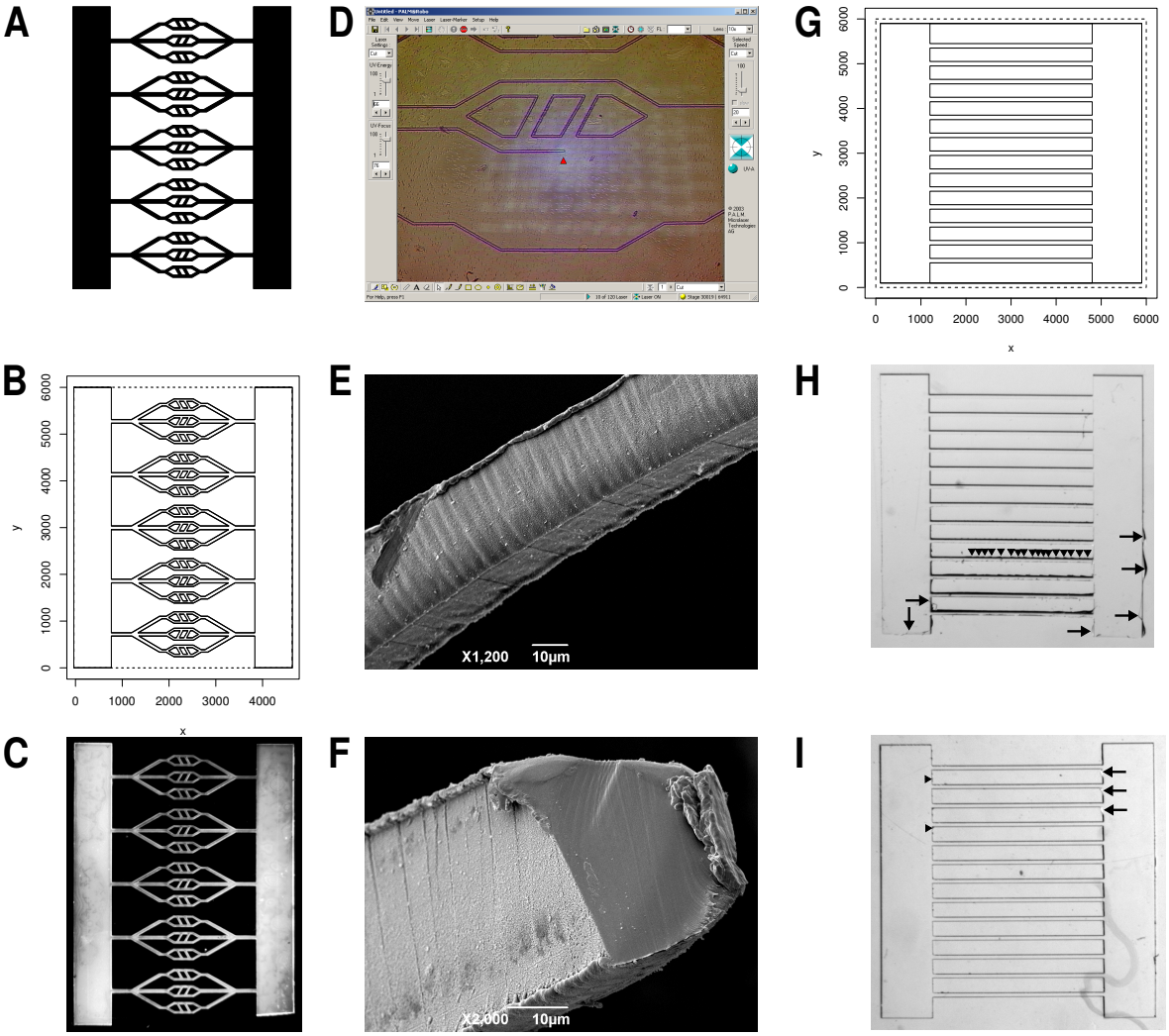

Figure 4.1: PEN-PDMS moulding. Networks for perfusion were designed as editable vector graphics (A) prior to conversion to a series of points for laser cutting (B); solid lines are laser cuts, while the dashed line is the bounding box of the coordinate system. The PEN template after cutting with this pattern is shown in (C). All three images are use the same (µm) scale shown in (B). The PEN with overlaid template during cutting is shown in (D). SEM analysis of 25 µm PEN is shown (D,E) showing striations in surface and ridges along cut edges, but with consistent 50 µm width. Using PEN cut with the pattern in (G), which uses the same scale and coordinate system as (B), elastomer moulds were made placing the PEN template on glass and overlaying with RTV (H) or on PDMS and overlaying with PDMS (I). When placed on glass, liquid elastomer can run under the PEN, sealing it within the cured elastomer, resulting in tearing of the mould during removal shown as large tabs (arrows) or multiple small tears (arrowheads indicate tears on one line) on the bottom four channels. When placed on PDMS and blocked with Pluronic F-127, underrun is eliminated and the cured elastomer can be cleanly separated, showing only minor imperfections such as very tiny tabs (arrows) and minute debris (arrowheads).

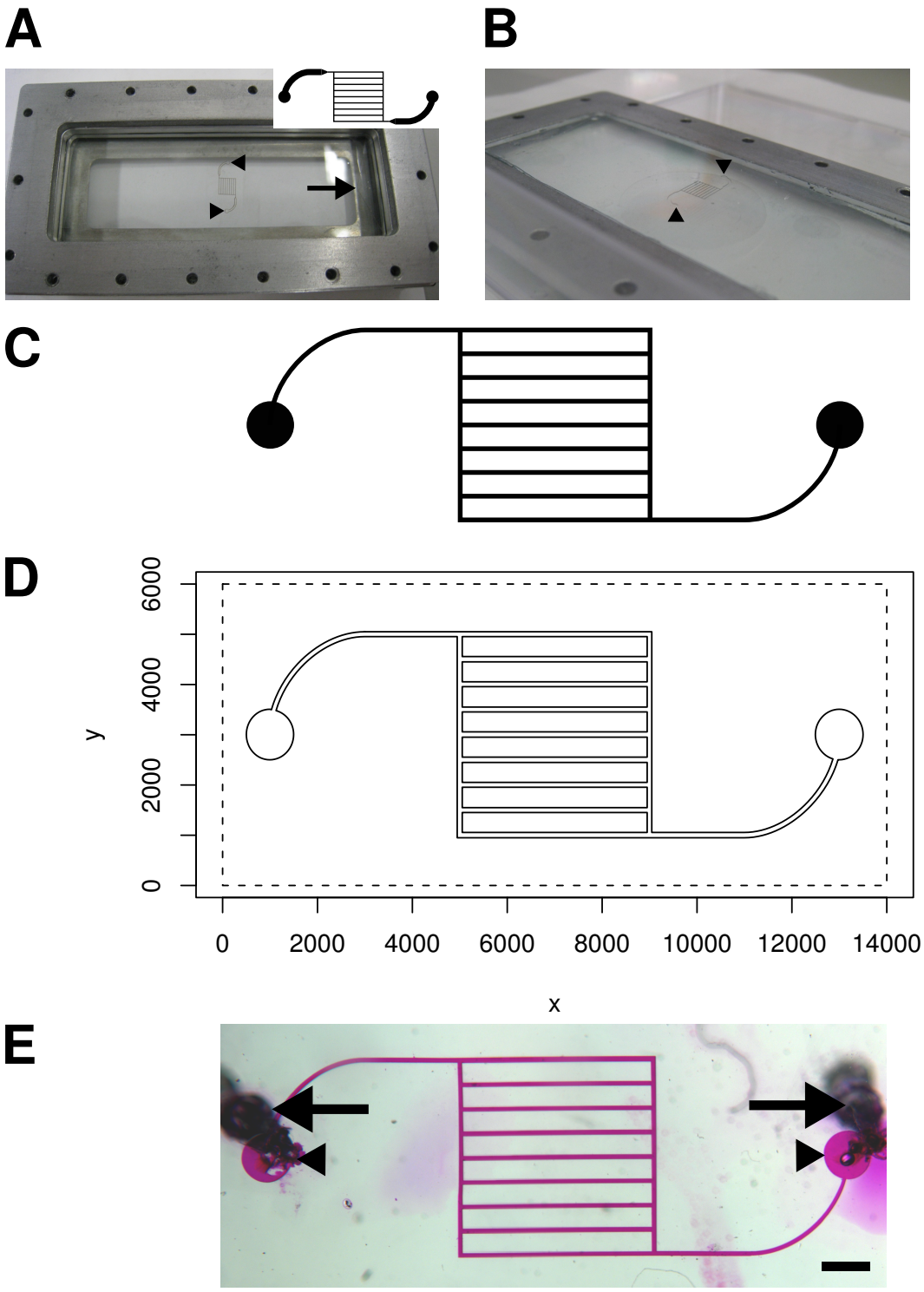

Figure 4.2: PDMS mould perfusion. An example of PEN in PDMS during moulding is shown in (A), with the template used shown inset. The tab of the acetate shim used to separate the PDMS layers is indicated with an arrow. The channels are shown in inverse relief (B) following removal of the PDMS backing and PEN template. Arrowheads indicate the perfusion endpoints. A branched network pattern (C) was converted to a series of lines (D); as before, the scale is in µm and the bounding box of the coordinate system is shown by a dashed line, with the lines to cut shown as solid lines. Following PEN cutting and PDMS-PDMS moulding as shown in Figure 4.1(F), holes cored through the PDMS (arrows) connect the perfusion apparatus to the perfusion endpoints in the network (arrowheads), allowing entry and exit of liquid via the perfusion manifold on the back side of the PDMS. The PDMS mould was compressed against coverslip glass and perfused (E) with lissamine-rhodamine doped gelatin; scale bar is 1 mm.

SEM analysis of cut material (E,F) showed vertical striations along the cut edges, presumably a result of the UV laser pulses; their frequency appears to correlate with the laser pulse frequency. While these introduced a small element of roughness into the sample, these are tiny (µm) in comparison to the material cross-section ($50 \times 50\,\mu m^2$), and should be insignificant.

PDMS moulding

RTV and PDMS were mixed and cured as described in Section 2.9.4 using the perfusion jig parts shown in Section 2.9.3. An example network moulded using both glass and PDMS backing is shown in Figure 4.1(H–J). The template pattern is shown in (H), with (I) showing the result of moulding using PEN on glass backing with RTV polymer, and (J) showing PEN on PDMS backing with PDMS polymer. Using glass backing resulted in polymer running underneath the PEN template, resulting in damage to the moulded elastomer during PEN template removal following curing. This is seen by the presence of several tabs, as well as a multitude of small tears along the length of several of the microchannels. Conversely, PEN on PDMS backing completely eliminates the polymer underrun issue, showing only minute imperfections in the microchannels, due to either alignment issues during cutting, or physical handling of the PEN network with insect pins and fine forceps. An example of a PDMS network during and after moulding is shown in Figure 4.2(A) and (B).

PDMS network perfusion

Plasma sterilisation of PDMS permitted direct bonding to glass substrate under the following conditions: 0.75–1.0 keV, 16-60 mA, and 700–1000 mTorr as also described in Bhattacharya *et al.* (2005). However, this resulted in only weak bonding and would require further optimisation in order to achieve a strong seal capable of withstanding fluid pressure in the absence of additional compressive sealing. Note that due to PDMS being hydrophobic, plasma treatment or use of a block copolymer such as Pluronic F-127 is required in order to obtain filling of microfluidic channels with aqueous solutions and prevent adsorption of material (Golden and Tien, 2007; Tien and Chen, 2002).

To permit perfusion, the channel endpoints were connected to the manifold by punching holes all the way through the PDMS block, using a blunt 23 gauge needle to core out a hole, a common practice for microfluidic interconnects (Christensen *et al.*, 2005). The PDMS block containing the microfluidic network and held with its shim was placed on top of a coverslip glass located within the slide guides of Figure 2.7(A) or (B). The top plate (C) was used to secure the perfusion manifold (D) on top of this, and screws passing through the unthreaded top plate to threaded base plate were used to apply uniform compression to seal the PDMS to the coverslip glass.

Excessive compression resulted in the coverslip glass cracking; too little in leakage due to having a weak seal. Blunt 23 gauge needles passing through the perfusion manifold and into the previously punched holes in the PDMS block were used as a source and sink for perfusion.

Lissamine-rhodamine (Gurr, BDH) was used to dope gelatin to allow visualisation using brightfield or epifluorescence microscopy. Perfusion was carried out at 37 °C to ensure that the gelatin was in a molten state. Untreated PDMS is hydrophobic, so the channels were first blocked with Pluronic F-127 1 % (w/v) for 20 min, injected into the network using a 10 mL syringe connected to one of the needles, followed by injecting water to wash, and then molten doped gelatin. Perfusion was performed at a rate of $\sim 50\,\mu L/s$, using negative pressure to retain the PDMS–coverslip seal. It was found that positive pressure alone would tend to push the perfused fluid out of the microchannels and between the PDMS and coverslip glass, breaking the seal. The perfused network was subsequently imaged using a stereo microscope with a colour CCD camera. The process is illustrated in Figure 4.2(C–E), showing initial network design in vector and line form, followed by an image of the network perfused with doped gelatin, showing complete filling of the channels without air bubbles. In particular, note the uniform channel width at all points in the network, confirming the accuracy of the initial PEN template cutting.

4.2.2 HUVECs form complex networks when cultured in 3-D

HUVECs were seeded in 3-D collagen gels with or without the addition of factors known to induce endothelial tube formation. Monomeric rat tail collagen was neutralised with 0.8 M $NaHCO_3$, seeded with HUVECs at a density of 5×10^6 cells/mL, then gelled at 37 °C for 60 min in a glass-bottomed dish (Iwaki), having approximate dimensions of 1 mm thickness, 14 mm diameter. Control gels were covered with 4 mL ECGM and treatment gels were covered with 4 mL tube forming medium (ECGM supplemented with 40 ng/mL $hVEGF_{165}$, 40 ng/mL bFGF, 50 ng/mL PMA and 50 µg/mL sodium ascorbate).

Following incubation at 37 °C with 5% CO_2 for 48 hours, an interconnected network of tubes was visible in the treatment gels using brightfield microscopy, while control gels showed no such structures (Figure 4.3, top). Treated gels were also seen to have contracted compared with control gels. In order to more accurately visualise and quantify the formation of tubes, the gels were fixed in 4% PFA for 10 min then stained with mouse anti-human CD31 clone 10G9 with a goat anti-mouse-AF594 secondary, phalloidin-Atto647 and YO-PRO-1 (Figure 4.3, middle). Phalloidin labelled F-actin, while YO-PRO-1 labelled DNA.

Analysis of HUVECs grown on glass in two dimensions (2-D) showed that, compared with the control gel, tube forming conditions induced alignment of the cytoskeleton between cells, and upregulation of CD31 expression. However, induction

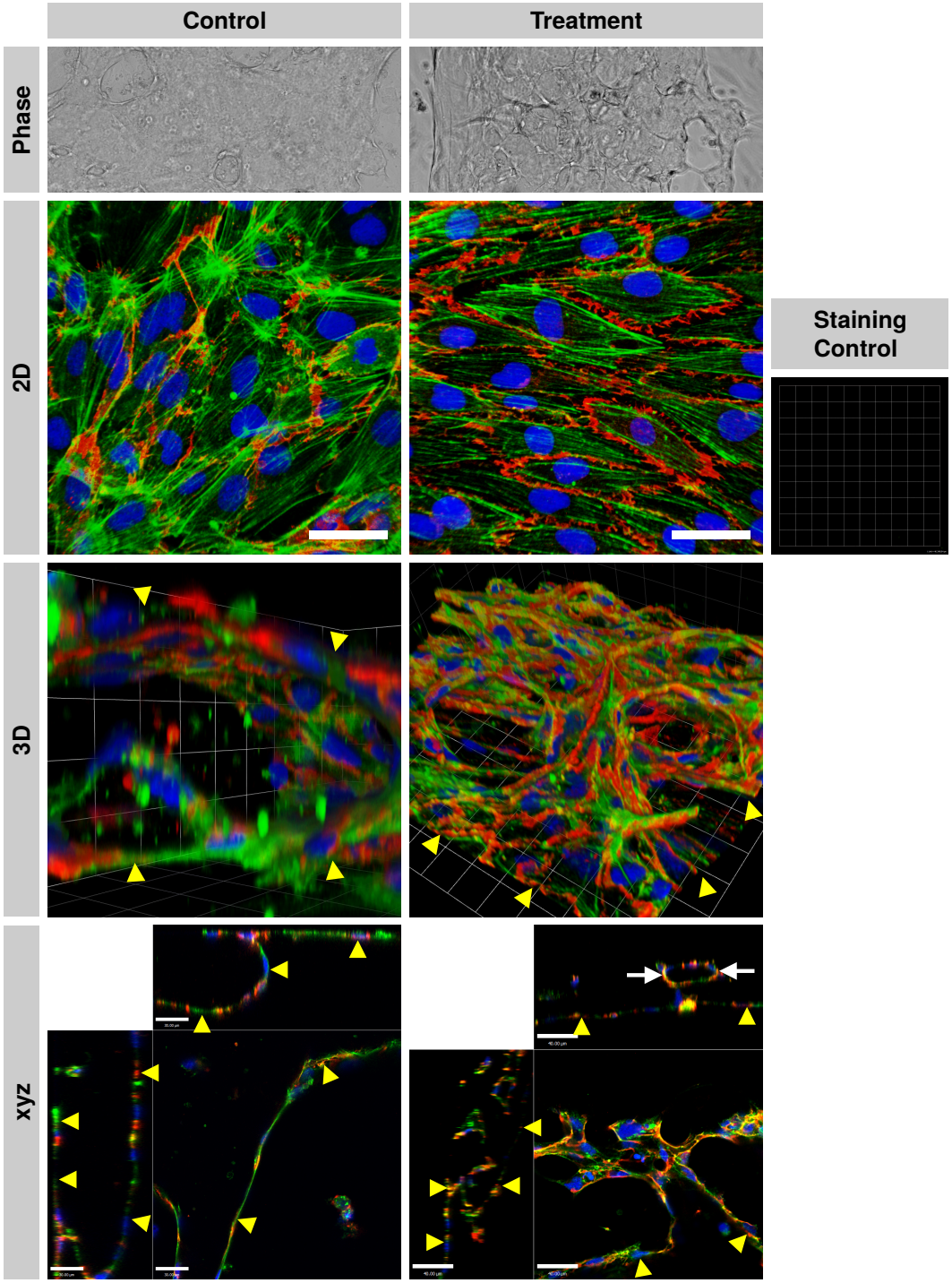

Figure 4.3: HUVEC tube formation with growth factors. HUVECs on glass in 2-D or in a collagen in 3-D were treated using using normal medium (control) or tube-forming medium (treatment). Brightfield imaging showed the presence of a capillary plexus-like structure, and greater matrix contraction and disruption in the treated gel. Cell nuclei are blue, CD31 is red and phalloidin (actin) is green. Growth of control cells in 2-D appears disorganised, and also in 3-D, as a disorganised 2-D monolayer on the surface of glass or collagen, the gel interior being devoid of cells. Treated cells have a common orientation and morphology in 2-D, with apparent upregulation of CD31, and in 3-D formed branched, interconnected cord-like structures running through the interior of the gel, similar to a capillary plexus *in vivo*. *xyz* projections of representative parts of the gels are shown below. Yellow arrowheads show the gel and glass surfaces, again showing an empty 2D gel interior (left side), and complex structures in the 3D gel interior are shown, with an open tube indicated with white arrows. 2D scale bar is 50 µm, 3D scale is 22.5 µm, *xyz* scale is 30 µm (2D) and 40 µm (3D).

of tube formation was not observed, cells having formed a confluent, aligned monolayer. HUVECs placed in collagen gels in the absence of the inducing conditions failed to form tubes; the gels were completely devoid of cells internally, though a 2-D monolayer was observed on all sides of the gel. Bright spots in the gel may be apoptotic blebs or fragments of dead cells. In contrast, the culture of HUVECs in 3-D collagen gels in the presence of inducing conditions lead to the formation of a dense 3-D network of branched, interconnected cord-like structures in the gel interior, and these gels also possessed a 2D monolayer on the gel surface. However, when observing the gel via xy and xz projections (Figure 4.3, bottom), it was not entirely clear if the tubular structures were infoldings of the collagen gel surface, or tubes in the interior. Some structures are clearly tubes, surrounded by collagen on all sides, whereas others are connected to the external surface. Tubes in 3-D had external diameters of 13–17 µm, while in 2-D cross-sections of larger flattened structures (arrows in figure) had diameters of 12–40 µm.

4.2.3 Scaling up HUVEC-seeded collagen gels

Work with HUVEC-seeded collagen gels had so far used glass-bottomed dishes with thin gels (≤ 1 mm thick) of large diameter (14 mm). In order to scale up the quantity of gels, which could then be used for several different treatments, with replicates, gels of 3 mm diameter, 3 mm thickness were created using the collagen culture plate shown in Figure 2.1(D).

HUVECs were seeded in collagen gels of varying concentration (0.75, 1.50, 2.25, 3.00, 3.75, 4.50, 5.25, and 6.00 mg/mL) with 5×10^6 HUVECs/mL for each concentration. These concentrations range span the practical concentration limits for collagen gels, from low density with little robustness to high density and almost solid. 30 µL aliquots (in triplicate for each concentration) were gelled in the support at 15 °C for 60 min. After the collagen was gelled, the gels were overlaid with 15 mL ECGM containing the same tube forming factors used in Section 4.2.2. The media was replaced every two days and the gels fixed with 4% PFA following 14 days of culture, observing tube formation daily by phase contrast microscopy. Some gels began visibly contracting after 2 days, with all contracted after 6 days. Lower density gels resulted in smaller gels following contraction.

Gels were stained overnight with CD31-AF488 at 1:200, 1:500 and 1:1000 dilutions, with control gels stained using block only, then imaged using a confocal microscope, shown in Figure 4.4(A,B). Only the 1:200 dilution is shown here; higher dilutions stained the same features, with 1:500 providing adequate staining, but 1:1000 losing some detail and requiring increased laser power to visualise adequately using confocal microscopy. As seen previously, a highly organised network composed of HUVECs formed following treatment with tube-forming factors. Imaging using second harmonics to visualise the collagen matrix showed that the network was in-

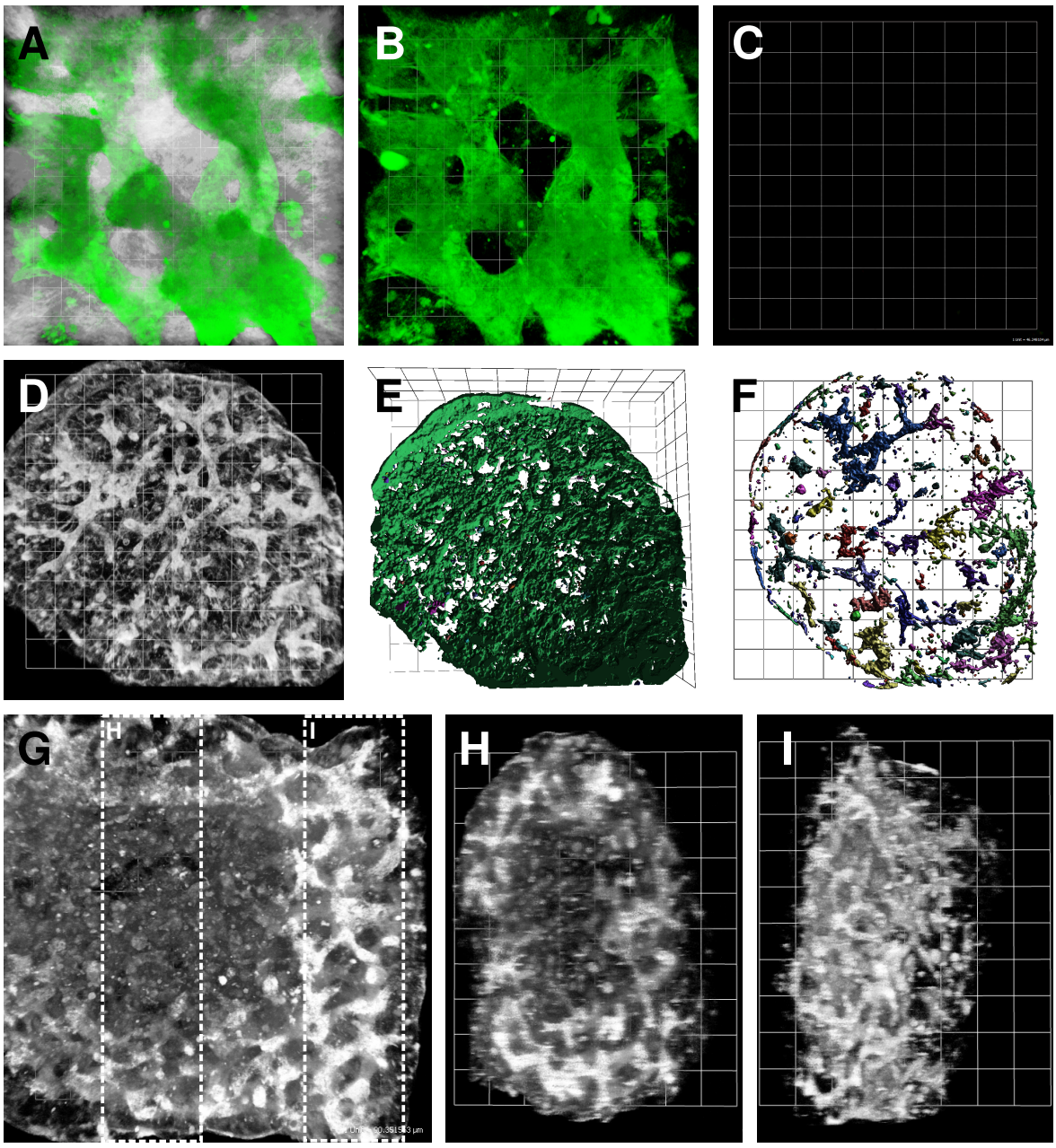

Figure 4.4: Thicker HUVEC gels. HUVECs seeded into 3 mm deep, 3 mm diameter collagen gels under tube-forming conditions form a highly organised network, seen with CD31 staining shown in green (A,B) and white (D,G–I); (C) is the staining control. The collagen extracellular matrix is clearly visible after condensation (A,B) with second harmonic generation showing collagen fibrils in white (A) and absent (B) with the HUVEC network ramifying through. After imaging an entire gel as a z-stack, a complex 3-D network is seen branching through the entire gel (D), shown converted to a single volume (E) or multiple volumes (F) for analysis using low and high intensity thresholds, respectively. When the gel interiors are examined by cropping half the z-stack (G), it is seen that the tubes surround an apparently necrotic central core, marked sections shown in cross-section in (H) showing necrosis in the centre and (I) showing no necrosis near the edge. Scales are 22.6 µm (A,B), 46.3 µm (C) and 90.3 µm (C–H).

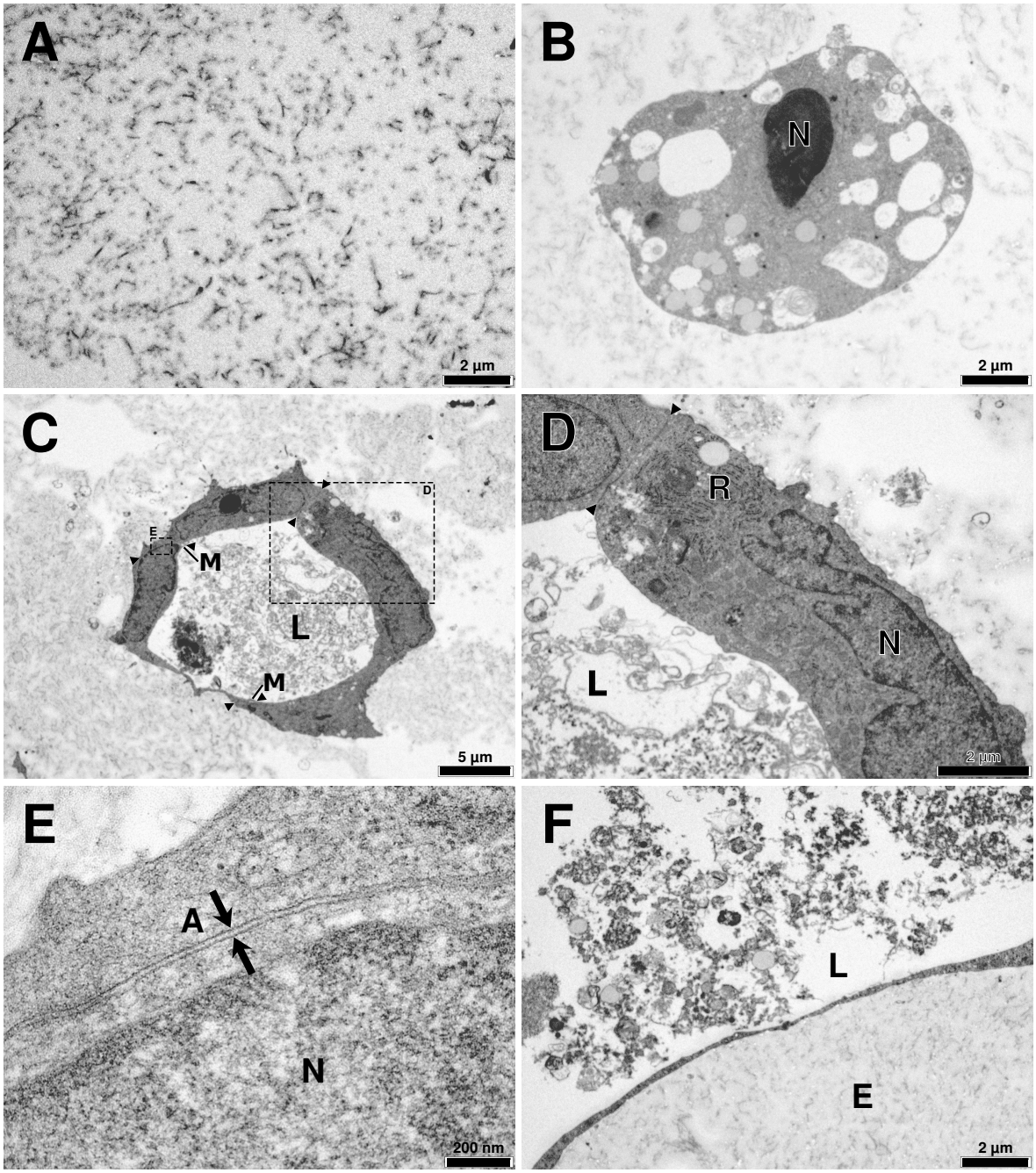

Figure 4.5: HUVEC tube formation by TEM. HUVECs seeded in a collagen matrix were grown in the absence (A, B) and presence (C-E) of tube-forming conditions. Collagen fibrils formed the majority of control gels without growth factors (A), with a very low frequency of single cells (B). Gels containing growth factors resulted in the formation of tube-like structures containing open lumens, surrounded by collagen extracellular matrix; a representative example is shown in (C), with magnified views of cell–cell junctions shown in (D) and (E). (C) is a putative vessel composed of three separate endothelial cells, the adherens junctions of which are marked with arrowheads. The lumenal ends of one of these junctions is marked by a small cytoplasmic protrusion (M), which may be a marginal fold. (D) is a magnification of the top adherens junction in (C), in close proximity to rough endoplasmic reticulum (R). (E) is a high magnification of the left adherens junction in (C); the adherens junction (A) is seen as two electron-dense bands marked with arrows. The difference in composition of lumenal contents and extracellular matrix are shown in (E). Major marked features include ECM (E), vessel lumen (L), and nucleus (N).

timately associated with the matrix, it being surrounded by a very dense collagen meshwork at all points, the matrix having been condensed to this point during culture from the initial low density, loose composition. However, the tubes in the network stained uniformly across their cross-section; lumens were not visible using confocal microscopy.

Due to the dense collagen preventing imaging at depth using MP microscopy, the gels were subsequently dehydrated and cleared, then re-imaged using the same microscope with a 10× air objective and single-photon confocal microscopy. Figure 4.4(D) shows a representative sample, containing a large network under the surface of the gel extending into the gel interior. Analysis was complicated by the presence of a confluent 2D monolayer on the gel surface; these cell-cell junctions show bright CD31 staining, seen as thin lines in the image. Measurement of the external tube diameters within the network showed the tubes to be 25 µm at their narrowest points, extending up to 50 µm at junctions. Volocity was used to segment the network to different extents using different intensity thresholds, shown in Figures 4.4(E) and (F). Setting a higher threshold prevented selection of the 2D layer and other features not of interest, but this was too crude a method for truly quantitative analysis. Volocity is capable of skeletonising a volume to a one voxel thick line, which *would* be usable as a basis for quantifying branch point and distance between branches, but the program does not make this information available to the user. Volocity was therefore not capable of performing the sophisticated analysis required. Further study of HUVEC network formation showed frequent occurrence of what appeared to be a central core devoid of endothelial tubes, but containing small punctate CD31 stained bodies, shown in Figure 4.4(G–I), which are possibly apoptotic blebs or cellular fragments resulting from necrosis.

4.2.4 HUVEC networks contain open lumens

The experiment described in Section 4.2.2 was repeated, creating 3 mm diameter, 3 mm thick gels using the collagen culture plate shown in Figure 2.1(D). Collagen was neutralised with 0.8 M $NaHCO_3$ and seeded with HUVECs at a density of 5×10^6 cells/mL, transferred in 20 µL aliquots into the wells, then gelled at 15 °C for 120 min. After the collagen was gelled, control gels were overlaid with 100 µL ECGM and treatment gels were covered with 100 µL tube forming medium (ECGM supplemented with 40 ng/mL $hVEGF_{165}$, 40 ng/mL bFGF, 50 ng/mL PMA, 50 µg/mL sodium ascorbate), and 1 % (v/v) penicillin/streptomycin.

Following culture for 48 hours, gels were visibly condensed, particularly under tube forming conditions. Samples were fixed and processed for TEM as described in Section 2.6.8. TEM of HUVEC networks was performed using thin sections of gels with and without the addition of growth factors (Figure 4.5). In all gels, the fibrils comprising the collagen extracellular matrix were clearly visible, shown in high

contrast in (A). No tube formation was seen in control gels (B), where cells are only seen as single rounded cells containing numerous micron-scale bodies, with no evidence of multicellular structure or lumen formation. The growth factor-treated gels showed the development of vessel-like structures, composed of several endothelial cells surrounding a central lumen (C). Control cells had a diameter of 8–10 µm, while treated cells were mainly 2.5-3.5 µm wide, 5 µm maximum and were approximately 15, 20, and 25 µm long each with a rounded rounded to flattened appearance. The lumen diameter was 13–16 µm, with the external vessel diameter being 20–25 µm. Collagen matrix surrounded the structures, and is distinctly different in composition that of the central lumen (F), which appears to be a void space free of matrix material, containing membranous debris. Examination of cell–cell junctions showed evidence of adherens junction formation (D,E). Additionally, cytoplasm at the ends of two of the junctions extends into the lumen; these processes may be marginal folds (Young and Heath, 2000). In (D), numerous vesicles are outlined between the lumen and nucleus.

4.2.5 Mouse aortic smooth muscle expresses NG2

Utilising the temperature-sensitive VSMC line, it was initially determined that the primary culture derived from mouse aorta expressed vascular smooth muscle markers.

VSMC were blocked with 1 % goat serum in PBS prior to staining with 1:400 rabbit anti-mouse NG2, 1:400 rabbit anti-mouse LYVE-1 (isotype) or no antibody, and then washed and stained with 1:500 goat anti-rabbit AF488. The cells were then run on a CyAn ADP flow cytometer (Dako Cytomation), with the results shown in Figure 4.6. Compared with the isotype control, over 90 % of the cells are $NG2^+$. However, a smaller population (under 10 %) is $NG2^-$.

The $NG2^+$ cells were sorted on a MoFlo cell sorter (Dako Cytomation) set to purify in single-cell mode in order to remove all of the $NG2^-$ cells; doublet discrimination was used as a matter of routine (data not shown). However, the $NG2^-$ cells were not removed from the culture. It appears that these cells are not a contaminating population—they differentiate from the $NG2^+$ population and are morphologically distinct in culture; the sorted population gained an increasing number of these morphologically distinct cells over time, demonstrating that their origin must be from the $NG2^+$ population; they are not a separate, contaminating population.

4.2.6 Co-culture of HUVEC and mouse aortic smooth muscle

Monomeric rat tail collagen was neutralised with 0.8 M $NaHCO_3$ and seeded with cells as follows: (A) collagen gel containing no cells overlaid with media containing 3×10^6 HUVECs/mL, (B) collagen gel containing 3×10^6 VSMCs/mL overlaid

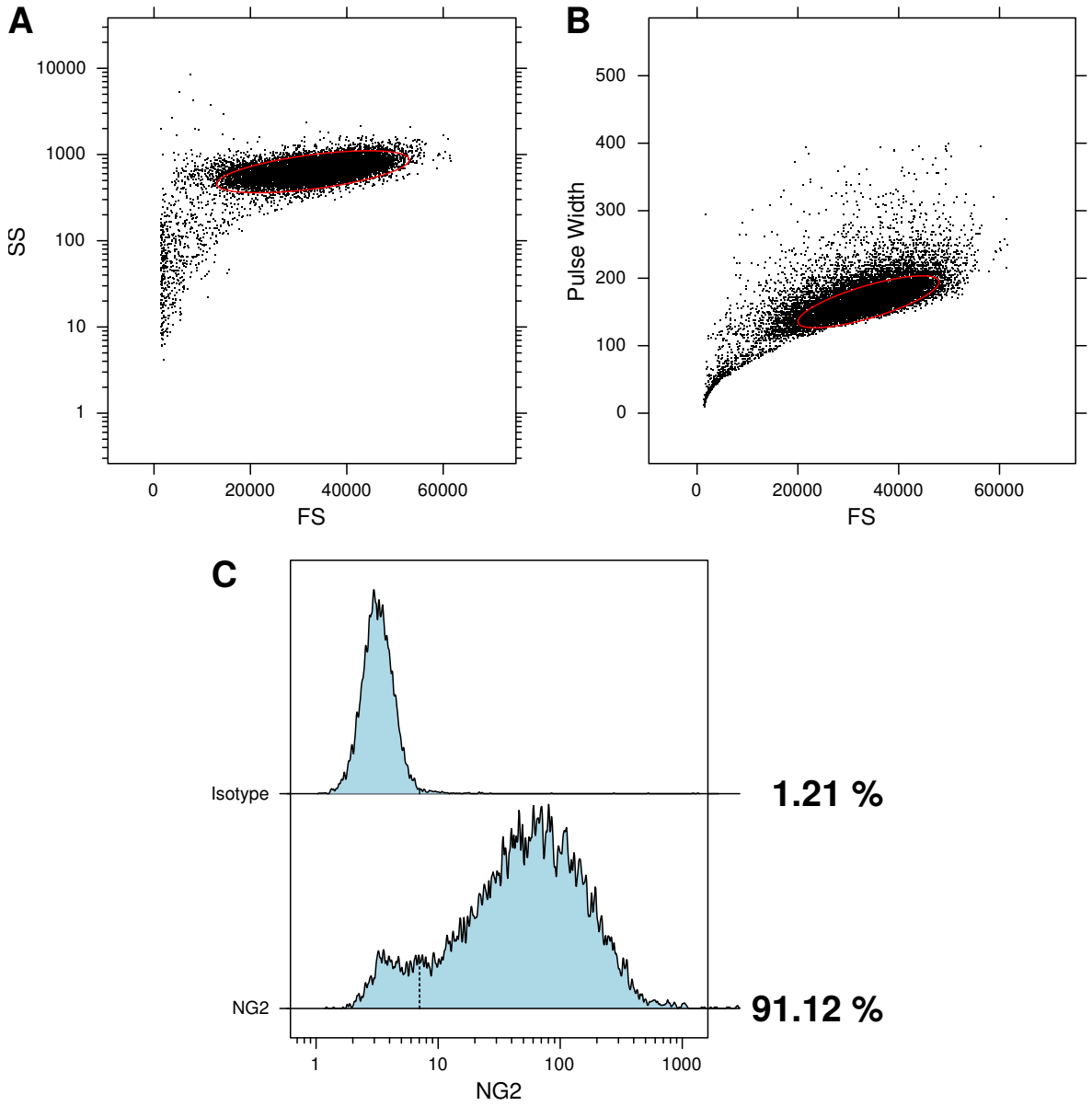

Figure 4.6: VSMC expression of NG2. Primary vascular smooth muscle derived from mouse aorta was stained with anti-NG2 antibody and compared with an isotype control. Cells were selected by gating on the population of cells in forward- and side-scatter (A) and doublets removed using the singlet population in forward-scatter and pulse-width (B). The gated populations for each treatment are shown in (C). The positive populations were selected using a 99 % one-tailed confidence interval on the isotype control, shown as a dashed line.

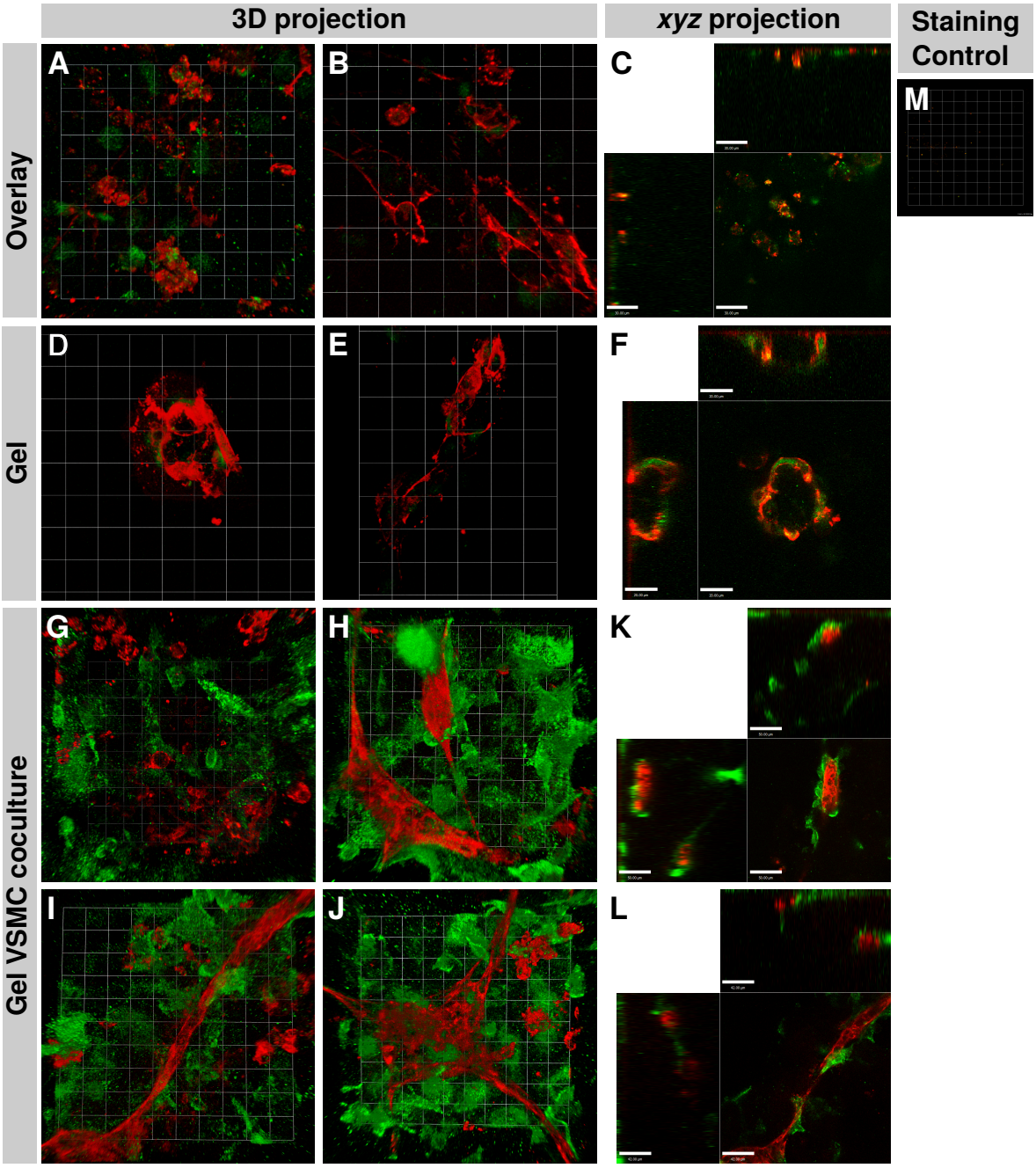

Figure 4.7: HUVEC-VSMC coculture, following five days of culture. CD31 (red) marks HUVECs, while NG2 (green) marks VSMCs. Collagen gels were created containing: no cells, overlaid with HUVECs (overlay), HUVECs only (gel) and VSMCs, overlaid with HUVECs (gel VSMC coculture). Empty gels overlaid with HUVECs contained only few cells, which did not form organised structures; cells are mostly confined to the surface (A–C). Gels containing HUVECs were again sparsely-populated; the examples shown here show instances of cells inside the gel, which have not formed organised structures (D–E). (A) and (D) are shown in cross-section in (C) and (F), respectively. Gels containing VSMCs overlaid with HUVECs were mostly contained little structure (G). However, discrete areas showed evidence of cord- or tube-formation and self-organisation at low frequency (H–J); H and I are shown in cross-section in (K) and (L), respectively. HUVECs have formed the tube-like structure seen crossing from the bottom-left to the top-right, while VSMCs are seen in close association with it (I). VSMCs are also seen in intimate contact with the presumptive tubes in (H) and (J), shown clearly wrapping around the tube in (K,L). (M) is the staining control. Scales are 22.5 µm (A,B,D,G–J) 20 µm (C), 29.0 µm (E), 30.0 µm (F), 50 µm (K), 29.0 µm (L) and 46.0 µm (M).

with media containing 3×10^6 HUVECs/mL and (C) collagen gel containing 3×10^6 HUVECs/mL and overlaid with media containing no cells. The seeding densities are with respect to the volume of the collagen gel (100 µL). Collagen was diluted in 1:1 ECGM:VSMC medium (HUVEC-seeded gels) or VSMC medium (VSMC-seeded gels). After setting in glass-bottomed dishes at 37 °C for 30 min, the gels were overlaid with a 1:1 mixture of HUVEC:VSMC media, containing cells as described.

Following incubation at 37 °C with 5% CO_2 for 5 days, the gels were fixed in 4% PFA for 10 min and stained with mouse anti-human CD31 with a goat anti-mouse-AF594 secondary, rabbit anti-mouse NG2 with a goat anti-rabbit-AF488 secondary, and phalloidin-Atto647 (not shown). Spontaneous formation of tube-like structures in HUVECs was only observed in treatment B, shown in Figure 4.7 (G–L), the only treatment in which both HUVECs and VSMCs could interact with each other. While formation of tube-like structures was seen, this occurred only at low frequency, and formation of larger-scale networks as seen with growth factor treatments was not observed.

HUVECs overlaid on an empty collagen gel grew in 2D on the surface of the gel. This is shown by the characteristic cuboid morphology seen in Figure 4.7(B) with CD31 staining localised to the cell borders. There were no cells located within the gel. Green staining is autofluorescence; there are no $NG2^+$ cells in (A–F). When embedded into the gel, HUVECs were not found within the gel in great numbers; Figure 4.7(D) shows some aggregation of cells, but possessing little structure. Note that looking at xz or yz projections shows these to be invaginations of the collagen surface; these cells are not actually inside the gel. The same is true of the cells in (E). The green autofluorescence in all samples appeared to be cell nuclei on cells adherent to the collagen surface, between the collagen and the coverslip; in the co-culture sample, the larger and brighter green objects are smooth muscle. In coculture samples (H–J), tube-like structures composed of endothelial cells were seen to run through the gel interior, with 2-D projections (K,L) demonstrating their intimate association with VSMCs, which directly contact and encircle the tubular structures with high frequency, while not providing complete coverage. However, only a minority of HUVECs formed tube-like structures, with the majority (G) remaining disorganised.

4.2.7 Differentiation of smooth muscle from C3H/10T½

Similarly to VSMC, it was determined that C3H/10T½ cells express the pericyte marker NG2. Unlike VSMC, which were fully differentiated into smooth muscle, C3H/10T½ are multipotent. TGF-β_1 was therefore used to induce differentiation into smooth muscle. C3H/10T½ were seeded on 6 well plates (Nunc) and glass-bottomed dishes (Iwaki) and covered in medium containing 0, 1.5, 3.0 or 6.0 ng/mL TGF-β_1 from a 50 µg/mL stock. Following three days of culture, the cells on glass-

bottomed dishes were 4% PFA fixed for 20 min, and the cells on plates recovered and stained for flow analysis.

C3H/10T½ were blocked with 0.3 % BSA in PBS prior to staining with 1:300 rabbit anti-mouse NG2, 1:300 rabbit anti-mouse LYVE-1 (isotype) or no antibody, and then washed and stained with 1:500 goat anti-rabbit AF488 and 1:5000 DAPI (5 mg/mL stock). The cells were then run on a CyAn ADP flow cytometer (Dako Cytomation), with the results shown in Figure 4.8. Compared with the isotype control, the entire population of C3H/10T½ is $NG2^+$ irrespective of the TGF-β_1 concentration used. The median NG2 expression is slightly higher for the untreated sample than for the three treated samples.

Cells on glass-bottomed dishes were blocked with 3% goat serum and stained with 1:300 α-SMA-Cy3 or 1:300 NG2 with 1:500 goat anti-rabbit AF594 followed with 1:1000 YO-PRO-1 (one hour per step, excluding washes). The results are shown in Figure 4.9. C3H/10T½ cells express the pericyte marker NG2 whether or not stimulated to differentiate with TGF-β_1. Likewise, α-SMA is expressed whether or not the cells are treated with TGF-β_1. However, while the intensity of NG2 and α-SMA staining did not change appreciably between control and treated samples, the cell morphology and actin cytoskeleton organisation changed dramatically upon treatment (Figure 4.9). Untreated cells possessed a fibroblastic morphology and random orientation, while treated cells adopt an elongated morphology with both the cells and actin cytoskeleton aligned in a uniform orientation, consistent with smooth muscle organisation.

4.2.8 Co-culture of HUVEC and C3H/10T½

Cells were co-cultured as follows:
(A) 5×10^6 HUVECs/mL with 1×10^6 C3H/10T½/mL (5:1),
(B) 5×10^6 HUVECs/mL with 5×10^5 C3H/10T½/mL (10:1),
(C) 5×10^6 HUVECs/mL with 2.5×10^5 C3H/10T½/mL (20:1),
(D) 5×10^6 HUVECs/mL only, and
(E) 5×10^5 C3H/10T½/mL only.
Each treatment was repeated in triplicate. C3H/10T½ were differentiated to a smooth muscle fate using 3 ng/mL human recombinant TGF-β_1 for 24 hours prior to use. Gels of 3 mm diameter, 3 mm thickness were created using the collagen culture plate shown in Figure 2.1(A). Collagen was neutralised with 0.8 M $NaHCO_3$ and seeded with cells at the above concentrations, transferred in 30 µL aliquots into the wells, then gelled at 15 °C for 60 min. After the collagen was gelled, the gels were overlaid with 15 mL ECGM.

Following 20 days of culture, monitoring progress of tube formation and changes in cell organisation via phase contrast microscopy, the gels were fixed in 4% PFA for 75 min, then washed twice in PBS and stored at 4 °C. The gels were transferred

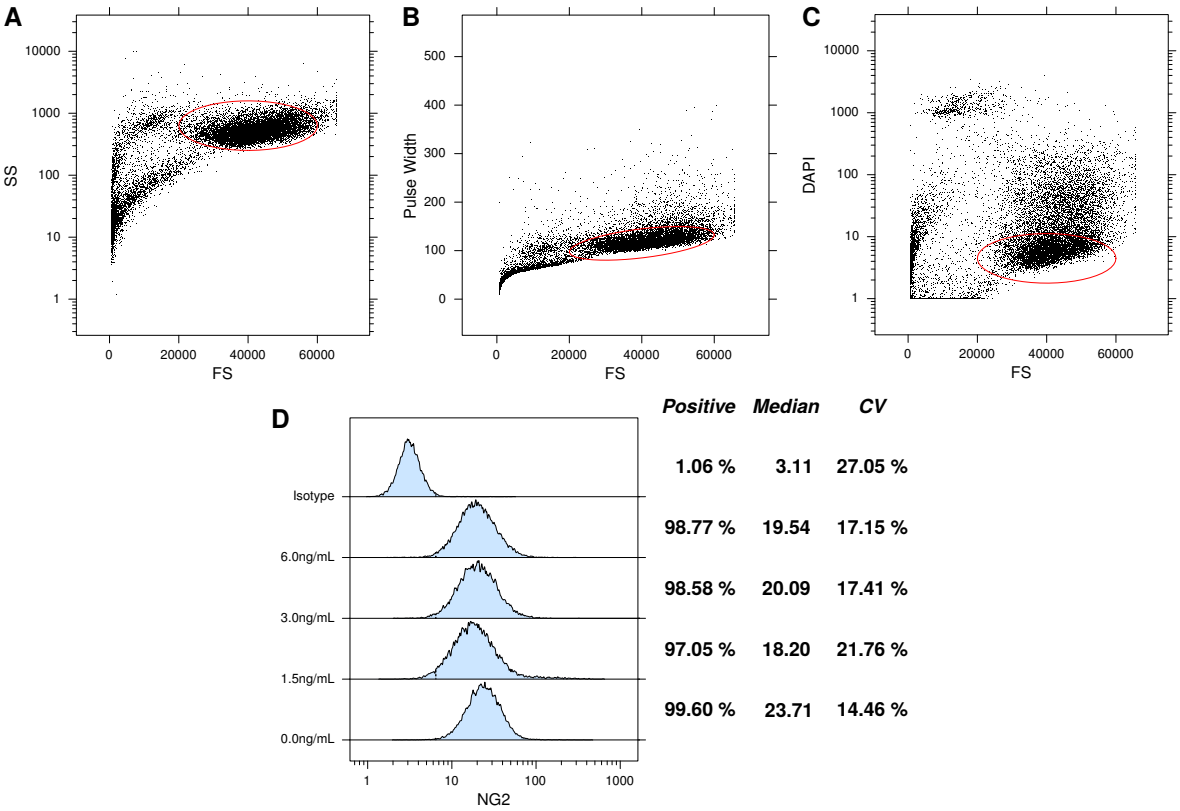

Figure 4.8: C3H/10T½ expression of NG2. C3H/10T½ cells were treated with increasing concentrations of TGF-β_1. Cells were selected by gating on the population of cells in forward- and side-scatter (A), doublets removed using the singlet population in forward-scatter and pulse-width (B), and live cells selected using the nuclear stain DAPI (C). The NG2 expression of the gated populations for each treatment are shown in (D). The positive populations were selected using a 99 % one-tailed confidence interval on the isotype control, shown as a dashed line. All C3H/10T½ treatments express similar levels of NG2, irrespective of the concentration of TGF-β_1 used.

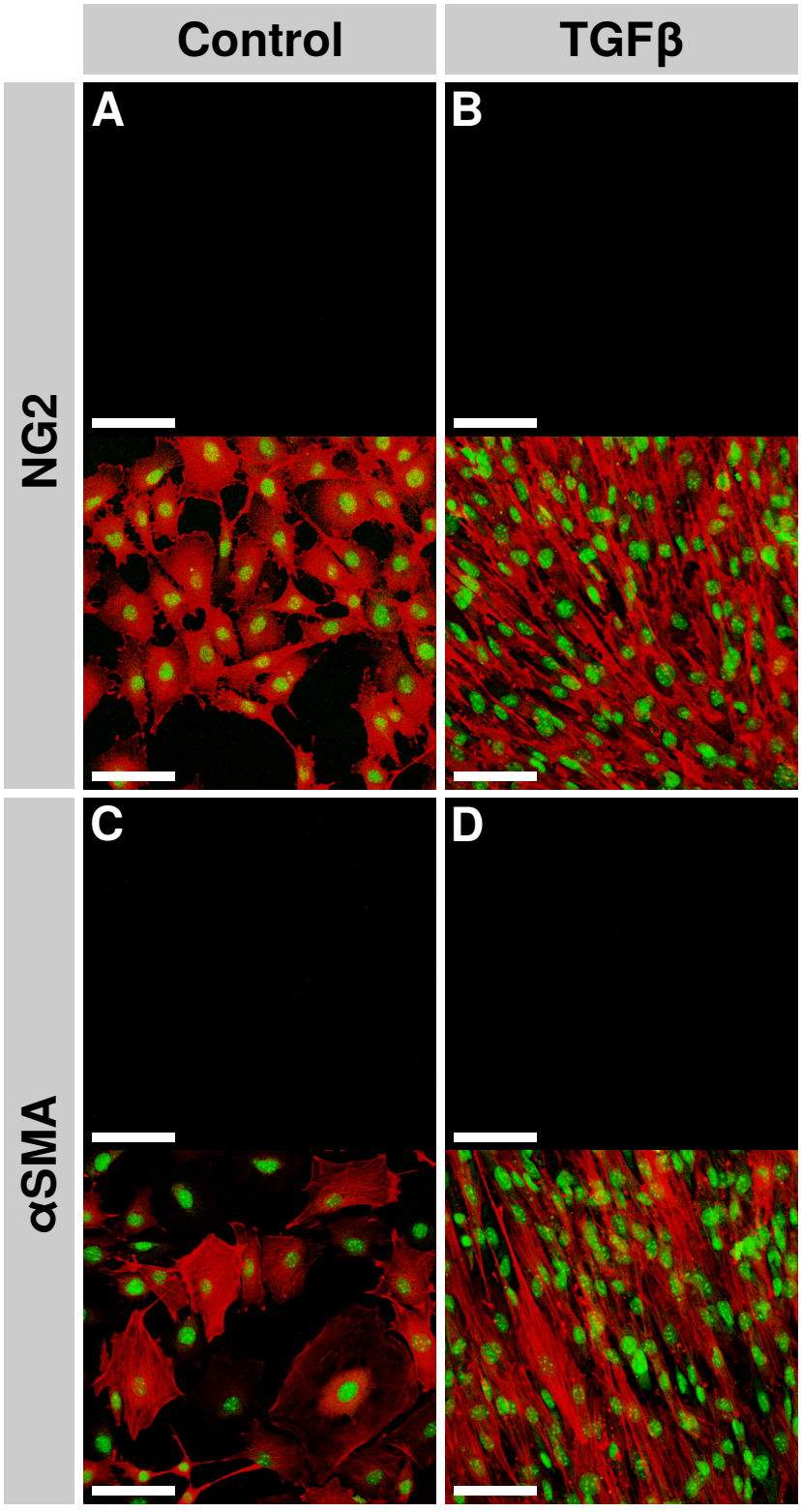

Figure 4.9: Differentiation of smooth muscle from C3H/10T½ cells. For each treatment and differentiation marker, the staining controls and stained samples are shown in the top and bottom images, respectively. The staining intensity of the smooth muscle markers NG2 (A,B) and α-SMA (C,D) did not change significantly between control and TGF-β_1-treated cells. However the morphology of the cells changes dramatically when treated with TGF-β_1. Treated cells change from being randomly organised (A,C) to having an elongated morphology and uniform orientation with a highly organised cytoskeleton (B,D). Scale bars are 100 µm.

to a 96 well plate (Nunc) prior to staining using the protocol detailed in Section 2.6.3. HUVEC-only gels were stained with 1:500 CD31-AF488 (mouse), while all the other gels were stained with 1:500 CD31-AF488 (mouse), 1:500 NG2 (rabbit), then stained with 1:500 goat anti-rabbit-AF647 and 1:1000 α-SMA-Cy3. One set of gels was stained with secondary antibodies only (1:500 goat anti-rabbit-AF647). The stained gels were dehydrated and cleared prior to imaging, as described in Section 2.6.2.

The results are shown in Figure 4.10. Only the gels from treatments C and E, plus staining controls, survived intact for imaging; the other gels were lost during staining or during dehydration and clearing. The dimensions of the images may be slightly smaller than expected due to a degree of gel shrinkage during dehydration. The control image (A) showed residual autofluorescence and non-specific staining in the co-culture gel when stained with secondary antibodies only. In the stained co-culture gel (B), branched tube-like structures were seen in the gel interior, which appeared to be similar to those seen in Figure 4.3, but as in this figure, it is not clear if these were vessels or mere aggregations of cells. These structures appeared to have smooth-muscle-like coverage with C3H/10T½, which were seen to encircle and follow the tube-like structures ramifying through the gel. C3H/10T½ only gels (C) showed the formation of a rather different, stromal-like, network which was not seen in the co-culture gels. It also showed that the TGF-β_1-differentiation may result in a heterogeneous population of smooth muscle cells, as seen by the variation in α-SMA and NG2 expression. While all of the cells were NG2$^+$, a small proportion were seen to have relatively higher levels of α-SMA.

4.2.9 Fluorescent labelling of HUVECs and C3H/10T½ for real-time imaging

Amaxa and Neon transfection

HUVECs at passage 6 (P6) were transfected with the plasmid pMAX-GFP using the Neon transfection system (Invitrogen). Using 1×10^5 cells per transfection. The cells were washed in PBS, spun down, and resuspended in 95 µL transfection buffer and 5 µL plasmid (1 µg/µL). The cells were transfected using the settings shown in Figure 4.11. Transfected cells were immediately transferred to a 24 well plate (Nunc) containing antibiotic-free ECGM. The transfection efficiency and cell death as a result of transfection were assessed by flow cytometry, shown in Figure 4.11. This showed the optimal protocol (1400 V, 30 ms pulse width) resulted in about 60 % of the cells being both live and expressing GFP. In general, it appeared that a higher voltage and short pulse width were optimal. When keeping the pulse width constant, a higher voltage gave a higher transfection efficiency, though at the expense of slightly more cell death.

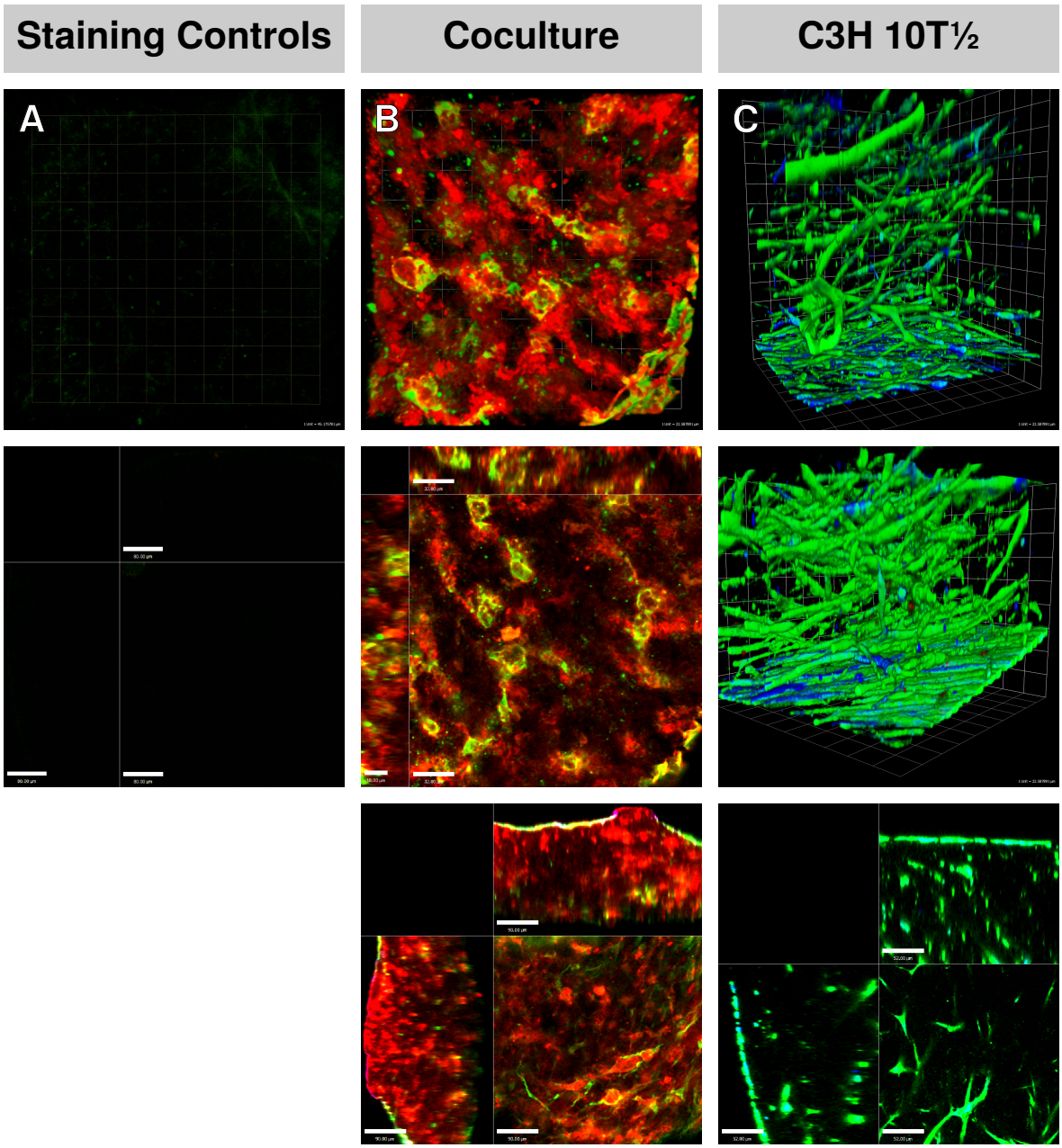

Figure 4.10: HUVEC-C3H/10T½ collagen spheroid coculture, following 20 days of culture. Cocultures were stained with anti-CD31 directly conjugated to AF488 (red), α-SMA-Cy3 (green) and NG2 with AF647 secondary (blue). Staining controls containing HUVECs and C3H/10T½ were stained with secondary antibodies only, showing autofluorescence intrinsic to the sample. HUVECs and C3H/10T½ coculture (20:1 ratio) showed formation of endothelial tubes which are seen in several cases to be encircled by, or in immediate contact with, smooth muscle, shown as a projection and 2D slices (top and middle, respectively). The bottom image shows a separate gel where most HUVECs have not formed tubes, are are rounded, but individual cells are encircled by or in contact with C3H/10T½ and are not rounded. In control gels containing C3H/10T½ cells only, highly directional organised networks are created on the gel surface (bottom of images) and organised networks are also present in the gel interior (top and centre of images). Not all C3H/10T½ cells are physiologically similar; some express high levels of α-SMA and NG2 (cyan) while others express mainly NG2 (blue). Scale bars are (A) 45 µm and 80 µm, (B) 22.6 µm, 32 µm and 90 µm and (C) 22.6 µm (top and middle) and 52 µm (bottom).

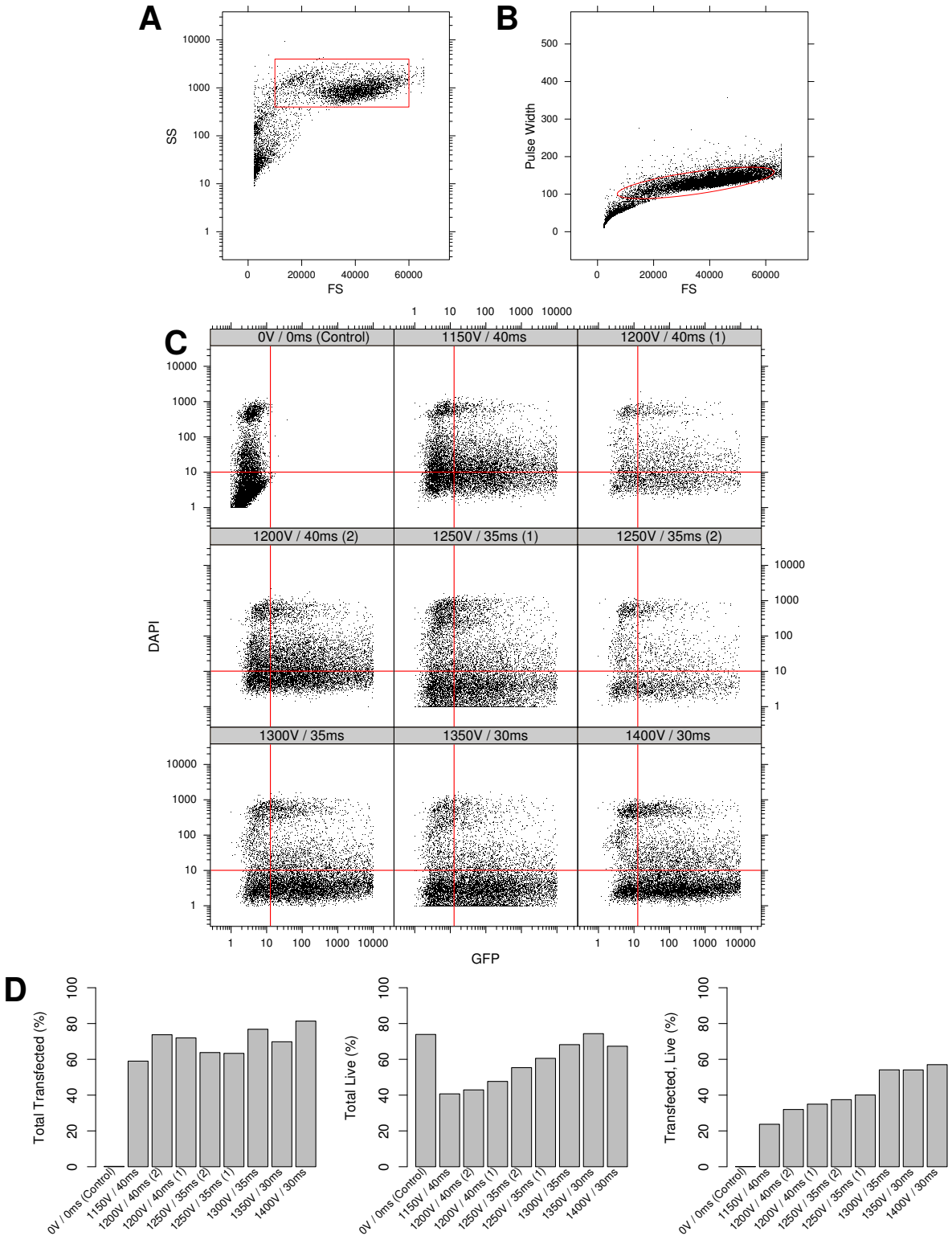

Figure 4.11: HUVEC transfection with Neon system. HUVECs transfected with GFP were analysed by flow cytometry using a range of different parameters. Cells were selected using an FS/SS plot (A) and doublets removed using FS/pulse width (B). Cells were assessed (C) for GFP expression and DAPI uptake (live/dead). Parameters are voltage (V) and pulse duration (ms), applied in a single pulse. Summary statistics are shown in (D), detailing transfection efficiency by means of the percentage transfected, percentage live and the percentage both transfected and live.

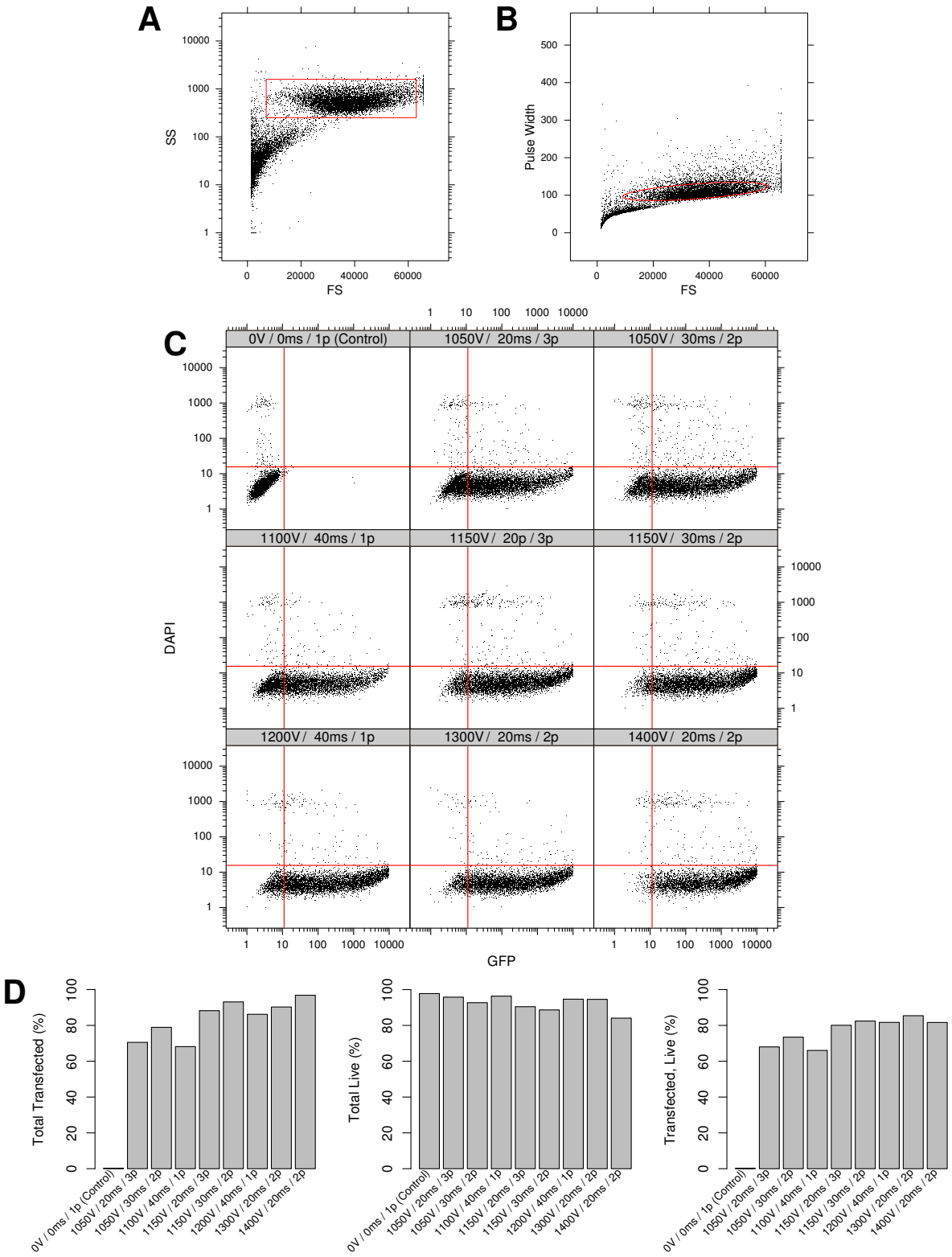

Figure 4.12: C3H/10T½ transfection with Neon system. C3H/10T½ transfected with GFP were analysed by flow cytometry using a range of different parameters. Cells were selected using an FS/SS plot (A) and doublets removed using FS/pulse width (B). Cells were assessed (C) for GFP expression and DAPI uptake (live/dead). Parameters are voltage (V), pulse duration (ms) and number of pulses (p). Summary statistics are shown in (D), detailing transfection efficiency by means of the percentage transfected, percentage live and the percentage both transfected and live.

C3H/10T½ cells were also transfected using the Neon system (Figure 4.12), showing much less cell death and higher transfection efficiency compared with HUVECs, having over 80 % live and transfected when using 1300 V, 20 ms pulse width and two pulses. Unlike HUVECs, which are far more limited in their potential for long-term culture, it was possible to transfect with cyan, citrine, tomato and dsRed fluorescent proteins inserted into a pCMV6-neo plasmid, using G418 to select for stable integration. HUVECs, in contrast, can not realistically be taken through sufficient passages to achieve stable integration and then subsequently be used for experiments. Without selecting for integration, fluorescence rapidly declines, due to dilution of plasmid during division, as well as loss or silencing.

In addition to the Neon system, the Amaxa system (Lonza) was used to transfect both HUVECs and C3H/10T½ with fluorescent proteins, using specific kits for HUVECs and smooth muscle, but was not as efficient as the Neon system, while being considerably more efficient than Lipofectamine (Invitrogen). Overall, Neon transfection appeared to cause far less damage to the cells and also achieved the highest transfection efficiencies.

Adenovirus transduction

HUVECs at P6 were transduced with GFP-adenovirus at an multiplicity of infection (MOI) of 0, 1, 10, 100 and 500. Flow analysis, shown in Figure 4.13(C), showed that an MOI of 1 resulted in 62 % expressing GFP at a low level, while an MOI of 10 resulted in 97 % expressing GFP, and an MOI of 100 99.8 %. An MOI of 500 resulted in the death of all cells. GFP intensity increased by approximately one order of magnitude as the MOI increased by an order of magnitude, showing a roughly linear relationship between viral transduction and the resulting GFP fluorescence.

HUVECs were subsequently transfected at P6 with an MOI of 100, and expression of GFP determined 24 hours later, and subsequently every 48 hours after passage at P7 and P8, shown in Figure 4.13(D). This showed high initial transduction efficiency, with GFP expression peaking at P8, though there is a shift in GFP fluorescence relative to the untransduced control which may have resulted in an artificially high percentage for this passage; it may, in fact be less than P7 when taking the peaks into account. By P9, GFP fluorescence is almost entirely absent, with most cells only having a very low level of GFP expression.

CFSE labelling

HUVECs were labelled with CFSE using M199 medium as the labelling buffer as described in Section 2.1.5. The cells were spun down and resuspended in neutralised collagen as described in Section 4.2.4 and were set in the matrix support slide with integral well shown in Figure 2.1(C). The gels were overlaid with tube forming medium, again as described in Section 4.2.4. Initial timelapse imaging to a depth of

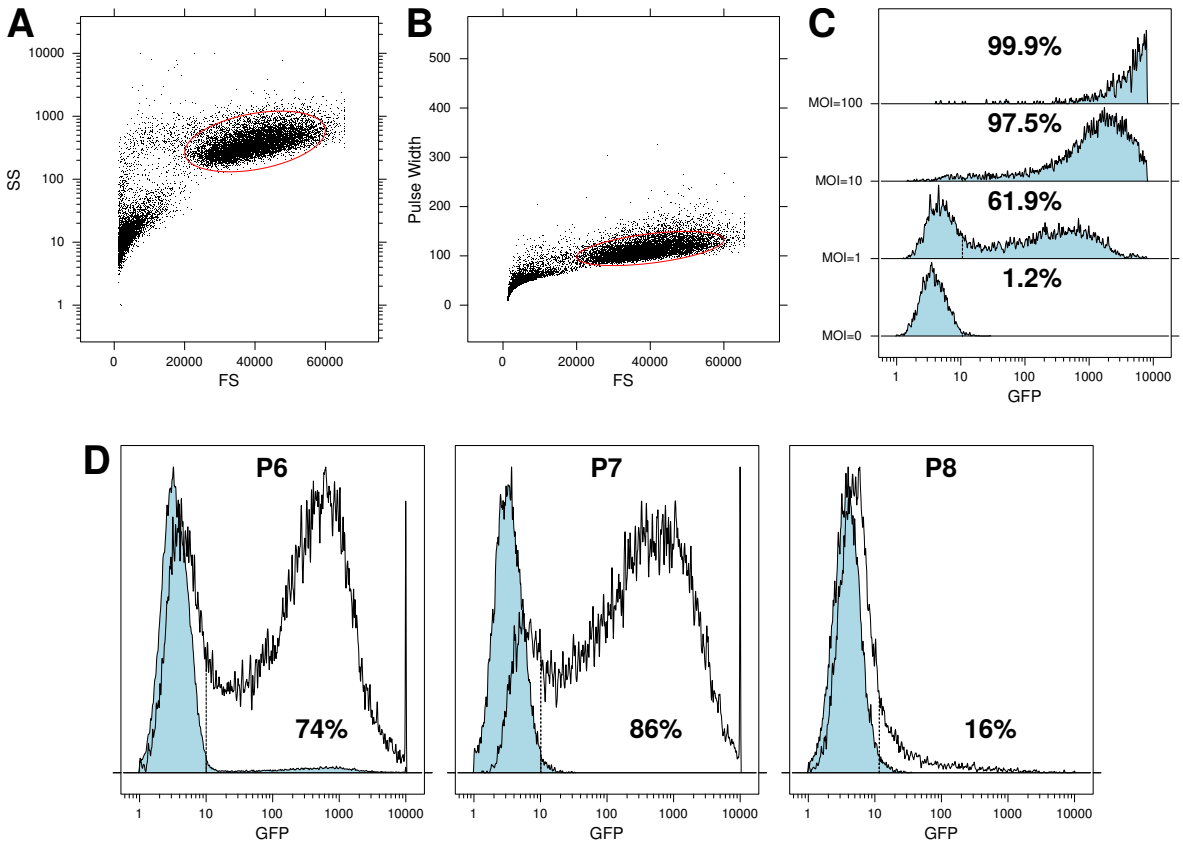

Figure 4.13: HUVEC transduction with adenovirus. HUVECs transduced to express adenovirus with GFP-adenovirus were assessed each passage (every 48 hours) post-transduction to assess the level of GFP expression. Cells were selected using FS/SS (A) and doublets removed using FS/pulse width (B). The effects of changing the MOI are shown in (C) with higher MOI resulting in higher GFP expression; at higher MOI, the GFP expression is so bright it exceeds the dynamic range of the instrument, and is clipped at 10000. The expression of GFP over time post-transduction with an MOI of 100, in comparison with an untransduced control of the same passage, is shown in (D). Expression 24 h post-transduction at P7 is high, but peaks at P8. However, by P9 expression levels dropped dramatically.

250 µm on a multiphoton microscope showed no evidence of either cell movement or tube formation. However, when repeated in triplicate using the matrix support in Figure 2.1(D) with both unlabelled and labelled HUVECs and with normal and tube forming medium (*i.e.* four combinations), after two days the unlabelled cells had contracted their collagen matrix, in particular under tube forming conditions, while the CFSE-labelled cells had not. The CFSE-labelled cells are shown in Figure 4.14, while the unlabelled cells were used for TEM, shown previously in Figure 4.5. As seen previously, the control gels showed HUVECs only as single cells, with no outgrowth or tube formation. Tube forming medium did not induce much tube outgrowth, with the majority of the cells in the gel existing as single cells, some visibly apoptotic. However, a very small number of cells in the gel did exhibit some evidence of tube outgrowth.

4.2.10 Spheroid models are an alternative to seeded collagen gels

Collagen spheroids were created by seeding 1×10^4 cells in 1 µL collagen drops on the surface of Petri dishes, gelling at 4 °C for 1 hour and then overlaying with medium. Small spheroids formed following two days of culture contracting the gel to a very small volume, shown in Figure 4.15(A). However, the spheroids are much larger than their methylcellulose counterparts (see below), their shape is less consistent, and they can stick to each other upon contact. Each spheroid also used a very large quantity of cells, making it difficult to scale up to large numbers. A quantity of 1×10^6 cells can produce just 100 collagen spheroids at 1×10^4 cells/spheroid, or 1333 methylcellulose spheroids at 750 cells/spheroid.

HUVEC methylcellulose spheroids were made using 2.4 % (w/v) methylcellulose, as described in Section 2.5, using unsupplemented ECGM as the basal medium. A commonly used method for making spheroids with methylcellulose is to use round-bottomed non-adherent (non-plasma treated polyethylene) 96 well plates, but when this method was used with HUVECs, the cells stuck to the sides of the round bottomed place, and did not aggregate into spheroids. Any aggregation observed was both inconsistent and nonuniform, having multiple aggregates per well, with most cells remaining stuck to the sides of the well. Hanging drop culture was attempted using the described method, which leads to spheroids forming with a high degree of consistency and uniformity. Example spheroids made using 1000 HUVECs in 25 µL 0.3 % (w/v) methylcellulose-ECGM drops are shown in Figure 4.15(B) following 24 hours of culture.

Both types of spheroid were subsequently embedded in collagen gels with the addition of different growth factors in order to determine their ability to grow out into the gel in response to the factors. Outgrowth from collagen spheroids was far poorer than for methylcellulose spheroids (data not shown). The larger quantity and smaller size of methylcellulose spheroids meant that more might be added to a single

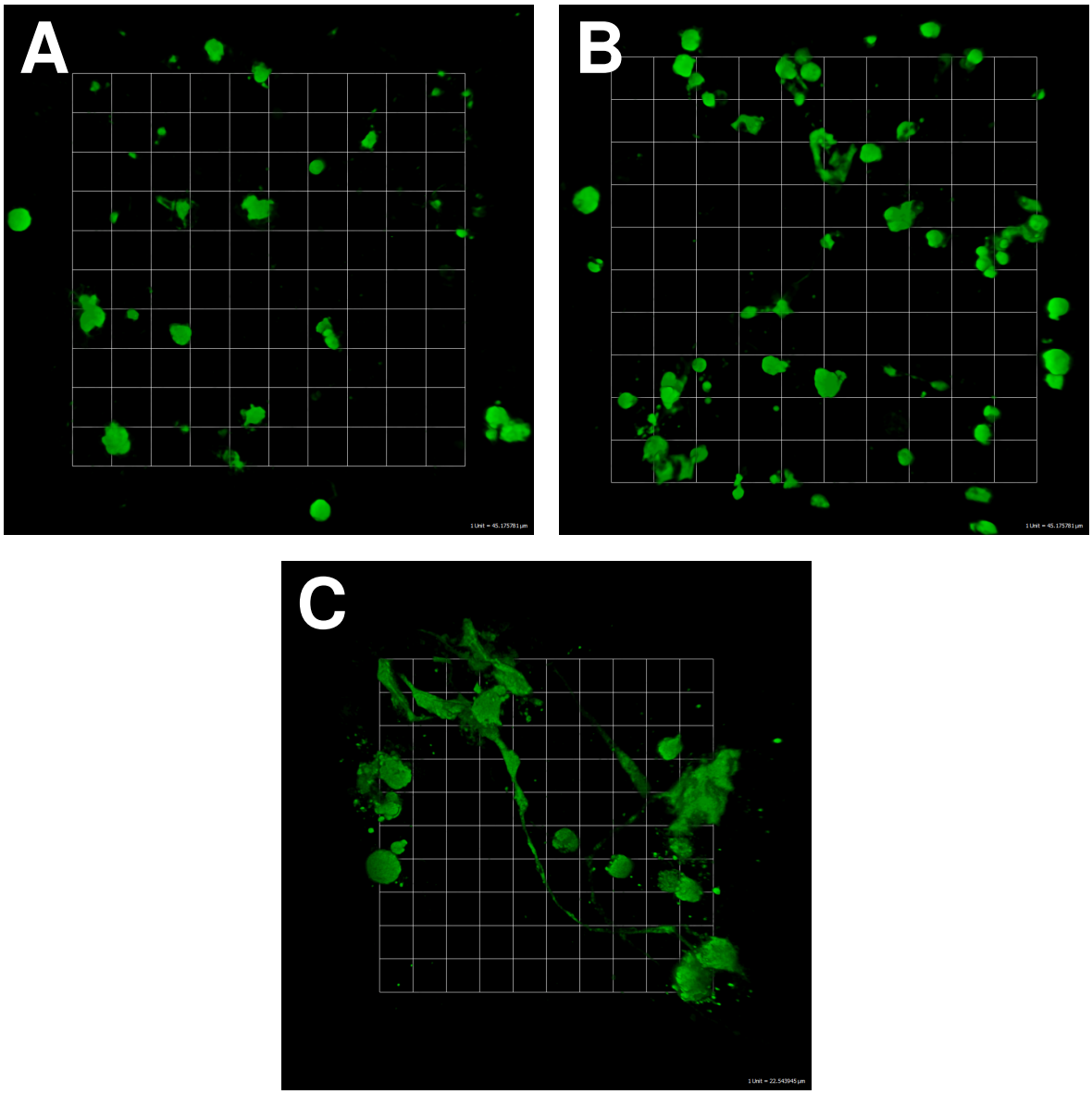

Figure 4.14: HUVEC labelling with CFSE. CFSE-labelled HUVECs were seeded in a collagen gels and overlaid with normal or tube forming media. (A) In normal growth medium, HUVECs showed no evidence of tube formation after 48 hours. The majority of cells under tube forming conditions also showed no evidence of tube formation (B), with some cells appearing fragmented and apoptotic, however a minority of cells did exhibit some evidence of tube formation (C). Scales are 45 µm (A, B) and 22.5 µm (C).

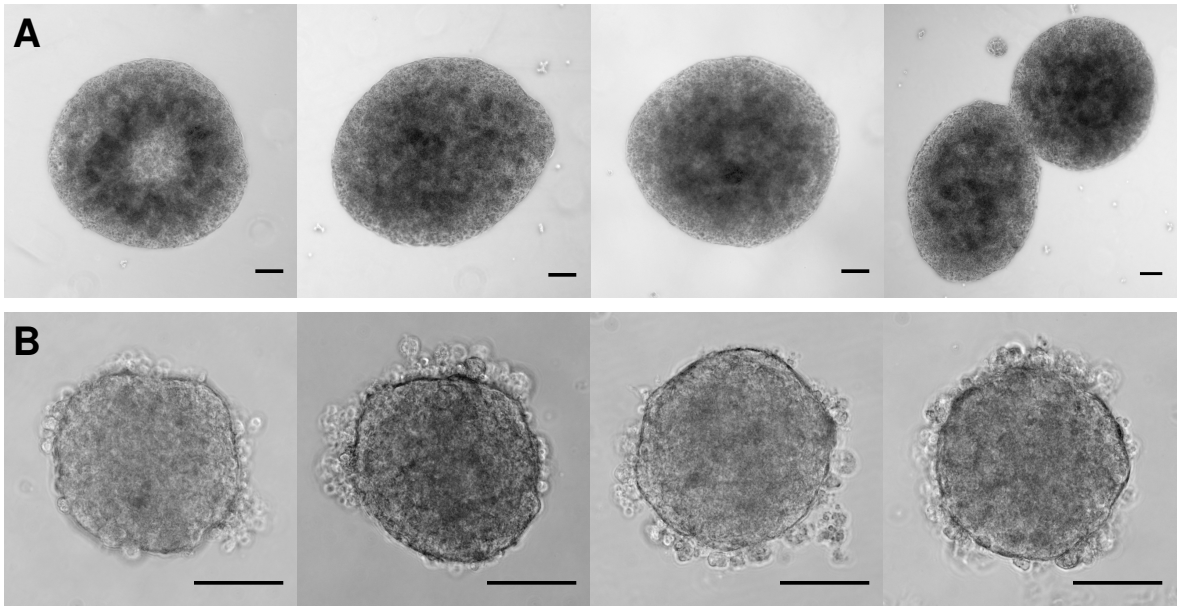

Figure 4.15: Methylcellulose and collagen spheroids. (A) HUVEC collagen spheroids (10000 cells/spheroid). The size and shape of collagen spheroids is variable, and they exhibit a tendency to adhere to each other (far right). (B) HUVEC methylcellulose spheroids (1000 cells/spheroid). All spheroids are seen to have a uniformly spherical appearance despite the presence of single cells on their surface. Collagen spheroids are approximately 3× the diameter of methylcellulose spheroids. Scale bars are 100 µm.

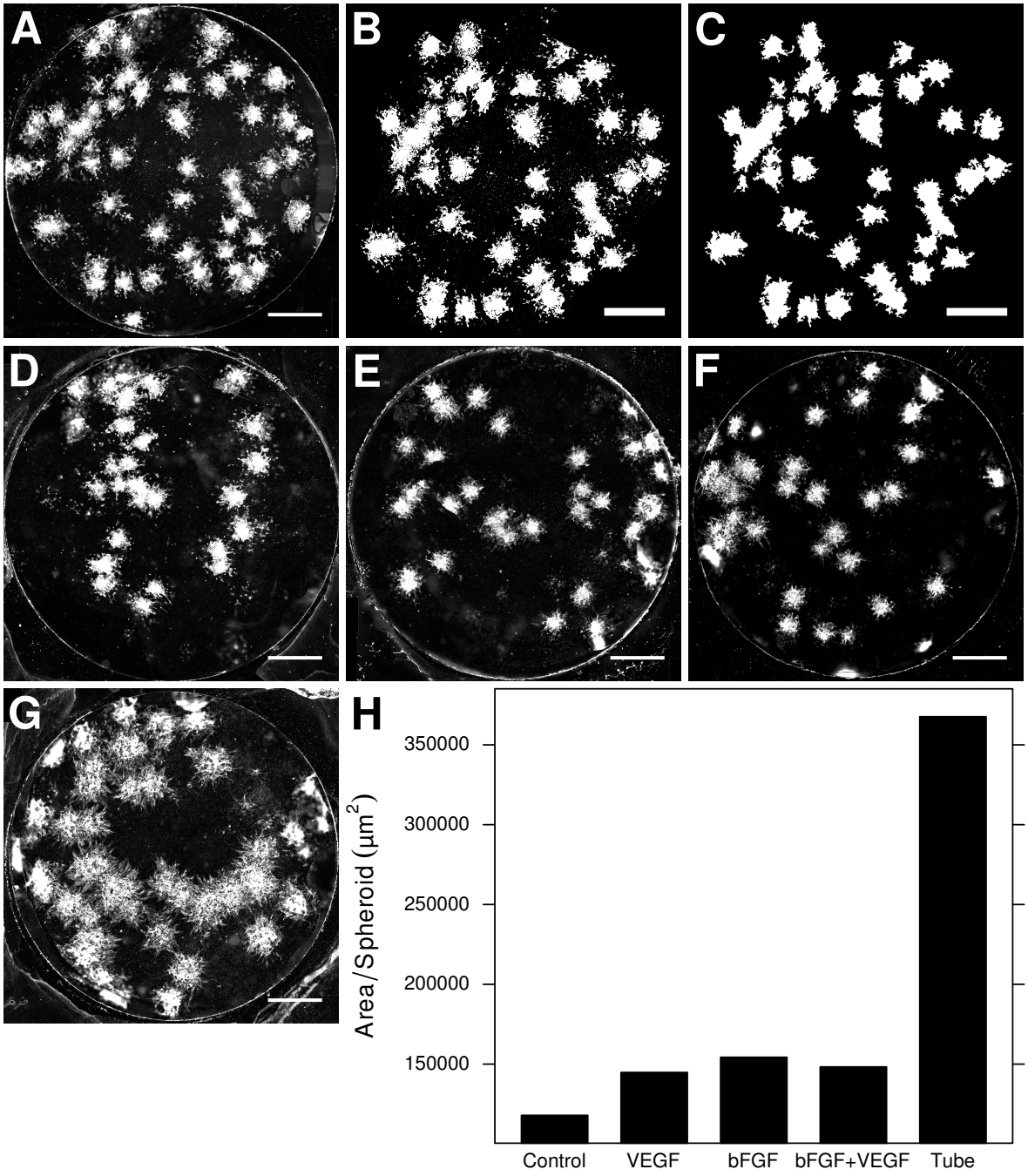

Figure 4.16: Spheroid outgrowth in response to different growth factors. Spheroids were grown in ECGM (A), shown cropped for analysis removing well edges and spheroids touching the edge, and having background correction (B) and then following thresholding and exclusion of small particles (C). Spheroids were also grown in ECGM supplemented with bFGF (D), VEGF (E), bFGF and VEGF (F) or under tube forming conditions (G). Outgrowth of tubes into the collagen extracellular matrix is observed in all cases, including the control (A), but under tube forming conditions (G), growth and cell proliferation appear to be greatly increased compared with all other treatments. The amount of outgrowth is shown graphically in (H), calculating the total area covered by each spheroid from total area measurements and spheroid counts. Per-spheroid measurements were not possible due to the spheroids touching, hence this plot does not include error bars. Scale bars are 1 mm.

gel, resulting in a greater number of observations and hence allowing more reliable statistics and robust conclusions to be drawn from the data.

4.2.11 HUVEC spheroids are responsive to growth factors

HUVEC methylcellulose spheroids (750 cells/spheroid) were suspended in 1 mm thick, 6 mm diameter collagen gels using support rings as shown in Figure 2.1(B), and treated with different growth factors. Control gels were covered with 4 mL ECGM and treated gels were covered with 40 ng/mL $hVEGF_{165}$, 40 ng/mL bFGF, 40 ng/mL $hVEGF_{165}$, 40 ng/mL bFGF and 4 mL tube forming medium. The gels were stained with mouse anti-human CD31 with a goat anti-mouse-AF594 secondary and imaged as sets of between 35–45 tiles which were later stitched together to form single images as described in Section 2.6.6. The assembled images are shown in Figure 4.16.

While spheroid outgrowth increased moderately compared with the control on the addition of bFGF, VEGF, or both, it dramatically increased when using the tube forming conditions used in previous experiments. In some of the treatments, the spheroids had grown so large that they were touching and visually inseparable, making per-spheroid measurements as detailed in Figure 2.3 impossible. Instead, the outgrowth was quantified by masking out all parts of the image except the collagen gel (excluding the well edge and metal ring). The spheroids in the gel were then quantified by subtracting the background using rolling ball background subtraction with a radius of 200 pixels, followed by thresholding to select the stained spheroids and outgrowths, and measurement of the total stained area. This allowed calculation of the mean area per spheroid; larger spheroids with more angiogenic outgrowth should have an increased mean area. However, this method had the disadvantage of selecting background staining in the gel in some samples; while some of this could be masked out, this was not feasible for all samples. This method precluded determining the error in the calculated area per spheroid, due to measuring the total area covered by all spheroids, rather than for each spheroid individually.

4.3 Discussion

4.3.1 Microfluidic networks in collagen gels

The PALM Microbeam laser capture microdissection system (Carl Zeiss) contains a pulsed nitrogen UV laser, used to cut biological sample sections placed upon glass slides coated with 1.5 µm PEN film. The UV laser is capable of cutting the PEN film, which is sensitive to 405 nm laser light, and this also results in cutting of the overlying sample. While 1.5 µm is too thin for practical microfluidics, it was hypothesised that if the system was capable of cutting thicker film, this would be able to substitute for photolithography by allowing the direct cutting of a template, and

hence be usable for PDMS moulding. The primary variable to control cutting was the stage speed, faster speeds implying less energy absorption by the PEN per unit distance, but also less cutting accuracy due to greater distance between pulses. Cutting therefore required a fine balance between travelling sufficiently slowly to accurately define features, but not so slowly that too much energy was put into the sample at a single point, resulting in excessive melting (and, at the extreme, burning). This was controlled through fine-tuning of the laser power.

In order to create PEN templates of defined dimensions, custom software was written to transform scale drawings into the specific format required by the PALM Robo software controlling the system. Using the PALM Microbeam system, PEN film was cut into precisely-defined network templates with ∼µm tolerance, which compares favourably with photolithography at large 50 µm thicknesses (Duffy *et al.*, 1998), though photolithography is capable of accuracy to tens of nanometres when used for very thin films, *e.g.* in semiconductor masking applications, as well as in thin film micromoulding (Kim *et al.*, 1996). The channel roughness is a function of the resolution of the photomask, and while this is not particularly apparent for straight edges and right angles in line with the pixel grid, it results in the introduction of roughness when curves and lines at other angles are used (Duffy *et al.*, 1998; McDonald *et al.*, 2000), *e.g.* a photomask printed at a resolution of 5000 pixels/inch will only achieve a resolution of 5 µm when used at a 1:1 scale and illuminated with parallel light (lens-free). This is a typical scenario when using thick photoresist layers, since using lenses would bend the light from a parallel path, resulting in features without uniformly vertical edges, moving away radially from the centre of focus. In comparison, laser cutting results in smooth undulations under 1 µm in depth as a result of the laser beam pulses overlapping to a large extent. The resolution is limited by the stage steppers, which have a movement of 78.125 nm/step and the laser pulse frequency, which is fixed at 30 Hz. In practice, the pulse frequency is limiting; resolution could be improved using a laser with higher frequency, but less power output which would result in the same total energy input into the sample, but resulting in finer control and smoother surface features. The fabrication of network templates in this fashion is a completely novel application, both of the PALM Microbeam system and for the production of microfluidic networks. In comparison with existing work using direct laser etching of silicon to create microchannels, for example, cutting of PEN results in smoother, more consistent feature reproduction which will translate to less turbulent, more laminar flow in moulded microfluidic channels (Kam, 2008).

Using the PEN template, networks in PDMS elastomer were successfully produced, and the functionality and integrity of the network was demonstrated by perfusion with gelatin. This highlighted the precise control of the channel dimensions, with the channel width being uniform within µm tolerance, and the height being determined by the thickness of the PEN film.

The overall aim was to use this technique to produce microfluidic collagen gels as outlined in Figure 2.6. Using this approach, the step of producing a defined gelatin network on glass substrate was reached. The following steps, overlaying the gelatin network with neutralised collagen, gelling the collagen, and then perfusing the network at raised temperature to remove the molten gelatin would have resulted in the production of a collagen gel containing a microfluidic network moulded within it. However, this was not possible using our current methods for creating collagen gels, a 3 mg/mL concentration resulting in a gel which was not sufficiently solid to retain such fine features or survive the forces imposed upon it during perfusion. Additionally, the observed behaviour of HUVEC-mediated gel contraction would result in rapid destruction of the moulded features, and a loss of sealing with the glass substrate.

Potential solutions to these problems include the use of higher mass fraction collagen gels. The Stroock group at Cornell University have recently successfully created perfused microfluidic collagen gels at concentrations of 10 mg/mL and above (Cross *et al.*, 2010); while gels at concentrations as low as 3 mg/mL were patterned, they rapidly deformed under perfusion. Our observations are that collagen at concentrations of 6 mg/mL and above, even at acidic pH in monomeric form, is effectively a solid which does not readily flow, making handling problematic. It can not be pipetted, even with 1000 µL pipette tips with the tips cut off, and it would not be possible to evenly mix cells or spheroids within it following gelation due to the high viscosity. Additionally, dense gels are also likely to present a barrier to cell migration, which would require degradation and remodelling of the matrix to allow movement; MMPs which cleave collagen I (collagenases) are not typically associated with angiogenesis and may even be anti-angiogenic, unlike gelatinases (Bergers, Brekken *et al.*, 2000; Saunders *et al.*, 2005; Vu, Shipley *et al.*, 1998). In contrast, collagen at 3 mg/mL is handled straightforwardly, cells and spheroids may be rapidly and evenly dispersed within the solution, and cells may freely migrate through the resulting matrix. Observations in the Coles lab using real-time MP imaging of the HT1080 fibrosarcoma line and OP9 bone stromal line in 3 mg/mL collagen gels (not shown) were able to freely migrate within the gel; higher concentrations have not yet been tested.

The "ideal" gel is of low mass fraction, with a pore size sufficiently large to permit migration and remodelling, permits direct incorporation of cells or cell aggregates during gelling, and is sufficiently strong to resist the forces exerted upon it during perfusion and tube formation. Potential solutions to improve the mechanical and structural properties of collagen could include composite gels composed of multiple matrix components, containing both collagen and other components which could resist contraction and provide additional structural integrity, or to increase the rigidity of the collagen fibrils by cross-linking. Various different cross-linking strategies are reported in the literature, varying from chemical cross-linking to enzymatic treat-

ment. Aldehydes such as formaldehyde and paraformaldehyde are widely used cross-linkers, but are incompatible with the direct incorporation of cells into monomeric collagen due to their toxicity. Other chemistries are also possible, such as using N-hydroxysuccinimide/ethyl(dimethylaminopropyl) carbodiimide to cross-link chondroitin sulphate and heparin to collagen I (Pieper, Hafmans *et al.*, 2000), but again the chemistry is rather toxic and incompatible with direct cell seeding. Molecules used in the tanning industry may be a source of useful biocompatible molecules suitable for this purpose, such as procyanidin, a plant-derived polyphenol and collagen cross-linker (He, Mu *et al.*, 2011), though their biocompatibility and any effects upon cellular physiology would require assessing. Enzymes such as lysyl oxidase are responsible for the establishment of inter-fibril cross-links *in vivo* (Mäki, Sormunen *et al.*, 2005), therefore mixing of recombinant lysyl oxidase with the prepolymer could potentially result in enzymatic cross-linking through the formation of reactive aldehyde groups, resulting in a stronger gel without any change in density. Non-chemical approaches include the use of UV cross-linking, but again is incompatible with direct cell seeding. The strength of collagen may also be increased through flow casting, resulting in axial orientation of fibrils, which may be built up in layers to produce, for example, biaxially oriented laminar sheets with great strength (Tanaka, Baba *et al.*, 2011), but is again incompatible with cell seeding during manufacture, and the processing also results in very dense collagen which may present an effective barrier to migration and remodelling.

While PEN cutting offers an alternative to photolithography, the approach also has its drawbacks. Networks are cut out, and hence detached from, both the material from which they are derived, and the substrate to which the material was attached. In consequence, the network may only consist of a single piece; if multiple pieces are cut from the same material, their relative spatial orientation will be lost following cutting, for example separate networks or channels oriented alongside each other. This limits the complexity of the systems which may be created using this approach. In contrast, with photolithography the photoresist remains attached to the silicon substrate, permitting the creation of precisely aligned discrete networks which are in close spatial proximity, but not in intimate contact. In order to mitigate issues with alignment tolerance when coring perfusion ports through the PDMS, large endpoints were created to allow for variability in needle placement, as shown in Figure 4.2(A) and (C). Photolithography permits much tighter alignment due to the fact that alignment marks and points for holes may be directly incorporated into the photomask and hence the SU-8 master and moulded PDMS.

Cracking of the coverslip glass under pressure was also an issue. In order to permit the use of live confocal and multiphoton imaging during perfusion, № 1½ slide-sized coverslip glass was used. However, this only permits visualisation of a tiny part of a much larger network. If these requirements were relaxed, low NA

objectives (*e.g.* 2× or 5×) or even a stereo microscope could be used to visualise the entire network at once, and thicker glass could be used in consequence since spherical aberration due to the glass thickness would not cause problems due to the low NA of the objective, which could be specifically corrected for the glass thickness.

4.3.2 Formation of vascular networks using exogenous factors

The vascular model should be capable of forming a complex vascular network in a 3-D environment. In order to determine if HUVECs were capable of being cultured in three dimensions in a collagen gel, and if they were capable of forming a network of tubes in the gel, HUVECs were seeded directly in the gel. The effects of the treatments in 2-D and 3-D environments are rather different, with control cells appearing to prefer a 2-D environment, on either glass or collagen surfaces. Cells were not found in the interior of the control gel, presumably either having migrated out after initial seeding, or died following apoptosis or anoikis, which could account for the presence of brightly-staining blobs within the gel as a consequence of blebbing and fragmenting. It is likely that in the absence of cell–cell contact, unstimulated HUVECs lack the survival signals needed to exist in a 3-D context (Bird *et al.*, 1999). HUVECs have been previously shown not to survive in 3D gels, even when supplemented with VEGF (Ilan, Mahooti *et al.*, 1998). Additionally ECs have very different morphology and migration strategies in 2-D versus 3-D (Martins and Kolega, 2006). Existing work and published protocols have focussed on 3-D invasion of collagen gels starting from a 2-D monolayer of ECs seeded onto the empty gel (Bayless, Kwak *et al.*, 2009; Davis *et al.*, 2000a; Yang *et al.*, 1999). These models require ECs to actively respond to stimulation via growth factors and invade the gel, rather than immediately transitioning from 2-D culture to direct seeding in the matrix. In Davis' reviews of the mechanisms of EC morphogenesis and lumen formation (Davis *et al.*, 2002, 2007), and in Tatin, Varon *et al.* (2006), protein kinase C (PKC) signalling via Rac1 and Cdc42 in order to control migration, tube assembly, cell–cell adhesion and survival were shown to be of critical importance. Following stimulation to invade in 3-D, phalanx ECs are required to undergo changes in cell-cell junctions (disassembly), cytoskeletal organisation changes to permit migration, including loss of polarity, and MMP expression to degrade the local ECM. In the absence of signalling to provide survival signals, for example via PKB or ERK as a result of VEGFR2 signalling and/or PMA-induced activation of PKC, it is very likely that cell death would occur in consequence (Ilan *et al.*, 1998).

This initial experimental work demonstrated that HUVECs may be used as a model endothelial cell. They may be induced to form a network of tubes in 3-D collagen gels by treatment with exogenous factors, as shown in Figure 4.3. However, the true extent of tube formation was not clear due to the possibility of the "tubes" being infoldings of the collagen gel surface. The gel was seen to contract from its

initial 14 mm diameter to less than three times this size. The reduction in surface area may have resulted in extensive infolding of the surface during contraction, in addition to contraction of the gel as a whole as individual fibrils are pulled closer together through the action of ECs. In consequence, apparent tubes and even branched structures may not have formed as a result of vasculogenesis or angiogenesis, and the cells may exist in the same 2D environment on the infolded gel surface as their counterparts on the exterior faces. This notwithstanding, tubes are clearly visible in the gel interior, and the tube forming conditions have resulted in clear morphological changes. However, it would be greatly desirable to separate the wanted changes (tube assembly and angiogenesis) from the unwanted side effects of microfolding of the collagen gel surface as a result of the gel contraction. One solution to this would be to use smaller, thicker gels with a lower surface area to volume ratio in order to increase the distance between the interior and gel surface, so that the unwanted surface changes may be ignored or eliminated entirely. Subsequent experiments in this chapter therefore used 3 mm diameter, 3 mm thick gels as shown in Figure 4.4, and these showed clear evidence of tube formation in the gel interior (albeit with the unwanted side-effect of necrosis in the gel centre), while eliminating surface infolding, since the entire surface is clearly visible showing 2-D cell–cell junctions. Later work used 6 mm diameter, 1 mm gels to additionally avoid necrosis and to provide a larger imageable area.

The 3 mm diameter, 3 mm deep collagen gels used for the majority of the experimental work allow for very large images to be taken of the gel, with a very deep z depth. Less dense collagen gels resulted in smaller gels. This is most likely not due to an increased amount of contraction within the gel, but rather that the cells contract the collagen until it reaches a density which limits further contraction; due to the presence a lower amount of collagen in less dense gels, this would result in a smaller final volume after contraction. This size of gel was not optimal due to the observed void space in the core of the growth-factor-treated gels, though this was not observed for coculture gels. While the specific nature of this phenomenon was not investigated, a probable cause would be necrosis and/or apoptosis of the cells in the gel core as a result of nutrient or oxygen starvation, or of waste product buildup. This is a phenomenon previously observed in both tissue, tumours and 3D culture models, due to the diffusion of oxygen and nutrients becoming limiting, of the concentration of waste products reaching toxic levels; the passive diffusion rate can not meet the metabolic demand of the cells, or remove waste sufficiently rapidly (Shweiki *et al.*, 1995). Cells nearer the edge of the gel are closer to the source of oxygen or nutrients or the waste sink, and so are correspondingly more likely to survive. One benefit of having microfluidic circulation in 3D collagen cultures is that oxygen and nutrients are actively perfused, and waste removed, in a similar manner to a real circulatory system. Recent work by Demol, Lambrechts *et al.* (2011) has attempted to quantify

some of these factors making both direct observations under controlled conditions, and mathematical modelling. Interestingly, the primary cause of hypoxia in their model is not the metabolic demand of cells within the gel, but as a result of cells on the gel surface inhibiting diffusion into the gel, resulting in extreme hypoxia in the gel centre. The HUVEC gels were observed to possess a confluent 2-D surface monolayer, hence the same process may be occuring in these gels.

HUVECs were shown to form tubes in a 3-D collagen gel when treated with factors to induce tube formation. However, it was not possible to determine if the tubes were vessels containing patent (open) lumens, or merely cell aggregates, from the confocal microscopy data. It is not clear why the CD31 staining appears across the entire vessel cross-section when it should be mainly restricted to the plasma membrane at cell–cell junctions, but may be due to the membranous debris filling the lumen, shown in Figure 4.5. In order to determine if the tubes were genuine vessels, transmission electron microscopy was used to visualise the tube morphology, repeating the tube formation experiment, but using 3 mm diameter, 3 mm thick collagen gels to ensure the presence of tubes in the interior, rather than simple surface infolding. TEM analysis (Figure 4.5) demonstrated that tubes were indeed formed by treatment under tube-forming conditions, and that they contained several key features of capillaries: apical–basal polarisation with the basal surface in contact with the matrix, the apical face exposed to the open lumen, and lateral faces in contact with neighbouring cells via adherens junctions (Adams and Alitalo, 2007; Dejana, Tournier-Lasserve *et al.*, 2009). The TEM images bear close similarities to previously published work, including Bishop *et al.* (1999); Davis *et al.* (2002), showing adherens junctions, and the presence of Wiebel-Palade bodies is potentially shown in Figure 4.5(D), filling the cytoplasm between the nucleus and lumen (Berriman, Li *et al.*, 2009). Additionally, at higher magnifications (not shown), the classic banding pattern of the collagen fibril structure was clearly visible (Bozec, van der Heijden *et al.*, 2007; Williams, Gelman *et al.*, 1978), demonstrating that the matrix was composed of correctly assembled collagen fibrils. The use of gels of reduced size could eliminate the problems identified here, but the final size after gel contraction could be under 0.5 mm in diameter and height, and would present additional technical challenges to mould a seeded gel due to issues with the gel viscosity and small gel volumes, and also during subsequent manual handling during immunohistochemical processing.

The observation that HUVECs are found mainly in a 2-D environment on the surface of the collagen gel when only overlaid with normal growth media, and in the absence of other cell types reflects the normal state of "phalanx" endothelial cells lining blood vessels. These cells experience a 2-D environment, given that they lie upon a 2-D basement membrane, which although rolled up as a cylindrical structure is effectively two dimensional from the perspective of an individual endothelial cell. In addition to the basement membrane which underlies the cell, the upper surface is

exposed to the lumenal contents of the vessel whilst to either side each endothelial cell makes intimate contact with its neighbours through adherens junctions. Phalanx cells are highly polarised, non-migratory and have very low rates of proliferation, being specialised to fulfilling their function. In order for cells to migrate into a 3-D environment, they must lose their specialised, polarised structure, decrease their attachment to their neighbours and adopt a more fibroblastic phenotype with a growth cone, in order to enable their migration through the basement membrane and into the surrounding tissue. In an artificial gel, the interface between cell and collagen provides an equivalent role to the vascular basement membrane and the volume of the gel a tissue analogue, providing a substrate for integrin engagement and adherence as well as a volume through which migration is possible. In order to transition from a 2-D to 3-D context, migrate and form new structures inside the gel, growth factors appear to be a major requirement, either provided exogenously or in a paracrine manner through neighbouring cells, as demonstrated.

In experiments using exogenous growth factors, four separate components were used: bFGF, VEGF, PMA and ascorbate. Ascorbate is not required for angiogenesis, but it is a requirement for collagen biosynthesis (Green and Goldberg, 1965). bFGF, VEGF and PMA all have broadly similar effects, due to activating many of the same signalling pathways. While the signalling pathways have many different effects, the major molecular players are as follows:

Both VEGFR and FGFR are activated by dimerisation upon binding of VEGF and bFGF, respectively. Both receptors activate phospholipase Cγ (PLCγ), catalysing the breakdown of phosphatidylinositol 4,5-bisphosphate (PIP_2) into diacylglycerol (DAG), resulting in PKC activation, and into inositol trisphosphate (IP_3), which triggers release of calcium from intracellular stores causing, amongst other effects, release of von Willebrand factor from Wiebel-Palade bodies and further PKC activation (Carew, Paleolog *et al.*, 1992; Gliki, Wheeler-Jones *et al.*, 2002; Yoshiji, Kuriyama *et al.*, 1999). Both additionally activate phosphatidylinositol 3-kinase (PI3K), resulting in the formation of phosphatidylinositol 3,4,5-trisphosphate (PIP_3), activating PKB and RhoA, though they may both activate different PI3K isoforms and hence have different effects (Gliki *et al.*, 2002; Graupera, Guillermet-Guibert *et al.*, 2008; van Nieuw Amerongen, Koolwijk *et al.*, 2003; Zeng, Zhao *et al.*, 2002). Both pathways additionally activate a Ras,Raf,MEK,ERK1/2 signalling cascade, resulting in transcriptional changes, and activate p38 MAPK which affects actin remodelling and migration (Cuadrado and Nebreda, 2010; Yoshiji *et al.*, 1999). p38 additionally induces apoptosis, though this is inhibited by ERK signalling (Eguchi, Suzuki *et al.*, 2007). The effect of PKB is to promote cell survival by inhibition of caspase and mitochondrial apoptotic machinery, as well as regulating proliferation via nitric oxide and regulating vascular permeability (Ilan *et al.*, 1998; Spyridopoulos, 2002). RhoA activated by VEGF is required for migration and cellular organisation during angiogenesis

(Hoang, Whelan *et al.*, 2004; Spyridopoulos, 2002). In some respects, VEGFR1 acts antagonistically to VEGFR2, signalling via nitric oxide, inhibiting proliferation and promoting network formation (Bussolati *et al.*, 2001).

In summary, bFGF, VEGF and PMA induce a wide range of changes upon gene expression, differentiation, survival, proliferation and tube formation. Similar models of vasculogenesis have been investigated by Davis and Camarillo (1996), Ilan *et al.* (1998) and Taylor, Motamed *et al.* (2006). From these, it may be concluded that in the absence of such stimulation, apoptosis is induced in HUVECs, which explains the absence of cells in the control gels. Cell–cell contact is also a critical requirement for HUVECs, CD31 contacts preventing apoptosis, not inducing migration, spreading or tube formation (Bird *et al.*, 1999). Thus untreated cells may exist as a confluent monolayer on the cell surface, but when seeded as a single cell suspension within the gel are unable to survive. Upon appropriate stimulation, cells are able to survive, migrate and form tubes in a 3-D context (Davis *et al.*, 2000a). PMA, being a DAG analogue and PKC agonist, strongly activates the PKC pathway, and also the PI3K pathway (Ilan *et al.*, 1998). PMA upregulates VEGFR1/2 making ECs responsive to VEGF, drives angiogenesis, and additionally allows VEGF to act as a survival factor after PMA withdrawal (Ilan *et al.*, 1998; Montesano and Orci, 1987).

These experiments demonstrated that the HUVECs were behaving as previously observed in the literature. However, the resulting networks posed a challenge for accurate quantification, and more importantly would be difficult to use for the observation of remodelling, especially after strong stimulation with PMA and other factors, which could make the system rather less responsive to subtle external changes such as in the influence of soluble growth factors and inhibitors. For these reasons, it was decided to induce network formation using coculture with pericytes, which should be both of greater physiological relevance and eliminate the need for exogenous factors.

4.3.3 Formation of vascular networks using VSMC coculture

Following the findings that HUVECs could be induced to form a primitive vascular network in a collagen gel, a more realistic and complete model was created through the introduction of smooth muscle or pericytes to cover the endothelial tubes. The initial experiments used a temperature-sensitive VSMC derived from aortic smooth muscle (Foo *et al.*, 2006; Jat *et al.*, 1991). In order to determine that the primary culture was vascular smooth muscle, the expression of the vascular smooth muscle marker NG2 was determined using flow cytometry (Figure 4.6). While 90 % of the population was shown to be positive for this marker, the primary culture of aortic smooth muscle was shown to contain a contaminating population of morphologically distinct non-NG2-expressing cells. Because these were not removed via the sorting of a pure NG2-positive population, it was assumed that this population was derived

from the NG2-positive population, as cells lost their smooth muscle differentiation over time in culture. Observation of the cells showed an increasing proportion of these cells with increasing passage number, lending credence to this hypothesis.

Endothelial cells can not be seeded sparsely in 2-D or 3-D without the loss of cell–cell contact, resulting in apoptosis (Dejana *et al.*, 2009; Yang *et al.*, 1999). Apoptosis is prevented by homotypic cell–cell interactions mediated through CD31 interactions (Bird *et al.*, 1999). The problem becomes more pronounced in 3-D, because the distances between cells is greatly increased with the addition of the third dimension unless the cells are seeded at very high densities, which introduce additional complications, such as the necrosis observed above. As an example, seeding at 5–10 $\times$ 10^3 cells/cm^2 in 2-D would require seeding at 354–1000 $\times$ 10^3 cells/cm^3 in 3-D to achieve equivalent spacing and density, a 70–100-fold increase. In practice, optimal tube formation was seen when seeding at even higher levels (5 $\times$ 10^6 cells/cm^3). It was hypothesised that unlike the previous experiments with HUVECs and growth factors, where the growth factor signalling can counteract apoptotic cues, HUVECs co-cultured with smooth muscle would not establish organised structures rapidly enough to prevent apoptosis, and that seeding HUVECs on the gel surface would be a potential solution to this problem. HUVECs were therefore seeded on top of the gel to form a confluent monolayer capable of invading the gel in response to angiogenic and/or migratory stimuli from the seeded VSMCs, an approach used in previous work (Bayless *et al.*, 2009; Darland and D'Amore, 2001; Davis *et al.*, 2000a). This should reduce the amount of cell death in the gel, at the expense of requiring directed migration into the gel from a 2-D environment. Endothelial cells may also undergo apoptosis when cell–matrix contact is lost, or when their geometric conformation with respect to the matrix is inappropriate (Dike, Chen *et al.*, 1999). Polarised phalanx cells conditioned to exist attached the surface of the matrix may be equally ill-equipped to survive when surrounded by matrix—a condition normally experienced by tip and stalk cells which have been signalled to migrate through, and have adopted a morphology suited to the task.

VSMCs induced tube formation in HUVECs at very low frequency, but did not give rise to the complete networks seen with growth factors (or C3H/10T½ coculture, below). The controls in Figure 4.7(A–F) showed that in the absence of VSMCs, HUVECs plated on the gel surface do not invade the gel, and that HUVECs seeded inside the gel do not form any organised structures; the only structures observed proved on close inspection to be 2-D adherent cells associated with invaginations of the collagen gel surface, rather than being truly in the gel interior. Figure 4.7(G–L) demonstrated that HUVECs form tubes and organised structures when co-cultured with VSMCs. When viewed as xz and yz projections, the majority of the structures are shown to arise from invasion from the gel surface, indicating that the presence of VSMCs inside the gel was sufficient to signal and induce the HUVECs to migrate

into the gel, and form organised tubular structures with VSMC coverage. In Figure 4.7(G), no organised structures are visible, and the HUVECs are mostly separated spatially from the VSMCs; in contrast the organised structures in (H-J) show a higher frequency of VSMCs, many of which are in close proximity to, or in intimate contact with, the HUVECs as shown in xz and yz projection.

There are a few possibilities why tube formation was only observed at low frequency. This may be due to not seeding the HUVECs directly in the gel as done in other experiments; overlaying HUVECs on the gel surface may not allow sufficient cell numbers to migrate into the gel to form a network, or there may be insufficient VSMCs to produce a strong enough signal to induce their inmigration. Stratman *et al.* (2009a, 2010) subsequently utilised EC–pericyte cocultures in their work, but have focussed upon direct seeding of both pericytes and ECs directly into a collagen matrix. This resulted in the formation of beautiful vascular networks with pericyte coverage and basement membrane assembly, thus invalidating our hypothesis that ECs would not be able to survive immediately after seeding. Alternatively, the cells may not be of the correct type to efficiently induce tube formation in HUVECs; they may not be producing the required factors to set up the paracrine signalling circuit to induce the process, *i.e.* be correctly responsive to EC-derived PDGF-B, required for recruitment to ECs (Hellström *et al.*, 1999). This may be because they are derived from the wrong tissue (smooth muscle from aorta, rather than pericytes), or they may have lost the ability to fully function as VSMCs whilst in culture. Stratman utilised pericytes derived from bovine retina and human brain, which may have greater competence in responding to PDGF.

Co-culture of endothelial cells and pericytes derived from bone marrow results in the formation of capillary networks, albeit in 2-D only (Pelletier, Regnard *et al.*, 2000). In this model, tube formation was related to the production of endogenous VEGF and NO; the presence of pericytes reduced the effect of VEGF neutralisation, which would reduce the number of tubes formed. Tube formation was also related to $\alpha_v\beta_5$ integrin binding of the matrix, demonstrating the importance of matrix contact. This model allowed the effect of different cytokines and growth factors to be quantified by comparing the basal number of tubes formed under control conditions with the addition of cytokines and growth factors. Interestingly the rate decreased slightly with bFGF or TGF-β_1, while PDGF-BB and VEGF resulted in a large increase. Neutralising bFGF and TGF-β_1 resulted in a return to the basal rate, while neutralisation of VEGF resulted in a dramatic decline from the basal rate, indicating the importance of endogenous VEGF in driving tube formation. The hæmatopoietic cytokines SCF, GM-CSF, EPO and G-CSF all raised the rates of tube formation above the basal rate in order of increasing effectiveness, with EPO being equivalent to PDGF-BB. These experiments demonstrate that endothelial cells and pericytes *alone* are sufficient to develop a vascular network, however the fact that the pericytes

were a contaminating population not removed during endothelial cell purification does not preclude other contaminating cell types from also being present, which may also influence endothelial behaviour and morphology. Other EC–VSMC models which might prove useful as a basis for modelling and quantifying angiogenesis include the fibroblast spheroid–EC cocultures of Kunz-Schughart, Schroeder *et al.* (2006), which result in the formation of branched vessels on the spheroid surface; differentiation of the fibroblasts into VSMC may also have occurred.

The model investigated here could be further improved, firstly by testing if direct seeding of ECs results in the production of a functional network. Stimulation of the ECs with PMA prior to seeding, and supplementing of the medium overlaying the gel with bFGF and/or VEGF may additionally overcome any apoptosis as a result of the transition to 3-D culture. However, the primary smooth muscle line had additional complications, given that it required seeding at very high densities and had a very slow growth rate, so obtaining sufficient quantities of cells for experimental work was difficult given that it could also only be used for a low number of passages. In consequence, alternative cell lines were investigated.

4.3.4 Formation of vascular networks using C3H/10T½ coculture

Due to the low frequency of tube formation and cell migration with VSMCs, the C3H/10T½, clone 8 cell line was also investigated. The cell line C3H/10T½ was used as a replacement for the primary smooth muscle line, given that the entire population expressed NG2, and that it could be rapidly differentiated into smooth muscle with human recombinant TGF-β_1, as shown by Figures 4.8 and 4.9. This line lacks the complications of the primary culture, being rapidly growing so that obtaining sufficient quantities of cells was not a problem. The literature describes C3H/10T½ as a multipotent mouse mesenchymal line, though its exact origin is unclear due to the method of isolation (Pinney and Emerson, 1989; Taylor and Jones, 1979), which may be differentiated toward a smooth muscle or pericyte lineage (Darland and D'Amore, 2001; Hirschi, Rohovsky *et al.*, 1999). C3H/10T½ clone 8 appears to express NG2 without deliberately inducing differentiation, so it is likely partially differentiated toward a smooth muscle or pericyte fate, but not yet committed. Differentiation with TGF-β_1 may therefore complete the process and induce complete differentiation and commitment (Darland and D'Amore, 2001).

The network formed by coculture of HUVEC and C3H/10T½ was similar in appearance to HUVEC only treated with growth factors, but with additional VSMC coverage of the network. The network formed with no exogenous growth factors, the process being entirely due to presence of VSMCs, but did take significant time to develop in comparison to Stratman *et al.* (2009a) (16 days instead of 5). VSMCs probably triggered formation of EC network due to the creation of a positive feedback paracrine signalling loop between HUVECs (secreting PDGF and TGF-β_1) and

VSMCs (secreting VEGF) (Darland, Massingham *et al.*, 2003; Hellström *et al.*, 1999; Hirschi *et al.*, 1998, 1999; Sato and Rifkin, 1989).

Interestingly, C3H/10T½ VSMC alone seeded in collagen form a stromal-like network. This network is very different from the endothelial network, being composed of interconnected long, elongated single cells, giving it a much more "spindly" appearance, similar to the stromal reticular networks seen in the lymph node (Katakai *et al.*, 2004; Ma *et al.*, 2007). This stromal network is not formed when in presence of HUVECs. The implication of this observation is that the default behaviour of the C3H/10T½ in 3-D is to form a stromal-like network. In the presence of endothelial cells, this process is disrupted, the stroma (C3H/10T½) being induced to play a different role: that of pericytes. ECs therefore appear to prevent formation of a stromal network, through the attraction of the smooth muscle cells to themselves and direction to a pericyte fate, and/or the stabilisation of the smooth muscle coverage once established.

It has been shown that TGF-β_1 is required for tube forming in endothelial–VSMC coculture using C3H/10T½ (Darland and D'Amore, 2001). Blocking TGF-β_1 lead to a reduction in the length, area and circumference of cords, in a 3D coculture of endothelial cells and C3H/10T½ in Matrigel. While these results have the appropriate controls, the use of Matrigel led to cord formation at both a very rapid rate and in unusual configurations. While TGF-β_1 clearly has an effect upon the EC organisation, its physiological relevance must be questioned. Montañez *et al.* (2002) clearly demonstrate that capillary-like network formation in collagen is very different from the "cord" formation observed in Matrigel, and that the tubes formed in collagen reproduce the lumen formation observed *in vivo* better than the Matrigel model. Our observations (not shown) have shown "cord formation" on Matrigel with a variety of non-endothelial cell types, implying that the process being studied is more likely to be merely aggregation of cells. The polygonal patterns observed in or on Matrigel are indicative of exclusion of cells from the matrix, adopting the most energetically stable organisation, which could be explained by the phase separation of immiscible colloids, in a manner analogous to the exclusion of phospholipids from the aqueous phase resulting in the self-organised formation of micelle, hexagonal and lamellar structures, and also in liquid crystals (Goodby, Görtz *et al.*, 2007; Kinoshita, Tsukada *et al.*, 2005; Lauzeral, Metens *et al.*, 1993; Milhaud, 2004).

4.3.5 Transfection and fluorescent labelling

Various different transfection strategies to establish fluorescent HUVEC and VSMC lines were employed, including Neon, Amaxa, Lipofectamine, adenoviral and lentiviral transfection and transduction systems. All techniques with the exception of lentiviral transduction (not shown) worked successfully. However, due to the inability of HUVECs to be passaged past P6–P7, selection of stably transformed cells

was not an option. Adenoviral transduction was most successful in terms of efficiency, copy number and cell death, but expression was too short-lived to be useful in longer-running cultures. Lentiviral transduction appears to be the best choice, having been successfully used to transduce both HUVECs and pericytes by others (Saunders *et al.*, 2006; Stratman *et al.*, 2010). Without having suitable fluorescent cell lines, live MP imaging was not a possibility.

CFSE labelling of HUVECs was demonstrated to alter the response of HUVECs to tube-forming media compared with unlabelled controls. Clearly, the CFSE labelling resulted in deleterious effects upon the cells. This could potentially be mitigated by further culture of the cells followed by sorting to select cells which are actively proliferating, using decreasing CFSE fluorescence to determine which cells have divided after labelling.

4.3.6 Spheroid models

HUVEC spheroids are a rather different solution to the issues identified with seeding single cells or inducing invasion of the gel (Korff and Augustin, 1998, 1999). Spheroids embedded into a collagen gel possess a number advantages over earlier methods. Each spheroid being composed of hundreds of cells, the cells are always in the presence of many neighbours, thus avoiding problems caused by sparse seeding and lack of neighbour contact. The cells at the edge of the spheroid contact the extracellular matrix, and can thus be partially exposed to a 2-D environment, in a polarised context (collagen basement), albeit with no lumen initially due to cells filling the space. Outgrowth of cells from the spheroid surface into the matrix mimics the adventitious nature of invasive sprouting angiogenesis, with tip cells leading and stalk cells following. Tube growth leads outwards radially from the spheroid. The reduction in complexity, in comparison with with whole-gel seeding, allows more robust analysis since each outgrowth may be measured and quantified separately, and each separate spheroid may be measured separately and treated as a biological replicate. Spheroids are distributed randomly in the gel, and their distance to embedded tissue or beads may be measured to observe and quantify spatial relationships.

Experiments to date have shown that HUVEC methylcellulose spheroids may be created in bulk and embedded in collagen gels, allowing quantification of the effects of pro- and anti-angiogenic factors present in their local environment, discussed in further detail below.

Neither the vascular network nor spheroid models contain fluid flow or pressure differentials. Our primary interest is in modelling mechanisms involved in organ and tissue vascularisation during development. While circulation is established when organs are vascularised, invasion of the tissues is most likely due to invasive sprouting angiogenesis. Given that this mechanism does not involve flow due to the invading tip cells and following stalk cells either being blind-ended or lacking a

lumen, this should not prove to be a major limitation.

4.3.7 Quantification of angiogenesis

Quantitative analysis of the acquired 3-D images remains an unresolved technical limitation. While software packages such as Volocity (Improvision/Perkin-Elmer) allow sophisticated visualisation of 3-D confocal images, analysis of such images to allow extraction of meaningful quantitative data remains a significant challenge. Volocity can be used to select features in the 3-D space as *volumes* comprised of voxels. From these volumes, several statistics may be derived, including dimensional limits (bounds along x, y and z axes), size measurements (surface area and volume), pixel intensity statistics (minimum, maximum, mean, standard deviation etc) and shape descriptors (centroid). A vascular network is a complex, branched, interconnected structure, and unfortunately the measurements one may extract from the identified volumes are not informative. The size, surface area and volume do not provide information about the *network structure*. Such parameters would include statistics concerning the total network length and volume, number of branch points, mean distance between branch points etc., which would allow comparison of different networks and assessment of the network size, complexity and degree of interconnectivity. Unfortunately, Volocity is not capable of computing such values, making it difficult to make practical use of the limited information which may be obtained.

In order to gain statistically meaningful data from either the vasculogenesis model or spheroid model, it is necessary to be able to analyse and extract useful quantitative data from the captured images. Existing approaches have mostly focussed upon the analysis of 2-D networks, though some of these may be adapted for use in 3-D. Using the chick chorioallantoic membrane model, Doukas, Maglogiannis *et al.* (2006) used skeletonisation to reduce the network to single pixel lines, from which the vessel length and branchpoints could be determined. This type of approach is suitable for repeatedly-branched networks, which may be imaged in sufficient detail to show all vessels. However, the approach falls short where thresholding tends to remove the finest detail, turning the capillary bed into a tree of discontinuous endpoints rather than it being a continuous web as it is in reality. Later work using similar 2-D models additionally permitted quantification of vessel area in addition to length (Egaña, Condurache *et al.*, 2009; Machens, Grzybowski *et al.*, 2006), and to classify vessels in a hierarchy depending upon their size and branching (Vickerman, Keith *et al.*, 2009). The approach of using iterative erosion to skeletonise images to determine branchpoints and linear segments between branches is illustrated nicely by Heinzer, Kuhn *et al.* (2008), though in this case this is a 2-D approximation of the process in 3-D, which decomposes a complex network into a graph consisting of edges and vertices. This representation allows comprehensive description of all networks of any degree of connectedness, *i.e.* any tubular structure from hierarchical branching to a capil-

lary plexus. This type of hierarchical ordering is termed *Strahler ordering* (Fenton and Zweifach, 1981). The same process should work in 3-D using confocal or MP images, providing the resolution and quality are sufficient to segment the vessel structure. While software such as Volocity can skeletonise 3-D volumes, it is not currently possible to retrieve the skeletons for further analysis or manipulation. Algorithms also exist based upon approaches other than skeletonisation, such as (Lee, Beighley *et al.*, 2007), which is based upon tracking vessels and branches from seed points in the 3-D volume, and has been used to map the vasculature of an entire organ; while this work used micro-CT imaging of the heart, the approach should also be usable with confocal data and artificial vascular networks.

The spheroid outgrowth model is somewhat different, radial outgrowths having a limited degree of branching, little interconnectedness and hence no large-scale structure. The above algorithms are based upon highly-branched tree and network structures, and hence a different approach is required in this case. For spheroid analysis, approaches for quantifying outgrowth in the rat aortic ring explant model may be more applicable, such as that taken by Blacher, Devy *et al.* (2001). Here, phase contrast microscopy was used to image the entire explant, and a series of contours were drawn around the explant at increasing distance from its edge, making the measurements independent of the explant shape. The number of microvessels present at each contour may then be determined. However, this approach does not take branching into account, and comparing treatments is complicated by the fact that the result is a frequency distribution. Korff, Kimmina *et al.* (2001) take a simpler and potentially more robust approach, determining the "cumulative sprout length" per spheroid, but this again does not take branching or sprout radii into account.

Two different approaches for analysing spheroid outgrowth are described in Section 2.7, and an example of the analysis and quantification of images of methylcellulose spheroids is illustrated graphically in Figures 2.3 and 2.4. It was not possible to use any of the above methods for analysing the spheroid outgrowth from Figure 4.16 due to the spheroids being spaced too closely, resulting in the sprouts being inseparable and hence not possible to measure accurately individually. Experiments in Chapter 5 using this model used less spheroids per unit area in order to reduce this problem and permit measurement of individual sprouts. The approach taken here was to calculate the total area occupied per spheroid, which does show differences between the different treatments, in particular the tube forming conditions result in a much more outgrowth than the control or other treatments. However, because the measurements are per-well rather than per-spheroid it was not possible to determine the error associated with these measurements. Using edge detection was not a viable approach, because the samples with large outgrowths had smaller differences in intensity change, equivalent to background changes in other samples. Using rolling ball background subtraction with a radius of 200 pixels effectively removed most of

the unwanted background staining in the gel, and this then allowed thresholding to more accurately segment the image, combined with removal of small objects to remove noise.

This crude measurement methodology permitted the quantification of the outgrowth in Figure 4.16, demonstrating that outgrowth was upregulated compared with the control when treated with bFGF, VEGF or both combined, and increased five-fold when tube-forming conditions were used, demonstrating the potency of PMA treatment in inducing angiogenic outgrowth. bFGF and VEGF act synergistically (Pepper *et al.*, 1992); each alone increased the length of tubes formed with increasing concentration, but when used in combination, dramatically increased the tube length. However, synergy between VEGF and bFGF signalling was not observed, possibly due to the error inherent in this analysis.

4.4 Conclusions

In this chapter, several of the required components of a "complete" *in vitro* vascular model have been experimented with in isolation. Two different models have been demonstrated: a vasculogenic model where ECs have self-assembled into a vascular plexus, with or without pericyte coverage, and an angiogenic model where ECs in a spheroid aggregate sprout into the surrounding matrix. While a very simple model, spheroid outgrowth is easier to quantify in terms of measurement parameters, accuracy and robustness than an entire interconnected network due to the fact that each separate spheroid is an individual biological replicate and that visualisation is simple and relatively unambiguous. In contrast, the vasculogenesis model was highly variable in terms of reproducibility and consistency, with analysis being complex, and its ability to extend and remodel being untested at present. Microfluidics and live imaging are yet to be incorporated into these models, though both were tested in isolation.

4.5 Future work

Live imaging of networks via confocal or multiphoton microscopy requires fluorescent cells. Transient transfection has been achieved using several different technologies, but in all cases is too transient for practical use with either the vasculogenesis or spheroid model due to the number of days the model requires for both set up and culture before the network or sprouting has occurred to a sufficient extent. The use of lentivirus to derive stable expression of fluorescent proteins is a potential solution, and has been shown to work with HUVECs previously, for example in Saunders *et al.* (2006). Other alternatives include label-free imaging using fluorescence life-

time imaging (FLIM), or even phase contrast provided that the gels are sufficiently thin to allow visualisation of fine detail.

A future alternative to both photolithography and PEN film for the creating of PDMS moulds is direct fabrication using 3-D printing technology. While such technologies are currently limited by resolution at the scale of the PEN networks created above, some efforts have been made to manufacture 3-D objects using 3-D photopolymerisation and 2 photon photoinitiator absorption to drive the polymerisation reaction, permitting an object to be created or patterned using multiphoton microscope-driven excitation or stereolithography (Arcaute, Mann *et al.*, 2006; Engelhardt, Hoch *et al.*, 2011; Lee, Moon *et al.*, 2008). Biomaterials mimicking collagen have also been created which could also take advantage of this technology (*e.g.* Lee, Lee *et al.* (2006a)), which could potentially allow direct polymerisation of a cell-seeded matrix with a functional microfluidic network within it, obviating the need for PDMS moulding entirely.

The current limiting factor is in the physical properties of the extracellular matrix, where the current choices are either using a biologically relevant but weak matrix such as collagen, or strong matrix based upon artificial polymers which is not biocompatible. The challenge is to find a biocompatible matrix which permits the biological processes of interest to take place whilst also having desirable physical characteristics. There is much ongoing work in the biomaterials field to produce vascularised constructs for surgical purposes, which may be equally adaptable for this use, or used as a basis for further research in this area. A different approach to micromoulding would be the use of scaffold material which may be selectively photopolymerised, or better, ablated, by MP laser excitation may permit direct creation of microfluidics in cell-laden hydrogels, providing that such direct control over microscope hardware is possible and that photopolymerisation and/or ablation is compatible with direct cell seeding.

Attempts to coculture HUVECs with VSMCs were not as successful as previously-published work. This might be due to the culture conditions or the smooth muscle types used, so further investigation of the coculture system might provide new insights into factors involved in the formation and stabilisation of a vascular network. Spheroids containing both cell types formed, but did not result in stable associations, with the C3H/10T½ migrating freely through the gel (not shown). Further work to integrate smooth muscle with the spheroid outgrowth model would allow more complex situations to be modelled, since EC–VSMC interactions result in the production of basement membrane proteins, such as laminin, fibronectin, collagen IV, perlecan, nidogen, *etc.*, which will stabilise and modulate cellular interactions and behaviour, being a more complete, and hence physiologically relevant, model. This would allow, for example, study of angiogenesis as a consequence of disruption of the smooth muscle layer.

This work did not explicitly investigate the proliferation and viability of cells in the culture models used. The issue with necrosis in larger gels, and potential apoptosis in control gels or under conditions where the necessary survival cues are not present, indicates a need to investigate the extent to which it occurs and its causes in order to use a model without these additional factors complicating observations. This would allow the observation of apoptosis as part of vascular regression and homeostasis without additional unwanted effects complicating interpretation.

In order to further understand the signalling and developmental processes at work in the spheroid model, it would be useful to examine the spheroid structure in more detail. Cells at the outer surface in contact with the matrix may show apical-basal polarity, while those in the centre surrounded entirely by cells may not, and may even have a tendency towards apoptosis if in an unsuitable environment (Korff and Augustin, 1998). This should be possible to investigate using TEM to examine cellular ultrastructure and immunofluorescence to localise junctional and basement-associated proteins, as well as to assess cell viability and proliferation within the spheroid.

Spheroid gels may also be a useful means for investigating the effects of growth factors, inhibitors and matrix properties used in combination with microfluidics. Shamloo and Heilshorn (2010) have used endothelial-coated dextran beads to investigate matrix stiffness and growth factor gradients in a microfluidic device. However, spheroids may provide a more realistic model, in particular beads may result in an incorrect polarisation of the EC layer, and were significantly larger, though they are readily be produced in greater quantity than spheroids, which require manual pipetting. Similar microfluidic designs, for example Jeong, Kwon *et al.* (2011), have also been used to model EC responses to growth factor gradients. The benefit of this type of device is precise control over growth factor or inhibitor concentration through the creation of a defined concentration gradient between the source and sink, which would allow much greater control over effective concentrations than in static 3-D cultures where diffusion is passive, though both are potentially affected by matrix interaction in addition. Such a system may be used to model the combination of bulk flow of interstitial fluid between capillaries and lymphatics (source and sink) combined with the effects of factors arising from cells and tissues within the gel, the diffusion and interactions of which will be modulated by the bulk flow.

Chapter 5

Role of vascularisation in lymph node development

5.1 Introduction

5.1.1 Cellular interactions and signalling during LN development

As discussed in Section 1.3.3, secondary lymphoid organs develop as a result of the interaction between lymphoid tissue inducer and organiser cells. Briefly, following initial attraction of LTis as a result of LTo expression of chemokines such as CXCL13 and CCL21, LTis activate the LTβR-bearing LTos by LT expression, leading to upregulation of cytokines, adhesion molecules and TRANCE with positive feedback as a result of increased LTi recruitment causing further increase in LTo activation (van de Pavert and Mebius, 2010; van de Pavert *et al.*, 2009; Vondenhoff *et al.*, 2009a). LTis express both TRANCE and TRANCER, leading to activation of LTis as they come into intimate contact, leading to further LT upregulation and local clustering and retention of LTis (Vondenhoff *et al.*, 2009a). The cellular interactions and signalling processes involved are now fairly well established, though the means by which the initial sites for LN development are specified are still not fully understood. The above interactions are required to establish a functional stromal environment in the LN, which is subsequently followed by compartmentalisation into T and B cell zones (Bajénoff *et al.*, 2006). However, the LN is also defined by its unique association of blood and lymphatic vasculature, which develop to some extent independently, and whose development is initiated *prior* to LTi infiltration (Bénézech *et al.*, 2010). The means by which the developing anlagen is subsequently vascularised are also not well understood, and the spheroid model developed by Korff and Augustin (1998) and in Chapter 4 could potentially be used to elucidate the mechanisms which drive this process.

Existing work shows LNs to be vascularised at later stages of development, for example after E17.5 when HEVs begin to express PNAd, subsequently permitting

lymphocytes to infiltrate the anlagen (Mebius, 2003; Randall, Carragher *et al.*, 2008). The process of lymphocyte entry into the anlagen is most likely to be dependent upon a functional vascular network, and particularly a HEV network to permit efficient extravasation and inmigration (Willard-Mack, 2006). In the adult LN, lymphatic and HEV maintenance is dependent upon LTβR (Liao and Ruddle, 2006), and this may also apply to the developing anlagen, which is surrounded by a lymph sac and contains vessels expressing LTβR (Vondenhoff *et al.*, 2009a). Initially the HEVs express MAdCAM, and only later express PNAd (Mebius, Streeter *et al.*, 1996), restricting initial lymphocyte migration to LTi and $\gamma\delta$ T cells, and only later permitting entry of naïve T and B cells, which act as a source of LT signalling in place of LTis (Randall *et al.*, 2008). Changes in LT signalling may drive maturation and expansion of the nacent blood vasculature in the anlagen. An alternative route for lymphocytes would be to migrate through the surrounding tissue after extravasation elsewhere, perhaps in a similar manner to the initial LTis, though the lymph sac may present a physical barrier to migration; this is however unlikely to play a major role following the establishment of a functional HEV network.

While blood vessels are clearly present at later stages, this does not preclude their presence at earlier stages, with blood vasculature being visible in at least the brachial node at E14.5 (Vondenhoff *et al.*, 2009a), containing both VEGFR2^{+}MECA32^{+} and VEGFR1^{+}VEGFR2^{+}MECA32$^{-/\mathrm{low}}$ vessels, which could represent venous and arterial supply, respectively. Other nodes such as the inguinal node could not be identified by Vondenhoff *et al.* (2009a), but this was not a problem using hCD2-GFP embryos, where the inguinal anlagen was clearly visible, albeit slightly smaller and having more diffuse LTi distribution than the axillary and brachial nodes. However, the embryonic origin of these vessels is not known, and the cells could have arisen from the surrounding lymph sac, which is known to contain cells of both blood and lymphatic character (Cupedo *et al.*, 2004), or infiltrated from external vessels through angiogenesis or migration of single cells. Despite this finding, most current models of lymph node development consider vascularisation to be a late stage development, prior to lymphocyte ingress, as discussed in a recent review by Coles *et al.* (2010). At other sites, such as the lymph sac adjacent to the cardinal vein, vessels are entirely absent at E14.5, as shown by Hirashima, Sano *et al.* (2008). This discrepancy may be explained by the majority of vascular development being extensive elaboration at later stages of a small network present at early stages, which may have been missed by other workers. This may have been due to the difficultly of obtaining anlagen at early stages; in particular due to identification of anlagen prior to LTi infiltration, early stage development has not been studied in the same detail as later stages. Prior to the advent of suitable transgenic mouse models such as the hCD2-GFP mouse enabling identification and isolation of the anlagen, study via serial sectioning was haphazard at best and may have resulted in miss-identification or lack of identific-

ation of important features of LN development. Endothelial and basement membrane marker expression change during development, for example the expression of endomucin only at later stages in comparison with CD31 (Foster *et al.*, 2008) which may lead to the mistaken assumption that vascular endothelium is not present when immunofluorescence, for example, fails to show endothelial staining. This may indeed have been an issue with the wholemount and frozen section imaging of LN anlagen in the Chapter 3.

Here, the assumption is made that the anlagen is initially avascular (bar the lymph sac), though the true state of vascularisation during early anlagen formation (prior to E14.5, and possibly later) is not well established. Given that this assumption is correct, it must therefore become vascularised at some point during development, and it was hypothesised that this is as a result of ingrowth of existing vasculature via angiogenesis in response to the production of pro-angiogenic signalling from the anlagen, possibly as a result of hypoxia and metabolic demands as the tissue condenses (Nanka *et al.*, 2006). Alternatively, this could be due to the infiltration of single endothelial cells followed by *de novo* assembly of the vascular bed (*i.e.* vasculogenesis), later followed by connection to the external vasculature, *i.e.* similar to lymph sac formation from local veins. This would presumably also depend upon the production of pro-angiogenic and/or chemoattractant molecules from the anlagen, such as VEGF and bFGF. It might additionally be hypothesised that the anlagen will also produce anti-angiogenic molecules to precisely regulate the point at which vascularisation occurs, which may lead to a switch between anti- and pro-angiogenic states, and potentially a switch back from pro- to anti-angiogenic (or at least a neutral state to maintain the vasculature) once vascularisation is complete, to prevent hypervascularisation.

5.1.2 Study of vascularisation mechanisms using an *in vitro* model

If the evidence of a vascular supply (arterial and venous vessels) at the centre of the anlagen at E14.5 is correct, this primitive network must expand and elaborate dramatically during subsequent days to give rise to the complex HEV-containing vascular network found in the mature organ. The spheroid model may be able to provide some insight into the processes driving these changes. In Chapter 4, it was demonstrated that the spheroid model was responsive to growth factors, seen as increased sprouting into the surrounding gel. More growth was seen when the spheroids were exposed to more potent combinations of factors. This model may be equally useful for studying LN development and vascularisation. If LN anlagen were carefully dissected from hCD2-GFP mice, and embedded into a gel containing endothelial spheroids, it should be possible to determine whether the rate of outgrowth of the spheroids is greater or less than a control gel containing spheroids only. Additionally, due to the placement of spheroids in the gel, it should also be additionally possible

to study *spatial* relationships as a consequence of soluble growth factors or inhibitors diffusing through the gel, as well as physical forces (Korff and Augustin, 1999). A schematic illustration of how the model would allow the study of spatial effects is shown in Figure 5.1. Using this model, it should therefore be possible to determine if the combination of all factors produced by the anlagen result in a *net* pro- or anti-angiogenic environment, and with the addition of inhibitors and exogenous growth factors it may be possible to use this model to dissect the signalling pathways via blockade and rescue of specific signalling steps.

5.1.3 Aims

1. To determine if the spheroid outgrowth model may be used to quantify the spatial distribution of growth factors and/or inhibitors.

2. To determine if developing lymphoid organs promote or retard angiogenesis using the spheroid outgrowth model.

3. To determine if during the timecourse of development there are changes in any observed effects.

4. To determine the general mechanisms by which any observed effects take place.

5.2 Results

5.2.1 Lymphoid explants suppress spheroid angiogenesis

LN anlagen (axillary, brachial, cervical and inguinal) and thymi were dissected from E15.5 hCD2-GFP mouse embryos and transferred into PBS on ice. HUVEC methylcellulose spheroids made as described in Section 2.5 were recovered, spun down and resuspended in neutralised collagen solution as described in Section 2.4.1. The spheroid–collagen suspension was then pipetted into three glass-bottomed dishes (Iwaki) containing ethanol-sterilised nylon rings of defined volume (6 mm diameter, 1 mm deep), on ice. To prevent leakage of the spheroid-collagen suspension, and to prevent the nylon rings from floating in the culture medium given their low density, the rings were sealed to the cover glass using vacuum grease (Dow Corning). Selected LN anlagen and thymi were transferred into the collagen gels and gently mixed in. No tissue was transferred into the control gel, which contained HUVEC spheroids only. Following gelling of the collagen at 15 °C for 1 hour, each gel was overlaid with ECGM and incubated at 37 °C for 48 hours. The gels were fixed in 4 % PFA for 1 hour, washed three times in PBS, and then stained for CD31 and GFP to allow visualisation of the HUVECs and hCD2-GFP$^+$ cells (LTi cells in the LN anlagen

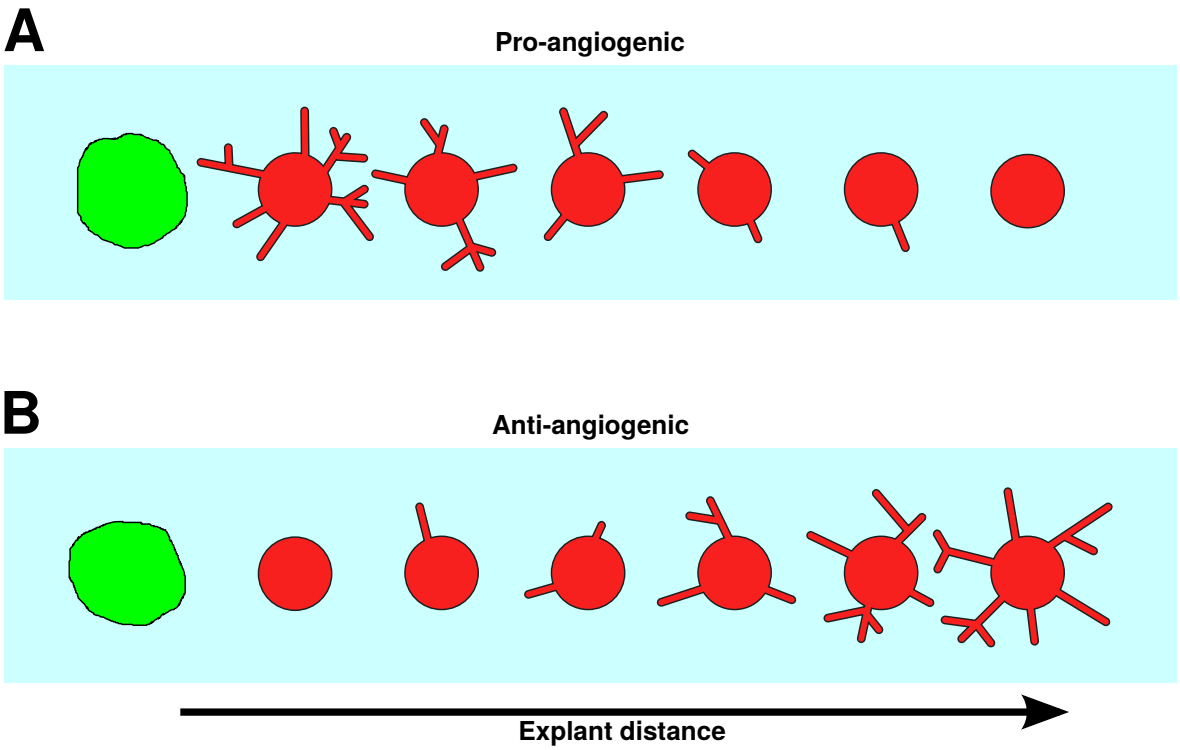

Figure 5.1: Predicted behaviour of the spheroid model. If a tissue explant produces predominantly pro-angiogenic soluble factors (A), these would be expected to increase angiogenesis locally, with the effect decreasing with distance as the concentration falls. If the explant is producing mainly anti-angiogenic soluble factors (B), the opposite effect would be predicted, with angiogenesis being suppressed in close proximity to the explant, the effect again decreasing with distance.

and LTis and lymphocytes in the thymus). Mouse anti-human CD31 clone 10G9 was used with goat anti-mouse AF594 secondary and GFP-AF488.

The gels were sufficiently large (3-4 mm approximate final minimum diameter following gel contraction) that it was not possible to image using a single field of view. The GFP (green) and CD31 (red) channels were imaged separately, comprising between 8–14 overlapping monochrome images per channel, which were later recombined as described in Section 2.6.6. The assembled images are shown in Figure 5.2, with image analysis data (described below) overlaid over each image. The edges of the LN and thymus explants were determined using thresholding to distinguish between local background and hCD2-GFP fluorescence.

There is a certain amount of variation in the amount of outgrowth between the spheroids in the control sample, with all but a few spheroids having multiple outgrowths of at least 100–200 µm. A similar observation may be made for the sample containing the thymus explant, however spheroids in close proximity to the explants appear to have reduced outgrowth in comparison to their counterparts at further distances. A directional effect was also seen; in several cases outgrowths were only seen on the side of the spheroid distant to the explant, while on the near side there was little or no outgrowth (examples: spheroids 16, 19, 20, 27 and 29). These spheroids appeared at an intermediate distance from the explant, while those nearer (*e.g.* 17, 23, 31, 34) showed suppression on all sides, and those at further distance (*e.g.* 4, 6, 30, 40) showed long outgrowths on all sides. A similar effect was seen in the LN explant gel, however due to the greater number of smaller LN explants in place, the maximum distance a spheroid may be found from an explant was reduced, and the close packing of spheroids in the gel made accurate analysis of all spheroids impossible, analysis of touching spheroids being omitted. However, it was again possible to make the general observation that spheroids in close proximity to an explant (*e.g.* 18, 28, 32, 36, 41, 42, 46) outgrew less than at greater distance (*e.g.* 3–7). Differential outgrowth at intermediate distances was not as clearly visible in this gel, but might be present (*e.g.* 14, 22, 25).

5.2.2 Determination of optimal image analysis strategy

Image analysis was performed using the strategies described in Figure 2.3 (panels C–F). The total number of sprout tips, initial minimum and final maximum radii, perimeter length, area and total outgrowth length were measured using ImageJ (Abràmoff, Magalhães *et al.*, 2004; Rasband, 1997-2011). Figures 5.3, 5.4 and 5.5 show the results of this analysis following export of the measured data and visualisation using the R statistical package (R Development Core Team, 2006). The primary measurement parameters in Figure 5.3 showed close correlation with each other with high R^2 values using linear regression. In order to determine which parameters most closely represent angiogenic outgrowth, an unbiased pairwise comparison without

a priori expectations was performed between each parameter correlation in order to rank the measurement parameters. This was performed for the control and thymus only, the LN sample having limited utility owing to the limited range of several of the parameters, which might have introduced bias. The process and results are detailed in Table 5.1. The ranks for each parameter were summed in order to compute a summed rank for each. Both control and thymus samples show similar results, with perimeter length and total sprout length being most highly correlated, *i.e.* measuring very similar features. In contrast, sprouts and surface area do not correlate as well overall, and do not correlate well with each other, *i.e.* are not measuring similar features. Outer radius is the poorest measure of outgrowth, showing limited correlation overall.

5.2.3 Quantification of angiogenesis suppression

In order to determine if distance from LN or thymus explant affected the amount of spheroid outgrowth, the number of sprouts and total sprout length were plotted against the distance from each spheroid to the explant. Additionally, the derived parameters radius ratio (outer/inner radius) and area ratio (perimeter/area) were also plotted (Figure 5.4). In all cases, a significant amount of variability complicated interpretation, reduced by grouping the measurements into 250 µm bands with distance from the explant in order to reduce the effects of noise, effectively the same strategy as employed by Blacher *et al.* (2001) to quantify aortic ring outgrowth. A positive relationship was seen for both the LN and thymus samples, the general trend being a reduction in spheroid outgrowth closer to the explant, *i.e.* local suppression of angiogenesis. The correlation was generally stronger for all measurement parameters for the LN sample, despite the thymus sample having an extended distribution over distance. R^2 values were generally low due to there being a large amount of intrinsic variation which could not be accounted for by the fitted line; while the LN relationship appeared to be approximately linear, this was not the case for the thymus, perhaps due to outgrowth reaching a plateau after a certain distance. The best correlation was seen with the total sprout length parameter, followed by the radius ratio parameter derived from the outer radius, which was unexpected due to the inner radius term serving mainly to introduce noise. The radius ratio was shown to correlate poorly with the other parameters in the previous section. The area ratio was extremely noisy and the thymus value was very poor; while the perimeter length appeared to be a good measure of outgrowth, combining it with the surface area introduced a large amount of noise. In contrast, the number of sprouts and total sprout length which were used underived showed a much higher R^2 values for the LN, which appeared to reflect the dataset more closely—the higher values seen for the derived parameters may be artefactual.

In order to determine if proximity of spheroids to each other, rather than the

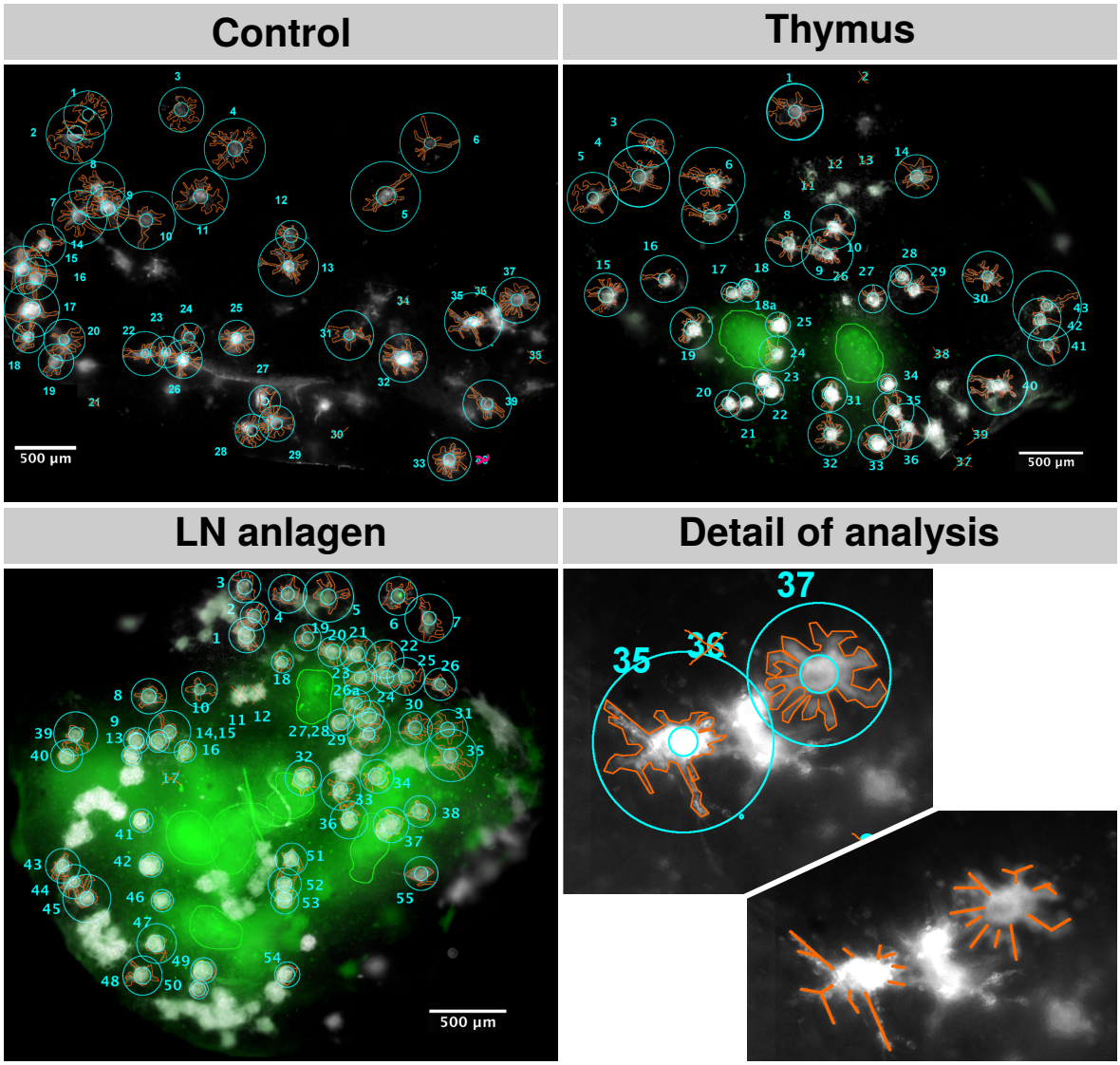

Figure 5.2: E15.5 lymphoid tissue explants suppress HUVEC spheroid tube outgrowth. HUVECs were stained using anti-CD31 with Alexa Fluor 594 (white) and explants using anti-GFP-Alexa Fluor 488 (green). Measurements are overlaid in cyan (inner and outer radius) and orange (perimeter/area and sprout length), with the borders of the GFP$^+$ explants outlined in green. Magnified views showing analysis of the control sample in greater detail are shown on the bottom right. The analysis is identical to that described in Figure 2.3. The control gel contained spheroids only, while the LN and thymus gels contained LNs and thymi from E15.5 hCD2-GFP embryos.

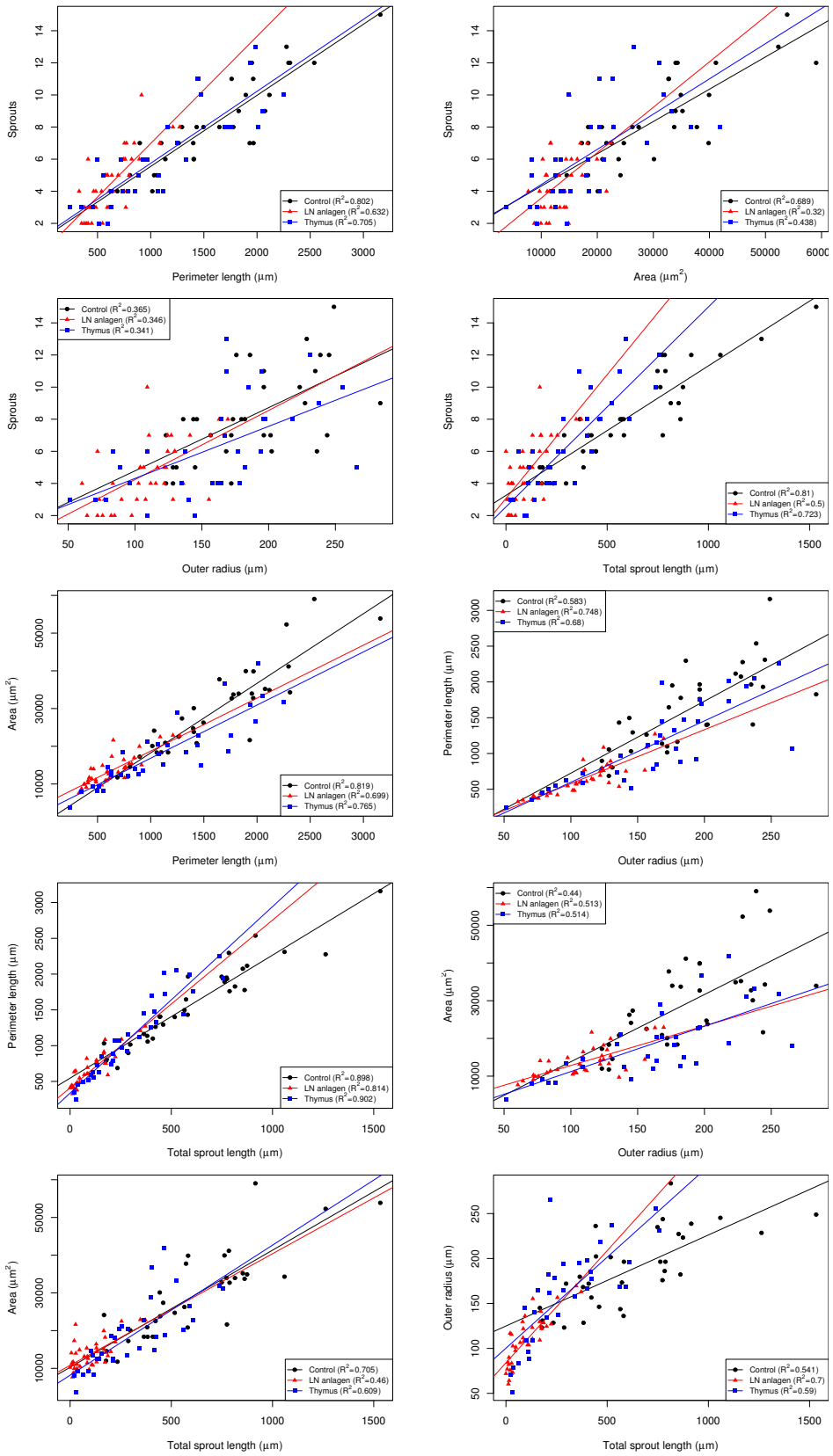

Figure 5.3: Correlations between E15.5 primary measurement parameters. The association between the measured parameters *sprouts perimeter length area,* and *total sprout length* are shown in all possible pairwise combinations. The coefficient of determination (R^2) for each sample shows the proportion of the variation accounted for by simple (least squares) linear regression.

Table 5.1: Determination of optimal image analysis strategy for E15.5 explants. Strategies were ranked in ascending order from highest to lowest correlation, using pairwise comparisons with the strategy listed under "rank" being common to the comparisons. The strategies are ordered by the sum of all their ranks, with perimeter length and total sprout length having the highest relative correlations overall. The rank sum is also shown excluding the outer radius, due to this measurement introducing a large amount of noise which could bias the other rankings. The lymph node sample was omitted here due to the limited range of explant distances biasing the measurements.

	Rank						
Strategy	*Perimeter length*	*Total sprout length*	*Sprouts*	*Area*	*Outer radius*	*Rank sum*[a]	*Rank sum*[b]
			Control				
Perimeter length	-	1	2	1	1	5	4
Total sprout length	1	-	1	2	2	6	4
Sprouts	3	2	-	3	4	12	8
Area	2	3	3	-	3	11	8
Outer radius	4	4	4	4	-	16	-
			Thymus				
Perimeter length	-	1	2	1	1	5	4
Total sprout length	1	-	1	2	2	6	4
Sprouts	2	2	-	4	4	12	7
Area	3	3	3	-	3	12	9
Outer radius	4	4	4	3	-	15	-

[a] Of all strategies
[b] Excluding outer radius

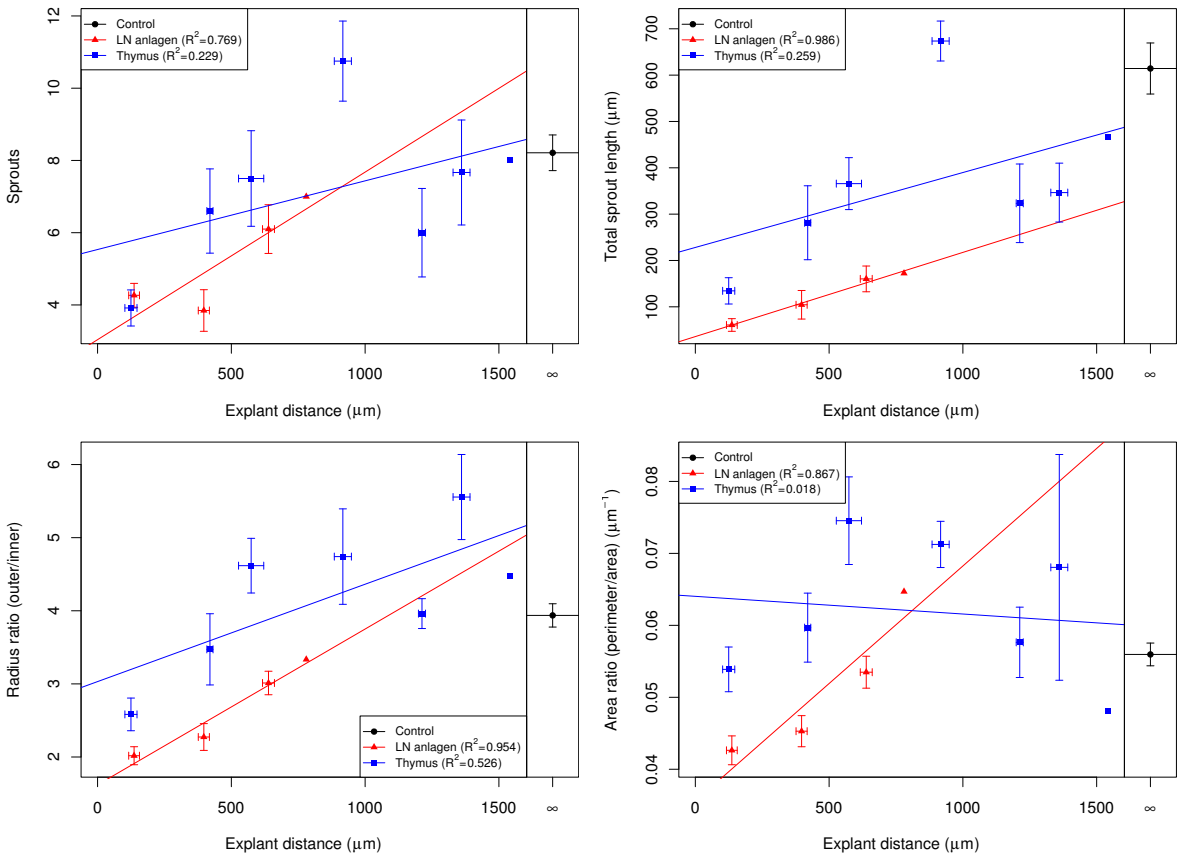

Figure 5.4: Relationship between E15.5 spheroid outgrowth and distance to tissue explant. The primary measurement parameters *sprouts* and *total sprout length* and derived parameters *perimeter:area ratio* and *outer:inner radius ratio* have been plotted against distance from the explant (shown as effectively infinite for the control). The measurements were grouped into 250 µm explant distance bands, with the mean and standard error of the mean calculated for the explant distance and measured parameter for each group. The coefficient of determination (R^2) for each sample shows the proportion of the variation accounted for by simple (least squares) linear regression. All parameters show suppression of angiogenesis in close proximity to the explant with the exception of the the thymus for *perimeter:area ratio* which shows a weak correlation only.

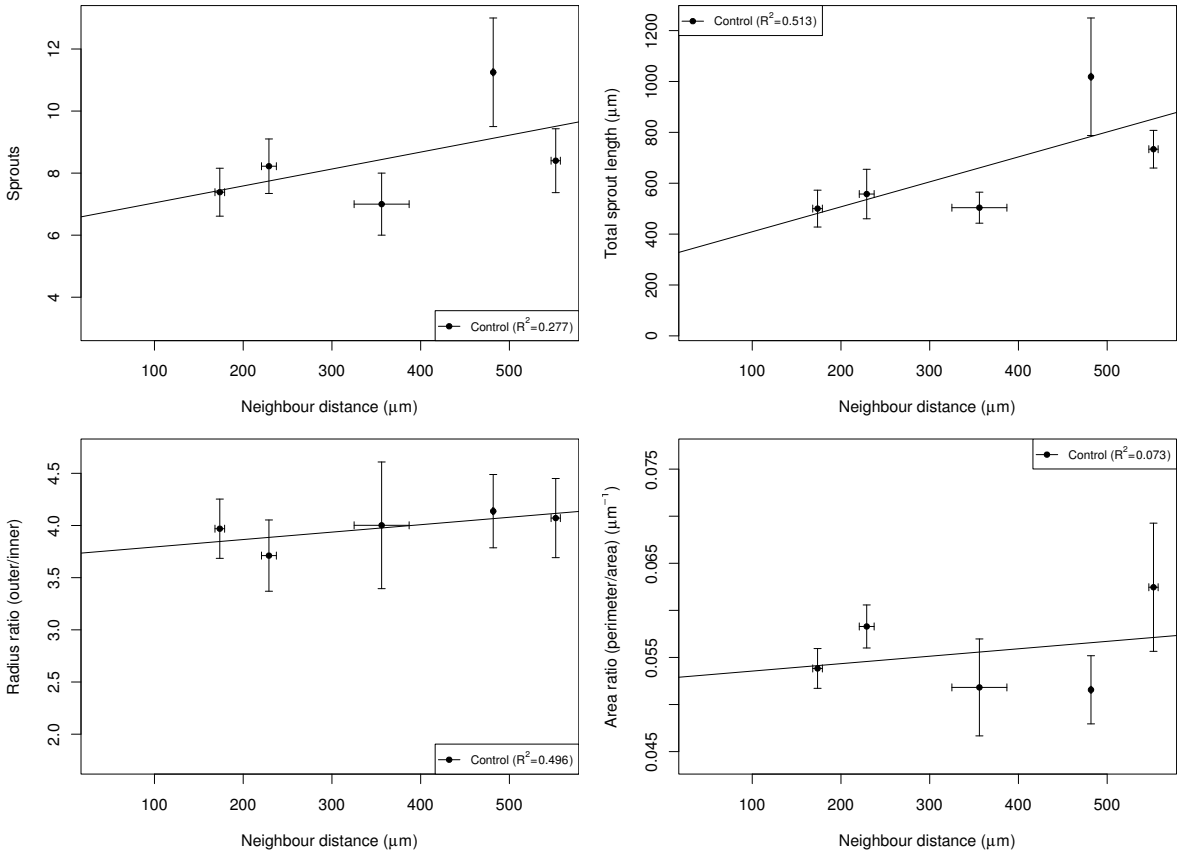

Figure 5.5: Relationship between E15.5 spheroid outgrowth and distance to neighbouring spheroids. The primary measurement parameters *sprouts* and *total sprout length* and derived parameters *perimeter:area ratio* and *outer:inner radius ratio* have been plotted against distance to nearest neighbouring spheroid. The measurements were grouped into 250 μm neighbour distance bands, with the mean and standard error of the mean calculated for the neighbour distance and measured parameter for each group. The coefficient of determination (R^2) for each sample shows the proportion of the variation accounted for by simple (least squares) linear regression. The control sample, which is not subject to the additional effects of tissue explants, shows a weak positive correlation for all parameters except *total sprout length* which shows a stronger correlation, possibly due to the influence of outliers.

LN anlagen or thymus explants, caused the observed differences in spheroid outgrowth, neighbour distance (distance from spheroid to nearest neighbour) was plotted against the same measurement parameters used above (Figure 5.5). The comments above regarding measurement parameters apply equally here. These data exhibited too much variability to show any robust trend, but there was a possible relationship between neighbour distance and total number of sprouts or total sprout length for the LN and thymus samples (not shown). In the LN and thymus samples, spheroids were more closely spaced nearer the explants, which would result in correlation between neighbour distance and the measured parameters when the effect was really due to the explant. For this reason, the control sample was the only useful sample to observe, the other samples being omitted from the plots, and this showed some correlation for several measurement parameters, but for sprouts and total sprout length it was biased by two very large measurements.

Due to noise in the measured outlines, the perimeter:area ratio for a spheroid without any outgrowths may actually be similar to a spheroid with large outgrowths, due to the roughness of the outline leading to a disproportionate increase in the perimeter length compared with the surface area. Adding several erosion or dilation steps to the analysis protocol may reduce the contribution of high-frequency noise and 2-D outgrowth under the collagen gel in the images, both of which introduce additional unwanted variation. Additionally, single large measurements exerted a disproportionate effect upon the mean of some points in the distribution plots. Spheroids of incorrect initial size were excluded, it being necessary to exclude small fragments of spheroids and joined spheroids which were too large, and not meaningful to include in the analysis.

5.2.4 Collagen matrix does not affect angiogenesis suppression

In order to determine if reduced tube outgrowth in proximity to tissue explants was due to a lack of collagen formation, perhaps due to dilution of the collagen with PBS or due to secretion of MMPs or MMP inhibitors by the explant, selected spheroids were imaged using MP microscopy to visualise the collagen fibres (Figure 5.6). Spheroids were imaged both near to the explants, where angiogenesis was seen to be suppressed, and at a distance of several millimetres where it was not. Collagen fibres were seen in all cases in intimate association with the spheroids. Spheroids adjacent to the explants were almost perfectly spherical with little evidence of outgrowth; a small number of round single cells were seen close to the spheroids, but were not in contact with them. In contrast, the control sample, and explant samples distant from the explant, contained spheroids with a large number of sprouts extending radially away from the spheroid surface, some showing evidence of branching. A larger number of rounded single cells were also in evidence at further distance than seen for the adjacent spheroids.

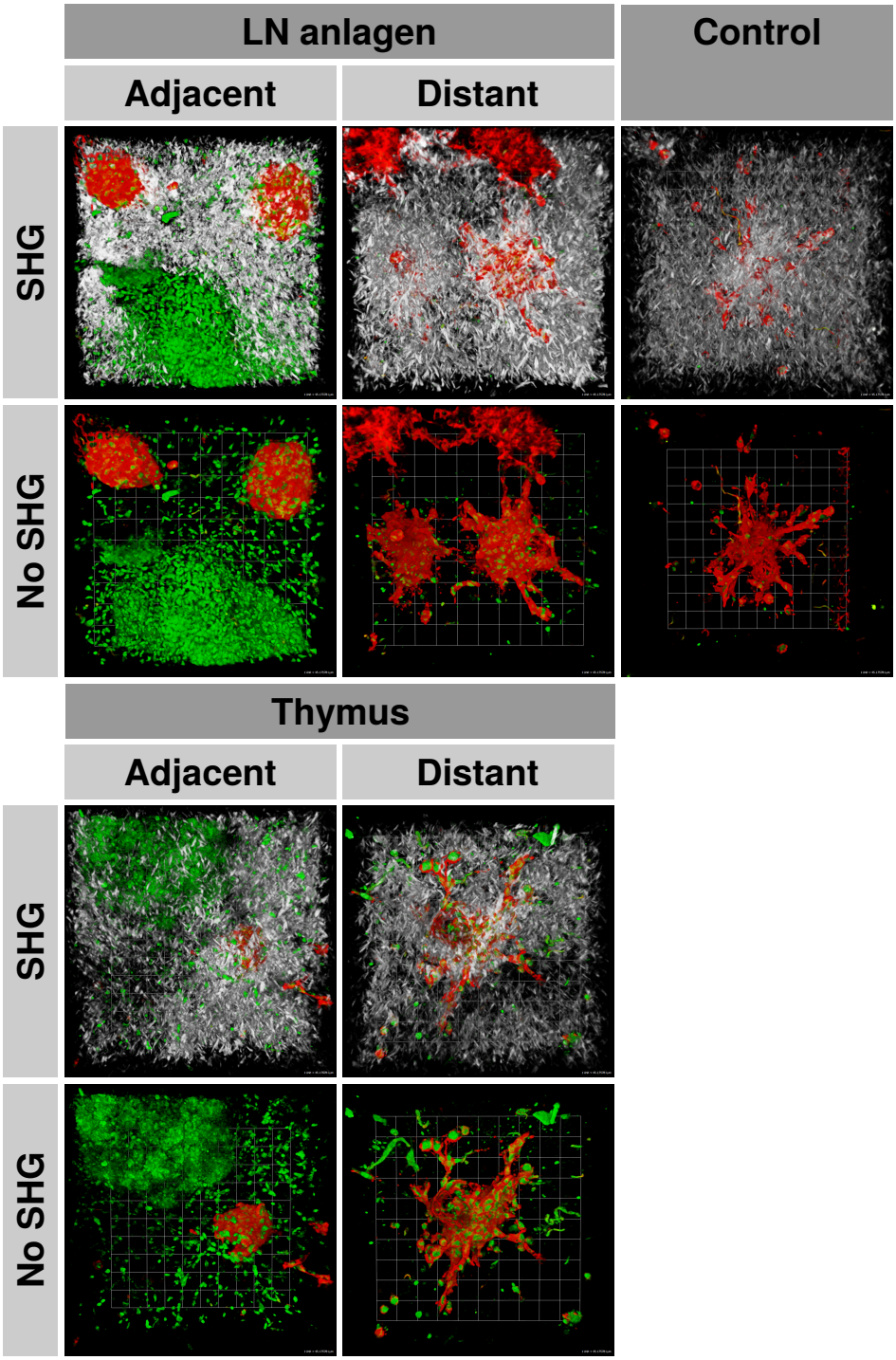

Figure 5.6: Effect of collagen matrix upon tube outgrowth. Using SHG, collagen fibres (white) were imaged in addition to hCD2-GFP (green) and CD31 (red). In treatments containing E15.5 tissue explants, spheroids were imaged both adjacent to and at a distance ($>$ 1 mm) from the explants. In all cases, collagen fibres are seen in intimate contact with both the spheroid and its outgrowing tubes, and additionally surrounding the explant. Collagen fibres are slightly denser where in intimate contact the the spheroid and any tube outgrowth, but are otherwise continuous with some variation in local density, possibly a result of gel contraction by nearby spheroids. The second harmonics have been removed in the bottom panels to permit an unobscured view of the spheroid and explant structures. Tube outgrowth in spheroids distant to the LN or thymus explant is comparable to the control sample containing no explant. Tube outgrowth in spheroids adjacent to explants is almost entirely absent, spheroids having an almost perfectly spherical shape. GFP^+ cells appear to have migrated out of the explanted tissues some way into the collagen gel. Scale is 45 µm.

In addition to the collagen structure, these images showed that for both the LN and thymus samples, GFP^+ cells were present in the matrix up to at least 300 µm from the tissue explant. It is not clear if these have migrated out into the gel from the explant, or were dispersed in the gel when mixing the tissue into the collagen solution prior to gelling.

5.2.5 High throughput screening of explant–spheroid interactions

Following the initial experiments using the HUVEC spheroid model with E15.5 tissue explants, the protocol was scaled up to allow larger scale experiments using multi-well plates. Axillary, brachial, cervical and inguinal LNs and thymi were taken from E14.5–E17.5 mice. Additionally, the skin above the brachial node was taken as a control for vascularised tissue. A spheroid-seeded 3 mg/mL neutralised collagen solution was introduced into 6 mm diameter, 1 mm thick steel rings in the wells of a 24-well plate, chilled to 4 °C on ice. Tissue explants were gently mixed into the collagen solution using fine forceps, and the collagen was then set at 37 °C for 10 mins before overlaying with ECGM. The gels were cultured for 24 hours prior to fixing with 4 % PFA for 1 hour and then washed with PBS before staining with GFP-AF488 and CD31 with an AF594 secondary, as for the previous experiment, followed by 1:5000 DAPI (5 mg/mL stock). Half of the tissue samples were fixed with PFA for 60 mins prior to addition to the collagen; these samples were controls to demonstrate that any effects were due to soluble factors being actively produced by the explant, since in fixed samples soluble factors should be fixed to the matrix and the cells should be killed and hence unable to actively produce more.

Images of gels in 24-well plates were obtained through high thoughput plate imaging using an ImageXpress epifluorescence system (Molecular Devices), which was used to acquire z-stacks of tiled epifluorescence images, which were subsequently assembled into colour z-stacks using ImageJ as described in Section 2.6.6. Representative wells for E14.5 explants are shown in Figure 5.7, and for E17.5 explants in Figure 5.8. Note that these images are maximum intensity projections of the z-stacks, and contain out of focus information due to each spheroid being in focus only in a specific subset of the planes; during analysis, each spheroid outgrowth was measured individually in the correct focal plane (or planes, for sprouts growing at angles passing through multiple focal planes).

The same trends observed previously with the E15.5 explants were also seen with the E14.5 and E17.5 explants: spheroid outgrowth was reduced or eliminated entirely in close proximity to the explants, while appearing normal at further distance. When PFA fixed explants were used, the outgrowth in close proximity to the explants appeared to be normal, equivalent to outgrowth at further distance. Additionally, skin explants did not appear to suppress angiogenesis either, showing equivalent outgrowth to the control sample, the same also applying to unfixed explants at fur-

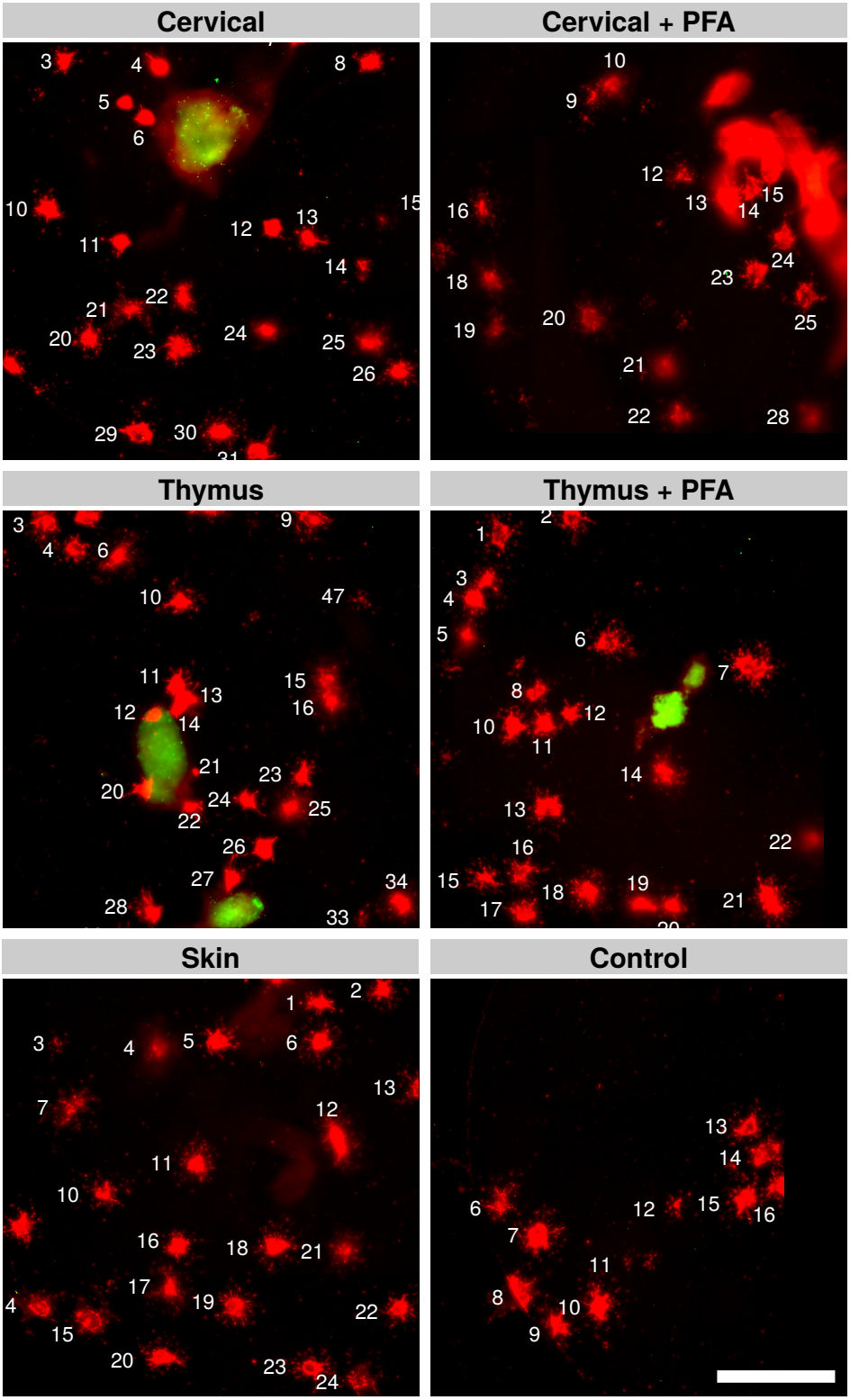

Figure 5.7: E14.5 explants suppress angiogenesis. Cervical node, thymus and skin from an E14.5 embryo were embedded in a collagen gel seeded with HUVEC spheroids. Inhibition of tube outgrowth from the spheroids is clearly visible in close proximity to the cervical LN explant, whilst the effect is not observed at distant sites. When the cervical node is PFA fixed prior to embedding in the gel, no inhibition of outgrowth is seen at any distance from the explant. The same trend was observed when repeating using the thymus in place of LNs. Using skin from above the brachial node, angiogenesis does not appear to be suppressed. The spheroid only control shows the basal outgrowth rate of sprouts from the spheroids. Spheroids have been annotated with numbers to allow identification during analysis. Images are representative views of 6 mm diameter wells; scale bar is 1 mm.

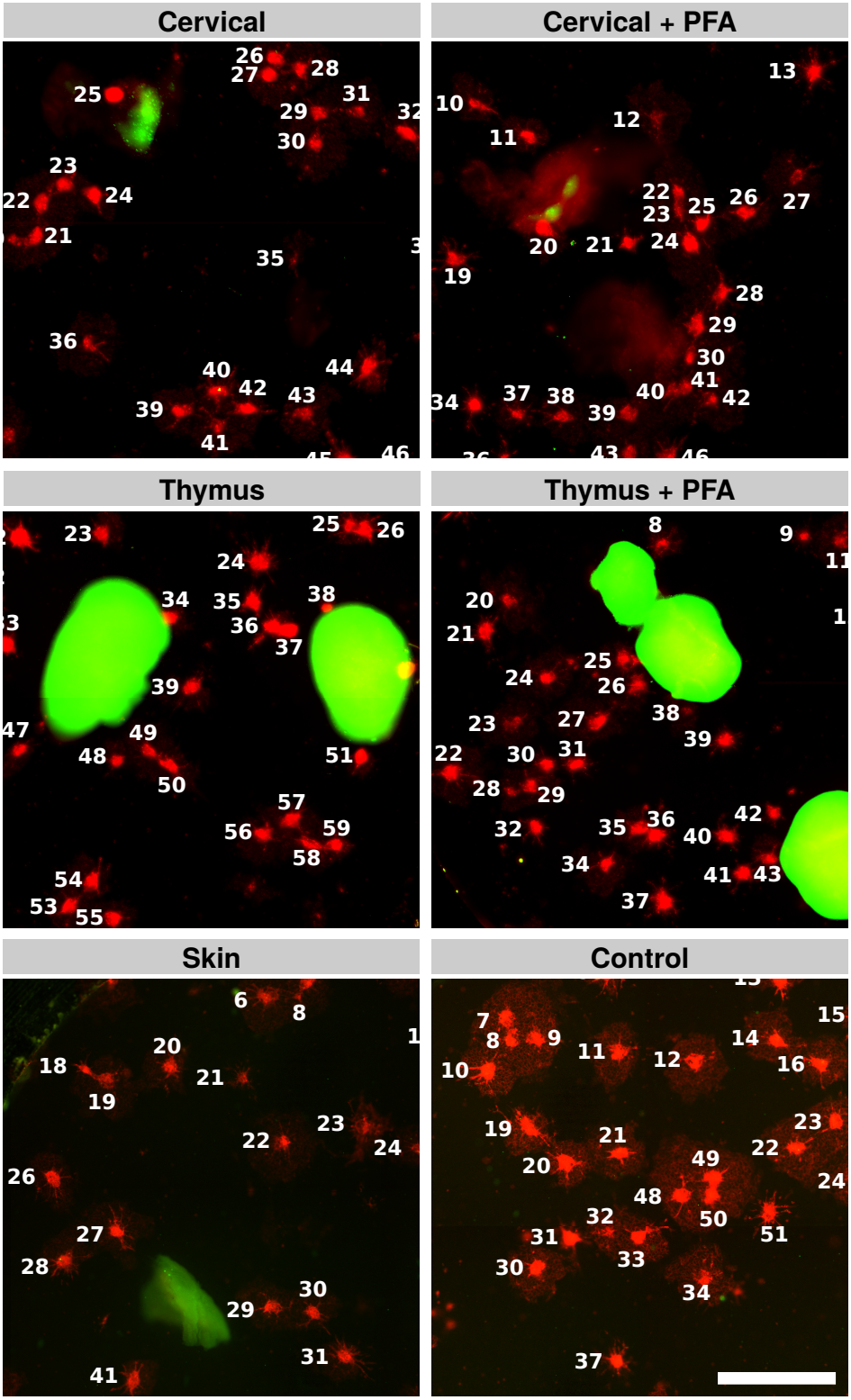

Figure 5.8: E17.5 explants suppress angiogenesis. Cervical node, thymus and skin from an E17.5 embryo were embedded in a collagen gel seeded with HUVEC spheroids. Inhibition of tube outgrowth from the spheroids is clearly visible in close proximity to the cervical LN explant, whilst the effect is not observed at distant sites. When the cervical node is PFA fixed prior to embedding in the gel, no inhibition of outgrowth is seen at any distance from the explant. The same trend was observed when repeating using the thymus in place of LNs. Using skin from above the brachial node, angiogenesis does not appear to be suppressed. The spheroid only control shows the basal outgrowth rate of sprouts from the spheroids. Spheroids have been annotated with numbers to allow identification during analysis. Images are representative views of 6 mm diameter wells; scale bar is 1 mm.

ther distance from the explants. The images were analysed using ImageJ using custom macros to analyse the images as detailed in Section 2.7.2 and Figure 2.4. Automated analysis was unfortunately incompatible with epifluorescence z-stacks, necessitating manual analysis as detailed in Section 2.7.1 and Figure 2.3. Using manual analysis, the total sprout outgrowth length was measured for both E14.5 and E17.5, in addition to the number of sprouts and maximum spheroid outgrowth length (Feret's diameter) for E14.5 only, using ImageJ to perform the measurements. The results are shown in Figures 5.10 and 5.11.

Correlation plots, as for the previous experiment, show relatedness between the different measurement parameters; ordering by rank is shown in Table 5.2. Overall, total sprout length was the most highly-correlated, followed, by maximum outgrowth length and then number of sprouts. Plots of spheroid outgrowth against distance from explant showed that the cervical LN and thymus resulted in a positive relationship due to the local suppression of outgrowth with a relatively high R^2 value (when taking into account the variation within the sample). Fixed cervical LN and thymus, and unfixed skin explants, resulted in a flat line with an R^2 value tending towards zero, *i.e.* showing no relationship between explant distance and spheroid outgrowth. The only exception is that the PFA-fixed cervical LN showed a positive relationship when considering total sprout outgrowth which appeared to be a result of two potential outliers close to the explant.

5.3 Discussion

5.3.1 Experimental details

The initial experiment using E15.5 explants was complicated by several factors which later experiments attempted to correct. In some of the gels, there were too many tissue explants and/or too many spheroids, which altered the spatial distribution of spheroids with respect to the explants. As shown in Figure 5.2, an increased number of explants increased the probability of a spheroid being in close proximity to an explant, while reducing the maximum distance, *e.g.* the LN sample contained no spheroids further away than $\sim 700\,\mu m$, while the thymus sample extended past $1500\,\mu m$.

Having multiple small explants also complicated finding the boundary of the explants during image analysis, particularly in the E15.5 LN sample where the edges were determined using thresholding on the GFP fluorescence, the large number of explants making determination of the local background difficult. Additionally, having too many spheroids complicated quantification of outgrowth since it was not possible to measure outgrowth for spheroids which touched, as seen for the LN sample, in particular in Figure 5.2 where the measurements are biased heavily in

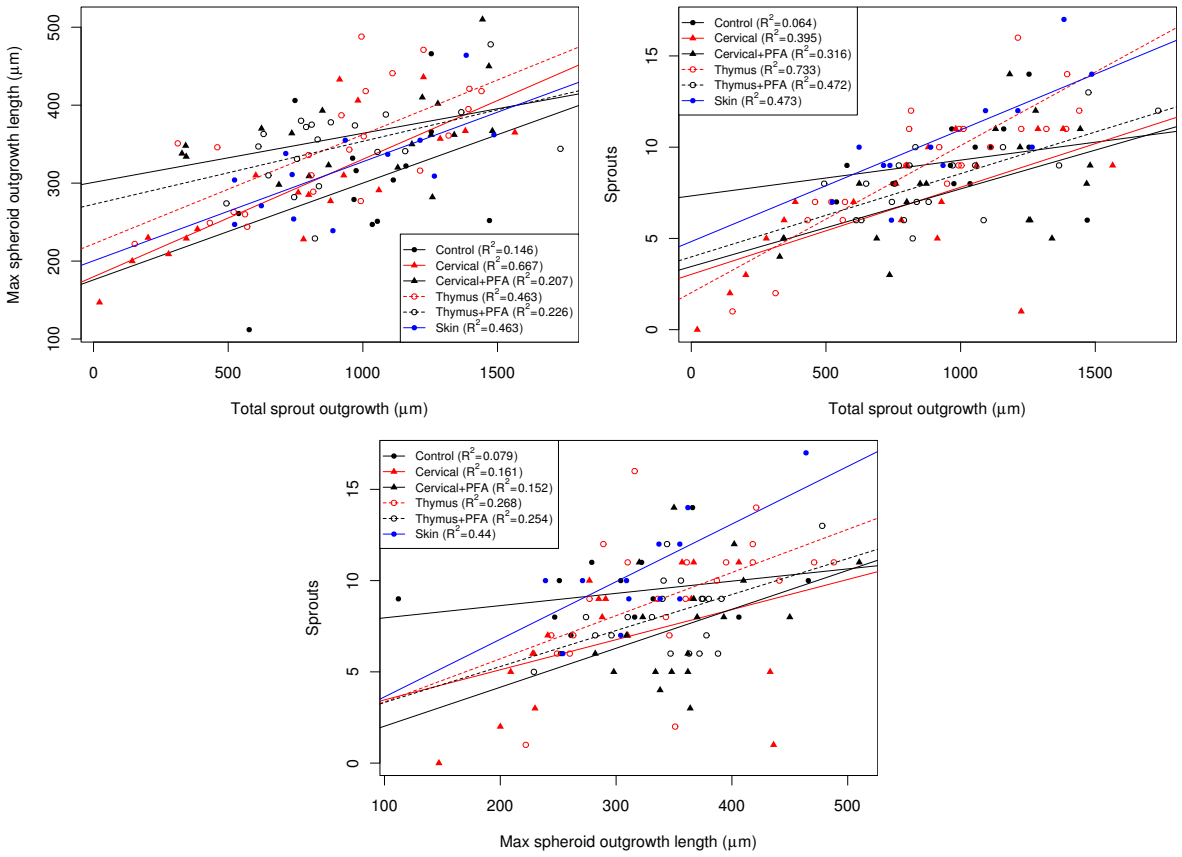

Figure 5.9: Correlations between E14.5 primary measurement parameters. The association between the measured parameters *total outgrowth*, *maximum outgrowth* and *sprouts* are shown in all possible pairwise combinations. The coefficient of determination (R^2) for each sample shows the proportion of the variation accounted for by simple (least squares) linear regression.

Table 5.2: Determination of optimal image analysis strategy for E14.5 and E17.5 explants. Strategies for E14.5 measurements were ranked in ascending order from highest to lowest correlation, using pairwise comparisons with the strategy listed under "rank" being common to the comparisons. The strategies are ordered by the sum of all their ranks, with total sprout length having the highest relative correlations overall.

	Rank			
Strategy	*Maximum outgrowth length*	*Total sprout length*	*Sprouts*	*Rank sum*
	Control			
Maximum outgrowth length	-	1	1	2
Total sprout length	1	-	2	3
Sprouts	2	2	-	4
	Cervical LN			
Maximum outgrowth length	-	2	2	4
Total sprout length	1	-	1	2
Sprouts	2	1	-	3
	Thymus			
Maximum outgrowth length	-	1	2	3
Total sprout length	1	-	1	2
Sprouts	2	2	-	4

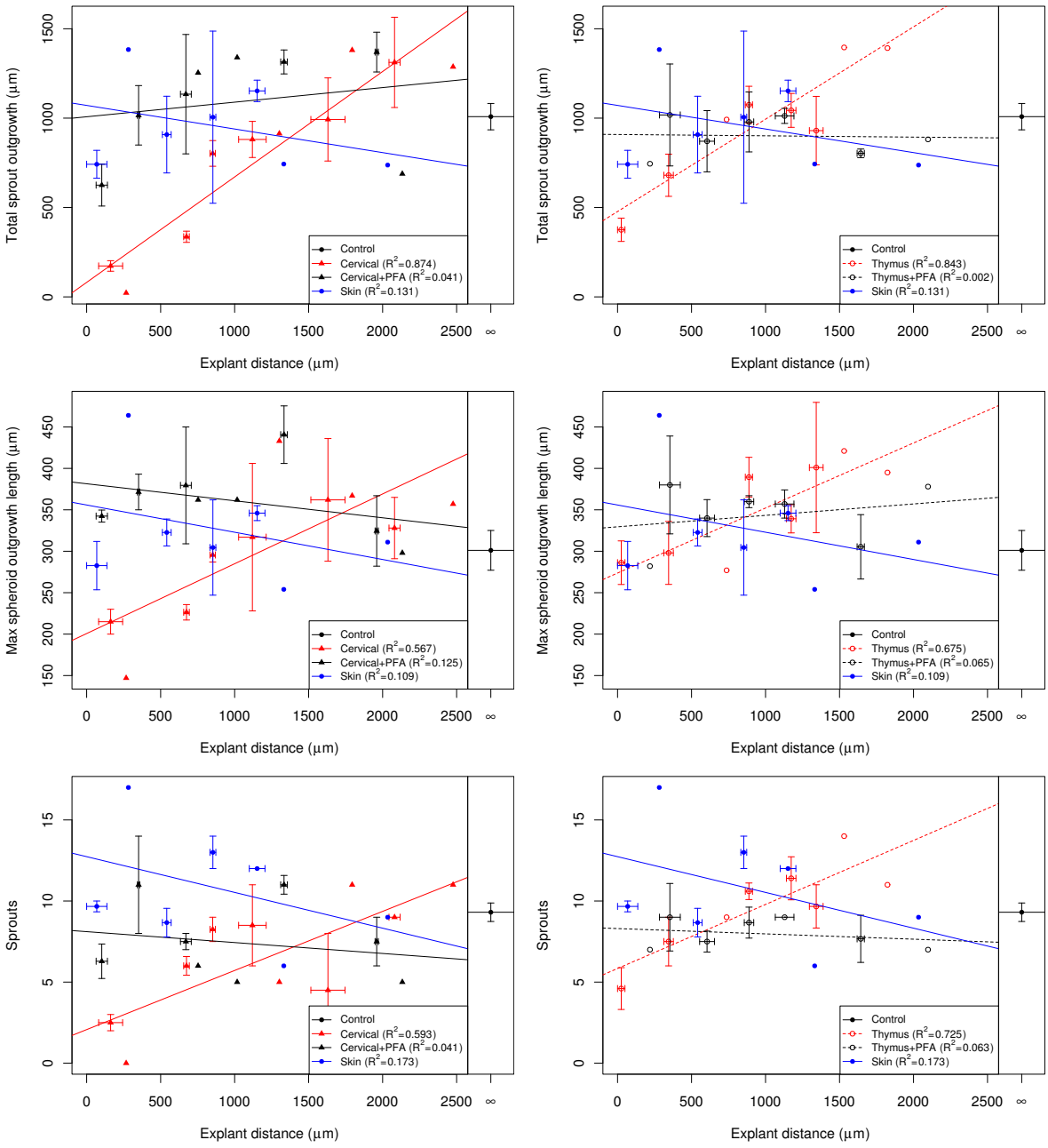

Figure 5.10: Analysis of spatial effects for E14.5 explants. The relationship between distance of spheroids from the explants and the measured parameters *total outgrowth*, *maximum outgrowth* and *sprouts* are shown. The measurements were grouped into 250 µm explant distance bands, with the mean and standard error of the mean calculated for the explant distance and measured parameter for each group. The coefficient of determination (R^2) for each sample shows the proportion of the variation accounted for by simple (least squares) linear regression. In all three cases, a positive linear relationship is seen for both the cervical LN and thymus, which is absent or less apparent with fixed tissue, and is also absent in the skin sample.

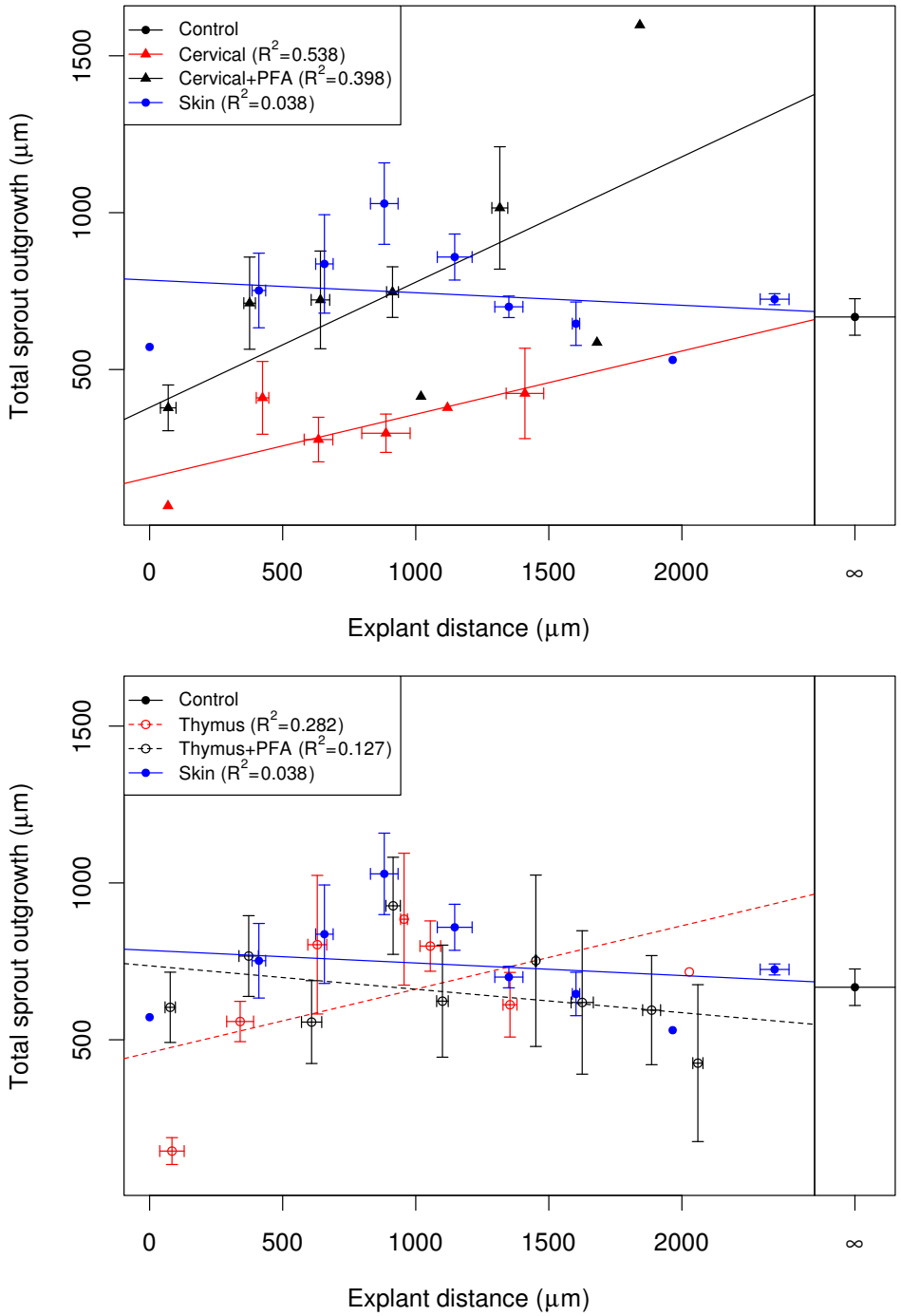

Figure 5.11: Analysis of spatial effects for E17.5 explants. The relationship between distance of spheroids from the explants and *total outgrowth* is shown. The measurements were grouped into 250 µm explant distance bands, with the mean and standard error of the mean calculated for the explant distance and total sprout outgrowth. The coefficient of determination (R^2) for each sample shows the proportion of the variation accounted for by simple (least squares) linear regression. A positive relationship is seen for both the cervical LN and thymus, though this relationship is not completely linear. Fixation of the cervical LN results in an increased amount of outgrowth, comparable to the skin sample. The skin sample showed less suppression of angiogenesis, however it and the thymus appeared to have a peak amount of outgrowth at 800–1000 µm, with less nearer to the explant and the well edge. Fixation of the thymus raised the amount of outgrowth within 500 µm from the explant to levels comparable to the skin sample.

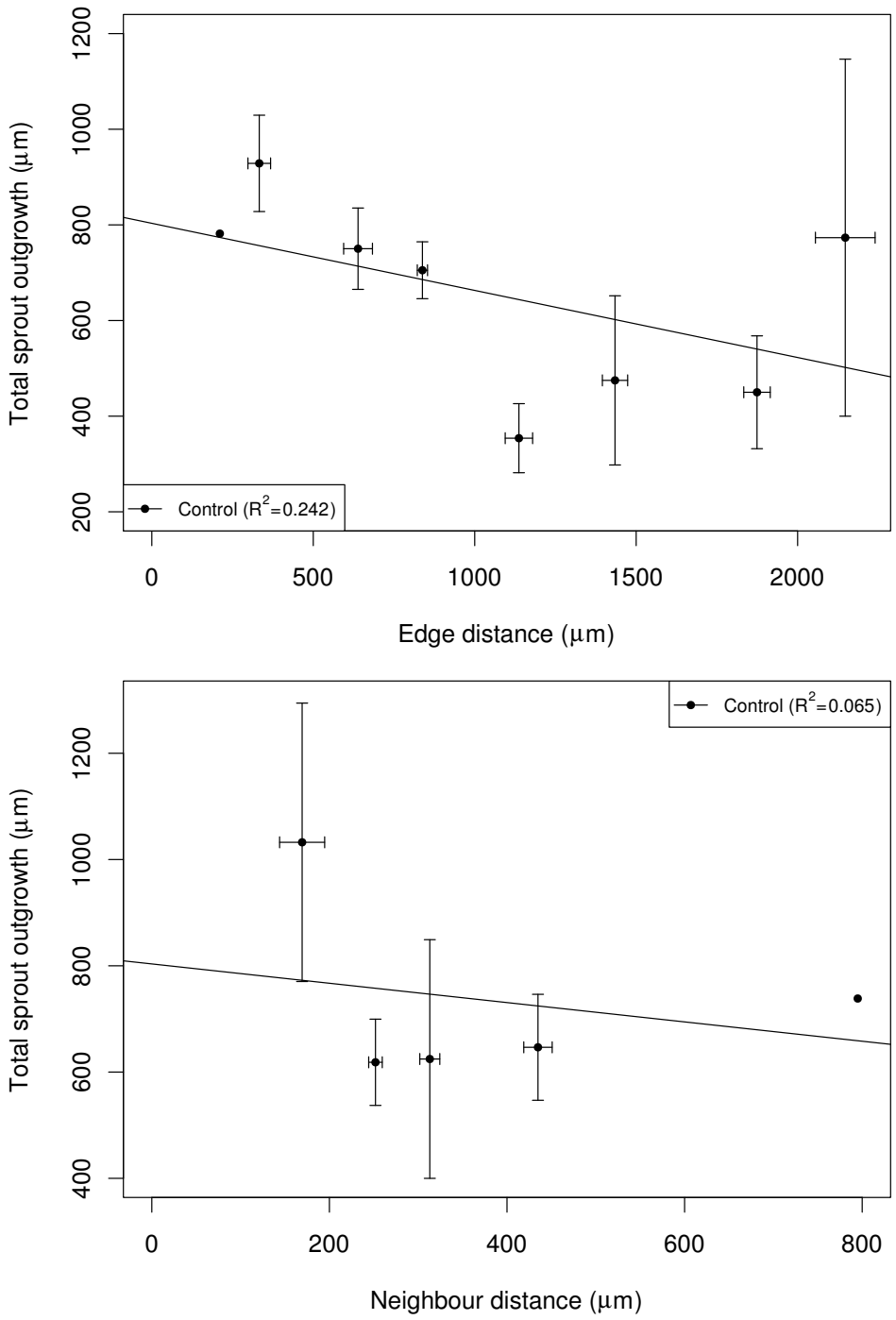

Figure 5.12: Edge and neighbour effects. Using the E17.5 control sample, spheroid outgrowth was plotted against edge distance (distance from spheroid to support ring edge) and neighbour distance (distance from spheroid to nearest neighbour). The measurements were grouped into 250 µm distance bands, with the mean and standard error of the mean calculated for the edge and neighbour distance and total sprout outgrowth. The coefficient of determination (R^2) for each sample shows the proportion of the variation accounted for by simple (least squares) linear regression. This showed a general decrease in outgrowth moving away from the ring edge toward the centre of the well. Plotting spheroid outgrowth against distance to nearest neighbour shows no clear trend.

favour of short distances. Later experiments attempted to rectify these problems by limiting the number of explants to one or two per gel, and by reducing the spheroid density. However, this change reduced the probability of spheroids being present in close proximity to the explant. This is illustrated graphically in Figure 5.13. Ideally, the number of spheroids should be evenly distributed over distance, but the radial arrangement precludes this. Increasing the number of explants reduces the range of distances, hence increasing the probability of finding a spheroid at shorter distance, but at the expense of not collecting information for further distances. These issues could be mitigated by alteration of the gel dimensions, discussed below.

Clustering of spheroids was also reduced by more efficient resuspension of spheroids in neutralised collagen solution, which was intended to result in a more even distribution of spheroids within and between treatments. Initially 48 hours, the outgrowth time prior to fixation was reduced to 24 hours in order to reduce total outgrowth, to prevent outgrowths from neighbouring spheroids touching, and to increase the robustness of quantification.

5.3.2 Secreted factor gradients

When considering the process of vascularisation of a developing organ, the initial working hypothesis was that initially avascular developing LN anlagen require vascularisation, and hence they would secrete factors which would collectively form a net pro-angiogenic environment, *e.g.* driven by hypoxia or some other mechanism. When taken and placed in close proximity to HUVEC spheroids embedded in a collagen gel, the spheroids would therefore respond to these factors. Due to the random placement of spheroids within the gel, gradient effects due to the diffusion of factors from the spheroid would result in spheroids nearest to the explant being exposed to a higher concentration of soluble factors than those at greater distance. In consequence, it was expected that tube outgrowth would be greatest at closest proximity to the anlagen, and least at a distance where diffusion of pro-angiogenic soluble factors (such as VEGF) from the anlagen would be limited. As the vascular bed becomes established, this might lead to a change in the balance of pro- and anti-angiogenic factors to switch to an anti-angiogenic or neutral state, which would result in a change in the spatial pattern of spheroid outgrowth.

The experimental data, however, show that in fact the opposite appears to be true. At E15.5, the LN explants collectively show an approximately linear relationship between outgrowth and distance from the explant, with spheroids closer to the explant having less sprout outgrowth, or total number of sprouts, than those at greater distance. A similar pattern was seen at E14.5 and E17.5. At both E14.5 and E17.5, PFA fixation resulted in outgrowth near to the explant to increase to levels similar to the control or unfixed tissue at further distance from the explant. The thymus showed a similar pattern, albeit with the relationship not appearing as lin-

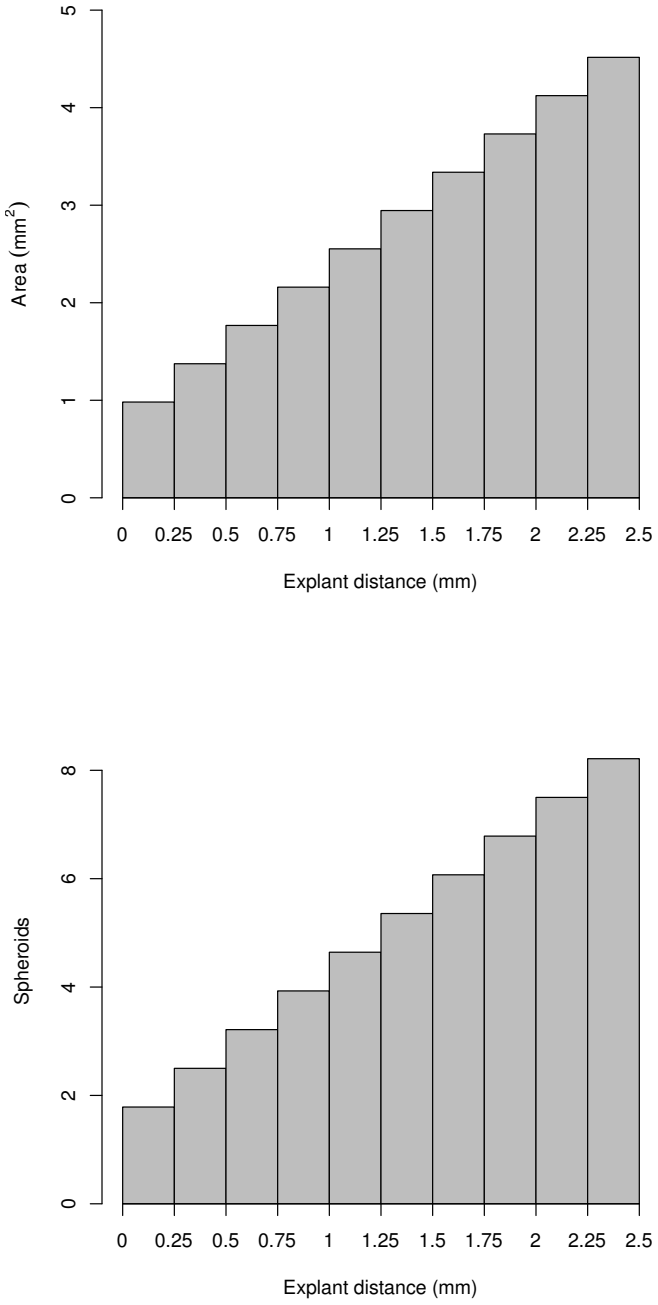

Figure 5.13: Spheroid distribution. Given a 6 mm diameter ring with a 1 mm diameter explant placed in the centre, the top plot illustrates that as the distance from the explant increases, the gel area increases linearly. The measurements have been split into into 250 µm radial bands for convenience, and to mimic the pooling of experimental measurements. If the gel was seeded with 50 spheroids, assuming even distribution within the gel, the bottom plot illustrates the number of spheroids which would be expected to be present within each band. Bands further away from the explant contain more spheroids, again as a linear function of distance. Note that this is a probability distribution; spheroids are discrete objects and hence only whole numbers are present in reality.

ear. In general the suppressive effect of the E15.5 thymus was less than the LNs, showing greater outgrowth overall with less suppression; only at distances under 250 µm is the suppression comparable to the LN suppression. The same trend was also seen at E14.5 and E17.5, but at E17.5 outgrowth increases with increasing distance before declining to a steady level. Skin did not appear to significantly affect outgrowth, being approximately similar to the control sample at E14.5; at E17.5 it was not linear, having a mean value similar to the control, but a peak in outgrowth at around 1000 µm from the explant. This was possibly a result of large explants affecting gel tension, discussed in more detail below. The most probable interpretation of these data is that soluble factors being actively produced by the LN or thymus explants exerted a net anti-angiogenic effect. The general trend which may be drawn from the data is that LN explants at all timepoints exhibited greater spheroid outgrowth with increasing distance from the explant, with a similar trend being shown for thymus explants but exerting a less potent effect. PFA fixation of the tissue restored angiogenic outgrowth in part or in full, indicating that this is likely to be an active process of secreted factor production. Failure to restore all outgrowth at very close distances may be a result of steric effects at close proximity to the explant (physical constraints upon tube outgrowth) or due to inhibition upon direct contact with the explant (*e.g.* upon contact with fixed or sequestered inhibitory factors). It may alternatively be a result of incomplete fixation of the tissue, resulting in continued production of inhibitory factors, but at a lower level than in unfixed tissue. At all timepoints the thymus samples, and also the skin sample at E17.5, showed a peak in angiogenic outgrowth at around 1000 µm, and this effect was reduced but not entirely eliminated by fixation. This effect was not seen for the LN samples at any timepoint.

In Figures 5.4, 5.5, 5.10, 5.11 and 5.12, linear regression was used to analyse the relationship between distance and the amount of angiogenic outgrowth quantified. This makes the assumption that the relationship is of a linear nature, which may not be the case. Diffusion and the establishment of a concentration gradient within the gel is affected by several factors, including the gel concentration (pore size, degree of cross-linking), affinity of the solute for the matrix, and the solute concentration and half life (if applicable). These effects have been explored in a recent review by Lieleg and Ribbeck (2011), considering these and other effects upon diffusive filtering mechanisms in extracellular matrix. Complex mathematical models of diffusion in biological matrices exist, such as that developed by Kapellos, Alexiou *et al.* (2007). However, the most appropriate models in this context are direct experimental measurements such as those of Ramanujan *et al.* (2002), which demonstrated that collagen increasingly hinders diffusion with increasing concentration, most likely to due an increase in the "effective tortuosity", that is the effective path a molecule must travel to get from a starting point to its destination compared with the straight line

path it could travel in the absence of such hindrance. The diffusion coefficient was also determined experimentally to decrease with increasing hydrodynamic radius (or Stokes radius; effectively the particle size or mass for the purpose of this discussion). The gel composition and solute–matrix interactions such as sequestration and adsorption should be *constants* however, which would affect the slope of the gradient as a result of altering the rate of diffusion, but would not alter the shape of the slope. The collagen gel is mostly acellular and so degradation of soluble factors by cellular processes is unlikely to be a major factor, though breakdown by non-cellular activity, *e.g.* if it is broken down spontaneously or degraded by chemical reaction with the media or matrix, may affect the gradient.

For the LN samples, the response appeared to be approximately linear. However, responses to growth factors are typically non-linear. Using VEGF as an example (Akeson, Herman *et al.*, 2010), cells are responsive to the factor only within a narrow range, with receptor phosphorylation having sigmoidal relationship with respect to the log dose of VEGF. A linear response may be a result of the spheroids being exposed only to a narrow range of concentrations, *i.e.* being only *apparently* linear, or alternatively if both the dose and response are non-linear, the combined effect could result in a linear relationship.

Making the assumption that the explant secretes factors at a fixed rate, the closest analogue in the literature is the study of diffusion from microfluidic networks into hydrogels. In these systems, a solute is introduced into the network at a fixed rate and concentration. For example, Choi *et al.* (2007) illustrated this using calcein-AM diffusion into a chondrocyte-seeded alginate scaffold, showing exponential decay over distance from the source. Because calcein is actively metabolised by the cells, this system reaches a steady state with a stable concentration gradient. This is also shown in the same paper with fluorescein isothiocyanate (FITC)-BSA, showing the same exponential decay gradient, but without reaching a steady state. The spheroid model does not have cells seeded uniformly throughout the gel, given that they are present in the spheroids at discrete points, which may result in a mixture of free diffusion and turnover in cell-free and spheroid parts of the gel, respectively. The diffusion of FITC-dextran within a collagen gel was investigated by Kothapalli, van Veen *et al.* (2011), observing changes in the concentration gradient over time. This was again an exponential decay curve, which approached steady state over time. This system was not subject to flow after initial loading, so represents passive diffusion only between source and sink reservoirs. Additionally, FITC dextran does not bind to the collagen matrix, unlike many of the growth factors and inhibitors which modulate angiogenesis, which may result in the formation of much steeper gradients in the spheroid model. VEGF binding to heparin is one such example (Ruhrberg *et al.*, 2002), but many other factors can bind to matrix components including bFGF and TGF-β_1, reviewed by Schultz and Wysocki (2009). The complex combinations of

differing concentrations of multiple factors, resulting as a consequence of the interaction between sequestered non-sequestered factors, as well as those with differing diffusion rates, half-lives and concentrations, may be responsible for the patterning of the vasculature, resulting in precise control of decisions regarding cellular fate, including proliferation, migration and branching.

The spheroid model is an effectively *closed system* with respect to solute diffusion. There is no sink other than the culture medium above the gel, which implies that in the absence of degradation of soluble factors, a steady state will not be reached. Thus the gradient set up by factor secretion from the explant will continue to expand in size over time, with consequent reduction in the steepness of the gradient, as illustrated by Kothapalli *et al.* (2011). The highest concentration (at the edge of the explant) will also be variable depending upon the size of the explant, assuming that this is related to the cellularity of the explanted material. If produced by a subset of cells within the explant, the proportion of which may change during development and/or between tissue types, the cellularity alone is also an unreliable indicator of the quantity of soluble factors arising from the explant. Due to imaging using epifluorescence, the size of the explants could not be determined by the visible surface area nor integrated DAPI fluorescence; the tissue size in the z dimension was indeterminate due to its height exceeding the microscope's working z range, and with out of focus fluorescence preventing accurate measurement, precluded drawing any conclusions regarding explant size and its effect upon spheroid outgrowth based upon the experimental data presented here.

In consequence, one would expect any factors arising from the explant to follow an exponential decay curve, though the extent of the gradient and how it changes during the 24 hour culture period are unknown. Given that multiple factors may be secreted, each of which may have a different gradient in the gel, a consequence of diffusing independently, having potentially different initial concentrations, diffusion rates due to size, shape and charge differences as well as differences in matrix affinity and half-life, the interaction between the various pro- and anti-angiogenic factors may be very complex. The spheroid model measured the response to the combined effects of all these factors at discrete points in the gel.

An alternative hypothesis to growth factor gradients being the cause of inhibition is that the effect is due to direct inhibition as a result of cells migrating out of the explant and into the gel, as seen in Figure 5.6. These migratory cells might themselves be secreting anti-angiogenic factors. While this may be a contributing factor to the observed effects, it is unlikely that this may invalidate the hypothesis that soluble factors arising from the explant are the primary cause. In the E15.5 samples, cells were seen to migrate at least 300 µm into the gel, however the inhibitory effects were observed up to at least 500 µm from the explant. In the E14.5 and E17.5, very little migration was seen for the cervical LNs (a small number migrated < 200 µm from

the E14.5 explant), and no migration from the thymus or skin samples was observed using GFP and DAPI fluorescence to identify individual cells. This may be an artefact of single cells liberated during dissection being mixed into the unpolymerised collagen gel, and their significance is unclear.

5.3.3 Candidate factors

The ECGM medium used to overlay the gels contained 1 ng/mL bFGF in addition to 2 % FBS and 0.4 % endothelial cell growth supplement / hypothalamus (ECGS/H), prepared from bovine hypothalamus containing growth factors including bFGF and VEGF (Ferrara and Henzel, 1989; Maciag, Cerundolo *et al.*, 1979), further supplemented with an additional 10 % FBS. The growth medium therefore contains at least 1 ng/mL bFGF in addition to an undefined concentration of VEGF as well as other factors.

Inhibition could be the result of two primary mechanisms: inhibition of pro-angiogenic signalling (*i.e.* loss of positive signal), or direct inhibition (*i.e.* gain of negative signal). The former could be the result of growth factor sequestration, breakdown, or blockade or competition with the receptor. The latter could be an inhibitor signalling directly and independently via a separate receptor. Both of these mechanisms are known to operate *in vivo* (Ho *et al.*, 2009; Jiménez *et al.*, 2000; Luque *et al.*, 2003). Loss of soluble pro-angiogenic factors can be ruled out as a major contributing factor; being present in the growth medium they are effectively constant, with any additional quantities secreted by the explant possibly having a local pro-angiogenic effect (which was not observed). The effect of these factors is seen as the basal rate of outgrowth observed in control samples, and in treatment samples separated from the explants by large distance. The number of soluble angiogenesis inhibitors found *in vivo* is limited, restricting the pool of candidates to just a few molecules, some of which have been reviewed by Nyberg *et al.* (2005). Both PEDF and thrombospondin are potential candidates, given their confirmed presence as shown in Section 3.2.5 (Figure 3.7).

Soluble VEGFR1 and ADAMTS1 Both the soluble alternative splice variant of VEGFR1 and ADAMTS1 are capable of sequestering VEGF, preventing VEGF-A from signalling via VEGFR2 and therefore reduce EC proliferation and sprouting (He, 1999; Luque *et al.*, 2003). However, for this form of inhibition to operate effectively, at least a 1:1 stoichiometry of inhibitor:VEGF would be required at sites close to the explant, and this would require the inhibitor to diffuse to the site. Nevertheless, this could still account for the gradient effect seen. However, sequestering of VEGF alone should not be sufficient to *completely* suppress angiogenesis, given the additional presence of bFGF in the media. Section 4.2.11 (Figure 4.16) showed that HUVECs responded to bFGF with increased outgrowth, and so it would be reason-

able to expect some level of outgrowth, even if reduced from the basal rate, to exist in the absence of all VEGF signalling given that this has previously been demonstrated by Pepper *et al.* (1992). However, as for the experiments described here and in Section 2.1.1, Pepper supplemented the medium with FBS, so a small possibility exists that if all of any VEGF present in the FBS was sequestered, this could have an negative effect which would not be encompassed by either of these experiments. As shown by Hood, Frausto *et al.* (2003), both VEGF and bFGF are required to prevent apoptosis due to differential activation of Ras and ERK pathways, preventing both cell-extrinsic and intrinsic apoptosis pathways. It is possible that if all VEGF were to be removed from the immediate environment that the cell-extrinsic pathway would no longer be inhibited.

PEDF PEDF is the single most likely candidate for the angiogenesis suppression observed, it being one of the only direct biological inhibitors of angiogenesis acting independently of pro-angiogenic growth factor signalling.

PEDF has recently been shown to bind collagen and other matrix proteins, using the same collagen binding site as heparan sulphate proteoglycans, as well as binding heparin itself (Sekiya *et al.*, 2011). This property could be used to investigate the involvement of PEDF with the addition of heparin sulphate to the collagen solution, which should cause a concomitant reduction in the radius of sprouting inhibition through the creation of a steeper concentration gradient as more PEDF is sequestered in closer proximity to the explant. However, this change could equally apply to other heparin sulphate-binding proteins, and would need require more specific experiments to definitively identify PEDF as the factor responsible.

PEDF has been shown to be a potent inhibitor of angiogenesis in the eye, with a $PEDF^{-/-}$ transgenic mouse model showing extensive hypervascularisation (Huang, Wang *et al.*, 2008), and recently its receptor was discovered (Subramanian *et al.*, 2010). Unfortunately, most work to date has been restricted to the vascularisation of the eye, and yet as the PEDF expression data in Chapter 3 clearly showed (Figures 3.8 and 3.8), it is also expressed in developing LN anlagen at all timepoints during development, as well as other tissues such as the thymus, liver and skin. While the expression pattern of PEDF and and pigment epithelium-derived factor receptor (PEDFR) in the whole organism have yet to be studied, it would make logical sense for PEDFR to be present upon all endothelial cell types, potentially with different levels of receptor or intracellular signalling between BEC and LEC. It is certainly present on HUVECs, given the presence of cytosolic phospholipase A_2-α signalling, downstream of PEDFR (Ho *et al.*, 2009). In section 3.2.6 (Figure 3.9), PEDF was shown to be upregulated in the MRCs relative to the FRCs in the human fœtal lymph node. As discussed in Chapter 3, its role in lymphatic development has yet to be determined through imaging or genomic methods, and functional assays such as the spheroid model may be useful for demonstrating the ability of anlagen to produce PEDF

and suppress angiogenesis. Use of the assay with LEC spheroids would also provide functional evidence of the differential effects of PEDF (if any) between blood and lymphatic endothelium. In a tumour environment, PEDF decreased blood vessel growth both in the tumour and surrounding tissue, but increased lymphangiogenesis in the surrounding tissue was also observed (Halin *et al.*, 2010). This would suggest that PEDF differentially regulates angiogenesis and lymphangiogenesis, in the absence of compensatory mechanisms and other compounding factors. The use of the assay with anlagen from the $PEDF^{-/-}$ mouse would also allow the contribution of PEDF to angiogenesis suppression to be compared with wild type anlagen, provided that LN anlagen development is not overtly abnormal.

Thrombospondin Thrombospondin is produced in large quantities by platelets, which play a significant role in controlling pathological angiogenesis, particularly in cancer (Zaslavsky *et al.*, 2010). It is a possibility that platelet-derived thrombospondin played some role in the observed suppression of angiogenesis, yet this is unlikely. When harvesting the LN anlagen, great care was taken not to include adjacent vessels; only the smallest of vessels could have been present in the samples, and the tissues were washed in a large volume of IMDM or PBS prior to embedding in the gel, which should have removed the vast majority of platelets capable of exiting the tissue. Additionally, no suppression of angiogenesis was noted in the skin samples, which were completely vascularised and contained blood; if any platelet-derived thrombospondin were to inhibit angiogenesis, it would have been expected to have arisen in this sample.

Thrombospondin has been shown to act in several ways, including antagonistically to VEGF signalling via Akt, reducing EC survival (Sun *et al.*, 2009). Its other suppressive function, the inhibition of MMP activation, is unlikely to have a significant effect in collagen I gels, ECs being able to freely migrate without the need for matrix degradation. Whether MMP inactivation plays a role could be further investigated using MMP inhibitors to observe if inhibitors further suppress angiogenesis.

Plasminogen, MMPs and TIMPs As mentioned for thrombospondin, MMP activity (or inhibition) is unlikely to have a direct effect on outgrowth. Experiments were performed using GM6001 (ilomastat) and BB2516 (marimastat) to determine if MMP activity was a requirement for spheroid outgrowth but due to technical problems with the collagen matrix did not produce usable results. Given the findings of Davis *et al.* (2000b) that MMP activation results in tube regression, it is possible that MMP activity could result in regression (or no initial outgrowth in this case). However, when analysing the spheroid outgrowth using MP SHG imaging to visualise individual collagen fibrils in the matrix, there was no evidence of matrix degradation, at least at the resolution of the microscope used. It is a possibility that MMP activity resulted in the formation of anti-angiogenic matrix fragments which this analysis

would not be able to detect. In an experiment to visualise GFP-expressing HUVEC spheroids in a collagen matrix (not shown), outgrowths were clearly visible ramifying through the matrix with what appeared to be a basement membrane (or at least, remodelled matrix) surrounding the tube; any tube regression would have left behind clearly visible tunnels in the matrix, which were not observed in this case. Given the absence of blood in the explants, plasminogen (an MMP activator) was unlikely to the present, and hence neither would its anti-angiogenic products plasmin or angiostatin (Davis *et al.*, 2000b).

Collagen-derived inhibitors The collagen IV-derived inhibitors arresten, canstatin and tumstatin and collagen XVIII-derived inhibitor endostatin are thought to act via integrin attachment, and arise through MMP-mediated degradation (Mundel and Kalluri, 2007), hence the observations regarding MMPs, above, apply equally here. Given the lack of collagen IV basement membrane surrounding the spheroids and new outgrowths, at least initially, such inhibitors are unlikely to originate locally, and would most likely result from degradation of basement membrane within the explant.

5.3.4 Explant effects

The fact that outgrowth is suppressed in close proximity to the spheroid suggests that this is a result of a soluble factor (or factors) arising from the tissue explant. However, this might also be due to other factors, for example localised depletion of oxygen and/or nutrients from the media due to the metabolic demands of the explant. Given that the collagen gel was of high porosity and should allow oxygen and metabolites to diffuse freely, this should not have been a contributing factor, especially given the fact that in the case of E17.5 LN suppression of outgrowth was observed at distances of at least 1 mm away from the explant, at which distance explant-mediated depletion should have little effect. Whether this is a contributing factor could be assessed by using *e.g.* pimonidazole or FLIM (Mik, Johannes *et al.*, 2008) to compare oxygen tension and metabolite concentration between spheroids. However, unlike in the previous chapter, these gels were not completely covered by a 2-D layer of HUVECs, 2-D coverage being both sparse and restricted to the lower surface of the gel when present. In consequence, diffusion restriction as a result of surface cell coverage could not have played a major role in these experiments.

At E14.5, the LN anlagen, at least in the neck and upper thorax (cervical, axillary and brachial) are at least partly vascularised (Mebius, 2003; Vondenhoff *et al.*, 2009a). Once vascularisation has begun, it may be hypothesised that in order to prevent further, hyper-vascularisation, the cells of the anlagen and/or the infiltrating vessels secrete anti-angiogenic factors. Subsequent repetition of the experiment at E14.5 and E17.5 showed similar effects at these timepoints in both thymus and cer-

vical LNs. Collectively, these do not show any obvious trend—it is possible that the LN vasculature is continuing to develop, or being restricted from developing, throughout this period. However, when observing the thymus and skin samples, there is an interesting difference. Both of these samples have one important feature in common: they both contain a complete vascular network, as shown in Figure 3.1 and observed during dissection where the skin microvasculature is clearly visible, and an established vasculature may result in a rather different angiogenic environment. Both tissues show a marked increase in angiogenic outgrowth around 1000 µm from the explant, and the reasons for this are not clear. More established vascular systems will be less responsive to pro-angiogenic factors as a result of their stabilisation by smooth muscle and through basement membrane biosynthesis and MMP inhibition (Saunders *et al.*, 2006; Stratman *et al.*, 2009a; Xian, Håkansson *et al.*, 2006), and consequently may not require as much active suppression of angiogenesis by soluble factors; this is indicated by the falling levels of Pedf and rising levels of Thbs mRNA in the skin sample in Figure 3.7.

Pro-angiogenic factors tend to have a lower molecular weight, while anti-angiogenic factors have a higher molecular weight; PEDF is 50 kDa, while thrombospondin is 190 kDa, bFGF is 18-19 kDa and VEGF-A_{165} is 46 kDa (Gautschi, Fràter-Schröder *et al.*, 1986; Holmes and Zachary, 2005; Zhang and Ma, 2007). Assuming equal matrix affinity and shape characteristics, it could be hypothesised that the pro-angiogenic VEGF-A_{165} and bFGF would be expected to diffuse faster, causing separation of the pro- and anti-angiogenic factors within the gel, which could hence be responsible for the band of pro-angiogenic activity observed at intermediate distance. At E17.5, where this effect is most pronounced, the amount of angiogenesis at this point is significantly higher than the control, indicating that this is a positive effect rather than a lack of negative regulation (unlike the other cases, where outgrowth is reduced relative to the control). Outgrowth nearer to the the explant is the same as the control in the case of the skin sample at E17.5; this may be due to a mostly equal balance of pro- and anti-angiogenic factors since both would be present. While this is also seen for the thymus sample, suppression at close distances was observed, which could be a result of incomplete smooth muscle coverage at this timepoint, as seen by the lack of collagen IV staining in Figure 3.1 and in Foster *et al.* (2008). Consequently, anti-angiogenic signalling may not have been downregulated, indicating that it is producing more anti-angiogenic factors than the skin sample. The correlation of the distance between the samples indicates that the same factor, or factors, are being produced by both samples, but in varying quantity.

Given that the overall environment in the developing LN is anti-angiogenic, this does not preclude angiogenesis in regions where pro-angiogenic factors are concentrated, overcoming the inhibitory effects. Combined with the precise control of sprouting with Dll4/Notch inhibition (Hellström, Phng *et al.*, 2007), this may result

in sprouting whilst the spheroid model is only responsive to the net effects.

The data resulting from image analysis show firstly that the different measured parameters (perimeter, area, radius and number of sprouts) correlate with each other, some to a greater extent than others, indicating that they are quantifying similar changes. This means that these different parameters are each quantifying different aspects of the same process: spheroid outgrowth as a result of sprouting angiogenesis. It was found that perimeter length and total sprout length correlated to the greatest extent, while the number of sprouts and area correlated less well, and outer radius rather poorly. These observations may be explained in terms of the error they introduce, the error being the difference between the quantified amount of angiogenic outgrowth and the "real" amount. Without an external calibrating measure, the most obvious means of determining the most reliable measure is to perform pairwise comparisons between the different measurement parameters.

The outer radius measurement is biased due to a single large outgrowth being treated equivalently to multiple outgrowths of similar length, despite the latter having experienced more outgrowth in total. In a similar vein, the total number of sprouts does not take outgrowth into account, treating spheroids with the same number of sprouts, but vastly different sprout lengths, as equal, when they are manifestly different. Area being an unreliable measure is perhaps less obvious, and is due to the area increase being disproportionately small compared with the amount of outgrowth. Due to the initial large area of the spheroid and the small diameter of any outgrowths, outgrowth resulted in only a modest increase in surface area, which may be statistically insignificant relative to the sample variation in initial spheroid surface area. In comparison, perimeter length and total sprout length both increase linearly with outgrowth and are both independent of factors such as the number of sprouts and individual sprout lengths, making them much less susceptible to bias. This is reflected in their almost equivalent ranking in Table 5.1. Future analyses dropped parameters which performed poorly (outer radius, area) or which were excessively time consuming to measure (perimeter length).

Lastly, there appeared to be a strong positive correlation between tube outgrowth and increasing distance from LN or thymus explants, showing that despite the rather large amount of variance in the data, there is an apparent relationship. The fact that perimeter length and area (not shown), as opposed to the derived area ratio, were more robust measurements may reflect amplification of error as a result of measurement inaccuracies, or the ratio may simply not represent outgrowth as well as either parameter alone. Curiously, the same does not apply to the derived radius ratio, despite the known poor suitability of the outer radius measurement, which is additionally compounded by the noise introduced by the inner radius, largely similar for all spheroids, but reduced for spheroids which are ovoid rather than spherical (Figure 2.3(D)).

The analysed images were tiled epifluorescence images taken in a single plane of focus and then stitched together. Because the spheroids may be present at different z depths within the gel, and tubes outgrow in all directions in three dimensions, getting accurate data from 2D images is challenging. Drawing an outline is difficult due to the outgrowing tubes going out of focus; indeed it is possible to discount tubes which have no visible connection to the spheroid, but which pass through the plane of focus at a distance. It is also difficult to separate spheroids in close proximity, whose outgrowths cross in different z planes, but appear to be joined. As a result, imaging entire gels using tiled confocal z-stacks has been undertaken, but this is currently impractical to both acquire and analyse.

5.3.5 Image analysis strategies

Data have now been acquired using the spheroid model for explanted anlagen from E14.5–E17.5. To gain useful information from this data, the analysis protocols require improving to remove the unwanted variance mentioned above.

When considering the distance between the explant and a spheroid, there are two obvious measurements which may be made: from the edge (or centre) of the inner spheroid mass to either the edge of the explant (determined using DAPI fluorescence or autofluorescence) or to the anlagen itself (determined using hCD2-GFP fluorescence). Given that the specific cellular source (or sources) of the soluble factors are unknown, and may be produced by the LTis, LTo or any other cell type present, the explant edge was used. This additionally allowed comparisons to be made with non-lymphoid explants such as skin, which do not contain any LTis.

Different types of outgrowth were observed during analysis, from thick multicellular outgrowths, to thin single cell adventitious sprouts and filopodia extending from the leading edge of the growth cone of tip cells. When quantifying spheroid size, *all* outgrowths of all sizes were included. However, this could potentially lead to underestimates of size for spheroids where fine filopodia, for example, are not visible due to the CD31 fluorescence being too faint or out of focus. The cells in some outgrowths also appeared to be rounded, connected to the spheroid and/or their neighbours only by fine slender threads of cytoplasm. Without further analysis, it was not possible to determine if these were apoptotic, dividing, or undergoing some other process relating to angiogenesis.

5.3.6 2-D outgrowth

Several experiments showed evidence of both 2-D and 3-D outgrowth; this was particularly apparent in the E17.5 images shown in Figure 5.8, where angiogenic sprouting is clearly distinguishable from a less intense region surrounding each spheroid. This complicated the image analysis by requiring careful examination of the differ-

ent z-planes in order to distinguish the two, and may have introduced some of the noise seen in the measurements, where such determination was ambiguous. The outgrowth was predominantly on the bottom surface of the collagen gel, in contact with the glass or plastic well bottom. Presumably, this was a result of the spheroids settling to the bottom of the collagen matrix during gelation, which took place over an hour at 15 °C in the case of the E15.5 experiment. In an attempt to reduce this effect, the gelling time was decreased to 10 mins at 37 °C. Unfortunately, this did not result in great improvement, and in fact some experiments (not shown) could not be analysed as a result of outgrowth being predominantly in 2-D, with 3-D outgrowth being absent entirely, or being indistinguishable from 2-D outgrowth. In Korff and Augustin (1999), 0.25 % (w/v) carboxymethylcellulose was present in the neutralised collagen solution, used to prevent spheroid sedimentation prior to gelling. This, or an equivalent which increases the solution density without interfering with collagen gelation or spheroid outgrowth, could be used to reduce or eliminate this undesirable complication.

5.3.7 Neighbour effects

There appeared to be a small but positive relationship between tube outgrowth and increasing neighbour distance, *i.e.* spheroids are themselves inhibiting the tube outgrowth of their neighbours, at least to some extent. Figure 5.5 showed an increase in outgrowth as the neighbour distance increased, which may imply that the spheroids themselves may inhibit their neighbours' outgrowth. However, the opposite appears to be the case at E17.5 (Figure 5.12, bottom plot). Only the control sample was used, to avoid the complication of the additional effects of the explants. However, given the errors involved and the fact that the group of measurements at 450 µm contains large outliers, it is unclear if this is a significant relationship at E15.5. At E17.5, neighbouring spheroids do not appear to have any significant influence upon spheroid outgrowth, but if truly present, the effect would appear to be negative rather than positive, *i.e.* angiogenesis increases with reduced neighbour distance.

The main difference between the initial E15.5 experiment and later experiments was the use of untreated nylon washers for the former, and PEI-coated steel rings for the latter, used to contain the collagen matrix. The differences may therefore be due to tensional forces within the collagen matrix. The collagen did not strongly bind to the collagen washers, and was observed to contract in the E15.5 control sample during culture, along with the gels containing explants. Conversely, the gels in PEI coated rings were bonded to the inner surface of the rings, and hence HUVEC-mediated collagen contraction would result in an increase in tension within the gel rather than radial contraction of the gel, which is physically constrained, as illustrated in Figure 5.14(A). Collagen contraction is likely to be mediated via integrin $\alpha_2\beta_1$, which has been previously shown to be responsible for collagen contraction

with other cell types (Riikonen, Koivisto *et al.*, 1995), and is known to be expressed by HUVECs and required for matrix invasion (Bayless, 2003).

In the case of collagen contraction being constrained, it is likely that local contraction of collagen by spheroids results in global changes in gel tension, at least in the radial (horizontal) plane. Contraction in the transverse (vertical) plane is not constrained, except at the edge where it is bonded to the ring. The effects of altering the constraints of contraction are shown in Figure 5.14. The effects of individual spheroids upon their neighbours was investigated by Korff and Augustin (1999), and shown to be a result of tension in the matrix resulting in directional outgrowth (and eventual anastomosing) of outgrowths between the two spheroids. This pattern was observed between spheroids in these experiments, but at such low frequency it was considered to be coincidental. While this appears to be a genuine phenomenon, it also appears to be dependent upon the type of gel support used, presumably as a consequence of the difference in the orientation and intensity of tensile forces within the gel. In the case of the E15.5 control, the apparent increase in outgrowth as neighbour distance increases is in direct contrast to the observations of Korff and Augustin (1999), who observed that directional sprouting occurs most at close separation ($< 200\,\mu m$).

5.3.8 Edge effects

The contribution of edge effects to spheroid outgrowth in the E17.5 control sample are shown in Figure 5.12 (top plot). With the exception of a few outliers, there is a clear relationship between the amount of outgrowth and the distance to the well edge, with spheroids closest to the edge exhibiting more outgrowth than their counterparts at the well centre.

Given the assumption that all conditions within the well are constant, except for the placement of the spheroids within the well, and that neighbour effects were shown to be insignificant, it is most likely that the observed biological effect is a result of physical forces within the gel. If the collagen gel is bonded only to the inner edge of the support ring, and each spheroid dispersed evenly within the gel exerts the same contractile forces in all directions upon the matrix surrounding it, the matrix will appear as in the idealised, exaggerated illustration shown in 5.14(A). The resistance to radial contraction as a result of the bonding to the inner edge of the ring will establish tension in this dimension, shown as lines within the gel. The spheroids will also exert force in the transverse dimension, shown here resulting in a concave shape as a result of differential contraction of the gel. In the centre of the gel, contraction is opposed only by the intrinsic resistance within the gel itself, whereas at the edge it is additionally opposed by the incompliant support ring, resulting in increased tension at the edge. Figure 5.14(E–F) additionally illustrate how matrix compliancy may affect tensional forces as a result of differences in edge distance around an indi-

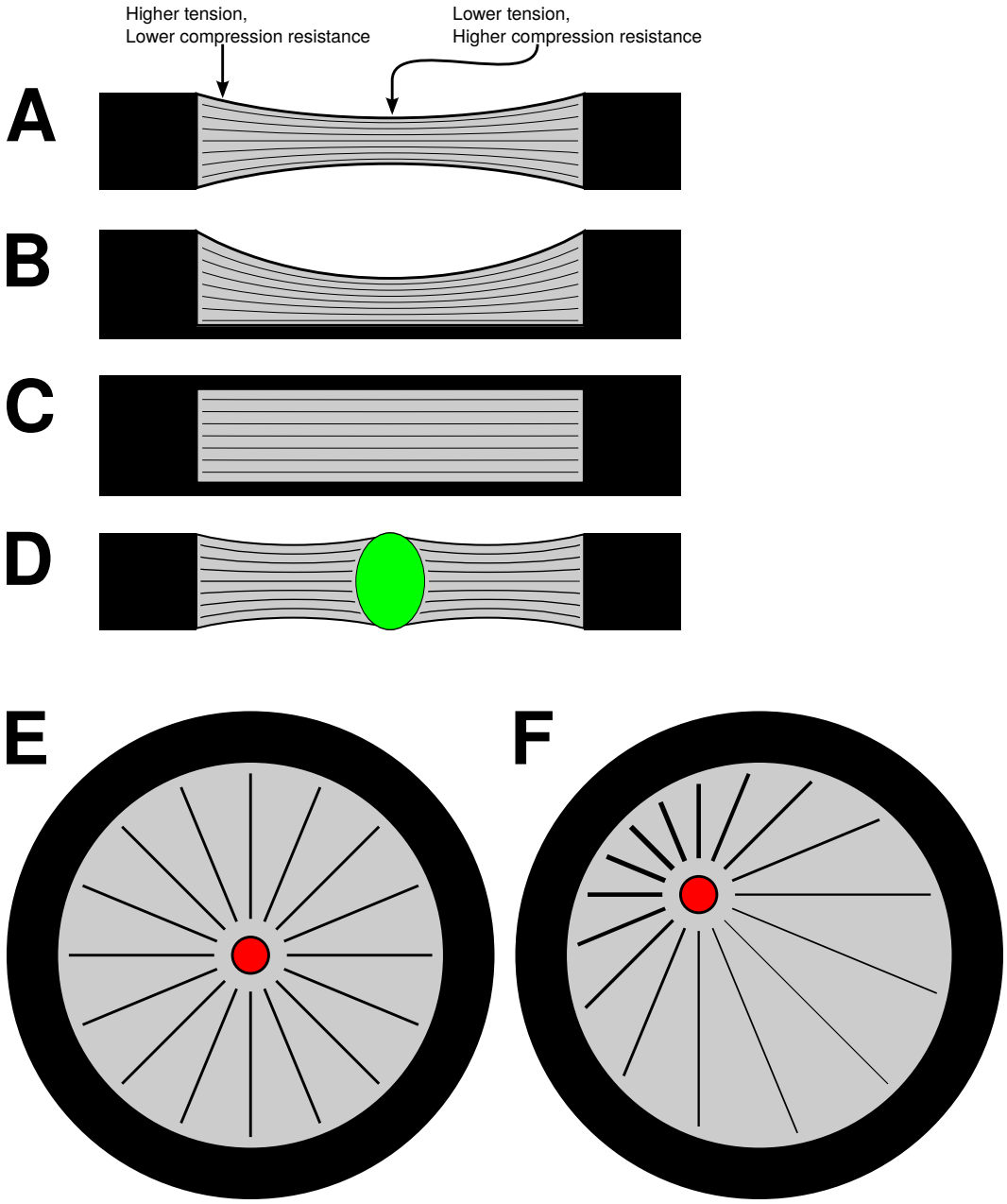

Figure 5.14: Effects of tensile forces within the matrix. (A–C) depict the distribution of lateral forces within a cross-section through the centre of the gel. (A) A collagen gel set in a PEI-coated glutaraldehyde-functionalised steel ring is shown in cross-section. Due to the attachment of collagen to the inner wall of the ring, if the gel is subject to uniform contractile force the forces exerted upon the gel vary with the radial position, shown here as in an idealised form assuming omnidirectional application of force by each cell or spheroid throughout the gel. The edges of the gel are attached to the rigid wall, providing an opposing force to contractile force. The centre of the gel contains no attachments, and so will tend to bow inwards due to local contractile forces. If the gel is anchored to the well bottom (B) or additionally the top (C), the distribution of lateral force would be altered, and the intensity would also be reduced as a consequence of the attachment, with a consequent increase in the role of vertical tensile forces. (D) A large explant such as an E17.5 thymus may be relatively incompliant and hence act to redistribute tensile forces within the gel, resulting in increased tension overall as a product of a shorter distance between edges. (E–F) depict the distribution of radial forces within the gel. (E) A spheroid placed in the centre of the gel will exert equal force in all directions. (F) A spheroid placed off-centre will exert force in each direction as a function of the edge distance as a result of differential gel compliancy.

vidual spheroid. These effects may therefore act to establish an overall radial tension gradient from well edge to centre.

The spheroid model has previously been used to study how tensional forces in extracellular matrix influence sprouting by Korff and Augustin (1999). Here, tension was imposed *externally* by pulling the collagen gel in one dimension using pins pushed into the gel. This resulted in directional sprouting in line with the tensile force. In contrast, in the ring model the tensional force arises *internally* due to the intrinsic effects of the HUVEC contraction of collagen. While Korff and Augustin (1999) examined the local effects of directed sprout growth between spheroids, the effect was only found to occur up to 700 µm, while Figure 5.12 shows this is present up to at least 2 mm when considering edge effects. This difference may be due to the fact that while Korff and Augustin (1999) used gels set in wells (as opposed to free-floating), these were not physically bonded to their container as in the case of the metal rings. This may limit the amount of tension in the gel because contraction is not opposed as strongly. It is thought that cells are capable of transducing mechanical forces into nuclear transcriptional changes (Wang, Tytell *et al.*, 2009), and in the case of smooth muscle experimental evidence suggests a role for RhoA (Peyton, Kim *et al.*, 2008). Given the role of RhoA in endothelial migration and angiogenesis, this may imply that RhoA in EC is responsible for increased angiogenesis in response to increased matrix tension (van Nieuw Amerongen *et al.*, 2003).

Potential improvements to the model to reduce edge effects are illustrated in Figure 5.15. The theme common to the different supports is to minimise the distance between edges to ensure that the minimum and maximum distances any spheroid is placed relative to an edge is strictly controlled. In its simplest form (A), this could be accomplished by placing the spheroids into a closed channel with a box or circular cross-section; such devices are commercially available, and allow live imaging of the gel (*e.g.* µ-slides from Ibidi, München, Germany). However, it would be necessary to use multiple channels to use such a model with tissue explants, shown in radial orientation in (B). Note that both strategies would result in an even distribution of spheroids over distance, eliminating the distribution bias discussed previously (Figure 5.13). Using a micropatterned surface substrate (*e.g.* of PDMS), either as a closed channel network or open at the top (C), would permit a cell- or spheroid-seeded collagen solution to be gelled within the channels and provide a larger total volume than single channels, and hence more replicates. This could be further improved with the use of micropegs or posts (D) which would oppose gel contraction and provide relatively uniform tensile forces within the gel. Such systems have been used previously for measuring forces imposed upon substrata by cells including epithelial cells (du Roure, Saez *et al.*, 2005) and fibroblasts (Li, Xie *et al.*, 2007). While these are at a small scale ($< 5\,\mu m$), pillars of larger dimensions and reduced compliancy are capable of opposing the contraction of a gel, for example as produced by Zheng,

Henderson *et al.* (2011).

5.3.9 Other effects

An additional effect of differential matrix tension is the known influence of matrix stiffness upon the cell cycle, reviewed by Assoian and Klein (2008). This may result in differential rates of cell proliferation, for example if the gel is stiffer at the edge due to increased tensile forces this may result in greater cell proliferation, which may additionally affect outgrowth rates. This could be assessed by staining with a cell cycle marker such as Ki67 or incorporation of thymidine analogue such as BrdU or EdU (Chehrehasa, Meedeniya *et al.*, 2009).

Given that increasing collagen concentration negatively affects the diffusion of solutes (Ramanujan *et al.*, 2002), and that EC in the spheroid were seen to visibly condense the matrix surrounding them, as shown in Figure 5.6, it may be the case *in vivo* that tissue condensation, perhaps driven in whole or in part by vascularisation, may be limited by negative feedback as a consequence of increasing diffusion limitations. Vascularisation may also arise due to positive feedback as EC invasion increases matrix tension, driving further invasion and tension increase, until limited by some other factor. As shown above and by Korff and Augustin (1999), vascularisation is partly driven by tensional forces in addition to the effects of growth factors. How these observations should influence our current understanding of *in vivo* vascularisation is limited by our lack of knowledge of the tensional forces within the developing embryo. In the adult, tension has been shown to play an important role in the revascularisation of granulation tissue (Kilarski *et al.*, 2009), and it may be equally important during development. In the case of the LN, which is surrounded by the lymph sac, tension may be reduced around the edges of what will become the subcapsular sinus and cortex, which may explain why the medulla and paracortex are highly vascularised while the edge of the cortex is not. While differential expression of pro- and anti-angiogenic factors undoubtedly play a role in the maintenance of this architecture, as discussed in Chapter 3, tensional forces may also play a role. As illustrated by Ohtani and Ohtani (2008), the reticular network of the developed node appears to run mainly radially through the cortex and continue through the subcapsular sinus to the fibrous cortex. This may be indicative of the node being subject to tensile forces in this direction, presumably to cope with expansion under both hydrostatic pressure and lymphocyte influx. Speculatively, this may explain how the looping of the HEVs is established within the stroma, by extension outward radially along a tensile force gradient from the hilus to cortex, then looping around as forces decrease (and inhibitory factors increase) as the subcapsular sinus is approached.

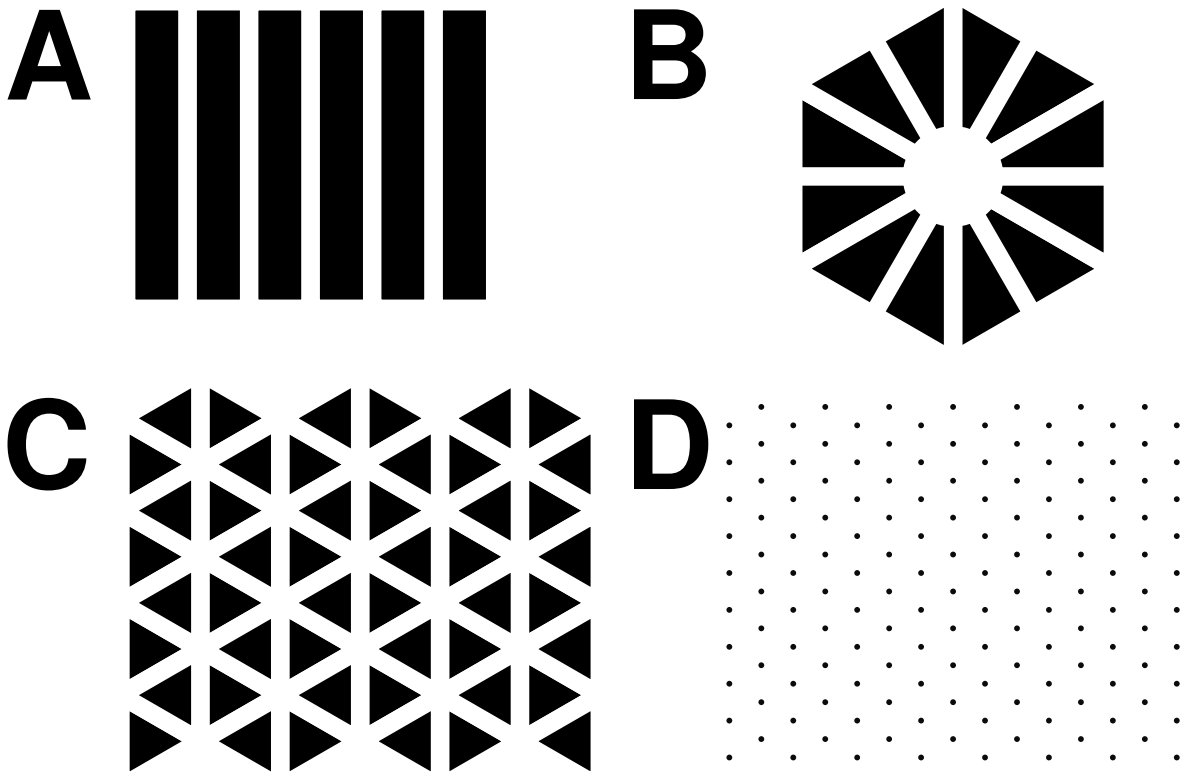

Figure 5.15: Minimising edge effects upon spheroid outgrowth. (A) The gel may be set in channels, to ensure that all parts of the gel are within a small distance of a rigid surface. Black areas are an incompliant substrate, while white areas are channels. (B) These may be arranged radially to allow study of diffusion effects *e.g.* arising from explants placed at a central point. (C) An optimal arrangement of microchannels for spheroid-seeded gels. (D) Micropegs protruding from the seeding surface provide a large contact area, and should not interfere appreciably with cell migration or diffusion of soluble factors.

5.4 Conclusions

This is, to the best of my knowledge, the first use of the Korff spheroid model as a means of assaying the presence of solute gradients and spatial patterns within an extracellular matrix. Using the spheroid model, differential angiogenic outgrowth was demonstrated in the presence of live explants of developing lymphoid tissue, reduced outgrowth being observed with increasing spatial proximity to the explants. The nature of the soluble anti-angiogenic molecule and its cellular source within the explant remain to be elucidated. This is also the first use of the spheroid model to demonstrate the response of endothelial cells to self-imposed intrinsic long distance tensile force gradients within a collagen gel.

5.5 Future Work

5.5.1 Spheroid model

Using the spheroid model as a means of creating embeddable biosensors to monitor pro- and anti- angiogenic signalling has many other uses in addition to developmental biology. They might, for example, be embedded into gels alongside solid tumours (either cultured cell aggregates or biopsies) in order to assay their metabolic state and metastatic potential. In this case the effects of pharmacological compounds could be screened for their effects upon tumour vascularisation and cell migration. The model may also be used to model aspects of LN development entirely *in vitro*. Recent work in the lab has shown that various cell lines of mesenchymal origin may be differentiated into FRC-like stroma through treatment with anti-lymphotoxin receptor antibody (in place of LTi signalling through LT). Thus it may be possible to combine differentiated LTos with vascular and lymphatic endothelium and model their interactions.

The role of cell proliferation and apoptosis in the spheroid model remains to be investigated. As demonstrated by Korff and Augustin (1998), cells in the centre of the spheroid are prone to apoptosis, and this is modulated by the presence of growth factors or blocking antibodies. This tendency might also prove useful as a sensing mechanism for VEGF and bFGF in the immediate environment of the spheroid. Single EC were also observed in close proximity to the spheroids, particularly those at a distance away from unfixed explants as shown in Figure 5.6. As observed by Korff and Augustin (1999), these cells undergo apoptosis following loss of contact with their neighbours, but this would be desirable to confirm independently, and to additionally observe if EC apoptosis (or lack of proliferation) of surface or sprouting EC is responsible for limiting sprouting or sprout outgrowth.

The principal deficiency with the spheroid model is excessive noise. In addition

to the issues regarding spheroid sedimentation and gel geometry, addressed above, the spheroid model could be further improved with a few simple modifications. For example, decreasing the spheroid size to permit more to be seeded within a single gel, would result in greater statistical significance to measurements. An additional improvement would be to incorporate smooth muscle coverage, which would modulate the response of HUVECs to pro-angiogenic factors (Korff *et al.*, 2001). HUVEC–C3H/10T½ spheroid cocultures were attempted (not shown), but C3H/10T½ migrated freely throughout the gel rather than forming stable interactions with the HUVECs. The use of a more appropriate pericyte line might result in formation of more physiologically-relevant structures (Stratman *et al.*, 2010).

5.5.2 Image analysis

Several strategies for imaging the spheroids have been tested, including phase contrast, epifluorescence, confocal z-stacks, tiled confocal z-stacks and high-throughput imaging using an ImageXpress system to image complete parts of, or entire, gels. Due to the fact that the spheroids outgrow in three dimensions within the gel, phase contrast images are hard to interpret and are not suitable for automated image analysis. Epifluorescence images allow visualisation of most of the features within a single spheroid, but due to the fact that spheroids are found within differing planes of focus within a gel, are not suited to imaging multiple spheroids in a single field of view. Confocal imaging of the entire volume should solve this problem, at the expense of greatly increased acquisition time and image size. Such data has been acquired, but is prohibitively expensive to acquire in terms of acquisition time and data storage, and additionally currently available software is incapable of sophisticated analysis and quantification in 3D.

High-throughput acquisition using the ImageXpress system avoids some of these problems, at the expense of reduced resolution, which in this case is perfectly acceptable for quantification purposes. However, the analysis requires further refinement to eliminate 2D outgrowth from the spheroids and to eliminate outliers which skew the data. Were epifluorescence imaging to be used again, deconvolution of the image stacks may remove sufficient out of focus information to permit reliable automated analysis of 3-D structures.

5.5.3 Signalling pathways

The cellular source of the soluble factors is currently unknown. Where sufficient cellular material may be obtained, such as in the case of the thymus, this could be investigated by sorting the cells into different major subsets (for example hCD2-GFP$^+$ thymocytes and hCD2-GFP$^-$ thymic stroma) and seeding these into a spheroid gel either as a single cell suspension or in spheroid form as an anlagen analogue. Re-

peated iteratively, this approach could be used to identify the specific cellular source (or sources) of pro- and anti-angiogenic factors in the developing anlagen. Given their small size, this would be rather more difficult for LN anlagen, but would also be possible given sufficient cellular material pooled from multiple embryos, or the use of a bigger animal model with larger LNs.

The identity of the soluble factors is also yet to be elucidated. These could potentially be identified using the spheroid model in combination with blocking agents against candidate factors. In order to investigate its specific role, PEDF is available in recombinant form, and PEDF blocking antibodies are also available. It should therefore be possible to use anti-PEDF to block PEDF activity in spheroid gels containing explants. Additionally, gels with PEDF, PEDF plus anti-PEDF and anti-PEDF alone could be used to demonstrate the effectiveness of the PEDF blockade, and show that anti-PEDF does not affect angiogenesis by itself. Anti-VEGF could be used to additionally assess the role of VEGF, and a number of small molecule tyrosine kinase inhibitors such as SU5416 (semaxinib) and SU11248 (sunitinib malate) are available, which inhibit the intracellular kinase activity of all the VEGFRs. MMP inhibitors such as GM6001 (ilomastat) and BB2516 (marimastat) could also be used to investigate the role of MMP activity in this model.

5.5.4 Tensile forces

Imaging the structure of the collagen gel either by SHG or direct labelling would allow the direction of forces within the gel to be determined by the local collagen fibril alignment. Clearly, to further investigate the phenomenon of gel tension, it is necessary to measure tensile forces within the gel. Several workers have attempted to measure the tensile force of gel contraction with various strategies, for example John, Quinlan *et al.* (2010) used the displacement of cantilevers attached to the gel edge. However, such strategies measure only the *bulk properties* of the gel, rather than being able to sense the direction and magnitude of force at discrete points in a gel, as would be experienced by a cell. An alternative would be make use of stress-sensing mechanisms used *in vivo*, for example the deformation of fibronectin. Under tension, fibronectin deforms to expose cryptic binding sites which could be used map stress forces within a gel (Klotzsch, Smith *et al.*, 2009). As demonstrated by this paper, a Förster resonance energy transfer (FRET) pair placed either side of the cryptic site may be used as an *in vitro* strain probe. An alternative would be to use an antibody to label the exposed cryptic sites, providing they were accessible.

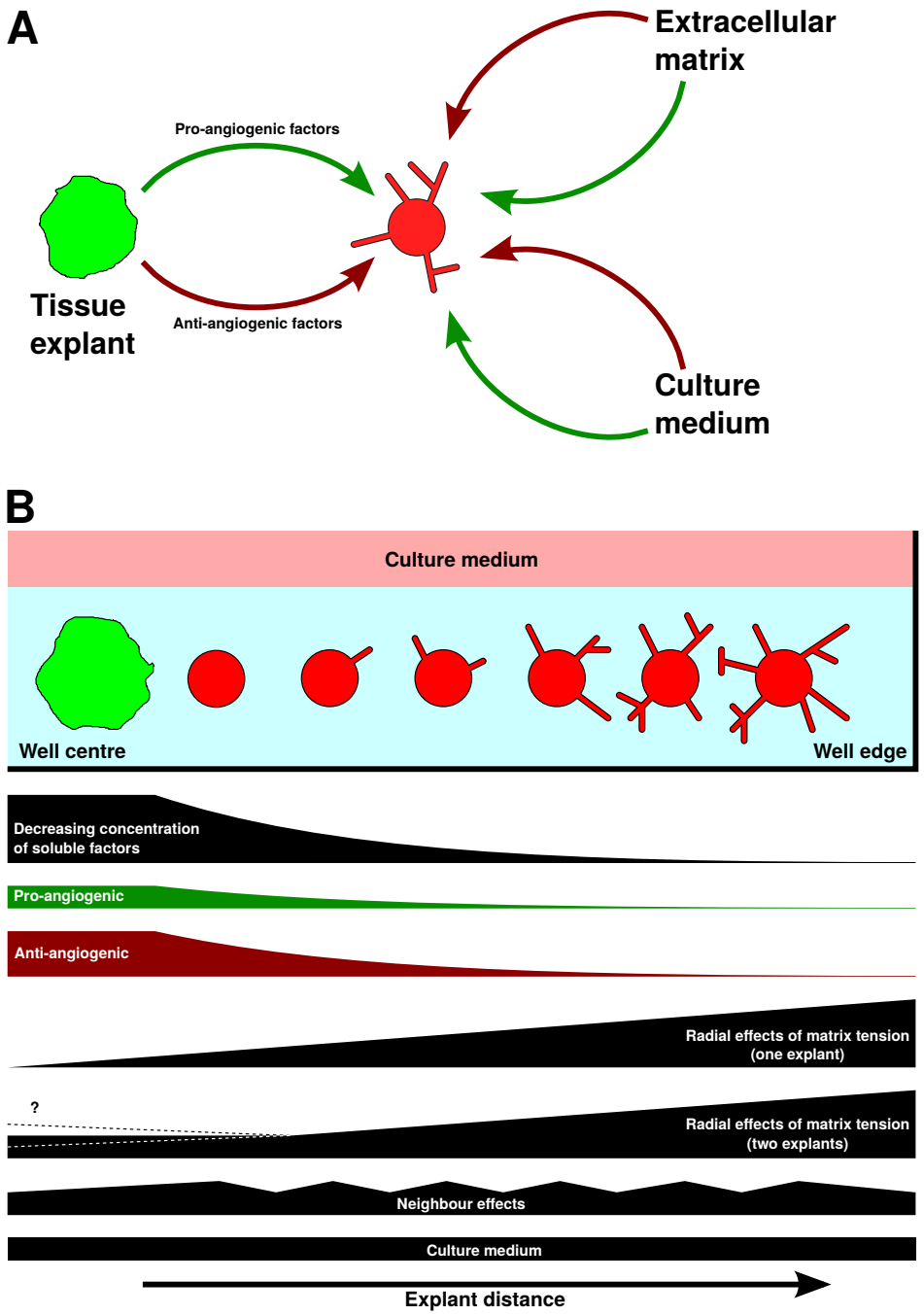

Figure 5.16: Major factors influencing spheroid outgrowth. (A) Tissue explants, extracellular matrix and culture medium are sources of both pro- and anti-angiogenic factors which collectively affect angiogenic sprouting. (B) These factors may be present as spatial gradients. Soluble factors arising from a tissue explant will establish a concentration gradient decreasing exponentially with distance away from the explant, additionally complicated by matrix interactions and sequestration. The data in this chapter indicate that anti-angiogenic factors predominate. Matrix tension additionally affects spheroid outgrowth, there being more outgrowth closer to the edge in a linear relationship. Single explants were placed in the well centre, while two explants were offset from the centre, which complicates the effect of matrix tension because spheroids at a given distance from the explant will have a distribution of distances to the well edge. Spheroids in close proximity may also influence the outgrowth of their neighbours. Factors in the culture medium are constant at all radial distances, bar any local depletion in close proximity to the explant, being above the gel and free to diffuse within it.

Chapter 6

Discussion

The aims behind the work presented in this thesis have been to investigate the processes and mechanisms by which the LN is vascularised during development. The aims were addressed using a combination of imaging, gene expression analysis and *in vitro* modelling of the effects of LN-derived soluble factors upon angiogenesis utilising a model developed for the purpose.

6.1 Summary of findings

6.1.1 *In vivo* observations

In Chapter 3, *in vivo* observations were made using both confocal microscopy to study structural aspects of cellular organisation and quantitative RTPCR to study gene expression within the developing LN anlagen. Imaging of wholemount preparations of the thymus at E15.5 (Figure 3.1) demonstrated that the vascular basement membrane is synthesised in stages, with laminin and fibronectin being laid down before collagen IV, which was observed to be present only in the cortex while laminin and fibronectin were also present in the medulla. This was additionally interpreted to imply that smooth muscle coverage of the nascent vascular network was acquired from the outside moving inwards to the centre, which would be the case if the source of the VSMCs was external to the thymus. Wholemount was however not suitable for imaging the developing LN anlagen due to excessive autofluorescence, which masked immunofluorescence and effectively prevented identification of the anlagen. LN anlagen imaged using live MP imaging (Figure 3.2) showed that the site of LTi clustering was structurally different from the surrounding tissue, being a pocket having less dense collagen I matrix than the surrounding mesenchyme, and being bounded by a dense collagen I band, identified by SHG reflectance, and being a double band around part of the pocket. Confocal imaging of frozen sections (Figure 3.3) showed a similar collagen I pattern, which appeared to stain the same structures as collagen IV, and additionally were at least in part positive for LYVE-1, indicating a

composition of LECs in part or in full. These structures, surrounding the clustering LTis, were assumed to be the lymph sac based upon comparisons with LN development data in the literature, appearing roughly hemispherical in shape enclosing the majority of the LTis (Vondenhoff *et al.*, 2009a). The anlagen also contained $VCAM^+$ stromal organisers in intimate association with LTis (Cupedo *et al.*, 2004). Staining for endothelial cells using the markers endomucin and MECA-32 showed little staining within the lymph sac, though some positive staining was observed around the sac, indicating a lack of vascularisation within the anlagen. Small spots of collagen IV staining were observed within the LTi clusters, however these were not sufficiently large to indicate the presence of blood vessels, unlike for the lymph sac.

RTPCR analysis of pro- and anti-angiogenic factors (Figures 3.7 and 3.8) illustrated a complex pattern of changes in different tissues during development, with PEDF, thrombospondin and the different VEGF-A isoforms all varying. However, due to relative quantification being used and the relationship between expression level and angiogenic activity being unknown, these data alone were insufficient to determine whether the anlagen were predominantly pro- or anti-angiogenic at any timepoint during development, and hence how these changes related to the process of LN vascularisation could not be determined. In consequence, a functional *in vitro* assay was developed in order that the net effect of all secreted factors could be assayed.

Additionally, gene expression in the MRC and FRC subsets of human fœtal LNs was measured using microarray analysis (Figure 3.9). These data highlighted a number of significant differences between the MRC and FRC populations which may have functional significance regarding their role in vascular maintenance and LN function. Chemokine, interleukin and adhesion molecule upregulation in the MRCs demonstrated their phenotypic similarity with LTos (Katakai *et al.*, 2008). Additionally, differences in factors promoting, inhibiting and regulating angiogenesis illustrated that the angiogenic environments of the two subsets were rather different, which may reflect their different functional roles.

6.1.2 *In vitro* vascular modelling

In order to develop a "complete" vascular model, containing endothelial cells, smooth muscle coverage of the endothelium and fluid flow, models of both vasculogenesis and angiogenesis were implemented. The technology to develop perfused microfluidic networks inside gels was successfully developed and demonstrated to work (Figures 4.1 and 4.2), but limitations in the strength of collagen type I gels prevented their use in experiments.

Modelling vasculogenesis required the use of a cocktail of growth factors and PMA to stimulate tube formation and permit EC survival within a collagen gel, resulting in formation of a complex interconnected network which was demonstrated

to contain tubes with patent lumens and other features of capillaries including adherens junctions (Figures 4.3, 4.4 and 4.5). However, thicker gels were observed to contain apparently necrotic central cores (Figure 4.4), a factor of their size and the high seeding densities required. Introduction of smooth muscle coverage using aortic VSMCs resulted in induction of tube formation at low frequency (Figure 4.7), which was increased through utilisation of TGF-β_1-differentiated C3H/10T½ cells (Figure 4.10), but which took significant time to develop a fully interconnected network. Vasculogenesis models with and without smooth muscle coverage both formed interconnected networks, but had the disadvantage of the network structure being difficult to analyse using existing image analysis strategies, and additional complications arose when considering how to subsequently measure changes in the network in response to different treatments. The images shown in Chapter 4 were fixed rather than live; due to the lack of stably-transfected GFP-expressing ECs, imaging and quantifying the remodelling of a single network over time was not feasible.

Angiogenesis was modelled utilising an existing model developed by Thomas Korff and Helmut Augustin, based around the concept of seeding EC spheroids (Figure 4.15) into a collagen gel, resulting in sprouting angiogenesis from the spheroid surface into the gel, as demonstrated in Figure 4.16 (Korff and Augustin, 1998). Quantification of the outgrowth allowed the response of the spheroids to different treatments to be measured, which was demonstrated using different growth factors. This model was subsequently adapted to permit the measure of spatial effects within a gel.

6.1.3 *In vitro* observations

Using LN anlagen and thymi dissected from E14.5–E17.5 embryos, explanted into collagen gels seeded with collagen spheroids, outgrowth of the spheroids was measured and correlated with the distance of the spheroid from the explanted material (Figures 5.2, 5.4, 5.6, 5.8, 5.7, 5.10 and 5.11). In all cases, angiogenesis was suppressed in close proximity to the explant, an effect which declined with distance indicating that the effect was due to a soluble factor emanating from the explant. Upon PFA fixation (Figures 5.8, 5.7, 5.10 and 5.11), outgrowth was shown to occur at baseline levels at all distances from the explant in most cases, interpreted to mean that the factors originating from the explant were being actively produced by the cells within the explant. An additional effect observed in particular with larger explants at later timepoints was a rise and fall in outgrowth moving away from the explant; due to anti-angiogenic factors such as PEDF having a lower molecular weight than pro-angiogenic factors such as VEGF, this was thought likely to be a result of separation of the factors during their diffusion through the gel (Ramanujan *et al.*, 2002), resulting in the formation of net pro- and anti-angiogenic radial bands.

The relationship between outgrowth and nearest-neighbour distance was also in-

vestigated (Figures 5.5 and 5.12), but no clear trends were visible; it was concluded that spheroids did not appear to significantly affect each other's outgrowth. However, when comparing outgrowth to edge distance (Figure 5.12) it was observed that growth was proportional to distance from the edge, with growth being highest at the edge. The most obvious variable which could be responsible for this effect was gel tension imposed by EC contraction of the gel as a result of contraction being constrained by the bonding of the gel edges to the support ring, which would result in a gradient of high to low tension from edge to centre (Figure 5.14), tension having been previously shown to affect angiogenesis by Korff and Augustin (1999).

6.2 A model of early LN vascularisation

The question of when and how the LN anlagen becomes vascularised remains outstanding, with the early development of the inguinal and axillary/brachial nodes as investigated by Bénézech *et al.* (2010) and Vondenhoff *et al.* (2009a), respectively, being apparently contradictory in their observations regarding the organisation of the endothelial and stromal layers, with the inguinal node shown to be composed of an endothelial bud surrounded by stroma while the opposite appeared to be the case for the brachial node. These apparent differences may be a result of the different timing of their development, or it may be the case that there are differences in the initial development of different LNs, as is the case for bronchus-associated lymphoid tissue, for example, which is induced by IL-17 and is LT-independent in its initial stages of formation, yet still requires CCL19 and CXCL13 (Rangel-Moreno, Carragher *et al.*, 2011). However, the development of the inguinal node at later stages does not appear to reflect axillary or brachial node development at any of the stages studied. The data shown in Figures 3.2 and 3.3 bear some structural similarities with the data presented by Vondenhoff *et al.* (2009a), both showing LTi and LTo cells surrounded by a lymph sac, albeit using different markers to identify the different cell types. The key difference is that in Figure 3.3 no vessels were seen to be present within the LTi clusters, while Vondenhoff *et al.* (2009a) convincingly showed that several different vessel types, identified using VEGFR1, VEGFR2 and MECA-32, were present inside the E14.5 brachial node anlagen, some potentially also expressing LTβR as present upon developed HEVs and lymphatic vessels within the LN (Liao and Ruddle, 2006). If present, these may have been missed in Figure 3.3 due to a combination of the antibodies used such as endomucin potentially not staining endothelial markers being expressed at this developmental timepoint (Foster *et al.*, 2008), and markers such as MECA-32 may have by chance not stained sections containing a full cross-section through the anlagen, and consequently these observations can not refute the findings of Vondenhoff *et al.* (2009a).

Given the observations from the spheroid model that the environment is pre-

dominantly anti-angiogenic, and the additional observation that physical forces such as matrix tension also influence angiogenesis, Figure 6.1 presents a tentative model which combines these effects, taking into account the above observations regarding early anlagen structure and also the observation that during development the cells of the anlagen progressively condense (Coles *et al.*, 2010). This model proposes that the mesenchyme, during the process of condensation, will impose contractile forces upon its surroundings. In the case of the adjacent lymph sac, this will be pulled around the mesenchyme, which could result in the the formation of the "pocket" containing the LTis observed in Figure 3.2. Contraction may also induce vascularisation, not by growth factors, given the net anti-angiogenic environment observed experimentally, but by pulling vascular loops into the condensing mass. This process of "looping angiogenesis" has been shown to be important in the revascularisation of granulation tissue by Kilarski *et al.* (2009), who demonstrated that a fibrin/collagen matrix could pull vessels from an existing vascular bed, and that the process was blocked by preventing gel contraction by mixing in glass fibres. This observation leads to the question of whether this plays a role in development, especially given the fact that repair processes appear to recapitulate developmental processes (Schultz and Wysocki, 2009; Sephel *et al.*, 1996).

Naturally, this model does not preclude the influence of pro- and anti-angiogenic factors and the more common forms of sprouting and intussusceptive angiogenesis, which would be required for elaboration of the initial vascular supply into the highly-branched structures seen in the developed node (Willard-Mack, 2006). However, biomechanical extrusion of vascular loops may play a role in the initial acquisition of blood vasculature by the anlagen, which may explain how the E14.5 brachial node observed by Vondenhoff *et al.* (2009a) came to contain MECA-32$^+$ vessels in a predominantly anti-angiogenic environment prior to extensive stromal activation by LTis. This process operates at a higher order of tissue organisation than sprouting and intussusceptive angiogenesis, which act at the level of single cells and small groups of cells respectively (sprouts and tissue pillars), whereas looping angiogenesis leads to the reorganisation of the route and positioning of entire groups of vessels (Burri and Djonov, 2002; Kilarski *et al.*, 2009). This process may therefore play a wider role in general vascular organisation during development. The *in vitro* findings that the anlagen generate a *net* anti-angiogenic environment does not preclude *local* pro-angiogenic environments where pro-angiogenic factors reach a threshold concentration capable of negating the anti-angiogenic background, resulting in controlled angiogenic outgrowth in specific locations (Chappell *et al.*, 2009; Kappas *et al.*, 2008). Such highly-localised effects would not have been detectable using RTPCR or the *in vitro* spheroid model.

In addition to condensation of the mesenchyme, the lymph sac structure might additionally arise due to matrix contraction by the lymphatic endothelium itself,

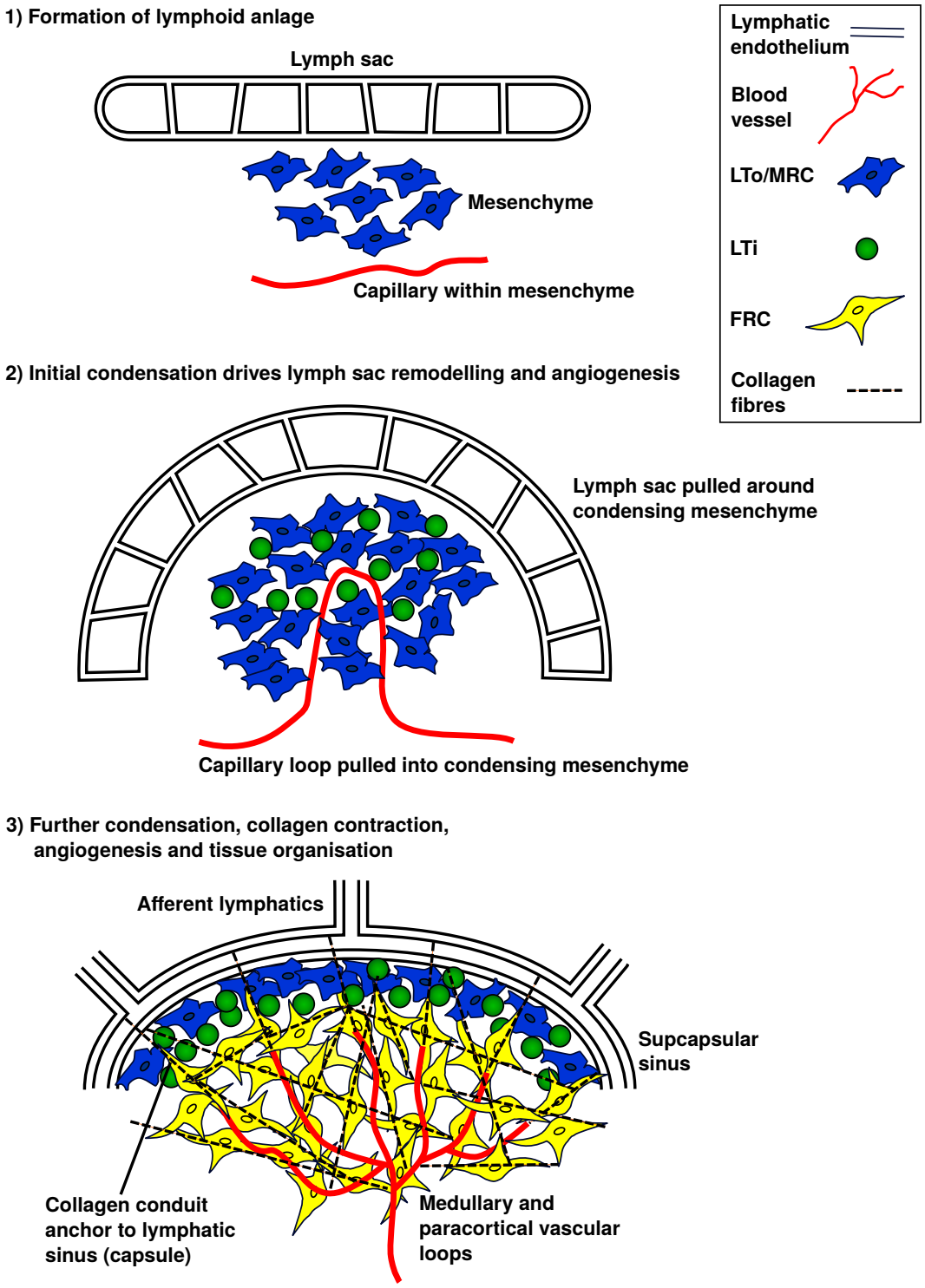

Figure 6.1: Model of condensation-driven LN vascularisation and organisation. The mesenchyme adjacent to the lymph sac is initially avascular, with capillaries present in the mesenchyme at a distance. LTi- and LTo-mediated condensation of the mesenchyme pulls a capillary loop into the anlage as a result of the resulting contractile forces, *i.e.* looping angiogenesis. The condensation also has the effect of pulling the lymph sac around the condensing structure. Further elaboration of this simple structure, including further tissue condensation, contraction of collagen fibres in the extracellular matrix, and further development of organised cellular structures results in the formation of the mature LN vasculature, including its HEVs in medullary and paracortical vascular loops, connected to the subcapsular sinus by the conduit system of reticular fibres ensheathed by FRCs.

given the observation that ECs are capable of matrix contraction. If the cells adjacent to the stroma contract the matrix more strongly than those on the outer face, this would result in eversion of the sac. In Figure 3.3 (panels A–D in particular), the density of cells outside the lymph sac shown by DAPI staining is significantly lower than inside. This might result in differential contraction of the lymph sac, or may arise in consequence of the contraction and/or condensation taking place. The structure may therefore arise due to stromal condensation, lymph sac-mediated matrix contraction, or a combination of the two.

6.3 Hypoxia, organogenesis and vascularisation

Hypoxia has been shown to be critically important during development, in particular its induction of VEGF-A demonstrates the importance of hypoxia-driven angiogenesis in the maintenance of a stable oxygen supply to tissues, and in inducing tissue vascularisation during development (Iyer *et al.*, 1998). The presence of differential hypoxia was demonstrated in the mouse embryo by Lee *et al.* (2001), for example in the heart ventricle and head mesenchyme while Nanka *et al.* (2006) demonstrated a direct link, albeit in the quail, between hypoxia, VEGF expression and the density of the vascular beds. In this model, the condensing mesenchyme of the limb buds became hypoxic; hypoxia resulting from mesenchymal condensation has also been found to occur in the developing endochondral bones as a result of chondrocyte condensation, resulting in the induction of HIF-1α-mediated responses, shown by Provot *et al.* (2007) and reviewed by Dunwoodie (2009). If condensation-induced hypoxia also occurs in the LN anlagen, this may therefore be both responsible for vascular remodelling as well as in mesenchymal differentiation.

Lymphocytes are unable to gain entry to the LN until P3, when the HEVs switch from expressing MAdCAM to PNAd (Randall *et al.*, 2008). In consequence, at this timepoint T and B cells expressing LT are able to replace LTis and in greater numbers given the low frequency of LTis in peripheral blood (Mebius *et al.*, 1997), which may result in increased oxygen demand from the increased cellularity of the LN, and hence an increase in hypoxia-induced angiogenesis. In addition, the reticular networks are formed as a result of contact with lymphocytes, and thus the completion of stromal development can not commence until the arrival of lymphocytes in the node (Katakai *et al.*, 2004). This may imply that the LN vascularisation proceeds in two stages: initial vascularisation during development, followed by remodelling to adapt to the increased metabolic demands of a functional node and completion of stromal organisation.

6.4 Coordination of vascular and stromal organisation

The development of a functional node depends upon two major events to occur in parallel: the formation of the lymph sac and the induction of the stroma. These events are to some extent independent; the stroma has been shown in at least some situations to be induced by CXCL13 signalling resulting from neuronal-derived RA signalling (van de Pavert *et al.*, 2009). Additionally, it has been shown by the same group that lymph sacs are not strictly required for stromal patterning (Vondenhoff *et al.*, 2009b), however the phenotype of the conditional Prox1 mutants used was complex. Defects were noted in stromal differentiation, and the authors suggested that this could be explained by the positioning of the LTis being affected by the lack of LECs. The model described in Figure 6.1 could potentially explain these changes: as the lymph sac is pulled around the condensing mesenchyme, it may act as a physical barrier to cellular migration (due to the presence of a basement membrane and high cell density) in addition to the adhesion molecules used to retain LTis after stromal activation. This may result in the retention of the LTis within a confined area and a consequent increase in the duration and frequency of their interaction with stromal cells. This physical boundary and LTi partitioning is particularly obvious in Figures 3.2(C) and 3.3(A–D). In consequence, the lack of lymph sac may result in decreased efficiency of LTi–stromal interactions, leading to reduced stromal activation and hence reduced LTi retention, decreasing the positive feedback observed to occur during normal development (Roozendaal and Mebius, 2011).

6.5 Future directions

The existing observations both in this thesis and by Vondenhoff *et al.* (2009a) do not include development prior to E14.5. However, at E14.5 LTis contained within the enclosing lymph sac indicate that development began at an earlier timepoint given the significant amount of structure already present. It is therefore necessary to study earlier timepoints through imaging, for example E12.5 and E13.5, in order to observe the initial events of LN induction. This would provide further insight into the structural changes taking place prior to LTi infiltration. Of particular importance would be to image the structures in 3-D using confocal or MP microscopy in order to fully comprehend the organisation in three dimensions, since from the existing 2-D data the "pocket" structure could be a fold rather than a pocket, which would have implications regarding the constraints imposed upon the movement of cells within it.

Given the requirement for the vascular and stromal organisation to be coordinated, it is possible that both these somewhat independent processes are coordinated by an as-yet unidentified signal. The trigger for LEC specification in the cardinal veins is unknown. Given the link between neural-derived RA in induction of stromal

CXCL13 expression, it is possible that neural-derived signals are also responsible for triggering lymphatic development, perhaps in combination with some other signal found at venous confluences in order to create the conditions for inducing the specific patterning observed. Correlation of the timescale of innervation, angiogenesis and lymphangiogenesis at the sites of LN development may provide further insights.

Given the discrepancies between the axillary/brachial and inguinal nodes in the observations of Bénézech *et al.* (2010) and Vondenhoff *et al.* (2009a), further study of all the peripheral nodes at all timepoints is required in order to understand the differences between the nodes, in particular, whether the differences are merely temporal, or if the different LNs have different requirements for the initial stromal and/or vascular specification. Differences are already known for other lymphoid tissues, for example the requirement in Peyer's patch formation for LTin cells in addition to LTis, and in bronchus-associated lymphoid tissue which is is LT- and LTi-independent, induced by IL-17, and also in the formation of tertiary lymphoid structures during inflammation (Coles *et al.*, 2010; Gräbner, Lötzer *et al.*, 2009; Muniz, Pacer *et al.*, 2011; Randall *et al.*, 2008; Rangel-Moreno *et al.*, 2011). It may therefore be the case that peripheral secondary lymphoid organs are not completely identical in the cellular and molecular requirements for their induction.

In vitro modelling may be used to study whether the model proposed in Figure 6.1 is possible by creating models containing sorted LTis and LTos or stromal cells contained within collagen gels of differing compliancy (concentration) and with defined shape, in order to constrain cellular movements. Such a model could prove whether constraining LTi movement affects the activation of LTos, which could be assessed by observing the upregulation of appropriate markers, for example adhesion molecules, using imaging or flow cytometry.

Definitions

2-D	two-dimensional
3-D	three-dimensional
ADAM	a disintegrin and metallopeptidase domain
ADAMTS	a disintegrin and metallopeptidase domain with thrombospondin motifs
AF	Alexa Fluor
APC	antigen presenting cell
BABB	benzyl alcohol benzyl benzoate
BAEC	bovine aortic endothelial cell
bFGF	basic fibroblast growth factor
BEC	blood endothelial cell
BSA	bovine serum albumin
CAD	computer aided design
CAM	computer aided manufacturing
CCL	CC chemokine ligand
CCR	CC chemokine receptor
CD	cluster of differentiation
CD144	See VE-cadherin
CD31	See PECAM-1
C3H/10T½	multipotent mesenchymal cell line, derived from the C3H mouse
CFSE	carboxyfluorescein succinimidyl ester
CMTMR	chloromethyl tetramethylrhodamine

CXCL CXC chemokine ligand

CXCR CXC chemokine receptor

DAG diacylglycerol

DAPI 4 ,6-diamidino-2-phenylindole

DC dendritic cell

DMDCS dimethyldichlorosilane

DMEM Dulbecco's modified Eagle's medium

DMSO dimethyl sulphoxide

DPBS Dulbecco's phosphate buffered saline

EC endothelial cell

ECGS/H endothelial cell growth supplement / hypothalamus

ECM extracellular matrix

ECGM endothelial cell growth medium

ECGM MV2 endothelial cell growth medium (microvascular) 2

EDTA ethylenediaminetetraacetic acid

EF eFluor quantum dot fluorophore

ERK extracellular-regulated kinase

FBS fœtal bovine serum

FDC follicular dendritic cell

FGF fibroblast growth factor

FGFR fibroblast growth factor receptor

FITC fluorescein isothiocyanate

FLIM fluorescence lifetime imaging

FRC fibroblastic reticular cell

FRET Förster resonance energy transfer

FS forward scatter

GFP green fluorescent protein

Gp38 glycoprotein 38; podoplanin

hCD2-GFP human-CD2-GFP

HDLEC human dermal lymphatic endothelial cell

HEPES-BSS 4-(2-hydroxyethyl)-1-piperazineethanesulfonic acid buffered saline solution

HEV high endothelial venule

HIF-1α hypoxia inducible factor-1α

HRE hypoxic response element

HUVEC human umbilical vein endothelial cell

ICAM intercellular adhesion molecule

ID2 inhibitor of DNA binding 2

IDC interdigiating dendritic cell

IL interleukin

IP_3 inositol trisphosphate

IMDM Iscove's modified Dulbecco's medium

LEC lymphatic endothelial cell

LN lymph node

LT lymphotoxin

LTβR lymphotoxin-β receptor

LTi lymphoid tissue inducer

LTo lymphoid tissue organiser

MAdCAM mucosal addressin cellular adhesion molecule

MAPK mitogen-activated protein kinase

MEK MAP kinase kinase

MOI multiplicity of infection

MØ macrophage

MP multiphoton

MMP matrix metallopeptidase

MRC marginal reticular cell

MT-MMP membrane-type matrix metallopeptidase

NA numerical aperture

NDD non-descanned detector

NG2 neuron-glial 2

NO nitric oxide

OCT optimal cutting temperature embedding medium

PBS phosphate buffered saline

PCR polymerase chain reaction

PDGF platelet-derived growth factor

PDGFRβ platelet-derived growth factor receptor β

PDMS poly(dimethylsiloxane)

PECAM-1 platelet/endothelial cell adhesion molecule 1

PEDF pigment epithelium-derived factor

PEDFR pigment epithelium-derived factor receptor

PEG polyethylene glycol

PEI poly(ethylenimine)

PEN poly(ethylene 2,6-napthalate)

PFA paraformaldehyde

PI3K phosphatidylinositol 3-kinase

PIP_2 phosphatidylinositol 4,5-bisphosphate

PIP_3 phosphatidylinositol 3,4,5-trisphosphate

PLCγ phospholipase Cγ

PKB protein kinase B

PKC protein kinase C

PLGA polylactic co-glycolic acid

PlGF	placental growth factor
PMA	phorbol 12-myristate 13-acetate
PNAd	peripheral node addressin
PPAR-γ	proliferator-activated receptor γ
RA	retinoic acid
RALDH2	retinaldehyde dehydrogenase 2
RANK	receptor activator of NF-κB
RANKL	receptor activator of NF-κB ligand
RARE	retinoic acid response element
RT	room temperature
RTPCR	quantitative real-time reverse transcriptase PCR
RTV	room temperature vulcanising
RORγt	retinoic acid receptor-related orphan receptor-γt
SEM	scanning electron microscopy
SHG	second harmonic generation
α-SMA	α-smooth muscle actin
S1P	sphingosine-1-phosphate
SS	side scatter
TEM	transmission electron microscopy
TGF-β_1	transforming growth factor β_1
TIMP	tissue inhibitor of metalloproteinases
TNF	tumour necrosis factor
TRANCE	TNF-related activation-induced cytokine
TRANCER	TNF-related activation-induced cytokine receptor
VCAM	vascular cell adhesion molecule
VE-cadherin	vascular endothelial cadherin
VEGF	vascular endothelial growth factor

VEGFR vascular endothelial growth factor receptor

VSMC vascular smooth muscle cell

Bibliography

Abràmoff, M., Magalhães, P., Ram, S. (2004). Image processing with ImageJ. *Biophotonics International* **11**: 36–42.

Adams, R. H., Alitalo, K. (2007). Molecular regulation of angiogenesis and lymphangiogenesis. *Nat Rev Mol Cell Biol* **8**: 464–478.

Adelman, D. M., Maltepe, E., Simon, M. C. (1999). Multilineage embryonic hematopoiesis requires hypoxic ARNT activity. *Genes Dev* **13**: 2478–2483.

Adobe Systems Incorporated (1999). PostScript language reference manual, 3rd edition.

Ahn, G.-O., Brown, J. M. (2008). Matrix metalloproteinase-9 is required for tumor vasculogenesis but not for angiogenesis: role of bone marrow-derived myelomonocytic cells. *Cancer Cell* **13**: 193–205.

Akeson, A., Herman, A., Wiginton, D., Greenberg, J. (2010). Endothelial cell activation in a VEGF-A gradient: relevance to cell fate decisions. *Microvasc Res* **80**: 65–74.

Alitalo, K., Tammela, T., Petrova, T. V. (2005). Lymphangiogenesis in development and human disease. *Nature* **438**: 946–953.

Arcaute, K., Mann, B. K., Wicker, R. B. (2006). Stereolithography of three-dimensional bioactive poly(ethylene glycol) constructs with encapsulated cells. *Ann Biomed Eng* **34**: 1429–1441.

Armstrong, L. C., Bornstein, P. (2003). Thrombospondins 1 and 2 function as inhibitors of angiogenesis. *Matrix Biol* **22**: 63–71.

Armulik, A., Abramsson, A., Betsholtz, C. (2005). Endothelial/pericyte interactions. *Circ Res* **97**: 512–523.

Armulik, A., Genové, G., Betsholtz, C. (2011). Pericytes: developmental, physiological, and pathological perspectives, problems, and promises. *Dev Cell* **21**: 193–215.

Assoian, R. K., Klein, E. A. (2008). Growth control by intracellular tension and extracellular stiffness. *Trends Cell Biol* **18**: 347–352.

Aszódi, A., Legate, K. R., Nakchbandi, I., Fässler, R. (2006). What mouse mutants teach us about extracellular matrix function. *Annu Rev Cell Dev Biol* **22**: 591–621.

Auerbach, R., Lewis, R., Shinners, B., Kubai, L., Akhtar, N. (2003). Angiogenesis assays: A critical overview. *Clin Chem* **49**: 32–40.

Augustin, H. G., Koh, G. Y., Thurston, G., Alitalo, K. (2009). Control of vascular morphogenesis and homeostasis through the angiopoietin-Tie system. *Nat Rev Mol Cell Biol* **10**: 165–177.

Bajénoff, M., Egen, J. G., Koo, L. Y., Laugier, J. P., Brau, F., Glaichenhaus, N., Germain, R. N. (2006). Stromal cell networks regulate lymphocyte entry, migration, and territoriality in lymph nodes. *Immunity* **25**: 989–1001.

Bayless, K. (2003). Sphingosine-1-phosphate markedly induces matrix metalloproteinase and integrin-dependent human endothelial cell invasion and lumen formation in three-dimensional collagen and fibrin matrices. *Biochem Biophys Res Commun* **312**: 903–913.

Bayless, K. J., Davis, G. E. (2004). Microtubule depolymerization rapidly collapses capillary tube networks *in vitro* and angiogenic vessels *in vivo* through the small GTPase Rho. *J Biol Chem* **279**: 11686–11695.

Bayless, K. J., Kwak, H.-I., Su, S.-C. (2009). Investigating endothelial invasion and sprouting behavior in three-dimensional collagen matrices. *Nat Protoc* **4**: 1888–1898.

Bazzoni, G., Dejana, E. (2004). Endothelial cell-to-cell junctions: molecular organization and role in vascular homeostasis. *Physiol Rev* **84**: 869–901.

Becerra, S. P. (1997). Structure-function studies on PEDF. A noninhibitory serpin with neurotrophic activity. *Adv Exp Med Biol* **425**: 223–237.

van Beijnum, J. R., van der Linden, E., Griffioen, A. W. (2008). Angiogenic profiling and comparison of immortalized endothelial cells for functional genomics. *Exp Cell Res* **314**: 264–272.

Benedito, R., Roca, C., Sörensen, I., Adams, S., Gossler, A., Fruttiger, M., Adams, R. H. (2009). The notch ligands Dll4 and Jagged1 have opposing effects on angiogenesis. *Cell* **137**: 1124–1135.

Bergers, G., Brekken, R., McMahon, G., Vu, T. H., Itoh, T., Tamaki, K., Tanzawa, K., Thorpe, P., Itohara, S., Werb, Z., Hanahan, D. (2000). Matrix metalloproteinase-9 triggers the angiogenic switch during carcinogenesis. *Nat Cell Biol* **2**: 737–744.

Bergers, G., Song, S. (2005). The role of pericytes in blood-vessel formation and maintenance. *Neuro Oncol* **7**: 452–464.

Berriman, J. A., Li, S., Hewlett, L. J., Wasilewski, S., Kiskin, F. N., Carter, T., Hannah, M. J., Rosenthal, P. B. (2009). Structural organization of Weibel-Palade bodies revealed by cryo-EM of vitrified endothelial cells. *Proc Natl Acad Sci USA* **106**: 17407–17412.

Bhattacharya, S., Datta, A., Berg, J., Gangopadhyay, S. (2005). Studies on surface wettability of poly(dimethyl) siloxane (PDMS) and glass under oxygen-plasma treatment and correlation with bond strength. *J Microelectromech S* **14**: 590.

Bird, I. N., Taylor, V., Newton, J. P., Spragg, J. H., Simmons, D. L., Salmon, M., Buckley, C. D. (1999). Homophilic PECAM-1 (CD31) interactions prevent endothelial cell apoptosis but do not support cell spreading or migration. *J Cell Sci* **112**: 1989–1997.

Bishop, E. T., Bell, G. T., Bloor, S., Broom, I. J., Hendry, N. F. K., Wheatley, D. N. (1999). An *in vitro* model of angiogenesis: Basic features. *Angiogenesis* **3**: 335–344.

Blacher, S., Devy, L., Burbridge, M. F., Roland, G., Tucker, G., Noël, A., Foidart, J. M. (2001). Improved quantification of angiogenesis in the rat aortic ring assay. *Angiogenesis* **4**: 133–142.

Blum, K. S., Pabst, R. (2006). Keystones in lymph node development. *J Anat* **209**: 585–595.

de Boer, J., Williams, A., Skavdis, G., Harker, N., Coles, M., Tolaini, M., Norton, T., Williams, K., Roderick, K., Potocnik, A. J., Kioussis, D. (2003). Transgenic mice with hematopoietic and lymphoid specific expression of Cre. *Eur J Immunol* **33**: 314–325.

Bohnsack, B. L., Hirschi, K. K. (2004). Red light, green light: signals that control endothelial cell proliferation during embryonic vascular development. *Cell Cycle* **2**: 1506–1511.

Bosco, M. C., Puppo, M., Pastorino, S., Mi, Z., Melillo, G., Massazza, S., Rapisarda, A., Varesio, L. (2004). Hypoxia selectively inhibits monocyte chemoattractant protein-1 production by macrophages. *J Immunol* **172**: 1681–90.

Bouck, N. (2002). PEDF: anti-angiogenic guardian of ocular function. *Trends Mol Med* **8**: 330–334.

Bozec, A., Gros, F.-X., Penault-Llorca, F., Formento, P., Cayre, A., Dental, C., Etienne-Grimaldi, M.-C., Fischel, J.-L., Milano, G. (2008). Vertical VEGF targeting: A combination of ligand blockade with receptor tyrosine kinase inhibition. *Eur J Cancer* **44**: 1922–1930.

Bozec, L., van der Heijden, G., Horton, M. (2007). Collagen fibrils: nanoscale ropes. *Biophys J* **92**: 70–75.

Burri, P. H., Djonov, V. (2002). Intussusceptive angiogenesis—the alternative to capillary sprouting. *Mol Aspects Med* **23**: S1–27.

Bussolati, B., Dunk, C., Grohman, M., Kontos, C. D., Mason, J., Ahmed, A. (2001). Vascular endothelial growth factor receptor-1 modulates vascular endothelial growth factor-mediated angiogenesis via nitric oxide. *Am J Pathol* **159**: 993–1008.

Butler, J., Lana, D., Round, O., LaMontagne, K. (2004). Functional characterization of sphingosine 1-phosphate receptor agonist in human endothelial cells. *Prostaglandins Other Lipid Mediat* **73**: 29–45.

Bénézech, C., White, A., Mader, E., Serre, K., Parnell, S., Pfeffer, K., Ware, C. F., Anderson, G., Caamaño, J. H. (2010). Ontogeny of stromal organizer cells during lymph node development. *J Immunol* **184**: 4521–4530.

Cabodi, M., Choi, N. W., Gleghorn, J. P., Lee, C. S. D., Bonassar, L. J., Stroock, A. D. (2005). A microfluidic biomaterial. *J Amer Chem Soc* **127**: 13788–13789.

Cao, G., O'Brien, C. D., Zhou, Z., Sanders, S. M., Greenbaum, J. N., Makrigiannakis, A., DeLisser, H. M. (2002). Involvement of human PECAM-1 in angiogenesis and *in vitro* endothelial cell migration. *Am J Physiol Cell Physiol* **282**: C1181–1190.

Cao, Y. (2001). Endogenous angiogenesis inhibitors and their therapeutic implications. *Int J Biochem Cell Biol* **33**: 357–369.

Carew, M. A., Paleolog, E. M., Pearson, J. D. (1992). The roles of protein kinase C and intracellular Ca^{2+} in the secretion of von Willebrand factor from human vascular endothelial cells. *Biochem J* **286**: 631–635.

Carl Zeiss MicroImaging GmbH (2007). PALM Robo – Import / Export Interface. Bernried, Germany, 2.2 edition.

Carmeliet, P., Ferreira, V., Breier, G., Pollefeyt, S., Kieckens, L., Gertsenstein, M., Fahrig, M., Vandenhoeck, A., Harpal, K., Eberhardt, C., Declercq, C., Pawling, J., Moons, L., Collen, D., Risau, W., Nagy, A. (1996). Abnormal blood vessel development and lethality in embryos lacking a single VEGF allele. *Nature* **380**: 435–439.

Ceradini, D. J., Kulkarni, A. R., Callaghan, M. J., Tepper, O. M., Bastidas, N., Kleinman, M. E., Capla, J. M., Galiano, R. D., Levine, J. P., Gurtner, G. C. (2004). Progenitor cell trafficking is regulated by hypoxic gradients through HIF-1 induction of SDF-1. *Nat Med* **10**: 858–864.

Cha, J., Kim, J., Ryu, S.-K., Park, J., Jeong, Y., Park, S., Park, S., Kim, H. C., Chun, K. (2006). A highly efficient 3D micromixer using soft PDMS bonding. *J Micromech Microeng* **16**: 1778.

Chan, D. A., Giaccia, A. J. (2007). Hypoxia, gene expression, and metastasis. *Cancer Metastasis Rev* **26**: 333–339.

Chappell, J. C., Taylor, S. M., Ferrara, N., Bautch, V. L. (2009). Local guidance of emerging vessel sprouts requires soluble Flt-1. *Dev Cell* **17**: 377–386.

Chehrehasa, F., Meedeniya, A. C. B., Dwyer, P., Abrahamsen, G., Mackay-Sim, A. (2009). EdU, a new thymidine analogue for labelling proliferating cells in the nervous system. *J Neurosci Methods* **177**: 122–130.

Choi, N. W., Cabodi, M., Held, B., Gleghorn, J. P., Bonassar, L. J., Stroock, A. D. (2007). Microfluidic scaffolds for tissue engineering. *Nat Mater* **6**: 908–915.

Christensen, A. M., Chang-Yen, D. A., Gale, B. K. (2005). Characterization of interconnects used in PDMS microfluidic systems. *J Micromech Microeng* **15**: 928.

Chrobak, K. M., Potter, D. R., Tien, J. (2006). Formation of perfused, functional microvascular tubes *in vitro*. *Microvasc Res* **71**: 185–196.

Chyou, S., Ekland, E. H., Carpenter, A. C., Tzeng, T. C., Tian, S., Michaud, M., Madri, J. A., Lu, T. T. (2008). Fibroblast-type reticular stromal cells regulate the lymph node vasculature. *J Immunol* **181**: 3887–3896.

Coles, M., Kioussis, D., Veiga-Fernandes, H. (2010). Cellular and molecular requirements in lymph node and Peyer's patch development. *Prog Mol Biol Transl Sci* **92**: 177–205.

Coles, M. C., Veiga-Fernandes, H., Foster, K. E., Norton, T., Pagakis, S. N., Seddon, B., Kioussis, D. (2006). Role of T and NK cells and IL7/IL7r interactions during neonatal maturation of lymph nodes. *Proc Natl Acad Sci USA* **103**: 13457–13462.

Coulet, F., Nadaud, S., Agrapart, M., Soubrier, F. (2003). Identification of hypoxia-response element in the human endothelial nitric-oxide synthase gene promoter. *J Biol Chem* **278**: 46230–46240.

Creusot, R. J., Mitchison, N. A., Terazzini, N. M. (2002). The immunological synapse. *Mol Immunol* **38**: 997–1002.

Cross, V. L., Zheng, Y., Won Choi, N., Verbridge, S. S., Sutermaster, B. A., Bonassar, L. J., Fischbach, C., Stroock, A. D. (2010). Dense type I collagen matrices that support cellular remodeling and microfabrication for studies of tumor angiogenesis and vasculogenesis *in vitro*. *Biomaterials* **31**: 8596–8607.

Cuadrado, A., Nebreda, A. R. (2010). Mechanisms and functions of p38 MAPK signalling. *Biochem J* **429**: 403–417.

Cupedo, T., Vondenhoff, M. F., Heeregrave, E. J., De Weerd, A. E., Jansen, W., Jackson, D. G., Kraal, G., Mebius, R. E. (2004). Presumptive lymph node organizers are differentially represented in developing mesenteric and peripheral nodes. *J Immunol* **173**: 2968–2975.

Curry, J. M., Eubank, T. D., Roberts, R. D., Wang, Y., Pore, N., Maity, A., Marsh, C. B. (2008). M-CSF signals through the MAPK/ERK pathway via Sp1 to induce VEGF production and induces angiogenesis *in vivo*. *PLoS ONE* **3**: e3405.

Darland, D. C., D'Amore, P. A. (2001). TGFβ is required for the formation of capillary-like structures in three-dimensional cocultures of 10T1/2 and endothelial cells. *Angiogenesis* **4**: 11–20.

Darland, D. C., Massingham, L. J., Smith, S. R., Piek, E., Saint-Geniez, M., D'Amore, P. A. (2003). Pericyte production of cell-associated VEGF is differentiation-dependent and is associated with endothelial survival. *Dev Biol* **264**: 275–288.

Davis, G. E., Bayless, K. J., Mavila, A. (2002). Molecular basis of endothelial cell morphogenesis in three-dimensional extracellular matrices. *Anat Rec* **268**: 252–275.

Davis, G. E., Black, S. M., Bayless, K. J. (2000a). Capillary morphogenesis during human endothelial cell invasion of three-dimensional collagen matrices. *In Vitro Cell Dev Biol Anim* **36**: 513–519.

Davis, G. E., Camarillo, C. W. (1996). An α2β1 integrin-dependent pinocytic mechanism involving intracellular vacuole formation and coalescence regulates capillary lumen and tube formation in three-dimensional collagen matrix. *Exp Cell Res* **224**: 39–51.

Davis, G. E., Koh, W., Stratman, A. N. (2007). Mechanisms controlling human endothelial lumen formation and tube assembly in three-dimensional extracellular matrices. *Birth Defects Res C Embryo Today* **81**: 270–285.

Davis, G. E., Pintar Allen, K. A., Salazar, R., Maxwell, S. A. (2000b). Matrix metalloproteinase-1 and -9 activation by plasmin regulates a novel endothelial cell-mediated mechanism of collagen gel contraction and capillary tube regression in three-dimensional collagen matrices. *J Cell Sc* **114**: 917–930.

Davis, G. E., Senger, D. R. (2005). Endothelial extracellular matrix: biosynthesis, remodeling, and functions during vascular morphogenesis and neovessel stabilization. *Circ Res* **97**: 1093–1107.

Dawson, D. W. (1999). Pigment epithelium-derived factor: A potent inhibitor of angiogenesis. *Science* **285**: 245.

Dejana, E., Tournier-Lasserve, E., Weinstein, B. M. (2009). The control of vascular integrity by endothelial cell junctions: molecular basis and pathological implications. *Dev Cell* **16**: 209–221.

Dejana, E., Valiron, O., Navarro, P., Lampugnani, M. G. (1997). Intercellular junctions in the endothelium and the control of vascular permeability. *Ann N Y Acad Sci* **811**: 36–43.

Demol, J., Lambrechts, D., Geris, L., Schrooten, J., Van Oosterwyck, H. (2011). Towards a quantitative understanding of oxygen tension and cell density evolution in fibrin hydrogels. *Biomaterials* **32**: 107–118.

Dike, L. E., Chen, C. S., Mrksich, M., Tien, J., Whitesides, G. M., Ingber, D. E. (1999). Geometric control of switching between growth, apoptosis, and differentiation during angiogenesis using micropatterned substrates. *In Vitro Cell Dev Biol Anim* **35**: 441–448.

Dormer, A., Beck, G. (2005). Evolutionary analysis of human vascular endothelial growth factor, angiopoietin, and tyrosine endothelial kinase involved in angiogenesis and immunity. *In Silico Biol* **5**: 323–339.

Doukas, C. N., Maglogiannis, I., Chatziioannou, A., Papapetropoulos, A. (2006). Automated angiogenesis quantification through advanced image processing techniques. *Conf Proc IEEE Eng Med Biol Soc* **1**: 2345–2348.

Duffy, D. C., McDonald, J. C., Schueller, O. J. A., Whitesides, G. M. (1998). Rapid prototyping of microfluidic systems in poly(dimethylsiloxane). *Anal Chem* **70**: 4974–4984.

Dunwoodie, S. L. (2009). The role of hypoxia in development of the mammalian embryo. *Dev Cell* **17**: 755–773.

Egaña, J. T., Condurache, A., Lohmeyer, J. A., Kremer, M., Stöckelhuber, B. M., Lavandero, S., Machens, H.-G. (2009). *Ex vivo* method to visualize and quantify vascular networks in native and tissue engineered skin. *Langenbecks Arch Surg* **394**: 349–356.

Eguchi, R., Suzuki, A., Miyakaze, S., Kaji, K., Ohta, T. (2007). Hypoxia induces apoptosis of HUVECs in an *in vitro* capillary model by activating proapoptotic signal p38 through suppression of ERK1/2. *Cell Signal* **19**: 1121–1131.

Eichmann, A., Makinen, T., Alitalo, K. (2005a). Neural guidance molecules regulate vascular remodeling and vessel navigation. *Genes Dev* **19**: 1013–1021.

Eichmann, A., Yuan, L., Moyon, D., Lenoble, F., Pardanaud, L., Breant, C. (2005b). Vascular development: from precursor cells to branched arterial and venous networks. *Int J Dev Biol* **49**: 259–267.

Ek, E. T. H., Dass, C. R., Choong, P. F. M. (2006). PEDF: a potential molecular therapeutic target with multiple anti-cancer activities. *Trends Mol Med* **12**: 497–502.

Elvert, G., Kappel, A., Heidenreich, R., Englmeier, U., Lanz, S., Acker, T., Rauter, M., Plate, K., Sieweke, M., Breier, G., Flamme, I. (2003). Cooperative interaction of hypoxia-inducible factor-2α (HIF-2α) and Ets-1 in the transcriptional activation of vascular endothelial growth factor receptor-2 (Flk-1). *J Biol Chem* **278**: 7520–7530.

Engelhardt, S., Hoch, E., Borchers, K., Meyer, W., Krüger, H., Tovar, G. E. M., Gillner, A. (2011). Fabrication of 2D protein microstructures and 3D polymer-protein hybrid microstructures by two-photon polymerization. *Biofabrication* **3**: 025003.

Esemuede, N., Lee, T., Pierre-Paul, D., Sumpio, B. E., Gahtan, V. (2004). The role of thrombospondin-1 in human disease. *J Surg Res* **122**: 135–142.

Evans, C. E., Mattock, K., Humphries, J., Saha, P., Ahmad, A., Waltham, M., Patel, A., Modarai, B., Porter, L., Premaratne, S., Smith, A. (2011). Techniques of assessing hypoxia at the bench and bedside. *Angiogenesis* **14**: 119–124.

Evans, K. D., Oberbauer, A. M. (2008). Spatiotemporal localization of VEGF-A isoforms in the mouse postnatal growth plate. *Anat Rec (Hoboken)* **291**: 6–13.

Fenton, B. M., Zweifach, B. W. (1981). Microcirculatory model relating geometrical variation to changes in pressure and flow rate. *Annals of Biomedical Engineering* **9**: 303–321.

Ferrara, N., Carver-Moore, K., Chen, H., Dowd, M., Lu, L., O'Shea, K. S., Powell-Braxton, L., Hillan, K. J., Moore, M. W. (1996). Heterozygous embryonic lethality induced by targeted inactivation of the VEGF gene. *Nature* **380**: 439–442.

Ferrara, N., Henzel, W. J. (1989). Pituitary follicular cells secrete a novel heparin-binding growth factor specific for vascular endothelial cells. *Biochem Biophys Res Commun* **161**: 851–858.

Fischer, C., Mazzone, M., Jonckx, B., Carmeliet, P. (2008). FLT1 and its ligands VEGFB and PlGF: drug targets for anti-angiogenic therapy? *Nat Rev Cancer* **8**: 942–956.

Folkman, J. (2004). Endogenous angiogenesis inhibitors. *APMIS* **112**: 496–507.

Fong, G.-H. (2009). Regulation of angiogenesis by oxygen sensing mechanisms. *J Mol Med* **87**: 549–560.

Foo, S. S., Turner, C. J., Adams, S., Compagni, A., Aubyn, D., Kogata, N., Lindblom, P., Shani, M., Zicha, D., Adams, R. H. (2006). Ephrin-B2 controls cell motility and adhesion during blood-vessel-wall assembly. *Cell* **124**: 161–173.

Ford, M. C., Bertram, J. P., Hynes, S. R., Michaud, M., Li, Q., Young, M., Segal, S. S., Madri, J. A., Lavik, E. B. (2006). A macroporous hydrogel for the coculture of neural progenitor and endothelial cells to form functional vascular networks *in vivo*. *Proc Natl Acad Sci USA* **103**: 2512–2517.

Forsythe, J. A., Jiang, B. H., Iyer, N. V., Agani, F., Leung, S. W., Koos, R. D., Semenza, G. L. (1996). Activation of vascular endothelial growth factor gene transcription by hypoxia-inducible factor 1. *Mol Cell Biol* **16**: 4604–4613.

Foster, K., Sheridan, J., Veiga-Fernandes, H., Roderick, K., Pachnis, V., Adams, R., Blackburn, C., Kioussis, D., Coles, M. (2008). Contribution of neural crest-derived cells in the embryonic and adult thymus. *J Immunol* **180**: 3183–3189.

Fraisl, P., Mazzone, M., Schmidt, T., Carmeliet, P. (2009). Regulation of angiogenesis by oxygen and metabolism. *Dev Cell* **16**: 167–179.

François, M., Caprini, A., Hosking, B., Orsenigo, F., Wilhelm, D., Browne, C., Paavonen, K., Karnezis, T., Shayan, R., Downes, M., Davidson, T., Tutt, D., Cheah, K. S. E., Stacker, S. A., Muscat, G. E. O., Achen, M. G., Dejana, E., Koopman, P. (2008). Sox18 induces development of the lymphatic vasculature in mice. *Nature* **456**: 643–647.

Freitas, C., Larrivée, B., Eichmann, A. (2008). Netrins and UNC5 receptors in angiogenesis. *Angiogenesis* **11**: 23–29.

Friedl, P., Zänker, K. S., Bröcker, E. B. (1998). Cell migration strategies in 3-D extracellular matrix: Differences in morphology, cell matrix interactions, and integrin function. *Microsc Res Tech* **43**: 369–378.

Gale, N. W., Dominguez, M., Noguera, I., Pan, L., Hughes, V., Valenzuela, D. M., Murphy, A. J., Adams, N. C., Lin, H. C., Holash, J., Thurston, G., Yancopoulos, G. D. (2004). Haploinsufficiency of delta-like 4 ligand results in embryonic lethality due to major defects in arterial and vascular development. *Proc Natl Acad Sci USA* **101**: 15949–15954.

Gao, J., DeRouen, M. C., Chen, C.-H., Nguyen, M., Nguyen, N. T., Ido, H., Harada, K., Sekiguchi, K., Morgan, B. A., Miner, J. H., Oro, A. E., Marinkovich, M. P. (2008). Laminin-511 is an epithelial message promoting dermal papilla development and function during early hair morphogenesis. *Genes Dev* **22**: 2111–2124.

Garl, P. J., Wenzlau, J. M., Walker, H. A., Whitelock, J. M., Costell, M., Weiser-Evans, M. C. M. (2004). Perlecan-induced suppression of smooth muscle cell proliferation is mediated through increased activity of the tumor suppressor PTEN. *Circ Res* **94**: 175–83.

Gautschi, P., Fràter-Schröder, M., Böhlen, P. (1986). Partial molecular characterization of endothelial cell mitogens from human brain: acidic and basic fibroblast growth factors. *FEBS Lett* **204**: 203–207.

Gerber, H. P., Condorelli, F., Park, J., Ferrara, N. (1997). Differential transcriptional regulation of the two vascular endothelial growth factor receptor genes. Flt-1, but not Flk-1/KDR, is up-regulated by hypoxia. *J Biol Chem* **272**: 23659–23667.

Gerhardt, H., Golding, M., Fruttiger, M., Ruhrberg, C., Lundkvist, A., Abramsson, A., Jeltsch, M., Mitchell, C., Alitalo, K., Shima, D., Betsholtz, C. (2003). VEGF guides angiogenic sprouting utilizing endothelial tip cell filopodia. *J Cell Biol* **161**: 1163–1177.

Gilbertson, D. G., Duff, M. E., West, J. W., Kelly, J. D., Sheppard, P. O., Hofstrand, P. D., Gao, Z., Shoemaker, K., Bukowski, T. R., Moore, M., Feldhaus, A. L., Humes, J. M., Palmer, T. E., Hart, C. E. (2001). Platelet-derived growth factor C (PDGF-C), a novel growth factor that binds to PDGF α and β receptor. *J Biol Chem* **276**: 27406–14.

Gliki, G., Wheeler-Jones, C., Zachary, I. (2002). Vascular endothelial growth factor induces protein kinase C (PKC)-dependent Akt/PKB activation and phosphatidylinositol 3′-kinase-mediated PKCδ phosphorylation: Role of PKC in angiogenesis. *Cell Biol Int* **26**: 751–759.

Godyna, S., Liau, G., Popa, I., Stefansson, S., Argraves, W. S. (1995). Identification of the low density lipoprotein receptor-related protein (LRP) as an endocytic receptor for thrombospondin-1. *J Cell Biol* **5**: 1403–1410.

Golden, A. P., Tien, J. (2007). Fabrication of microfluidic hydrogels using molded gelatin as a sacrificial element. *Lab Chip* **7**: 720–725.

Good, D. J., Polverini, P. J., Rastinejad, F., Le Beau, M. M., Lemons, R. S., Frazier, W. A., Bouck, N. P. (1990). A tumor suppressor-dependent inhibitor of angiogenesis is immunologically and functionally indistinguishable from a fragment of thrombospondin. *Proc Natl Acad Sci USA* **87**: 6624–6628.

Goodby, J. W., Görtz, V., Cowling, S. J., Mackenzie, G., Martin, P., Plusquellec, D., Benvegnu, T., Boullanger, P., Lafont, D., Queneau, Y., Chambert, S., Fitremann, J. (2007). Thermotropic liquid crystalline glycolipids. *Chem Soc Rev* **36**: 1971–2032.

Graupera, M., Guillermet-Guibert, J., Foukas, L. C., Phng, L.-K., Cain, R. J., Salpekar, A., Pearce, W., Meek, S., Millan, J., Cutillas, P. R., Smith, A. J. H., Ridley, A. J., Ruhrberg, C., Gerhardt, H., Vanhaesebroeck, B. (2008). Angiogenesis selectively requires the p110α isoform of PI3K to control endothelial cell migration. *Nature* **453**: 662–666.

Green, H., Goldberg, B. (1965). Synthesis of collagen by mammalian cell lines of fibroblastic and nonfibroblastic origin. *Proc Natl Acad Sci USA* **53**: 1360–1365.

Greenberg, J. I., Shields, D. J., Barillas, S. G., Acevedo, L. M., Murphy, E., Huang, J., Scheppke, L., Stockmann, C., Johnson, R. S., Angle, N., Cheresh, D. A. (2008). A role for VEGF as a negative regulator of pericyte function and vessel maturation. *Nature* **456**: 809–813.

Greijer, A. E., van der Groep, P., Kemming, D., Shvarts, A., Semenza, G. L., Meijer, G. A., van de Wiel, M. A., Belien, J. A. M., van Diest, P. J., van der Wall, E. (2005). Up-regulation of gene expression by hypoxia is mediated predominantly by hypoxia-inducible factor 1 (HIF-1). *J Pathol* **206**: 291–304.

Gridley, T. (2007). Notch signaling in vascular development and physiology. *Development* **134**: 2709–2718.

Gräbner, R., Lötzer, K., Döpping, S., Hildner, M., Radke, D., Beer, M., Spanbroek, R., Lippert, B., Reardon, C. A., Getz, G. S., Fu, Y. X., Hehlgans, T., Mebius, R. E., van der Wall, M., Kruspe, D., Englert, C., Lovas, A., Hu, D., Randolph, G. J., Weih, F., Habenicht, A. J. (2009). Lymphotoxin β receptor signaling promotes tertiary lymphoid organogenesis in the aorta adventitia of aged *ApoE*$^{-/-}$ mice. *J Exp Med* **206**: 233–248.

Halama, T., Èger, M. G., Pillinger, M., Staffler, G., Prager, E., Stockinger, H., Holnthoner, W., Lechleitner, S., Wolff, K., Petzelbauer, P. (2001). Platelet endothelial cell adhesion molecule-1 and vascular endothelial cadherin cooperatively regulate fibroblast growth factor-induced modulations of adherens junction functions. *J Invest Dermatol* **116**: 110–117.

Halin, C., Tobler, N. E., Vigl, B., Brown, L. F., Detmar, M. (2007). VEGF-A produced by chronically inflamed tissue induces lymphangiogenesis in draining lymph nodes. *Blood* **110**: 3158–3167.

Halin, S., Rudolfsson, S. H., Doll, J. A., Crawford, S. E., Wikström, P., Bergh, A. (2010). Pigment epithelium-derived factor stimulates tumor macrophage recruitment and is downregulated by the prostate tumor microenvironment. *Neoplasia* **12**: 336–345.

Hallmann, R., Horn, N., Selg, M., Wendler, O., Pausch, F., Sorokin, L. M. (2005). Expression and function of laminins in the embryonic and mature vasculature. *Physiol Rev* **85**: 979–1000.

Hangai, M., Kitaya, N., Xu, J., Chan, C. K., Kim, J. J., Werb, Z., Ryan, S. J., Brooks, P. C. (2002). Matrix metalloproteinase-9-dependent exposure of a cryptic migratory control site in collagen is required before retinal angiogenesis. *Am J Pathol* **161**: 1429–1437.

Harrington, L. S., Sainson, R. C. A., Williams, C. K., Taylor, J. M., Shi, W., Li, J.-L., Harris, A. L. (2008). Regulation of multiple angiogenic pathways by Dll4 and Notch in human umbilical vein endothelial cells. *Microvasc Res* **75**: 144–154.

Harvey, N. L., Oliver, G. (2004). Choose your fate: artery, vein or lymphatic vessel? *Curr Opin Genet Dev* **14**: 499–505.

He, L., Mu, C., Shi, J., Zhang, Q., Shi, B., Lin, W. (2011). Modification of collagen with a natural cross-linker, procyanidin. *Int J Biol Macromol* **48**: 354–359.

He, Y. (1999). Alternative splicing of vascular endothelial growth factor (VEGF)-R1 (FLT-1) pre-mRNA is important for the regulation of VEGF activity. *Molecular Endocrinology* **13**: 537.

Heinzer, S., Kuhn, G., Krucker, T., Meyer, E., Ulmann-Schuler, A., Stampanoni, M., Gassmann, M., Marti, H. H., Müller, R., Vogel, J. (2008). Novel three-dimensional analysis tool for vascular trees indicates complete micro-networks, not single capillaries, as the angiogenic endpoint in mice overexpressing *human* VEGF_{165} in the brain. *Neuroimage* **39**: 1549–1558.

Hellström, M., Kalén, M., Lindahl, P., Abramsson, A., Betsholtz, C. (1999). Role of PDGF-B and PDGFR-β in recruitment of vascular smooth muscle cells and pericytes during embryonic blood vessel formation in the mouse. *Development* **126**: 3047–3055.

Hellström, M., Phng, L.-K., Hofmann, J. J., Wallgard, E., Coultas, L., Lindblom, P., Alva, J., Nilsson, A.-K., Karlsson, L., Gaiano, N., Yoon, K., Rossant, J., Iruela-Arispe, M. L., Kalén, M., Gerhardt, H., Betsholtz, C. (2007). Dll4 signalling through Notch1 regulates formation of tip cells during angiogenesis. *Nature* **445**: 776–780.

Hirashima, M., Sano, K., Morisada, T., Murakami, K., Rossant, J., Suda, T. (2008). Lymphatic vessel assembly is impaired in Aspp1-deficient mouse embryos. *Dev Biol* **316**: 149–159.

Hirschi, K. K., Rohovsky, S. A., Beck, L. H., Smith, S. R., D'Amore, P. A. (1999). Endothelial cells modulate the proliferation of mural cell precursors via platelet-derived growth factor-BB and heterotypic cell contact. *Circ Res* **84**: 298–305.

Hirschi, K. K., Rohovsky, S. A., D'Amore, P. A. (1998). PDGF, TGF-β, and heterotypic cell–cell interactions mediate endothelial cell-induced recruitment of 10T1/2 cells and their differentiation to a smooth muscle fate. *J Cell Biol* **141**: 805–814.

Ho, M. S. P., Böse, K., Mokkapati, S., Nischt, R., Smyth, N. (2008). Nidogens-extracellular matrix linker molecules. *Microsc Res Tech* **71**: 387–395.

Ho, Q. T., Kuo, C. J. (2007). Vascular endothelial growth factor: biology and therapeutic applications. *Int J Biochem Cell Biol* **39**: 1349–1357.

Ho, T.-C., Chen, S.-L., Yang, Y.-C., Lo, T.-H., Hsieh, J.-W., Cheng, H.-C., Tsao, Y.-P. (2009). Cytosolic phospholipase A_2-α is an early apoptotic activator in PEDF-induced endothelial cell apoptosis. *Am J Physiol Cell Physiol* **296**: C273–284.

Hoang, M. V., Whelan, M. C., Senger, D. R. (2004). Rho activity critically and selectively regulates endothelial cell organization during angiogenesis. *Proc Natl Acad Sci USA* **101**: 1874–1879.

Hofmann, A., Ritz, U., Verrier, S., Eglin, D., Alini, M., Fuchs, S., Kirkpatrick, C. J., Rommens, P. M. (2008). The effect of human osteoblasts on proliferation and neovessel formation of human umbilical vein endothelial cells in a long-term 3D co-culture on polyurethane scaffolds. *Biomaterials* **29**: 4217–4226.

Holmes, D. I., Zachary, I. (2005). The vascular endothelial growth factor (VEGF) family: angiogenic factors in health and disease. *Genome Biol* **6**: 209.

Hood, J. D., Frausto, R., Kiosses, W. B., Schwartz, M. A., Cheresh, D. A. (2003). Differential α_v integrin-mediated Ras-ERK signaling during two pathways of angiogenesis. **162**: 933–943.

Hoorweg, K., Cupedo, T. (2008). Development of human lymph nodes and Peyer's patches. *Semin Immunol* **20**: 164–170.

Hou, T. Z., Mustafa, M. Z., Flavell, S. J., Barrington, F., Jenkinson, E. J., Anderson, G., Lane, P. J. L., Withers, D. R., Buckley, C. D. (2010). Splenic stromal cells mediate IL-7 independent adult lymphoid tissue inducer cell survival. *Eur J Immunol* **40**: 359–365.

Hsu, S., Thakar, R., Liepmann, D., Li, S. (2005). Effects of shear stress on endothelial cell haptotaxis on micropatterned surfaces. *Biochem Biophys Res Commun* **337**: 401–409.

Huang, K., Andersson, C., Roomans, G., Ito, N., Claesson-Welsh, L. (2001). Signaling properties of VEGF receptor-1 and -2 homo- and heterodimers. *Int J Biochem Cell Biol* **33**: 315–324.

Huang, Q., Wang, S., Sorenson, C. M., Sheibani, N. (2008). PEDF-deficient mice exhibit an enhanced rate of retinal vascular expansion and are more sensitive to hyperoxia-mediated vessel obliteration. *Exp Eye Res* **87**: 226–241.

Hudson, B. G., Tryggvason, K., Sundaramoorthy, M., Neilson, E. G. (2003). Alport's syndrome, Goodpasture's syndrome, and type IV collagen. *N Engl J Med* **348**: 2543–2556.

Ilan, N., Mahooti, S., Madri, J. A. (1998). Distinct signal transduction pathways are utilized during the tube formation and survival phases of *in vitro* angiogenesis. *J Cell Sci* **111**: 3621–3631.

Inkscape Project (2011). Inkscape: an open source vector graphics editor, 0.48 edition. URL `http://inkscape.org/`

Iruela-Arispe, M. L. (2008). Regulation of Thrombospondin1 by extracellular proteases. *Curr Drug Targets* **9**: 863–868.

Iruela-Arispe, M. L., Bornstein, P., Sage, H. (1991). Thrombospondin exerts an antiangiogenic effect on cord formation by endothelial cells *in vitro*. *Proc Natl Acad Sci USA* **88**: 5026–5030.

Iyer, N. V., Kotch, L. E., Agani, F., Leung, S. W., Laughner, E., Wenger, R. H., Gassmann, M., Gearhart, J. D., Lawler, A. M., Yu, A. Y., Semenza, G. L. (1998). Cellular and developmental control of O_2 homeostasis by hypoxia-inducible factor 1α. *Genes Dev* **12**: 149.

Jackman, R. J., Duffy, D. C., Ostuni, E., Willmore, N. D., Whitesides, G. M. (1998). Fabricating large arrays of microwells with arbitrary dimensions and filling them using discontinuous dewetting. *Anal Chem* **70**: 2280–2287.

Jaffe, E. A., Ruggiero, J. T., Leung, L. L. K., Doyle, M. J., McKeown-Longo, P. J., Mosher, D. F. (1983). Cultured human fibroblasts synthesize and secrete thrombospondin and incorporate it into extracellular matrix. *Proc Natl Acad Sci USA* **80**: 998–1002.

Jat, P. S., Noble, M. D., Ataliotis, P., Tanaka, Y., Yannoutsos, N., Larsen, L., Kioussis, D. (1991). Direct derivation of conditionally immortal cell lines from an *H-2K^b*-tsA58 transgenic mouse. *Proc Natl Acad Sci USA* **88**: 5096–5100.

Jat, P. S., Sharp, P. A. (1989). Cell lines established by a temperature-sensitive simian virus 40 large-T-antigen gene are growth restricted at the nonpermissive temperature. *Mol Cell Biol* **9**: 1672–1681.

Jean, C., Gravelle, P., Fournie, J.-J., Laurent, G. (2011). Influence of stress on extracellular matrix and integrin biology. *Oncogene* **30**: 2697–2706.

Jeon, N. L., Choi, I. S., Xu, B., Whitesides, G. M. (1999). Large-area patterning by vacuum-assisted micromolding. *Adv Mater* **11**: 946–950.

Jeong, G. S., Kwon, G. H., Kang, A. R., Jung, B. Y., Park, Y., Chung, S., Lee, S.-H. (2011). Microfluidic assay of endothelial cell migration in 3D interpenetrating polymer semi-network HA-collagen hydrogel. *Biomed Microdevices* **13**: 717–723.

Jiménez, B., Volpert, O. V., Crawford, S. E., Febbraio, M., Silverstein, R. L., Bouck, N. (2000). Signals leading to apoptosis-dependent inhibition of neovascularization by thrombospondin-1. *Nat Med* **6**: 41–48.

John, J., Quinlan, A. T., Silvestri, C., Billiar, K. (2010). Boundary stiffness regulates fibroblast behavior in collagen gels. *Ann Biomed Eng* **38**: 658–673.

Jonca, F., Ortéga, N., Gleizes, P. R., Bertrand, N., Plouët, J. (1997). Cell release of bioactive fibroblast growth factor 2 by exon 6-encoded sequence of vascular endothelial growth factor. *J Biol Chem* **272**: 24203–24209.

Jones, E. A. V., le Noble, F., Eichmann, A. (2006). What determines blood vessel structure? genetic prespecification vs. hemodynamics. *Physiology (Bethesda)* **21**: 388–395.

Joukov, V., Sorsa, T., Kumar, V., Jeltsch, M., Claesson-Welsh, L., Cao, Y., Saksela, O., Kalkkinen, N., Alitalo, K. (1997). Proteolytic processing regulates receptor specificity and activity of VEGF-C. *EMBO J* **16**: 3898–3911.

Kaluz, S., Kaluzová, M., Stanbridge, E. J. (2008). Regulation of gene expression by hypoxia: integration of the HIF-transduced hypoxic signal at the hypoxia-responsive element. *Clin Chim Acta* **395**: 6–13.

Kam, J., Dong Hyuck amd Mazumder (2008). 3-D biomimetic micro-channel network by laser direct writing. *J Laser Appl* **20**: 185.

Kamei, M., Saunders, W. B., Bayless, K. J., Dye, L., Davis, G. E., Weinstein, B. M. (2006). Endothelial tubes assemble from intracellular vacuoles *in vivo*. *Nature* **442**: 453–456.

Kamphaus, G. D., Colorado, P. C., Panka, D. J., Hopfer, H., Ramchandran, R., Torre, A., Maeshima, Y., Mier, J. W., Sukhatme, V. P., Kalluri, R. (2000). Canstatin, a novel matrix-derived inhibitor of angiogenesis and tumor growth. *J Biol Chem* **275**: 1209–1212.

Kapellos, G. E., Alexiou, T. S., Payatakes, A. C. (2007). A multiscale theoretical model for diffusive mass transfer in cellular biological media. *Math Biosci* **210**: 177–237.

Kappas, N. C., Zeng, G., Chappell, J. C., Kearney, J. B., Hazarika, S., Kallianos, K. G., Patterson, C., Annex, B. H., Bautch, V. L. (2008). The VEGF receptor Flt-1 spatially modulates Flk-1 signaling and blood vessel branching. *J Cell Biol* **181**: 847–858.

Katakai, T., Hara, T., Sugai, M., Gonda, H., Shimizu, A. (2004). Lymph node fibroblastic reticular cells construct the stromal reticulum via contact with lymphocytes. *J Exp Med* **200**: 783–795.

Katakai, T., Suto, H., Sugai, M., Gonda, H., Togawa, A., Suematsu, S., Ebisuno, Y., Katagiri, K., Kinashi, T., Shimizu, A. (2008). Organizer-like reticular stromal cell layer common to adult secondary lymphoid organs. *J Immunol* **181**: 6189–6200.

Kato, S. (1997). Thymic microvascular system. *Microsc Res Tech* **38**: 287–299.

Kay, H. H., Zhu, S., Tsoi, S. (2007). Hypoxia and lactate production in trophoblast cells. *Placenta* **28**: 854–60.

Khetani, S. R., Bhatia, S. N. (2006). Engineering tissues for *in vitro* applications. *Curr Opin Biotechnol* **17**: 524–531.

Kilarski, W. W., Samolov, B., Petersson, L., Kvanta, A., Gerwins, P. (2009). Biomechanical regulation of blood vessel growth during tissue vascularization. *Nat Med* **15**: 657–664.

Kim, E., Xia, Y., Whitesides, G. M. (1996). Micromolding in capillaries: Applications in materials science. *J Am Chem Soc* **118**: 5722–5731.

Kim, E., Xia, Y. N., Whitesides, G. M. (1995). Polymer microstructures formed by moulding in capillaries. *Nature* **376**: 581–584.

Kim, S., Bakre, M., Yin, H., Varner, J. A. (2002). Inhibition of endothelial cell survival and angiogenesis by protein kinase A. *J Clin Invest* **110**: 933–941.

Kinoshita, T., Tsukada, T., Hozawa, M., Yokoyama, C., Kobayashi, M. (2005). Phase separation behavior in a binary mixture fluid layer subjected to vertical temperature and concentration gradients. *Chem Eng Sci* **60**: 6939.

Klotzsch, E., Smith, M. L., Kubow, K. E., Muntwyler, S., Little, W. C., Beyeler, F., Gourdon, D., Nelson, B. J., Vogel, V. (2009). Fibronectin forms the most extensible biological fibers displaying switchable force-exposed cryptic binding sites. *Proc Natl Acad Sci USA* **106**: 18267–18272.

Koike, N., Fukumura, D., Gralla, O., Au, P., Schechner, J. S., Jain, R. K. (2004). Tissue engineering: creation of long-lasting blood vessels. *Nature* **428**: 138–139.

Korff, T., Augustin, H. G. (1998). Integration of endothelial cells in multicellular spheroids prevents apoptosis and induces differentiation. *J Cell Biol* **143**: 1341–1352.

Korff, T., Augustin, H. G. (1999). Tensional forces in fibrillar extracellular matrices control directional capillary sprouting. *J Cell Sci* **112**: 3249–3258.

Korff, T., Kimmina, S., Martiny-Baron, G., Augustin, H. G. (2001). Blood vessel maturation in a 3-dimensional spheroidal coculture model: direct contact with smooth muscle cells regulates endothelial cell quiescence and abrogates VEGF responsiveness. *FASEB J* **15**: 448–457.

Kothapalli, C. R., van Veen, E., de Valence, S., Chung, S., Zervantonakis, I. K., Gertler, F. B., Kamm, R. D. (2011). A high-throughput microfluidic assay to study neurite response to growth factor gradients. *Lab Chip* **11**: 497–507.

Krüssel, J. S., Behr, B., Milki, A. A., Hirchenhain, J., Wen, Y., Bielfeld, P., Lake Polan, M. (2001). Vascular endothelial growth factor (VEGF) mRNA splice variants are differentially expressed in human blastocysts. *Mol Hum Reprod* **7**: 57–63.

Kunz-Schughart, L. A., Schroeder, J. A., Wondrak, M., van Rey, F., Lehle, K., Hofstaedter, F., Wheatley, D. N. (2006). Potential of fibroblasts to regulate the formation of three-dimensional vessel-like structures from endothelial cells *in vitro*. *Am J Physiol Cell Physiol* **290**: C1385–1398.

Kurpinski, K., Chu, J., Hashi, C., Li, S. (2006). Anisotropic mechanosensing by mesenchymal stem cells. *Proc Natl Acad Sci USA* **103**: 16095–16100.

Lacal, P. M., Morea, V., Ruffini, F., Orecchia, A., Dorio, A. S., Failla, C. M., Soro, S., Tentori, L., Zambruno, G., Graziani, G., Tramontano, A., D'Atri, S. (2008). Inhibition of endothelial cell migration and angiogenesis by a vascular endothelial growth factor receptor-1 derived peptide. *Eur J Cancer* **44**: 1914–1921.

Ladhani, O., Sánchez-Martinez, C., Orgaz, J. L., Jimenez, B., Volpert, O. V. (2011). Pigment epithelium-derived factor blocks tumor extravasation by suppressing amoeboid morphology and mesenchymal proteolysis. *Neoplasia* **13**: 633–642.

Laib, A. M., Bartol, A., Alajati, A., Korff, T., Weber, H., Augustin, H. G. (2009). Spheroid-based human endothelial cell microvessel formation *in vivo*. *Nat Protoc* **4**: 1202–1215.

Languino, L. R., Gehlsen, K. R., Wayner, E., Carter, W. G., Engvall, E., Ruoslahti, E. (1989). Endothelial cells use $\alpha_2\beta_1$ integrin as a laminin receptor. **109**: 2455–2462.

Lauzeral, J., Metens, S., Walgraef, D. (1993). On the phase dynamics of hexagonal patterns. *Europhys Lett* **24**: 707–712.

Lee, H. J., Lee, J.-S., Chansakul, T., Yu, C., Elisseeff, J. H., Yu, S. M. (2006a). Collagen mimetic peptide-conjugated photopolymerizable PEG hydrogel. *Biomaterials* **27**: 5268–5276.

Lee, J., Beighley, P., Ritman, E., Smith, N. (2007). Automatic segmentation of 3D micro-CT coronary vascular images. *Med Image Anal* **11**: 630–647.

Lee, M. J., Thangada, S., Claffey, K. P., Ancellin, N., Liu, C. H., Kluk, M., Volpi, M., Sha'afi, R. I., Hla, T. (1999a). Vascular endothelial cell adherens junction assembly and morphogenesis induced by sphingosine-1-phosphate. *Cell* **99**: 301–312.

Lee, N. V., Sato, M., Annis, D. S., Loo, J. A., Wu, L., Mosher, D. F., Iruela-Arispe, M. L. (2006b). ADAMTS1 mediates the release of antiangiogenic polypeptides from TSP1 and 2. *EMBO J* **25**: 5270–5283.

Lee, S., Kang, J., Yoo, J., Ganesan, S. K., Cook, S. C., Aguilar, B., Ramu, S., Lee, J., Hong, Y.-K. (2009a). Prox1 physically and functionally interacts with COUP-TFII to specify lymphatic endothelial cell fate. *Blood* **113**: 1856–1859.

Lee, S.-H., Moon, J. J., West, J. L. (2008). Three-dimensional micropatterning of bioactive hydrogels via two-photon laser scanning photolithography for guided 3D cell migration. *Biomaterials* **29**: 2962–2968.

Lee, T.-Y., Muschal, S., Pravda, E. A., Folkman, J., Abdollahi, A., Javaherian, K. (2009b). Angiostatin regulates the expression of antiangiogenic and proapoptotic pathways via targeted inhibition of mitochondrial proteins. *Blood* **114**: 1987–1998.

Lee, Y. M., Jeong, C. H., Koo, S. Y., Son, M. J., Song, H. S., Bae, S. K., Raleigh, J. A., Chung, H. Y., Yoo, M. A., Kim, K. W. (2001). Determination of hypoxic region by hypoxia marker in developing mouse embryos *in vivo*: a possible signal for vessel development. *Dev Dyn* **220**: 175–186.

Lee, Y. M., O. H. Kim, Lee, Y. M., Moon, E. J., Lee, D. J., Kim, J. H., Kim, K. W., Kwon, Y. G. (1999b). Sphingosine 1-phosphate induces angiogenesis: Its angiogenic action and signaling mechanism in human umbilical vein endothelial cells. *Biochem Biophys Res Commun* **264**: 743–750.

Lewis, F. T. (1905). The development of the lymphatic system in rabbits. *Am J Anat* **5**: 95–111.

Li, B., Xie, L., Starr, Z. C., Yang, Z., Lin, J.-S., Wang, J. H.-C. (2007). Development of micropost force sensor array with culture experiments for determination of cell traction forces. *Cell Motil Cytoskeleton* **64**: 509–518.

Liao, S., Ruddle, N. H. (2006). Synchrony of high endothelial venules and lymphatic vessels revealed by immunization. *J Immunol* **177**: 3369–3379.

Lieleg, O., Ribbeck, K. (2011). Biological hydrogels as selective diffusion barriers. *Trends Cell Biol* **21**: 543–551.

Liersch, R., Detmar, M. (2007). Lymphangiogenesis in development and disease. *Thromb Haemost* **98**: 304–310.

Lindblom, P., Gerhardt, H., Liebner, S., Abramsson, A., Enge, M., Hellström, M., Bäckström, G., Fredriksson, S., Landegren, U., Nystrom, H. C., Bergström, G., Dejana, E., Östman, A., Lindahl, P., Betsholtz, C. (2003). Endothelial PDGF-B retention is required for proper investment of pericytes in the microvessel wall. *Genes Dev* **17**: 1835–1840.

Ling, Y., Rubin, J., Deng, Y., Huang, C., Demirci, U., Karp, J. M., Khademhosseini, A. (2007). A cell-laden microfluidic hydrogel. *Lab Chip* **7**: 756–762.

Link, A., Vogt, T. K., Favre, S., Britschgi, M. R., Acha-Orbea, H., Hinz, B., Cyster, J. G., Luther, S. A. (2007). Fibroblastic reticular cells in lymph nodes regulate the homeostasis of naive T cells. *Nat Immunol* **8**: 1255–1265.

Livak, K. J., Schmittgen, T. D. (2001). Analysis of relative gene expression data using real-time quantitative PCR and the $2^{-\Delta\Delta C_T}$ method. *Methods* **25**: 402–408.

Lohela, M., Bry, M., Tammela, T., Alitalo, K. (2009). VEGFs and receptors involved in angiogenesis versus lymphangiogenesis. *Curr Opin Cell Biol* **21**: 154–165.

Luque, A., Carpizo, D. R., Iruela-Arispe, M. L. (2003). ADAMTS1/METH1 inhibits endothelial cell proliferation by direct binding and sequestration of $VEGF_{165}$. *J Biol Chem* **278**: 23656–23665.

Ma, B., Jablonska, J., Lindenmaier, W., Dittmar, K. E. J. (2007). Immunohistochemical study of the reticular and vascular network of mouse lymph node using vibratome sections. *Acta Histochem* **109**: 15–28.

Machens, H. G., Grzybowski, S., Bucsky, B., Spanholtz, T., Niedworok, C., Maichle, A., Stöckelhuber, B., Condurache, A., Liu, F., Egana, J. T., Kaun, M., Mailänder, P., Aach, T. (2006). A technique to detect and to quantify fasciocutaneous blood vessels in small laboratory animals ex vivo. *J Surg Res* **131**: 91–96.

Maciag, T., Cerundolo, J., Ilsley, S., Kelley, P. R., Forand, R. (1979). An endothelial cell growth factor from bovine hypothalamus: identification and partial characterization. *Proc Natl Acad Sci USA* **76**: 5674–5678.

Maciag, T., Hoover, G. A., Stemerman, M. B., Weinstein, R. (1981). Serial propagation of human endothelial cells *in vitro*. *J Cell Biol* **91**: 420–426.

Maciag, T., Kadish, J., Wilkins, J., Stemerman, M. B., Weinstein, R. (1982). Organizational behavior of human umbilical vein endothelial cells. *J Cell Biol* **94**: 511–520.

Madan, A., Curtin, P. T. (1993). A 24-base-pair sequence 3′ to the human erythropoietin gene contains a hypoxia-responsive transcriptional enhancer. *Proc Natl Acad Sci USA* **90**: 3928–3932.

Madri, J. A., Williams, S. K. (1983). Capillary endothelial cell cultures: Phenotypic modulation by matrix components. *J Cell Biol* **97**: 53–65.

Martins, G. G., Kolega, J. (2006). Endothelial cell protrusion and migration in three-dimensional collagen matrices. *Cell Motil Cytoskeleton* **63**: 101–115.

Matloubian, M., Lo, C. G., Cinamon, G., Lesneski, M. J., Xu, Y., Brinkmann, V., Allende, M. L., Proia, R. L., Cyster, J. G. (2004). Lymphocyte egress from thymus and peripheral lymphoid organs is dependent on S1P receptor 1. *Nature* **427**: 355–360.

Mazzucchelli, R. I., Warming, S., Lawrence, S. M., Ishii, M., Abshari, M., Washington, A. V., Feigenbaum, L., Warner, A. C., Sims, D. J., Li, W. Q., Hixon, J. A., Gray, D. H. D., Rich, B. E., Morrow, M., Anver, M. R., Cherry, J., Naf, D., Sternberg, L. R., McVicar, D. W., Farr, A. G., Germain, R. N., Rogers, K., Jenkins, N. A., Copeland, N. G., Durum, S. K. (2009). Visualization and identification of IL-7 producing cells in reporter mice. *PLoS ONE* **4**: e7637.

McDonald, J., Duffy, D., Anderson, J. R., Chiu, D., Wu, H., Schueller, O., Whitesides, G. M. (2000). Fabrication of microfluidic systems in poly(dimethylsiloxane). *Electrophoresis* **21**: 27–40.

McDonald, J. C., Whitesides, G. M. (2002). Poly(dimethylsiloxane) as a material for fabricating microfluidic devices. *Acc Chem Res* **35**: 491–499.

Mebius, R. E. (2003). Organogenesis of lymphoid tissues. *Nat Rev Immunol* **3**: 292–303.

Mebius, R. E., Rennert, P., Weissman, I. L. (1997). Developing lymph nodes collect $CD4^+CD3^-$ $LT\beta^+$ cells that can differentiate to APC, NK cells, and follicular cells but not T or B cells. *Immunity* **7**: 493–504.

Mebius, R. E., Streeter, P. R., Michie, S., Butcher, E. C., Weissman, I. L. (1996). A developmental switch in lymphocyte homing receptor and endothelial vascular addressin expression regulates lymphocyte homing and permits $CD4^+$ $CD3^-$ cells to colonize lymph nodes. *Proc Natl Acad Sci USA* **93**: 11019–11024.

Mik, E. G., Johannes, T., Zuurbier, C. J., Heinen, A., Houben-Weerts, J. H. P. M., Balestra, G. M., Stap, J., Beek, J. F., Ince, C. (2008). *In vivo* mitochondrial oxygen tension measured by a delayed fluorescence lifetime technique. *Biophys J* **95**: 3977–3990.

Milhaud, J. (2004). New insights into water-phospholipid model membrane interactions. *Biochim Biophys Acta* **1663**: 19–51.

Mongiat, M., Sweeney, S. M., San Antonio, J. D., Fu, J., Iozzo, R. V. (2003). Endorepellin, a novel inhibitor of angiogenesis derived from the C terminus of perlecan. *J Biol Chem* **278**: 4238–4249.

Montañez, E., Casaroli-Marano, R. P., Vilaró, S., Pagan, R. (2002). Comparative study of tube assembly in three-dimensional collagen matrix and on matrigel coats. *Angiogenesis* **5**: 167–172.

Montesano, R., Mouron, P., Orci, L. (1985). Vascular outgrowths from tissue explants embedded in fibrin or collagen gels: a simple *in vitro* model of angiogenesis. *Cell Biol Int Rep* **9**: 869–875.

Montesano, R., Orci, L. (1987). Phorbol esters induce angiogenesis *in vitro* from large-vessel endothelial cells. *J Cell Physiol* **130**: 284–291.

Morikawa, S., Baluk, P., Kaidoh, T., Haskell, A., Jain, R. K., McDonald, D. M. (2002). Abnormalities in pericytes on blood vessels and endothelial sprouts in tumors. *Am J Pathol* **160**: 985–1000.

Morwood, S. R., Nicholson, L. B. (2006). Modulation of the immune response by extracellular matrix proteins. *Arch Immunol Ther Exp (Warsz)* **54**: 367–374.

Mosher, D. F., Doyle, M. J., Jaffe, E. A. (1982). Synthesis and secretion of thrombospondin by cultured human endothelial cells. *J Cell Biol* **93**: 343–348.

Muller, P. Y., Janovjak, H., Miserez, A. R., Dobbie, Z. (2002). Processing of gene expression data generated by quantitative real-time RT-PCR. *Biotechniques* **32**: 1378–1379.

Mundel, T. M., Kalluri, R. (2007). Type IV collagen-derived angiogenesis inhibitors. *Microvasc Res* **74**: 85–89.

Muniz, L. R., Pacer, M. E., Lira, S. A., Furtado, G. C. (2011). A critical role for dendritic cells in the formation of lymphatic vessels within tertiary lymphoid structures. *J Immunol* **187**: 828–834.

Murdoch, C., Lewis, C. E. (2005). Macrophage migration and gene expression in response to tumor hypoxia. *Int J Cancer* **117**: 701–708.

Murdoch, C., Muthana, M., Lewis, C. E. (2005). Hypoxia regulates macrophage functions in inflammation. *J Immunol* **175**: 6257–6263.

Murphy, M., Walter, B. N., Pike-Nobile, L., Fanger, N. A., Guyre, P. M., Browning, J. L., Ware, C. F., Epstein, L. B. (1998). Expression of the lymphotoxin β receptor on follicular stromal cells in human lymphoid tissues. *Cell Death Differ* **5**: 497–505.

Myllyharju, J., Schipani, E. (2010). Extracellular matrix genes as hypoxia-inducible targets. *Cell Tissue Res* **339**: 19–29.

Mäki, J. M., Sormunen, R., Lippo, S., Kaarteenaho-Wiik, R., Soininen, R., Myllyharju, J. (2005). Lysyl oxidase is essential for normal development and function of the respiratory system and for the integrity of elastic and collagen fibers in various tissues. *Am J Pathol* **167**: 927–936.

Nagy, N., Mwizerwa, O., Yaniv, K., Carmel, L., Pieretti-Vanmarcke, R., Weinstein, B. M., Goldstein, A. M. (2009). Endothelial cells promote migration and proliferation of enteric neural crest cells via β1 integrin signaling. *Dev Biol* **330**: 263–272.

Nakatsu, M. N., Sainson, R. C., Aoto, J. N., Taylor, K. L., Aitkenhead, M., Pérez-del Pulgar, S., Carpenter, P. M., Hughes, C. C. (2003). Angiogenic sprouting and capillary lumen formation modeled by human umbilical vein endothelial cells (HUVEC) in fibrin gels: the role of fibroblasts and angiopoietin-1 . *Microvasc Res* **66**: 102–112.

Nanka, O., Valásek, P., Dvoráková, M., Grim, M. (2006). Experimental hypoxia and embryonic angiogenesis. *Dev Dyn* **235**: 723–733.

NCBI (2009). Primer-BLAST. U.S. National Library of Medicine 8600 Rockville Pike, Bethesda MD, 20894 USA.
URL `http://www.ncbi.nlm.nih.gov/tools/primer-blast/`

Nelson, C. M., Tien, J. (2006). Microstructured extracellular matrices in tissue engineering and development. *Curr Opin Biotechnol* **17**: 518–523.

Neufeld, G., Cohen, T., Gengrinovitch, S., Poltorak, Z. (1999). Vascular endothelial growth factor (VEGF) and its receptors. *FASEB J* **13**: 9–22.

Neumann, T., Nicholson, B. S., Sanders, J. E. (2003). Tissue engineering of perfused microvessels. *Microvascular Research* **66**: 59–67.

Nguyen, T.-H., Eichmann, A., Le Noble, F., Fleury, V. (2006). Dynamics of vascular branching morphogenesis: The effect of blood and tissue flow. *Physical Review E* **73**.

van Nieuw Amerongen, G. P., Koolwijk, P., Versteilen, A., van Hinsbergh, V. W. (2003). Involvement of RhoA/Rho kinase signaling in VEGF-induced endothelial cell migration and angiogenesis *in vitro*. *Arterioscler Thromb Vasc Biol* **23**: 211.

Nishikawa, S., Honda, K., Vieira, P., Yoshida, H. (2003). Organogenesis of peripheral lymphoid organs. *Immunol Rev* **195**: 72–80.

le Noble, F., Moyon, D., Pardanaud, L., Yuan, L., Djonov, V., Matthijsen, R., Bréant, C., Fleury, V., Eichmann, A. (2004). Flow regulates arterial-venous differentiation in the chick embryo yolk sac. *Development* **131**: 361–375.

Nyberg, P., Xie, L., Kalluri, R. (2005). Endogenous inhibitors of angiogenesis. *Cancer Res* **65**: 3967–3979.

Oh, H., Takagi, H., Suzuma, K., Otani, A., Matsumura, M., Honda, Y. (1999). Hypoxia and vascular endothelial growth factor selectively up-regulate angiopoietin-2 in bovine microvascular endothelial cells. *J Biol Chem* **274**: 15732–15739.

Ohtani, O., Ohtani, Y. (2008). Structure and function of rat lymph nodes. *Arch Histol Cytol* **71**: 69–76.

Olander, J. V., Bremer, M. E., Marasa, J. C., Feder, J. (1985). Fibrin-enhanced endothelial cell organization. *J Cell Physiol* **125**: 1–9.

Oliver, G. (2004). Lymphatic vasculature development. *Nat Rev Immunol* **4**: 35–45.

Ozerdem, U., Grako, K. A., Dahlin-Huppe, K., Monosov, E., Stallcup, W. B. (2001). NG2 proteoglycan is expressed exclusively by mural cells during vascular morphogenesis. *Dev Dyn* **222**: 218–227.

O' Reilly, M. S., Holmgren, L., Shing, Y., Chen, C., Rosenthal, R. A., Moses, M., Lane, W. S., Cao, Y., Sage, E. H., Folkman, J. (1994). Angiostatin: A novel angiogenesis inhibitor that mediates the suppression of metastases by a Lewis lung carcinoma. *Cell* **79**: 315–328.

Palmer, L. A., Semenza, G. L., Stoler, M. H., Johns, R. A. (1998). Hypoxia induces type II NOS gene expression in pulmonary artery endothelial cells via HIF-1. *Am J Physiol* **274**: L212–219.

Park, J. E., Keller, G. A., Ferrara, N. (1993). The vascular endothelial growth factor (VEGF) isoforms: Differential deposition into the subepithelial extracellular matrix and bioactivity of extracellular matrix-bound VEGF. *Mol Biol Cell* **4**: 1317–1326.

van de Pavert, S. A., Mebius, R. E. (2010). New insights into the development of lymphoid tissues. *Nat Rev Immunol* **10**: 664–674.

van de Pavert, S. A., Olivier, B. J., Goverse, G., Vondenhoff, M. F., Greuter, M., Beke, P., Kusser, K., Höpken, U. E., Lipp, M., Niederreither, K., Blomhoff, R., Sitnik, K., Agace, W. W., Randall, T. D., de Jonge, W. J., Mebius, R. E. (2009). Chemokine CXCL13 is essential for lymph node initiation and is induced by retinoic acid and neuronal stimulation. *Nat Immunol* **10**: 1193–1199.

Pelletier, L., Regnard, J., Fellmann, D., Charbord, P. (2000). An *in vitro* model for the study of human bone marrow angiogenesis: Role of hematopoietic cytokines. *Lab Invest* **80**: 501–511.

Pepper, M. S., Ferrara, N., Orci, L., Montesano, R. (1992). Potent synergism between vascular endothelial growth factor and basic fibroblast growth factor in the induction of angiogenesis *in vitro*. *Biochem Biophys Res Commun* **189**: 824–831.

Petitclerc, E., Boutaud, A., Prestayko, A., Xu, J., Sado, Y., Ninomiya, Y., Sarras, M. P. J., Hudson, B. G., Brooks, P. C. (2000). New functions for non-collagenous domains of human collagen type IV. *J Biol Chem* **275**: 8051–8061.

Peyton, S. R., Kim, P. D., Ghajar, C. M., Seliktar, D., Putnam, A. J. (2008). The effects of matrix stiffness and RhoA on the phenotypic plasticity of smooth muscle cells in a 3-D biosynthetic hydrogel system. *Biomaterials* **29**: 2597–2607.

Pfaffl, M. W. (2001). A new mathematical model for relative quantification in real-time RT-PCR. *Nucleic Acids Res* **29**: e45.

Pham, T. H., Baluk, P., Xu, Y., Grigorova, I., Bankovich, A. J., Pappu, R., Coughlin, S., McDonald, D. M., Schwab, S. R., Cyster, J. G. (2010). Lymphatic endothelial cell sphingosine kinase activity is required for lymphocyte egress and lymphatic patterning. *J Exp Med* **207**: 17–27.

Pieper, J. S., Hafmans, T., Veerkamp, J. H., van Kuppevelt, T. H. (2000). Development of tailor-made collagen-glycosaminoglycan matrices: EDC/NHS crosslinking, and ultrastructural aspects. *Biomaterials* **21**: 581–593.

Pinney, D. F., Emerson, C. P. J. (1989). 10T1/2 cells: an *in vitro* model for molecular genetic analysis of mesodermal determination and differentiation. *Environ Health Perspect* **80**: 221–227.

Preibisch, S., Saalfeld, S., Tomancak, P. (2009). Globally optimal stitching of tiled 3D microscopic image acquisitions. *Bioinformatics* **25**: 1463–1465.

Price, G. M., Wong, K. H. K., Truslow, J. G., Leung, A. D., Acharya, C., Tien, J. (2010). Effect of mechanical factors on the function of engineered human blood microvessels in microfluidic collagen gels. *Biomaterials* **31**: 6182–6189.

Provot, S., Zinyk, D., Gunes, Y., Kathri, R., Le, Q., Kronenberg, H. M., Johnson, R. S., Longaker, M. T., Giaccia, A. J., Schipani, E. (2007). Hif-1α regulates differentiation of limb bud mesenchyme and joint development. *J Cell Biol* **177**: 451–464.

R Development Core Team (2006). R: A Language and Environment for Statistical Computing. Vienna, Austria. ISBN 3-900051-07-0.
URL `http://www.R-project.org`

Raleigh, J. A., Calkins-Adams, D. P., Rinker, L. H., Ballenger, C. A., Weissler, M. C., Fowler, W. C. J., Novotny, D. B., Varia, M. A. (1998). Hypoxia and vascular endothelial growth factor expression in human squamous cell carcinomas using pimonidazole as a hypoxia marker. *Cancer Res* **58**: 3765–3768.

Ramanujan, S., Pluen, A., McKee, T. D., Brown, E. B., Boucher, Y., Jain, R. K. (2002). Diffusion and convection in collagen gels: Implications for transport in the tumor interstitium. *Biophys J* **83**: 1650–1660.

Randall, T. D., Carragher, D. M., Rangel-Moreno, J. (2008). Development of secondary lymphoid organs. *Annu Rev Immunol* **26**: 627–650.

Randolph, G. J. (2001). Dendritic cell migration to lymph nodes: cytokines, chemokines, and lipid mediators. *Semin Immunol* **13**: 267–274.

Rangel-Moreno, J., Carragher, D. M., de la Luz Garcia-Hernandez, M., Hwang, J. Y., Kusser, K., Hartson, L., Kolls, J. K., Khader, S. A., Randall, T. D. (2011). The development of inducible bronchus-associated lymphoid tissue depends on IL-17. *Nat Immunol* **12**: 639–646.

Rasband, W. (1997-2011). ImageJ. Bethesda, Maryland, USA.
URL `http://imagej.nih.gov/ij/`

Raugi, G. J., Mumby, S. M., Abbott-Brown, D., Bornstein, P. (1982). Thrombospondin: Synthesis and secretion by cells in culture. *J Cell Biol* **95**: 351–354.

Reznikoff, C. A., Brankow, D. W., Heidelberger, C. (1973). Establishment and characterization of a cloned line of C3H mouse embryo cells sensitive to postconfluence inhibition of division. *Cancer Res* **33**: 3231–3238.

Rhim, J. S., Tsai, W., Chen, Z., van Waes, C., Burger, A. M., Lautenberger, J. A. (1998). A human vascular endothelial cell model to study angiogenesis and tumorigenesis. *Carcinogenesis* **19**: 673–681.

Riikonen, T., Koivisto, L., Vihinen, P., Heino, J. (1995). Transforming growth factor-β regulates collagen gel contraction by increasing $\alpha_2\beta_1$ integrin expression in osteogenic cells. *J Biol Chem* **270**: 376–382.

Robinson, C. J., Stringer, S. E. (2001). The splice variants of vascular endothelial growth factor (VEGF) and their receptors. *J Cell Sci* **114**: 853–865.

Roozendaal, R., Mebius, R. E. (2011). Stromal cell–immune cell interactions. *Annu Rev Immunol* **29**: 23–43.

Roozendaal, R., Mempel, T. R., Pitcher, L. A., Gonzalez, S. F., Verschoor, A., Mebius, R. E., von Andrian, U. H., Carroll, M. C. (2009). Conduits mediate transport of low-molecular-weight antigen to lymph node follicles. *Immunity* **30**: 264–276.

du Roure, O., Saez, A., Buguin, A., Austin, R. H., Chavrier, P., Silberzan, P., Ladoux, B. (2005). Force mapping in epithelial cell migration. *Proc Natl Acad Sci USA* **102**: 2390–2395.

Roy, R., Zhang, B., Moses, M. A. (2006). Making the cut: Protease-mediated regulation of angiogenesis. *Exp Cell Res* **312**: 608–622.

Rozario, T., DeSimone, D. W. (2010). The extracellular matrix in development and morphogenesis: a dynamic view. *Dev Biol* **341**: 126–140.

Ruhrberg, C., Gerhardt, H., Golding, M., Watson, R., Ioannidou, S., Fujisawa, H., Betsholtz, C., Shima, D. T. (2002). Spatially restricted patterning cues provided by heparin-binding VEGF-A control blood vessel branching morphogenesis. *Genes Dev* **16**: 2684–2698.

Sabin, F. R. (1909). The lymphatic system in human embryos, with a consideration of the morphology of the system as a whole. *Am J Anat* **9**: 43–91.

Sabin, F. R. (1913). The origin and development of the lymphatic system. The John Hopkins Press, Baltimore.

Sabin, F. R. (1916). The method of growth of the lymphatic system. *Science* **44**: 145–158.

Sacharidou, A., Koh, W., Stratman, A. N., Mayo, A. M., Fisher, K. E., Davis, G. E. (2010). Endothelial lumen signaling complexes control 3D matrix-specific tubulogenesis through interdependent Cdc42- and MT1-MMP-mediated events. *Blood* **115**: 5259–5269.

Sandoval, R., Malik, A. B., Minshall, R. D., Kouklis, P., Ellis, C. A., Tiruppathi, C. (2001). Ca^{2+} signalling and PKCα activate increased endothelial permeability by disassembly of VE-cadherin junctions. *J Physiol* **533**: 433–445.

Sato, Y., Rifkin, D. B. (1989). Inhibition of endothelial cell movement by pericytes and smooth muscle cells: activation of a latent transforming growth factor-β1-like molecule by plasmin during co-culture. *J Cell Biol* **109**: 309–315.

Saunders, W. B., Bayless, K. J., Davis, G. E. (2005). MMP-1 activation by serine proteases and MMP-10 induces human capillary tubular network collapse and regression in 3D collagen matrices. *J Cell Sci* **118**: 2325–2340.

Saunders, W. B., Bohnsack, B. L., Faske, J. B., Anthis, N. J., Bayless, K. J., Hirschi, K. K., Davis, G. E. (2006). Coregulation of vascular tube stabilization by endothelial cell TIMP-2 and pericyte TIMP-3. *J Cell Biol* **175**: 179–191.

Schechner, J. S., Nath, A. K., Zheng, L., Kluger, M. S., Hughes, C. C. W., Sierra-Honigmann, M. R., Lorber, M. I., Tellides, G., Kashgarian, M., Bothwell, A. L. M., Pober, J. S. (2000). *In vivo* formation of complex microvessels lined by human endothelial cells in an immunodeficient mouse. *Proc Natl Acad Sci USA* **97**: 9191–9196.

Schmutz, S., Bosco, N., Chappaz, S., Boyman, O., Acha-Orbea, H., Ceredig, R., Rolink, A. G., Finke, D. (2009). Cutting edge: IL-7 regulates the peripheral pool of adult RORγ^+ lymphoid tissue inducer cells. *J Immunol* **183**: 2217–2221.

Schultz, G. S., Wysocki, A. (2009). Interactions between extracellular matrix and growth factors in wound healing. *Wound Repair Regen* **17**: 153–162.

Sechler, J. L., Schwarzbauer, J. E. (1998). Control of cell cycle progression by fibronectin matrix architecture. *J Biol Chem* **273**: 25533–25526.

Seghezzi, G., Patel, S., Ren, C. J., Gualandris, A., Pintucci, G., Robbins, E. S., Shapiro, R. L., Aubrey, S., Galloway, C., Rifkin, D. B., Mignatti, P. (1998). Fibroblast growth factor-2 (FGF-2) induces vascular endothelial growth factor (VEGF) expression in the endothelial cells of forming capillaries: An autocrine mechanism contributing to angiogenesis. *J Cell Biol* **141**: 1659–1673.

Sekiya, A., Okano-Kosugi, H., Yamazaki, C. M., Koide, T. (2011). Pigment epithelium-derived factor (PEDF) shares binding sites in collagen with heparin/heparan sulfate proteoglycans. *J Biol Chem* **286**: 26364–26374.

Seliktar, D., Zisch, A. H., Lutolf, M. P., Wrana, J. L., Hubbell, J. A. (2004). MMP-2 sensitive, VEGF-bearing bioactive hydrogels for promotion of vascular healing. *J Biomed Mater Res A* **68A**: 704–716.

Semenza, G. L., Jiang, B. H., Leung, S. W., Passantino, R., Concordet, J. P., Maire, P., Giallongo, A. (1996). Hypoxia response elements in the aldolase a, enolase 1, and lactate dehydrogenase a gene promoters contain essential binding sites for hypoxia-inducible factor 1. *J Biol Chem* **271**: 32529–32537.

Sephel, G., Kennedy, R., S., K. (1996). Expression of capillary basement membrane components during sequential phases of wound angiogenesis. *Matrix Biol* **15**: 263–279.

Shalaby, F., Rossant, J., Yamaguchi, T. P., Gertsenstein, M., Wu, X. F., Breitman, M. L., Schuh, A. C. (1995). Failure of blood-island formation and vasculogenesis in Flk-1-deficient mice. *Nature* **376**: 62–66.

Shamloo, A., Heilshorn, S. C. (2010). Matrix density mediates polarization and lumen formation of endothelial sprouts in VEGF gradients. *Lab Chip* **10**: 3061–3068.

Shin, J. W., Min, M., Larrieu-Lahargue, F., Canron, X., Kunstfeld, R., Nguyen, L., Henderson, J. E., Bikfalvi, A., Detmar, M., Hong, Y.-K. (2006). Prox1 promotes lineage-specific expression of fibroblast growth factor (FGF) receptor-3 in lymphatic endothelium: a role for FGF signaling in lymphangiogenesis. *Mol Biol Cell* **17**: 576–584.

Shweiki, D., Neeman, M., Itin, A., Keshet, E. (1995). Induction of vascular endothelial growth factor expression by hypoxia and by glucose deficiency in multicell spheroids: implications for tumor angiogenesis. *Proc Natl Acad Sci USA* **92**: 768–772.

Siekmann, A. F., Covassin, L., Lawson, N. D. (2008). Modulation of VEGF signalling output by the Notch pathway. *Bioessays* **30**: 303–313.

Simon, M. C., Keith, B. (2008). The role of oxygen availability in embryonic development and stem cell function. *Nat Rev Mol Cell Biol* **9**: 285–296.

Sixt, M., Kanazawa, N., Selg, M., Samson, T., Roos, G., Reinhardt, D. P., Pabst, R., Lutz, M. B., Sorokin, L. (2005). The conduit system transports soluble antigens from the afferent lymph to resident dendritic cells in the T cell area of the lymph node. *Immunity* **22**: 19–29.

Sorokin, L. (2010). The impact of the extracellular matrix on inflammation. *Nat Rev Immunol* **10**: 712–723.

Sottile, J. (2004). Regulation of angiogenesis by extracellular matrix. *Biochim Biophys Acta* **1654**: 13–22.

Sottile, J., Hocking, D. C. (2002). Fibronectin polymerization regulates the composition and stability of extracellular matrix fibrils and cell-matrix adhesions. *Mol Biol Cell* **13**: 3546–3559.

Spyridopoulos, I. (2002). Divergence of angiogenic and vascular permeability signaling by VEGF: Inhibition of protein kinase C suppresses VEGF-induced angiogenesis, but promotes VEGF-induced, NO-dependent vascular permeability. *Arteriosclerosis, Thrombosis, and Vascular Biology* **22**: 901.

Srinivasan, R. S., Dillard, M. E., Lagutin, O. V., Lin, F.-J., Tsai, S., Tsai, M.-J., Samokhvalov, I. M., Oliver, G. (2007). Lineage tracing demonstrates the venous origin of the mammalian lymphatic vasculature. *Genes Dev* **21**: 2422–2432.

Srinivasan, R. S., Geng, X., Yang, Y., Wang, Y., Mukatira, S., Studer, M., Porto, M. P. R., Lagutin, O., Oliver, G. (2010). The nuclear hormone receptor Coup-TFII is required for the initiation and early maintenance of Prox1 expression in lymphatic endothelial cells. *Genes Dev* **24**: 696–707.

Stetler-Stevenson, W. G. (2008). The tumor microenvironment: regulation by MMP-independent effects of tissue inhibitor of metalloproteinases-2. *Cancer Metastasis Rev* **27**: 57–66.

Stratman, A. N., Malotte, K. M., Mahan, R. D., Davis, M. J., Davis, G. E. (2009a). Pericyte recruitment during vasculogenic tube assembly stimulates endothelial basement membrane matrix formation. *Blood* **114**: 5091–5101.

Stratman, A. N., Saunders, W. B., Sacharidou, A., Koh, W., Fisher, K. E., Zawieja, D. C., Davis, M. J., Davis, G. E. (2009b). Endothelial cell lumen and vascular guidance tunnel formation requires MT1-MMP-dependent proteolysis in 3-dimensional collagen matrices. *Blood* **114**: 237–247.

Stratman, A. N., Schwindt, A. E., Malotte, K. M., Davis, G. E. (2010). Endothelial-derived PDGF-BB and HB-EGF coordinately regulate pericyte recruitment during vasculogenic tube assembly and stabilization. *Blood* **116**: 4720–4730.

Subramanian, P., Notario, P. M., Becerra, S. P. (2010). Pigment epithelium-derived factor receptor (PEDF-R): A plasma membrane-linked phospholipase with PEDF binding affinity. *Adv Exp Med Biol* **664**: 29–37.

Suchting, S., Freitas, C., le Noble, F., Benedito, R., Bréant, C., Duarte, A., Eichmann, E. (2007). The Notch ligand Delta-like 4 negatively regulates endothelial tip cell formation and vessel branching. *Proc Natl Acad Sci USA* **104**: 3225–3230.

Sun, J., Hopkins, B. D., Tsujikawa, K., Perruzzi, C., Adini, I., Swerlick, R., Bornstein, P., Lawler, J., Benjamin, L. E. (2009). Thrombospondin-1 modulates VEGF-A-mediated Akt signaling and capillary survival in the developing retina. *Am J Physiol Heart Circ Physiol* **296**: H1344–1351.

Takei, T., Sakai, S., Ono, T., Ijima, H., Kawakami, K. (2006). Fabrication of endothelialized tube in collagen gel as starting point for self-developing capillary-like network to construct three-dimensional organs *in vitro*. *Biotechnol Bioeng* **95**: 1–7.

Takei, T., Sakai, S., Yokonuma, T., Ijima, H., Kawakami, K. (2007). Fabrication of artificial endothelialized tubes with predetermined three-dimensional configuration from flexible cell-enclosing alginate fibers. *Biotechnol Prog* **23**: 182–186.

Tanaka, Y., Baba, K., Duncan, T. J., Kubota, A., Asahi, T., Quantock, A. J., Yamato, M., Okano, T., Nishida, K. (2011). Transparent, tough collagen laminates prepared by oriented flow casting, multi-cyclic vitrification and chemical cross-linking. *Biomaterials* **32**: 3358–3366.

Tang, M., Golden, A., Tien, J. (2004). Fabrication of collagen gels that contain patterned, micrometer-scale cavities. *Advanced Materials* **16**: 1345–1348.

Tang, M. D., Golden, A. P., Tien, J. (2003). Molding of three-dimensional microstructures of gels. *J Amer Chem Soc* **125**: 12988–12989.

Tatin, F., Varon, C., Génot, E., Moreau, V. (2006). A signalling cascade involving PKC, Src and Cdc42 regulates podosome assembly in cultured endothelial cells in response to phorbol ester. *J Cell Sci* **119**: 769–781.

Taylor, C. J., Motamed, K., Lilly, B. (2006). Protein kinase C and downstream signaling pathways in a three-dimensional model of phorbol ester-induced angiogenesis. *Angiogenesis* **9**: 39–51.

Taylor, S. M., Jones, P. A. (1979). Multiple new phenotypes induced in 10T½ and 3T3 cells treated with 5-azacytidine. *Cell* **17**: 771–779.

Thyboll, J., Kortesmaa, J., Cao, R., Soininen, R., Wang, L., Iivanainen, A., Sorokin, L., Risling, M., Cao, Y., Tryggvason, K. (2002). Deletion of the laminin α4 chain leads to impaired microvessel maturation. *Mol Cell Biol* **22**: 1194–1202.

Tian, H., McKnight, S. L., Russell, D. W. (1997). Endothelial PAS domain protein 1 (EPAS1), a transcription factor selectively expressed in endothelial cells. *Genes Dev* **11**: 72.

Tien, J., Chen, C. S. (2002). Patterning the cellular microenvironment. *IEEE Eng Med Biol Mag* **21**: 95–98.

Tolsma, S. S., Volpert, O. V., Good, D. J., Frazier, D. J., Polverini, P. J., Bouck, N. (1993). Peptides derived from two separate domains of the matrix protein thrombospondin-1 have anti-angiogenic activity. *J Cell Biol* **122**: 497–511.

Vailhé, B., Vittet, D., Feige, J. J. (2001). *In vitro* models of vasculogenesis and angiogenesis. *Lab Invest* **81**: 439–452.

Varia, M. A., Calkins-Adams, D. P., Rinker, L. H., Kennedy, A. S., Novotny, D. B., Fowler, W. C. J., Raleigh, J. A. (1998). Pimonidazole: a novel hypoxia marker for complementary study of tumor hypoxia and cell proliferation in cervical carcinoma. *Gynecol Oncol* **71**: 270–277.

Velling, T., Risteli, J., Wennerberg, K., Mosher, D. F., Johansson, S. (2002). Polymerization of type I and III collagens is dependent on fibronectin and enhanced by integrins $\alpha_{11}\beta_1$ and $\alpha_2\beta_1$. *J Biol Chem* **277**: 37377–37381.

Vickerman, M. B., Keith, P. A., McKay, T. L., Gedeon, D. J., Watanabe, M., Montano, M., Karunamuni, G., Kaiser, P. K., Sears, J. E., Ebrahem, Q., Ribita, D., Hylton, A. G., Parsons-Wingerter, P. (2009). VESGEN 2D: automated, user-interactive software for quantification and mapping of angiogenic and lymphangiogenic trees and networks. *Anat Rec (Hoboken)* **292**: 320–332.

Vivien, L., Benoist, C., Mathis, D. (2001). T lymphocytes need IL-7 but not IL-4 or IL-6 to survive *in vivo*. *Int Immunol* **13**: 763–768.

Volpert, O. V., Lawler, J., Bouck, N. P. (1998). A human fibrosarcoma inhibits systemic angiogenesis and the growth of experimental metastases via thrombospondin-1. *Proc Natl Acad Sci USA* **95**: 6343–6348.

Vondenhoff, M. F., Greuter, M., Goverse, G., Elewaut, D., Dewint, P., Ware, C. F., Hoorweg, K., Kraal, G., Mebius, R. E. (2009a). LTβR signaling induces cytokine expression and up-regulates lymphangiogenic factors in lymph node anlagen. *J Immunol* **182**: 5439–5445.

Vondenhoff, M. F., van de Pavert, S. A., Dillard, M. E., Greuter, M., Goverse, G., Oliver, G., Mebius, R. E. (2009b). Lymph sacs are not required for the initiation of lymph node formation. *Development* **136**: 29–34.

Vu, T. H., Shipley, J. M., Bergers, G., Berger, J. E., Helms, J. A., Hanahan, D., Shapiro, S. D., Senior, R. M., Werb, Z. (1998). MMP-9/gelatinase B is a key regulator of growth plate angiogenesis and apoptosis of hypertrophic chondrocytes. *Cell* **99**: 411–422.

Waltenberger, J., Claesson-Welsh, L., Siegbahn, A., Shibuya, M., Heldin, C. H. (1994). Different signal transduction properties of KDR and Flt1, two receptors for vascular endothelial growth factor. *J Biol Chem* **269**: 26988–26995.

Wan, J., Chai, H., Yu, Z., Ge, W., Kang, N., Xia, W., Che, Y. (2011). HIF-1α effects on angiogenic potential in human small cell lung carcinoma. *J Exp Clin Cancer Res* **30**: 77.

Wang, F., van Brocklyn, J. R., Hobson, J. P., Movafagh, S., Zukowska-Grojec, Z., Milstien, S., Spiegel, S. (1999). Sphingosine 1-phosphate stimulates cell migration through a G_i-coupled cell surface receptor. *J Biol Chem* **274**: 35343–35350.

Wang, N., Tytell, J. D., Ingber, D. E. (2009). Mechanotransduction at a distance: mechanically coupling the extracellular matrix with the nucleus. *Nat Rev Mol Cell Biol* **10**: 75–82.

Wang, Y., Nakayama, M., Pitulescu, M. E., Schmidt, T. S., Bochenek, M. L., Sakakibara, A., Adams, S., Davy, A., Deutsch, U., Lüthi, U., Barberis, A., Benjamin, L. E., Mäkinen, T., Nobes, C. D., Adams, R. H. (2010). Ephrin-B2 controls VEGF-induced angiogenesis and lymphangiogenesis. *Nature* **465**: 483–486.

White, A., Carragher, D., Parnell, S., Msaki, A., Perkins, N., Lane, P., Jenkinson, E., Anderson, G., Caamaño, J. H. (2007). Lymphotoxin a-dependent and -independent signals regulate stromal organizer cell homeostasis during lymph node organogenesis. *Blood* **110**: 1950–1959.

Wigle, J. T., Oliver, G. (1999). Prox1 function is required for the development of the murine lymphatic system. *Cell* **98**: 769–778.

Wijelath, E. S. (2002). Novel vascular endothelial growth factor binding domains of fibronectin enhance vascular endothelial growth factor biological activity. *Circulation Research* **91**: 25–31.

Willard-Mack, C. L. (2006). Normal structure, function, and histology of lymph nodes. *Toxicol Pathol* **34**: 409–424.

Williams, B. R., Gelman, R. A., Poppke, D. C., Piez, K. A. (1978). Collagen fibril formation: optimal *in vitro* conditions and preliminary kinetic results. *J Biol Chem* **253**: 6578–6585.

Xia, Y., McClelland, J. J., Gupta, R., Qin, D., Zhao, X.-M., Sohn, L. L., Celotta, R. J., Whitesides, G. M. (1997). Replica molding using polymeric materials: A practical step toward nanomanufacturing. *Adv Mater* **9**: 147–149.

Xian, X., Håkansson, J., Ståhlberg, A., Lindblom, P., Betsholtz, C., Gerhardt, H., Semb, H. (2006). Pericytes limit tumor cell metastasis. *J Clin Invest* **116**: 642–651.

Yamakawa, M., Liu, L. X., Date, T., Belanger, A. J., Vincent, K. A., Akita, G. Y., Kuriyama, T., Cheng, S. H., Gregory, R. J., Jiang, C. (2003). Hypoxia-inducible factor-1 mediates activation of cultured vascular endothelial cells by inducing multiple angiogenic factors. *Circ Res* **93**: 664–73.

Yang, S., Graham, J., Kahn, J. W., Schwartz, E. A., Gerritsen, M. E. (1999). Functional roles for PECAM-1 (CD31) and VE-cadherin (CD144) in tube assembly and lumen formation in three-dimensional collagen gels. *Am J Pathol* **155**: 887–895.

Yoshiji, H., Kuriyama, S., Ways, D. K., Yoshii, J., Miyamoto, Y., Kawata, M., Ikenaka, Y., Tsujinoue, H., Nakatani, T., Shibuya, M., Fukui, H. (1999). Protein kinase C lies on the signaling pathway for vascular endothelial growth factor-mediated tumor development and angiogenesis. *Cancer Res* **59**: 4413–4418.

Young, B., Heath, J. W. (2000). Wheater's Functional Histology. Churchill Livingstone, fourth edition.

Zaslavsky, A., Baek, K.-H., Lynch, R. C., Short, S., Grillo, J., Folkman, J., Italiano, J. E., Ryeom, S. (2010). Platelet-derived thrombospondin-1 is a critical negative regulator and potential biomarker of angiogenesis. *Blood* **115**: 4605–4613.

Zeng, H., Zhao, D., Mukhopadhyay, D. (2002). KDR stimulates endothelial cell migration through heterotrimeric G protein Gq/11-mediated activation of a small GTPase RhoA. *J Biol Chem* **277**: 46791–46798.

Zhang, F., Tang, Z., Hou, X., Lennartsson, J., Li, Y., Koch, A. W., Scotney, P., Lee, C., Arjunan, P., Dong, L., Kumar, A., Rissanen, T. T., Wang, B., Nagai, N., Fons, P., Fariss, R., Zhang, Y., Wawrousek, E., Tansey, G., Raber, J., Fong, G. H., Ding, H., Greenberg, D. A., Becker, K. G., Herbert, J. M., Nash, A., Yla-Herttuala, S., Cao, Y., Watts, R. J., Li, X. (2009). VEGF-B is dispensable for blood vessel growth but critical for their survival, and VEGF-B targeting inhibits pathological angiogenesis. *Proc Natl Acad Sci USA* **106**: 6152–6157.

Zhang, S. X., Ma, J.-x. (2007). Ocular neovascularization: Implication of endogenous angiogenic inhibitors and potential therapy. *Prog Retin Eye Res* **26**: 1–37.

Zheng, Y., Henderson, P. W., Choi, N. W., Bonassar, L. J., Spector, J. A., Stroock, A. D. (2011). Microstructured templates for directed growth and vascularization of soft tissue *in vivo*. *Biomaterials* **32**: 5391–5401.

Zoellner, H., Höfler, M., Beckmann, R., Hufnagl, P., Vanyek, E., Bielek, E., Wojta, J., Fabry, A., Lockie, S., Binder, B. R. (1996). Serum albumin is a specific inhibitor of apoptosis in human endothelial cells. *J Cell Sci* **109**: 2571–2580.